

Deposit & Copying of Thesis Declaration



UNIVERSITY OF
CAMBRIDGE

Please note that you will also need to bind a copy of this Declaration into your final, hardbound copy of thesis - this has to be the very first page of the hardbound thesis.

1	Surname (Family Name)	Forenames(s)	Title
2	Title of Thesis as approved by the Degree Committee		

In accordance with the University Regulations in *Statutes and Ordinances* for the PhD, MSc and MLitt Degrees, I agree to deposit one print copy of my thesis entitled above with the Secretary of the Postgraduate Committee who shall deposit the thesis in the University Library under the following terms and conditions:

1. Thesis Author Declaration

I am the author of this thesis and hereby give the University the right to make my thesis available in print form as described in 2. below.

My thesis is my original work and a product of my own research endeavours and includes nothing which is the outcome of work done in collaboration with others except as declared in the Preface and specified in the text. I hereby assert my moral right to be identified as the author of the thesis.

The deposit and dissemination of my thesis by the University does not constitute a breach of any other agreement, publishing or otherwise, including any confidentiality or publication restriction provisions in sponsorship or collaboration agreements governing my research or work at the University or elsewhere.

2. Access to Dissertation

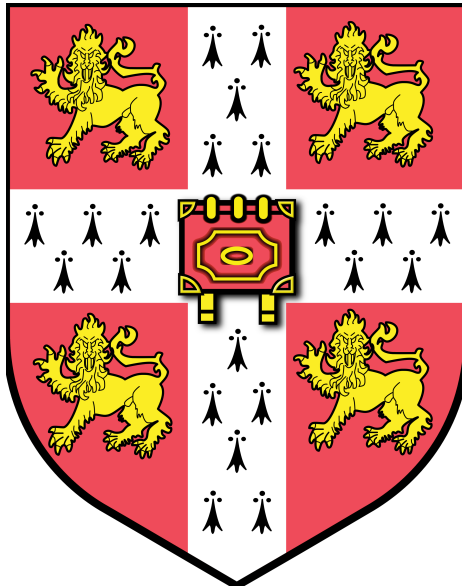
I understand that one print copy of my thesis will be deposited in the University Library for archival and preservation purposes, and that, unless upon my application restricted access to my thesis for a specified period of time has been granted by the Postgraduate Committee prior to this deposit, the thesis will be made available by the University Library for consultation by readers in accordance with University Library Regulations and copies of my thesis may be provided to readers in accordance with applicable legislation.

3	Signature	Date

Corresponding Regulation

Before being admitted to a degree, a student shall deposit with the Secretary of the Postgraduate Committee one copy of his or her hard-bound thesis, in a form approved by the Committee. The Secretary shall deposit the copy of the thesis in the University Library where, subject to restricted access to the thesis for a specified period of time having been granted by the Postgraduate Committee, it shall be made available for consultation by readers in accordance with University Library Regulations and copies of the thesis provided to readers in accordance with applicable legislation.

Numerical Modelling of the Dynamics and Gravitational Radiation of Compact Binaries in General Relativity



Robin Croft

Supervisor: Dr. Ulrich Sperhake
Darwin College
University of Cambridge

This thesis is submitted for the degree of
Doctor of Philosophy

October 2022

Declaration

This thesis is the result of my own work and includes nothing which is the outcome of work done in collaboration except as declared in the Preface and specified in the text. I further state that no substantial part of my thesis has already been submitted, or, is being concurrently submitted for any such degree, diploma or other qualification at the University of Cambridge or any other University or similar institution except as declared in the Preface and specified in the text. It does not exceed the prescribed word limit for the relevant Degree Committee.

Robin Croft
October 2022

Abstract

Numerical Modelling of the Dynamics and Gravitational Radiation of Compact Binaries in General Relativity

General relativity (GR), published in 1915 by Albert Einstein, is the modern description of gravity. GR poses that gravitational physics should be described by matter fields existing in a curved space described by differential geometry. The Newtonian gravitational force is viewed as a fictitious force arising from curvature; on the flipside, matter and energy tell space how to curve as described by Einstein's equation. GR can explain a plethora of gravitational phenomena that are beyond the scope of the traditional Newtonian theory of gravity. Some examples of these phenomena are gravitational time dilation, inspiralling and precessing orbits, gravitational waves, inflation and the big bang. Other examples are self gravitating compact objects such as black holes (BH) and the precise modelling neutron stars (NS). The gravitational waves from the inspirals and collisions of BHs and NSs can be measured by large interferometer experiments such as the Laser Interferometer Gravitational-Wave Observatory (LIGO) which lead to the 2017 Nobel prize in physics.

This thesis is concerned with the modelling of collisions of compact objects using numerical relativity (NR) and developing diagnostics for these simulations. The code used for the simulations is GRChombo, a modern NR code with adaptive mesh refinement (AMR) that supports both the BSSN and CCZ4 formulations. The compact objects modelled are black holes and boson stars.

Boson stars are a theoretical self gravitating complex scalar field configuration governed by the Klein Gordon equation in curved space. These are stars composed of spin zero boson particles rather than atoms like regular fermionic stars. Collisions of these boson stars emit gravitational waves that are detectable at LIGO and other gravitational wave detectors. Boson stars are also a candidate for dark matter clusters permeating galaxies.

In order to collide compact objects one must superpose the initial data for two objects; this generally is not valid in GR and violates the Einstein Equation. While the initial data for black-hole binaries is well known, the initial data for two boson stars is not. The plain superposition of two boson star solutions causes significant artefacts in simulations and an important part of this thesis is the exploration of improvements to naive superposition methods.

Conservation laws have many applications in numerical relativity. However, it is not straightforward to define local conservation laws for general dynamic spacetimes due the lack of coordinate translation symmetries. In flat space, the rate of change of energy-momentum within a finite spacelike volume is equal to the flux integrated over the surface of this volume; for general spacetimes it is necessary to include a volume integral of a source term arising from spacetime curvature. In this work a study of continuity of matter in general relativity is extended to include angular momentum of matter and Noether currents associated with gauge symmetries. Expressions for the Noether charge and flux of complex scalar fields and complex Proca fields are found using this formalism. Expressions for the angular momentum density, flux and source are also derived which are then applied to a numerical relativity collision of boson stars in 3D with non-zero impact parameter as an illustration of the methods.

The previous innovations for the binary initial data, which significantly reduce spurious initial excitations of the scalar field profiles, as well as a measure for the angular momentum are used to study the long-lived post-merger gravitational wave signature of a boson-star binary coalescence. We use full numerical

relativity to simulate the post-merger and track the gravitational afterglow over an extended period of time. We find the afterglow to last much longer than the spin-down timescale. This prolonged gravitational wave afterglow provides a characteristic signal that may distinguish it from other astrophysical sources.

Finally, we investigate the impact of nonzero eccentricity on the kick magnitude and gravitational-wave emission of non-spinning, unequal-mass black-hole binaries. Here "kick" refers to the radiation of linear momentum to the centre of mass of a merging black-hole binary system. Recent numerical relativity calculations have shown that eccentricity can lead to an approximate 25 percent increase in recoil velocities for equal-mass, spinning binaries with spins lying in the orbital plane; these are "superkick" configurations. We confirm that nonzero eccentricities at merger can lead to kicks which are larger by up to approximately 25 percent relative to the quasicircular case for non-spinning, unequal-mass black-hole binaries. We also find that the kick velocity has an oscillatory dependence on eccentricity, which we interpret as a consequence of changes in the angle between the infall direction at merger and the apoapsis (or periapsis) direction.

Robin Croft
October 2022

DECLARATION OF ORIGINAL AND COLLABORATIVE WORK

Chapter 1 is my own work introducing the reader to the topics of Differential Geometry, Tensor Calculus and Relativity.

Chapter 2 is my own work introducing the reader to topics in Numerical Relativity and Boson Stars.

Chapter 3 is a mix of my own work with a collaboration. Section 3.1 is my own work introducing numerical methods. The description of GRCHOMBO in section 3.2.1 is heavily inspired by the collaboration paper [1]; the rest of section 3.2 is my own work and research.

Chapter 4 is based on the collaboration paper [2] with Thomas Helper, Ulrich Sperhake, Miren Radia, Bo-Xuan Ge and Eugene Lim.

Chapter 5 is based on my own work in paper [3].

Chapter 6 is based on the collaboration paper [4] with Thomas Helper, Bo-Xuan Ge, Miren Radia, Tamara Evstafyeva, Eugene Lim, Ulrich Sperhake and Katy Clough.

Chapter 7 is based on the collaboration paper [5] with Miren Radia, Ulrich Sperhake and Emanuele Berti.

Contents

1	Introduction to Differential Geometry and General Relativity	1
1.1	Introduction	2
1.1.1	Introduction to General Relativity	2
1.1.2	Introduction to Compact Objects and Boson Stars	3
1.1.3	Conventions	4
1.2	Differential Geometry	5
1.2.1	Introduction to Geometry and Manifolds	5
1.2.2	Functions, Curves and Tensors on Manifolds	6
1.2.3	The Inner Product and the Metric	7
1.2.4	Maps Between Manifolds	8
1.2.5	Lie Derivatives	10
1.2.6	Lengths on Manifolds	12
1.2.7	Volumes on Manifolds	12
1.2.8	Geodesics	13
1.3	Tensor Calculus and Curvature	15
1.3.1	General Covariance and Coordinate transformations	15
1.3.2	The Covariant Derivative	17
1.3.3	The Connection	19
1.3.4	Curvature Tensors	22
1.3.5	The Divergence Theorem	24
1.4	Relativity	27
1.4.1	Special Relativity	27
1.4.2	General Relativity	28
1.4.3	Physics in Curved Space	29
1.4.4	The Einstein Equation	32
1.4.5	Black Holes	33
1.4.6	The Lagrangian Formulation of General Relativity	36
2	Numerical Relativity and Boson Stars	40
2.1	Numerical Relativity	41
2.1.1	Spacetime Foliation	41
2.1.2	The 3+1 Decomposition	41
2.1.3	Gauss, Codazzi and Ricci Equations	43
2.1.4	Decomposition of Einstein's Equation	44
2.1.5	Foliation Adapted Coordinates	46
2.1.6	ADM Equations	47
2.1.7	BSSN Formalism	47
2.1.8	Z4 Formalism	48
2.1.9	CCZ4 Formalism	49
2.1.10	Gauge Conditions	51

2.2	Mathematical Modelling of Boson Stars	54
2.2.1	Action and Lagrangian	54
2.2.2	Solitons	55
2.2.3	3+1 Klein Gordon System	56
2.2.4	Klein Gordon's Noether Charge	57
2.2.5	Boosted Boson Stars and Black Holes	58
3	Numerical Methods and GRCHOMBO	62
3.1	Numerical Methods	63
3.1.1	Introduction to Numerical Methods	63
3.1.2	Numerical Discretisation of Spacetime	63
3.1.3	Boundary Conditions	64
3.1.4	The Method of Lines	65
3.1.5	Integration of ODEs	66
3.2	GRCHOMBO	68
3.2.1	Overview of GRCHOMBO	68
3.2.2	Simulation Units	69
3.2.3	Boson Star Initial Data	69
3.2.4	Single Star Evolution	73
3.2.5	Superposition of Initial Data	73
3.2.6	Collisions of Boson Stars	74
4	Malaise and Remedy of Binary Boson Star Initial Data	79
4.1	Introduction	80
4.1.1	Boson Star Initial Data	82
4.2	Boson Star Binary Initial Data	83
4.2.1	Simple Superposition of Boson Stars	83
4.2.2	Improved Superposition	85
4.3	Models and Results	86
4.3.1	Initial Constraint Violations	86
4.3.2	Convergence and Numerical Uncertainties	88
4.3.3	Radiated Gravitational Wave Energy	88
4.3.4	Evolution of the Scalar Amplitude and Gravitational Collapse	90
4.4	Conclusions	94
4.5	Analytic Treatment of the Hamiltonian Constraint	95
5	Local Continuity of Angular Momentum and Noether Charge for Matter in General Relativity	96
5.1	Local Continuity of Angular Momentum and Noether Charge for Matter in General Relativity	97
5.1.1	Introduction	97
5.1.2	Derivation of the QFS System	98
5.1.3	Application to Spherical extraction	101
5.1.4	Noether Currents	103
5.1.5	Energy-Momentum Currents	105
5.1.6	Numerical Application	107
5.1.7	Conclusion	112
5.1.8	Source Term Calculation	113
5.1.9	Generality of Result	114
6	The Gravitational Afterglow of Boson Stars	118
6.1	The Gravitational Afterglow of Boson Stars	119

6.1.1	Introduction	119
6.1.2	Simulation Setup	120
6.1.3	The Merger Remnant	121
6.1.4	Gravitational Wave Signal	123
6.1.5	Conclusion	126
6.1.6	Angular Momentum Measure	128
6.1.7	Numerical Accuracy	130
7	Anomalies in the Gravitational Recoil of Eccentric Black-Hole Mergers with Unequal Mass Ratios	131
7.1	Introduction	132
7.2	Computational Framework and Set of Simulations	134
7.2.1	Numerical Methods	134
7.2.2	Black-Hole Binary Configurations	135
7.2.3	Diagnostics	136
7.3	Results	138
7.4	Conclusions	143
7.5	Numerical Accuracy	144
7.5.1	GRCHOMBO Convergence	144
7.5.2	LEAN Convergence	146
7.5.3	Comparison between GRCHOMBO and LEAN	146
7.6	GRCHOMBO Tagging Criterion	147
8	Conclusions and Bibliography	149
8.1	Concluding Remarks	150

Chapter 1

Introduction to Differential Geometry and General Relativity

1.1 Introduction

1.1.1 Introduction to General Relativity

The modern theory of gravity, published by Albert Einstein in 1915, is general relativity (GR). It is a geometric theory relying on curved spaces and differential geometry. GR is a generalisation of Einstein's theory of special relativity (SR) to include matter and gravity. Where the main idea behind SR was that the laws of physics are identical in any non-accelerating frame¹, GR includes the gravitational force (and subsequently matter) by postulating that the laws of physics are identical in any free-falling frame. In a universe without gravity or matter GR is equivalent to SR.

GR also supersedes Newton's theory of gravity when gravity becomes strong. In Newtonian theory, two masses orbit each other in a constant circle or ellipse; the ellipses can precess in the presence of extra masses. However, the calculated precession rate of Mercury about the sun using Newton's theory of gravity was too slow; Einstein correctly calculated the precession rate using GR. This initial success proved to the world that Einstein's theory was the best current description of gravity. In the weak gravity limit, GR replicates Newton's theory of gravity; the precession of Mercury is a particularly prominent deviation from Newton's theory in the solar system as it is closest planet to the sun where gravity is the strongest. On top of this precession GR predicts that the time averaged separation of a two-body orbit can be seen to decrease, hence the objects are inspiralling. The orbital energy lost is released as a gravitational wave (GW) signal. Inspiral and radiation become more pronounced at lower separations and with heavier objects. Approximations to GR can be used in this regime, for example post Newtonian (PN) theory which expands GR in powers of c (the speed of light in vacuum).

Other new effects predicted by GR include gravitational time dilation and the correction to light ray deflection. Gravitational time dilation is similar to time dilation in SR which states that an observer at rest would age more quickly (in their own frame) compared to a quickly moving observer. Gravitational time dilation states that an observer in a stronger gravitational field will age more slowly than one in a weaker gravitational field; this effect has been verified by comparing two atomic clocks where one is left on the surface of the earth and one is elevated. Light ray deflection occurs when a beam of light passes close by an object with a strong gravitational field - the stronger the field the more the light beam is deflected. This can be seen when distant bright objects pass behind matter such as black holes or large clusters of matter. While one can model light ray deflection using Newtonian physics, this description is not correct and general relativity is needed for accurate predictions.

In the strong gravity regime GR deviates entirely from Newtonian theory leading to a plethora of exotic results. One major group of examples are black holes (BHs), the most compact known macroscopic objects with such a strong gravitational pull that even light cannot escape. These dense objects can be produced by the collapse of heavy dying stars, implosions of supernovae, and collisions of very dense objects such as NSs or other heavy stars; the collapse of matter to a black hole itself is not described by Newtonian physics. Another example is the neutron star (NS), an object so dense that all of the electrons in an atom are forced to combine with nearby protons and reduce all matter to a dense lattice of neutrons. The gravitational field on the surface of a NS is of order 10^{11} times stronger than on earth's surface and the internal physics of NSs is not well known to date.

At the centre of a black hole, GR predicts a gravitational singularity; a point (or set of points) where spacetime curvature diverges. It is presumed that Einstein's theory breaks down towards a singularity which is deemed unphysical. Theories such as loop quantum gravity (LQG) and string theory (ST) try to reconcile GR with quantum mechanics which might alleviate this problem. Sadly there is no definitive answer as to what happens near a gravitational singularity, this is in part due to the lack of experimental data to draw from. The weak cosmic censorship conjecture states that all physical singularities are hidden inside an event horizon (EH). Informally the EH can be thought of as the surface containing the black

¹What is meant here is that one cannot determine the absolute velocity of a frame of reference from an experiment, not that special relativity fails to describe accelerating frames.

hole interior; the set of all points that cannot send information to a distant external observer. Formally, the EH is the causal past of *future null infinity*, denoted \mathcal{I}^+ , the surface reached by outward directed photons in the infinite future. Points inside an EH are *causally disconnected* from the exterior.

GR also describes physics at the largest scales. The universe can be modelled as an isotropic (but not necessarily flat) spatial hypersurface with a time dependent scale factor; this spacetime is known as the Friedmann–Lemaître–Robertson–Walker (FLRW) spacetime. The application of GR to the entire universe is called Cosmology and can be used to describe the big bang, early universe expansion and late universe inflation. Cosmology is also very successfully modelled in the framework of perturbation theory on an FLRW background.

One final noteworthy prediction of GR is gravitational waves. In 2015 GWs were detected by the Laser Interferometer Gravitational-Wave Observatory (LIGO) which lead to the 2017 Nobel prize in physics. Many subsequent signals from inspiralling BH-BH and BH-BS inspirals have been measured which agree with the waveforms predicted by NR simulations and PN theories. This recent discovery has lead to an increase in interest in gravitational physics - especially systems with observable GWs.

1.1.2 Introduction to Compact Objects and Boson Stars

The first non-trivial solution to Einstein's equation found was that of the spherically symmetric, static and asymptotically flat vacuum spacetime by Karl Schwarzschild in 1916. The solution was designed to be used outside a spherically symmetric, non-spinning, body of mass; however it also turned out to provide use in describing black holes. This metric was then modified by Tolman, Oppenheimer and Volkov in 1939 to describe the non-vacuum case of a spherically symmetric neutron star; this required a non-zero matter distribution.

Black holes in the universe generally spin; any black hole forming from the collapse of matter will inherit the angular momentum of the matter as it collapses. Another way to see this is that non-spinning black holes are a subset of measure zero in the set of spinning black holes; the non-spinning black hole is a fine tuned black hole with spin zero. Rotating black holes were first described by Roy Kerr in 1963, and are subsequently called Kerr black holes. The collisions of black holes (with or without spin) are also successfully described by GR, however this phenomenon is far too complicated to solve analytically. Numerical relativity (NR), the exact ² simulation of GR using methods to solve partial differential equations (PDEs), is needed to describe black hole collisions and inspirals.

The study of compact exotic objects can be traced back to John Wheeler who investigated Geons in 1955 for their potential similarity to elementary particles. Geons are gravito-electromagnetic objects with the name arising from “gravitational electromagnetic entity”. In 1968 David Kaup discovered a solution dubbed *Klein-Gordon Geons* [6], nowadays called boson stars. Importantly, boson stars are a localised complex Klein-Gordon configuration, with the real counterparts being unstable. Variants such as (Spin 1) Proca stars [7], electromagnetically charged boson stars and many others have been studied.

Interest in boson stars remains strong for many reasons. Given the recent discovery of the Higgs boson, we know that at least one scalar field exist in nature and any gravitational wave signals created by compact objects could theoretically be detected with modern gravitational wave interferometers. Secondly, boson stars are a good candidate for dark matter halos [8] [9]. Boson stars are also useful as a proxy to other compact objects in general relativity; there is a lot of freedom in the construction of different types of boson star and they can be tuned to provide an approximate model of dense neutron stars for one example. The advantage this would have over simulating a real fluid is that the Klein Gordon equation is linear in the principal part and is less prone to shocks and instabilities; consequently, conserved quantities are relatively well conserved with less sophisticated numerical schemes.

²Exact up to numerical error.

On a slightly different topic, collisions of boson stars could be a natural method to produce scalar hair around black holes which will be discussed later in more detail in section 3.2.6.

1.1.3 Conventions

Throughout this thesis physical quantities will be expressed as a dimensionless ratio of the Planck length L_{pl} , time T_{pl} and mass M_{pl} unless stated otherwise; for example Newtons equation of gravity would be written as

$$F = \frac{GMm}{r^2} \rightarrow \left(\frac{F}{F_{\text{pl}}} \right) = \frac{\left(\frac{M}{M_{\text{pl}}} \right) \left(\frac{m}{M_{\text{pl}}} \right)}{\left(\frac{r}{L_{\text{pl}}} \right)^2}, \quad (1.1.1)$$

where $F_{\text{pl}} = M_{\text{pl}} L_{\text{pl}} T_{\text{pl}}^{-2}$ is the Planck force. Consequently c , G and \hbar take the numerical value of 1.

The Einstein summation convention for tensor indices will be used extensively; this means $A_\mu B^\mu \equiv \sum_\mu A_\mu B^\mu$ where the sum over μ is implied by contracting indices of same latter. Tensors and tensor fields will be denoted using bold font (\mathbf{T}) for index free notation and normal font ($T_{\mu\nu}, \dots$) for the components. The dot product between two vectors or vector fields will be written interchangeably as $\mathbf{A} \cdot \mathbf{B} \leftrightarrow A_\mu B^\mu$ for readability. Additionally, ∇_μ denotes the covariant derivative and ∂_μ is the partial derivative, both with respect to coordinate x^μ . The metric signature will always be $(-, +, +, +)$.

When considering the ADM decomposition, as in section 2.1, objects can be associated with both a $3+1$ dimensional manifold \mathcal{M} or a 3 dimensional hypersurface Σ . To distinguish between these, standard Roman letters such as R represent the object belonging to \mathcal{M} and calligraphic letters such as \mathcal{R} correspond to the object belonging to Σ .

Finally, unless stated otherwise, Greek indices such as $\{\alpha, \beta, \dots, \mu, \nu, \dots\}$ label generic dimension tensor components (often 4 dimensions) whereas late Latin indices such as $\{i, j, k, \dots\}$ label three dimensional tensor components and early Latin indices such as $\{a, b, \dots\}$ label two dimensional ones.

1.2 Differential Geometry

1.2.1 Introduction to Geometry and Manifolds

Everyone's first encounter with geometry will cover Pythagoras' theorem; arguably the most famous and useful equation in existence. Pythagoras' equation relates the sidelengths of a right angled triangle, it says that $s^2 = x^2 + y^2$ for a triangle with height y , width x and hypotenuse length s . This can be shown very simply by looking at Fig. 1.1. The area of the partially rotated square is s^2 , but we can also calculate it from the the area of the larger square A_{sq} and subtracting four times the area of one of the triangles A_{tr} . Given that $A_{sq} = (x+y)^2$ and $A_{tr} = \frac{1}{2}xy$, then

$$s^2 = (x+y)^2 - 4 \cdot \frac{1}{2}xy = x^2 + y^2, \quad (1.2.1)$$

and we have proved Pythagoras' theorem. Using an infinitesimally small triangle, we can write $ds^2 = dx^2 + dy^2$ and this can be trivially extended to arbitrary dimensions like

$$ds^2 = dx^2 + dy^2 + dz^2 + \dots . \quad (1.2.2)$$

The infinitesimal form of Pythagoras' theorem is very powerful as it can be used to calculate the length of a generic curve by approximating the curve as a collection of infinitesimally small straight lines with length ds . So far we have assumed that space is flat meaning Eq. (1.2.2) is true for all points in space, this is an assumption we will have to drop if we want to study the curved spaces arising in strong gravity. In the next sections we will explore the generalisation of Pythagoras' equation to curved spaces and use it to measure curve lengths as well as volumes and areas.

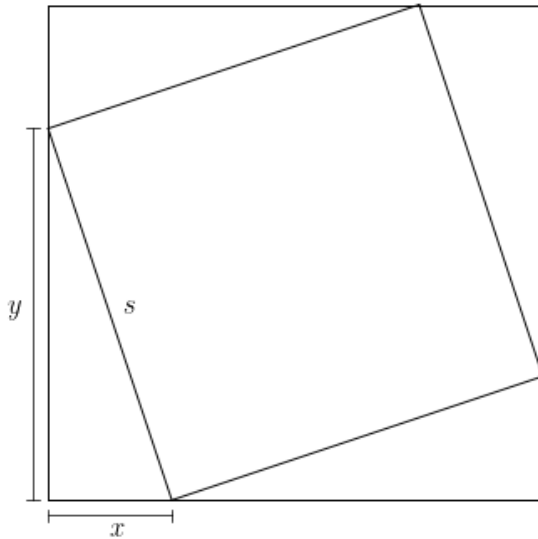


Figure 1.1: Diagram for proof of Pythagoras' theorem.

Differential Geometry (DG) is the extension of calculus, linear algebra and multilinear algebra to curved geometries. Einstein's Theory of Relativity is written using the language of DG as it is the natural way to deal with curves, tensor calculus and differential tensor equations in curved spaces. For a basic introduction to DG, we should start with a manifold \mathcal{M} which is an N dimensional space that locally looks like \mathbb{R}^N , N dimensional Euclidean space. This is important as at a point $p \in \mathcal{M}$ we can find infinitesimally close neighbouring points $p + \delta p \in \mathcal{M}$. In the following sections we will explore curves, functions, tensors and calculus on manifolds using DG. Two introductory texts covering the basics of DG, for application to general relativity, are [10] and [11]. For a more dedicated DG textbook the reader is directed to [12].

1.2.2 Functions, Curves and Tensors on Manifolds

A real scalar function f over \mathcal{M} maps any point $p \in \mathcal{M}$ to a real number, denoted $f : p \rightarrow \mathbb{R}$. An important example of a set of scalar functions is the coordinate system ϕ , $\phi : p \rightarrow \mathbb{R}^N$ on some neighbourhood of p . This is normally written x^μ where $\mu \in \{0, 1, \dots, N - 1\}$ is an index labelling the coordinate. The map ϕ is called a chart, and unlike Euclidean space one chart may not be enough to cover the entire manifold; in this case a set of compatible charts should be smoothly³ joined, collectively known as an atlas.

Now that functions have been discussed, the next simplest object we can discuss is a curve, or path, through \mathcal{M} . A curve Γ is a set of smoothly connected points $p(\lambda) \in \mathcal{M}$ that smoothly depend on an input parameter $\lambda \in [\lambda_0, \lambda_1]$. This can be expressed in terms of coordinates as $x^\mu(\lambda)$ where $\phi : p(\lambda) \rightarrow x^\mu(\lambda)$. Differentiating a function f along Γ with respect to λ gives

$$\frac{d}{d\lambda} f(x^\mu(\lambda)) = \frac{dx^\nu}{d\lambda} \frac{\partial f(x^\mu)}{\partial x^\nu} = \frac{dx^\nu}{d\lambda} \partial_\nu f, \quad (1.2.3)$$

where the Einstein summation convention was invoked, summing over all values of ν , and $\partial_\nu = \partial/\partial x^\nu$. Equation (1.2.3) was derived independently of the choice of f , therefore we can generally write

$$\frac{d}{d\lambda} = \frac{dx^\nu}{d\lambda} \partial_\nu. \quad (1.2.4)$$

The operator $d/d\lambda$ can act on any function f and return a new function \tilde{f} over Γ , this is written as $d/d\lambda(f) = \tilde{f}$ where $\tilde{f} : p(\lambda) \rightarrow \mathbb{R}$. We can also think of $d/d\lambda$ as a vector \mathbf{X} with components $X^\mu = dx^\mu/d\lambda$ and basis vectors $\mathbf{e}_\mu := \partial_\mu$ taken from Eq. (1.2.4). The vector \mathbf{X} can be written as $\mathbf{X} = X^\mu \mathbf{e}_\mu$ and can act on a general function f over \mathcal{M} as $\mathbf{X}(f) = X^\mu \mathbf{e}_\mu(f) = X^\mu \partial_\mu f$. Considering the set of all possible curves through a points $p \in \mathcal{M}$, the tangent vector components $dx^\mu/d\lambda$ span an N dimensional space with basis $\mathbf{e}_\mu = \partial_\mu$; this space is called the tangent space and is denoted as $T_p(\mathcal{M})$ at a point $p \in \mathcal{M}$.

The next object to discuss is the co-vector which is defined as a map from vectors to real numbers; not to be confused with the dot product in section 1.2.3. Similarly to vectors, a co-vector ω can be expressed as a sum of components ω_μ and basis co-vectors θ^μ like $\omega = \omega_\mu \theta^\mu$. Contrary to vectors, co-vector components have downstairs indices and the basis has upstairs indices; this choice improves the readability of tensor equations when working with components. A co-vector can map a vector to a real number like $\omega : \mathbf{X} \rightarrow \mathbb{R}$ or $\omega(\mathbf{X}) \rightarrow \mathbb{R}$. Vectors are equally able to map co-vectors to real numbers, denoted as $\mathbf{X} : \omega \rightarrow \mathbb{R}$. The co-vectors basis is defined such that $\theta^\mu : \mathbf{e}_\nu = \delta_\nu^\mu$ where δ_ν^μ are the components of the Kronecker delta equating to zero unless $\mu = \nu$ in which case they are one. The operation of a generic co-vector ω on a generic vector \mathbf{X} is

$$\omega : \mathbf{X} = \omega_\mu X^\nu \theta^\mu : \mathbf{e}_\nu = \omega_\mu X^\nu \delta_\nu^\mu = \omega_\mu X^\mu \in \mathbb{R}. \quad (1.2.5)$$

This map is linear and identical under reversing the order of operation; $\omega : \mathbf{X} = \mathbf{X} : \omega$. Similarly to vectors, the set of all possible co-vectors at a point $p \in \mathcal{M}$ span an N -dimensional space called the co-tangent space, written as $T_p^*(\mathcal{M})$.

Multilinear Maps and Tensors

Generalising the previous linear maps between vectors and co-vectors gives the multilinear map. Consider a tensor \mathbf{T} , this can be expressed in component form like

$$\mathbf{T} = T_{\mu\nu,\dots}^{\alpha\beta,\dots} \mathbf{e}_\alpha \otimes \mathbf{e}_\beta \otimes \dots \otimes \theta^\mu \otimes \theta^\nu \otimes \dots \quad (1.2.6)$$

³Smoothness here referring to infinite differentiability, C^∞ .

for an arbitrary number of outer products of vector and co-vector bases. A tensor with m co-vector bases and n vector bases is called an (m, n) tensor and has a rank of $m + n$. Vectors, co-vectors and scalars are $(1, 0)$, $(0, 1)$ and $(0, 0)$ tensors respectively. Tensors can act as multilinear maps between tensors. We have already seen how a vector and co-vector can map each other to a scalar, let's extend this with an example. An $(0, 2)$ tensor, $\mathbf{T} = T_{\mu\nu}\theta^\mu \otimes \theta^\nu$ at $p \in \mathcal{M}$, can map two vectors \mathbf{X} and \mathbf{Y} to a scalar as shown,

$$\mathbf{T}(\mathbf{X}, \mathbf{Y}) = T_{\mu\nu}X^\alpha Y^\beta \theta^\mu \otimes \theta^\nu(e_\alpha, e_\beta), \quad (1.2.7)$$

$$= T_{\mu\nu}X^\alpha Y^\beta (\theta^\mu : e_\alpha)(\theta^\nu : e_\beta), \quad (1.2.8)$$

$$= T_{\mu\nu}X^\alpha Y^\beta \delta_\alpha^\mu \delta_\beta^\nu, \quad (1.2.9)$$

$$= T_{\mu\nu}X^\mu Y^\nu. \quad (1.2.10)$$

The multilinear map can also output generic tensors, for example consider

$$\mathbf{T}(\mathbf{X}, \star) = T_{\mu\nu}X^\alpha(\theta^\mu : e_\alpha)\theta^\nu = T_{\mu\nu}X^\mu\theta^\nu, \quad (1.2.11)$$

which uses the $(0, 2)$ tensor \mathbf{T} to map the vector \mathbf{X} to a co-vector \mathbf{W} with components $W_\mu = T_{\mu\nu}X^\mu$.

One final example of a mapping is from a single tensor to a lower rank tensor, this is called contraction. To illustrate this, let's take a $(1, 3)$ tensor $\mathbf{Z} = Z_{\mu\nu\rho}^\alpha e_\alpha \otimes \theta^\mu \otimes \theta^\nu \otimes \theta^\rho$. We can choose to use the basis vector e_α to act on any of the three co-vector bases, choosing θ^μ this is

$$Z_{\mu\nu\rho}^\alpha (e_\alpha : \theta^\mu) \theta^\nu \otimes \theta^\rho = Z_{\mu\nu\rho}^\mu \theta^\nu \otimes \theta^\rho = \tilde{Z}_{\nu\rho} \theta^\nu \otimes \theta^\rho, \quad (1.2.12)$$

where $\tilde{Z}_{\nu\rho} = Z_{\mu\nu\rho}^\mu$. Tensors are central to general relativity, objects such as curvature, matter and paths will be described by tensor fields ⁴.

1.2.3 The Inner Product and the Metric

To introduce the notion of length on a tangent plane $\mathcal{T}_p(\mathcal{M})$ at a point $p \in \mathcal{M}$ the metric tensor \mathbf{g} is introduced. The metric tensor defines the inner product (or dot product) on $\mathcal{T}_p(\mathcal{M})$ like,

$$e_\mu \cdot e_\nu = g_{\mu\nu}. \quad (1.2.13)$$

The metric is symmetric by construction which ensures that $e_\mu \cdot e_\nu = e_\nu \cdot e_\mu$. The inner product can be thought of as a multilinear map,

$$\mathbf{g} : (\mathbf{X}, \mathbf{Y}) \rightarrow \mathbb{R}, \quad \text{or} \quad \mathbf{g}(\mathbf{X}, \mathbf{Y}) = g_{\mu\nu}X^\mu Y^\nu, \quad (1.2.14)$$

where $\mathbf{X} \in \mathcal{T}_p(\mathcal{M})$, $\mathbf{Y} \in \mathcal{T}_p(\mathcal{M})$ and $\mathbf{g} \in \mathcal{T}_p^*(\mathcal{M}) \otimes \mathcal{T}_p^*(\mathcal{M})$. The inner product can also be represented by a second map

$$\mathbf{X} : \mathbf{Y} \rightarrow \mathbb{R}, \quad \text{or} \quad \mathbf{X} \cdot \mathbf{Y} = X^\mu Y^\nu e_\mu \cdot e_\nu = X^\mu Y^\nu g_{\mu\nu}, \quad (1.2.15)$$

which is a new mapping. The inner product also gives the length (or magnitude) $|\mathbf{X}|$ of any vector $\mathbf{X} \in \mathcal{T}_p(\mathcal{M})$ as,

$$|\mathbf{X}|^2 = \mathbf{X} \cdot \mathbf{X} = g_{\mu\nu}X^\mu X^\nu. \quad (1.2.16)$$

Another way to think of the inner product is that the metric maps a vector \mathbf{X} to an equivalent or *dual* co-vector $\mathbf{\Xi}$ such that $\mathbf{X} : \mathbf{\Xi} = X^\mu \Xi_\mu = g_{\mu\nu}X^\mu X^\nu$. In component form $\mathbf{\Xi}$ is

$$\Xi_\mu = g_{\mu\nu}X^\nu; \quad (1.2.17)$$

⁴A tensor field assigns a tensor to each point on a manifold \mathcal{M} . In this work the assignment will be smooth except for where coordinate singularities, or physical singularities, occur.

this use of the metric to map a vector to its corresponding co-vector (and vice-versa) is extremely useful. Without loss of information we can write $\Xi_\nu = X_\nu$ to make it obvious that $X_\nu = X^\mu g_{\mu\nu}$ and this convention will be used from now on.

The metric also assigns an inner product and a length measure on the co-tangent plane $\mathcal{T}_p^*(\mathcal{M})$ but instead using the inverse components $g^{\mu\nu} \equiv (g^{-1})_{\mu\nu}$,

$$g^{\mu\nu} = \boldsymbol{\theta}^\mu \cdot \boldsymbol{\theta}^\nu. \quad (1.2.18)$$

Similarly to before, the inner product of two co-vectors $\boldsymbol{\omega}$ and $\boldsymbol{\sigma}$ is

$$\boldsymbol{\omega} \cdot \mathbf{Y} = \omega_\mu \sigma_\nu \boldsymbol{\theta}^\mu \cdot \boldsymbol{\theta}^\nu = \omega_\mu \sigma_\nu g^{\mu\nu} = \omega_\mu \sigma^\mu. \quad (1.2.19)$$

The reason that $g^{\mu\nu}$ must be the inverse matrix of $g_{\mu\nu}$ is as follows. For a vector $X^\mu \mathbf{e}_\mu$ and a co-vector $\omega_\mu \boldsymbol{\theta}^\mu$ we would like,

$$\mathbf{X} : \boldsymbol{\omega} = \mathbf{g}(\mathbf{X}, \star) : \mathbf{g}^{-1}(\boldsymbol{\omega}, \star), \quad (1.2.20)$$

$$X^\mu \omega_\mu = X_\mu \omega^\mu, \quad (1.2.21)$$

$$= X^\rho g_{\rho\mu} g^{\mu\sigma} \omega_\sigma \quad (1.2.22)$$

which is only true if $g_{\rho\mu} g^{\mu\sigma} = \delta_\rho^\sigma$ which is true by definition if $(g^{-1})_{\mu\nu} = g^{\mu\nu}$.

Not only has the metric provided us with an inner product and a length on tangent planes and cotangent planes, but it has also given a mapping between the two tangent planes. Therefore the metric can raise and lower indices on general tensors such as

$$T^{\mu\nu\dots}_{\alpha\beta} = g^{\mu\rho} g_{\beta\sigma} T^{\nu\sigma\dots}_{\rho\alpha}. \quad (1.2.23)$$

1.2.4 Maps Between Manifolds

We now discuss the maps between two manifolds M and N . This has many uses such as pushing and pulling tensors between manifolds, allowing us to calculate a Lie derivative of tensor fields and finding the metric (or any tensor field) on an embedded surface; this property is crucial in the 3+1 spacetime decomposition in section 2.1.2.

Define a smooth map $\Phi : M \rightarrow N$ between manifolds on some coordinate patch labelling coordinates $x^\mu \in M$ and $y^\mu \in N$. The map $\Phi : x^\mu \rightarrow y^\mu$ gives $y^\mu = \Phi^\mu(x^\nu)$, or equivalently $y^\mu(x^\nu)$. Scalar functions must also map trivially,

$$f_N(y^\mu(x^\nu)) = f_M(x^\mu), \quad (1.2.24)$$

where f_N and f_M span N and M respectively, thus we will no longer identify which manifold a function is on. The map Φ allows us to push the vector $\mathbf{X} \in \mathcal{T}_p(M)$ to $\Phi_* \mathbf{X} \in \mathcal{T}_q(N)$, where $q = \Phi(p)$, in a way such that its action on a function f is the same in either manifold.

$$\mathbf{X}(f)\Big|_p = \Phi_* \mathbf{X}(f)\Big|_q, \quad (1.2.25)$$

$$X^\mu \frac{\partial f}{\partial x^\mu} = (\Phi_* X)^\nu \frac{\partial f}{\partial y^\nu}, \quad (1.2.26)$$

$$\left(X^\mu \frac{\partial y^\nu}{\partial x^\mu} \right) \frac{\partial f}{\partial y^\nu} = (\Phi_* X)^\nu \frac{\partial f}{\partial y^\nu}, \quad (1.2.27)$$

and hence the components of the push-forward $\Phi_* \mathbf{X}$ can be read off,

$$(\Phi_* X)^\mu = \frac{\partial y^\mu}{\partial x^\nu} X^\nu. \quad (1.2.28)$$

Given a co-vector field $\omega \in \mathcal{T}_p^*(N)$ we can pull the field back from $\mathcal{T}_p^*(M) \leftarrow \mathcal{T}_q^*(N)$, denoted $\Phi^*\omega$, by demanding that $\Phi^*\omega(\mathbf{X})|_p = \omega(\Phi_*\mathbf{X})|_q$. Evaluating this gives

$$\Phi^*\omega(\mathbf{X})|_p = \omega(\Phi_*\mathbf{X})|_q, \quad (1.2.29)$$

$$(\Phi^*\omega)_\mu X^\mu = \omega_\nu (\Phi_* X)^\nu, \quad (1.2.30)$$

$$(\Phi^*\omega)_\mu X^\mu = \omega_\nu \frac{\partial y^\nu}{\partial x^\mu} X^\mu, \quad (1.2.31)$$

and the components of the pull-back $\Phi_*\omega$ can be read off,

$$(\Phi^*\omega)_\mu = \frac{\partial y^\nu}{\partial x^\mu} \omega_\nu. \quad (1.2.32)$$

Considering an $(0, 2)$ tensor $\mathbf{T} \in N$, the pullback $\Phi^*\mathbf{T} \in M$ follows simply from demanding that $\mathbf{T}(\Phi_*\mathbf{X}, \Phi_*\mathbf{Y})|_q = \Phi^*\mathbf{T}(\mathbf{X}, \mathbf{Y})|_p$ where \mathbf{X} and \mathbf{Y} are vector fields on M . The components of the pull-back of \mathbf{T} are therefore

$$(\Phi^*\mathbf{T})_{\mu\nu} = \frac{\partial y^\rho}{\partial x^\mu} \frac{\partial y^\sigma}{\partial x^\nu} T_{\rho\sigma}. \quad (1.2.33)$$

The pull-back of a generic $(0, q)$ tensor and the push-forward of a generic $(p, 0)$ tensor can be found similarly by contracting with an extra $\frac{\partial y^\mu}{\partial x^\nu}$ for each downstairs index or $\frac{\partial x^\mu}{\partial y^\nu}$ for each upstairs index of the tensor considered.

Diffeomorphisms

So far we have only discussed the one way mapping $\Phi : M \rightarrow N$ which requires a well behaved $\partial y^\nu / \partial x^\mu$. A diffeomorphism is an isomorphism⁵ between smooth manifolds $\Phi : M \rightarrow N$, meaning M and N have the same number of dimensions. Two infinitesimally close points $\{p, p + \delta p\} \in \mathcal{M}$ map to two infinitesimally close points $\{q, q + \delta q\} \in \mathcal{N}$ meaning that open sets are preserved. Given that a diffeomorphism is smooth bijective map then it must be inevitable with inverse map $\Phi^{-1} : N \rightarrow M$, and $y^\nu(x^\mu)$ has a smooth inverse $x^\nu(y^\mu)$. When an inverse map Φ^{-1} is defined then the pull-back of $(p, 0)$ tensors from N to M along with the push-forward of $(0, q)$ tensors from M to N is possible. This means it is possible to push or pull generic tensors between M and N in any direction. The tangent spaces associated with $p \in \mathcal{M}$ or $q \in \mathcal{N}$ are therefore also preserved under mapping meaning that local structure on the manifold is preserved under the mapping. Two common examples of diffeomorphisms are coordinate changes and translations.

Projection Mappings

As mentioned, maps between manifolds can be used to project tensors to lower dimensional embedded surfaces. This requires us to consider an m -dimensional manifold M with metric $g_{\mu\nu}$ and coordinates x^μ as well as an embedded n -dimensional surface N where $n < m$. We can treat N as a separate n -dimensional manifold with metric $h_{\mu\nu}$. As before, we can define a map $\Phi : x^\mu \rightarrow y^\mu$ and the pullback of the metric demands that,

$${}^{(m)}h_{\rho\sigma} = {}^{(n)}h_{\mu\nu} \frac{\partial y^\mu}{\partial x^\rho} \frac{\partial y^\nu}{\partial x^\sigma}, \quad (1.2.34)$$

where ${}^{(m)}\mathbf{h}$ represents m -dimensional the tensor on M and ${}^{(n)}\mathbf{h}$ represents n -dimensional the tensor on N ; of course ${}^{(n)}\mathbf{h}$ and \mathbf{h} are completely identical.

In the case that $n = m - 1$, which is a projection into one less dimension, a convenient form for ${}^{(n)}\mathbf{h}$ can be found. If the image of N in M has everywhere an m -dimensional unit normal \mathbf{n} , then a vector

⁵An isomorphism is a structure preserving bijective map between sets; in this context structure preserving applies to the preservation of open sets allowing for the mapping of derivatives.

$\mathbf{X} \in \mathcal{T}_p(\mathcal{M})$ for $p \in N$ can be projected onto N like,

$$({}^{(m)}\vec{\mathbf{X}})^\mu = (\delta_\nu^\mu \mp n^\mu n_\nu) X^\nu, \quad (1.2.35)$$

where the sign is negative if $|\mathbf{n}|^2 = 1$ and positive if $|\mathbf{n}|^2 = -1$. It should be noted that strictly, $\vec{\mathbf{X}} \in \mathcal{T}_p(\mathcal{M})$. To avoid confusion we will denote the m -dimensional projected vector as ${}^{(m)}\vec{\mathbf{X}}$ and vector existing in the n -dimensional manifold N as ${}^{(n)}\vec{\mathbf{X}}$. The projection guarantees that,

$${}^{(n)}\mathbf{h}({}^{(n)}\vec{\mathbf{X}}, {}^{(n)}\vec{\mathbf{X}}) = \mathbf{g}({}^{(m)}\vec{\mathbf{X}}, {}^{(m)}\vec{\mathbf{X}}), \quad (1.2.36)$$

$$= {}^{(m)}h_{\mu\nu}(\delta_\alpha^\mu \mp n^\mu n_\alpha) X^\alpha (\delta_\beta^\nu \mp n^\nu n_\beta) X^\beta, \quad (1.2.37)$$

$$= {}^{(m)}\mathbf{h}(\mathbf{X}, \mathbf{X}), \quad (1.2.38)$$

which gives a formula for the projected metric ${}^{(m)}\mathbf{h} \in \mathcal{M}$,

$${}^{(m)}h_{\mu\nu} = g_{\mu\nu} \mp n_\mu n_\nu. \quad (1.2.39)$$

The use of this projected metric to project general tensors to lower dimensions is explored in detail in section 2.1.2 and heavily relied upon in chapter 5.

Mapping to lower dimensional surface of d -dimensions can be done similarly by adding an extra mutually-orthogonal unit vector for each reduced dimension like,

$${}^{(m)}h_{\mu\nu} = g_{\mu\nu} \mp n_\mu^{(1)} n_\nu^{(1)} \mp n_\mu^{(2)} n_\nu^{(2)} + \dots. \quad (1.2.40)$$

The metric $\tilde{\mathbf{h}}$ on an a -dimensional sub-surface $A \in \mathcal{M}$ can be explicitly calculated from the pushforward of ${}^{(m)}\tilde{\mathbf{h}}$ considering the diffeomorphism Φ^A that maps the image of A embedded in \mathcal{M} to an a -dimensional manifold \mathcal{A} . The resulting metric is,

$$(\Phi_*^A g)_{ij} = \tilde{h}_{ij} = \frac{\partial x^\mu}{\partial z^i} \frac{\partial x^\nu}{\partial z^j} {}^{(m)}\tilde{h}_{\mu\nu} = \frac{\partial x^\mu}{\partial z^i} \frac{\partial x^\nu}{\partial z^j} \left(g_{\mu\nu} \mp n_\mu^{(1)} n_\nu^{(1)} \mp n_\mu^{(2)} n_\nu^{(2)} + \dots \right), \quad (1.2.41)$$

where the $\mathbf{n}^{(i)}$ are a set of orthogonal unit vectors perpendicular to A ; x^μ span \mathcal{M} and z^i span \mathcal{A} .

Null Hypersurfaces

So far we have avoided mentioning projections onto null hypersurfaces. For a 2-dimensional hypersurface Σ_{UV} (which is a sub-manifold of \mathcal{M}) to be null it must have two distinct null vectors \mathbf{U} and \mathbf{V} at all points $p \in \Sigma_{UV}$. By construction, $\mathbf{U}^2 = \mathbf{V}^2 = 0$, but we are free to specify $\mathbf{U} \cdot \mathbf{V}$; it will be useful to define $\mathbf{U} \cdot \mathbf{V} = 1$ for this purpose. Now the pullback of the metric on Σ_{UV} to \mathcal{M} is given by,

$${}^{(m)}h_{\mu\nu} = U_\mu V_\nu + V_\mu U_\nu, \quad (1.2.42)$$

which, as expected, satisfies ${}^{(m)}\mathbf{h}(\mathbf{U}, \mathbf{U}) = 0$, ${}^{(m)}\mathbf{h}(\mathbf{V}, \mathbf{V}) = 0$ and ${}^{(m)}\mathbf{h}(\mathbf{U}, \mathbf{V}) = 1$. Suppose we have another vector \mathbf{Z} (not necessarily null) which is orthogonal to Σ_{UV} we must have $\mathbf{U} \cdot \mathbf{Z} = \mathbf{V} \cdot \mathbf{Z} = 0$ and therefore ${}^{(m)}\mathbf{h}(\mathbf{Z}, \star) = 0$; as expected \mathbf{Z} is annihilated by the pullback of the metric as it has no projected length on Σ_{UV} .

1.2.5 Lie Derivatives

The Lie derivative of a tensor at a point p is the rate of change of a tensor field with respect to a pull-back from a diffeomorphism Φ mapping infinitesimally close points $(p = x^\mu, q = x^\mu + \epsilon\xi^\mu) \in \mathcal{M}$ with $\Phi : p \rightarrow q$

for some vector field ξ . Like any good differential operator, the Lie derivative \mathcal{L}_ξ along ξ (and \mathcal{L}_ζ along vector field ζ) should obey,

$$\mathcal{L}_{a\xi+b\zeta}\mathbf{T} = a\mathcal{L}_\xi\mathbf{T} + b\mathcal{L}_\zeta\mathbf{T}, \quad (1.2.43)$$

$$\mathcal{L}_\xi(a\mathbf{T} + b\mathbf{W}) = a\mathcal{L}_\xi\mathbf{T} + b\mathcal{L}_\xi\mathbf{W}, \quad (1.2.44)$$

$$\mathcal{L}_\xi(\mathbf{S} \otimes \mathbf{T}) = \mathbf{T} \otimes \mathcal{L}_\xi\mathbf{S} + \mathbf{S} \otimes \mathcal{L}_\xi\mathbf{T}, \quad (1.2.45)$$

for constant $\{a, b\}$, tensor field \mathbf{S} and tensor fields \mathbf{T} and \mathbf{W} of same rank. This final property is known as Leibniz rule. Note that while the partial derivative is linear in first argument like $\partial_{f\xi} = f\partial_\xi$ for a function f , the Lie derivative is only linear in first argument if f is a constant.

The simplest example is the Lie derivative of a scalar field ϕ , denoted $\mathcal{L}_\xi\phi$ with respect to vector field ξ ,

$$\mathcal{L}_\xi\phi = \lim_{\epsilon \rightarrow 0} \left[\frac{\Phi^*\phi|_q - \phi|_p}{\epsilon} \right], \quad (1.2.46)$$

$$= \lim_{\epsilon \rightarrow 0} \left[\frac{\phi(x^\mu + \epsilon\xi^\mu) - \phi(x^\mu)}{\epsilon} \right], \quad (1.2.47)$$

$$= \xi^\mu \partial_\mu \phi, \quad (1.2.48)$$

which reduces to the partial derivative of ϕ with along ξ . Next let's calculate the Lie derivative of a vector field \mathbf{X} with respect to vector field ξ . Starting with the same definition as Eq. (1.2.46), and using $y^\mu = x^\mu + \epsilon\xi^\mu$, the Lie derivative of \mathbf{X} is,

$$(\mathcal{L}_\xi X)^\mu = \lim_{\epsilon \rightarrow 0} \left[\frac{(\Phi^*X|_q)^\mu - X|_p{}^\mu}{\epsilon} \right], \quad (1.2.49)$$

$$= \lim_{\epsilon \rightarrow 0} \left[\frac{\frac{\partial x^\mu}{\partial y^\nu} X^\nu(x^\rho + \epsilon\xi^\rho) - X^\mu(x^\rho)}{\epsilon} \right], \quad (1.2.50)$$

$$= \lim_{\epsilon \rightarrow 0} \left[\frac{(\delta_\nu^\mu - \epsilon\partial_\nu\xi^\mu) X^\nu(x^\rho + \epsilon\xi^\rho) - X^\mu(x^\rho)}{\epsilon} \right], \quad (1.2.51)$$

$$= \lim_{\epsilon \rightarrow 0} \left[\frac{-\epsilon\partial_\nu\xi^\mu X^\nu(x^\rho + \epsilon\xi^\rho) + X^\mu(x^\rho + \epsilon\xi^\rho) - X^\mu(x^\rho)}{\epsilon} \right], \quad (1.2.52)$$

$$= \lim_{\epsilon \rightarrow 0} \left[\frac{-\epsilon\partial_\nu\xi^\mu X^\nu(x^\rho) + X^\mu(x^\rho + \epsilon\xi^\rho) - X^\mu(x^\rho) + \mathcal{O}(\epsilon^2)}{\epsilon} \right], \quad (1.2.53)$$

$$= \xi^\nu \partial_\nu X^\mu - X^\nu \partial_\nu \xi^\mu. \quad (1.2.54)$$

The Lie derivative for co-vectors and tensors can be derived in the same way, but can be quickly derived from the Leibniz rule as follows. Define a scalar field ψ , vector field \mathbf{X} and co-vector field ω , where $\psi = X^\mu \omega_\mu$, then it follows that,

$$\mathcal{L}_\xi\psi = \xi^\mu \partial_\mu \psi = X^\nu \xi^\mu \partial_\mu \omega_\nu + \omega_\nu \xi^\mu \partial_\mu X^\nu, \quad (1.2.55)$$

$$= \mathcal{L}_\xi(X^\mu \omega_\mu), \quad (1.2.56)$$

$$= \omega_\mu (\mathcal{L}_\xi X)^\mu + X^\mu (\mathcal{L}_\xi \omega)_\mu, \quad (1.2.57)$$

$$X^\mu (\mathcal{L}_\xi \omega)_\mu = X^\nu \xi^\mu \partial_\mu \omega_\nu + \omega_\nu \xi^\mu \partial_\mu X^\nu - \omega_\mu (\mathcal{L}_\xi X)^\mu, \quad (1.2.58)$$

$$(\mathcal{L}_\xi \omega)_\mu = \xi^\nu \partial_\nu \omega_\mu + \omega_\nu \partial_\mu \xi^\nu. \quad (1.2.59)$$

Derivatives of a generic tensor \mathbf{T} follows simply, for example,

$$(\mathcal{L}_\xi T)^{\alpha\beta\dots}_{\mu\nu\dots} = \xi^\sigma \partial_\sigma T^{\alpha\beta\dots}_{\mu\nu\dots} + T^{\alpha\beta\dots}_{\sigma\nu\dots} \partial_\mu \xi^\sigma + T^{\alpha\beta\dots}_{\mu\sigma\dots} \partial_\nu \xi^\sigma + \dots - T^{\sigma\beta\dots}_{\mu\nu\dots} \partial_\sigma \xi^\alpha - T^{\alpha\sigma\dots}_{\mu\nu\dots} \partial_\sigma \xi^\beta - \dots. \quad (1.2.60)$$

Lie derivatives will prove useful in section 2.1.4 and 2.1.9 to describe the time evolution of tensors in general relativity. The flow of time can be described as a diffeomorphism with respect to a suitable time vector \tilde{t} and the Lie derivative $\mathcal{L}_{\tilde{t}}$ gives the rate of change of objects with respect to this flow of time.

1.2.6 Lengths on Manifolds

The natural entry point for studying curved geometry is to revisit Pythagoras' theorem. For this we need a manifold \mathcal{M} equipped with a metric \mathbf{g} , written as $(\mathcal{M}, \mathbf{g})$ for short. The distance ds between two infinitesimally close points $p \in \mathcal{M}$ and $p + \delta p \in \mathcal{M}$, with coordinates $p = x^\mu$ and $p + \delta p = x^\mu + dx^\mu$, is given by

$$ds^2 = \mathbf{g}(\mathbf{dx}, \mathbf{dx}) = g_{\mu\nu} dx^\mu dx^\nu, \quad (1.2.61)$$

where $g_{\mu\nu}$ are the components of the metric tensor. This is the generalisation of Eq. (1.2.2) to curved space; notably the line element can now have varying coefficients from $g_{\mu\nu}$ and cross terms such as $dxdy$. The special choice of $g_{\mu\nu} = \delta_{\mu\nu}$ gives us flat Euclidean space; $\delta_{\mu\nu} = 1$ if $\mu = \nu$ and vanishes otherwise. With the line element defined, we can immediately apply it to calculating the length of a general curve in \mathcal{M} . Consider the curve Γ consisting of a set of connected points $p(\lambda) \in \mathcal{M}$ smoothly parameterised by λ . We can calculate the length Δs of the curve between $\lambda_1 \geq \lambda \geq \lambda_0$ by parameterising ds ,

$$ds^2 = g_{\mu\nu} \frac{\partial x^\mu}{\partial \lambda} \frac{\partial x^\nu}{\partial \lambda} d\lambda^2, \quad (1.2.62)$$

and integrating ds along Γ ,

$$\Delta s = \int_{\lambda_0}^{\lambda_1} \sqrt{\left(g_{\mu\nu} \frac{\partial x^\mu}{\partial \lambda} \frac{\partial x^\nu}{\partial \lambda} \right)} d\lambda. \quad (1.2.63)$$

In the simplified case where λ is one of the coordinates, say ξ , the length Δs becomes,

$$\Delta s = \int_{\xi_0}^{\xi_1} \sqrt{g_{\xi\xi}} d\xi. \quad (1.2.64)$$

1.2.7 Volumes on Manifolds

Following from measuring the length of a curve now we can now measure volumes on a manifold; of course we still require a manifold with metric $(\mathcal{M}, \mathbf{g})$. In a coordinate system x^μ we can calculate the volume V of a subregion M by integrating some weight function $w(x^\mu)$,

$$V = \int_M w(x^\mu) dx^1 dx^2 \dots dx^n, \quad (1.2.65)$$

over M . To find $w(x^\mu)$, start by defining a smooth and invertible orthogonal coordinate transformation $x^\mu \rightarrow \tilde{x}^\mu$ such that $\tilde{\mathbf{g}}$ is diagonal and $\det(\mathbf{g}) = \det(\tilde{\mathbf{g}})$; this is always possible as \mathbf{g} is real and symmetric. In this coordinate system, the volume δV in an infinitesimal cuboid, with i 'th sidelength $\delta \tilde{x}^i$, is

$$\delta V = \left(\sqrt{\tilde{g}_{11}} \delta \tilde{x}^1 \right) \left(\sqrt{\tilde{g}_{22}} \delta \tilde{x}^2 \right) \dots \left(\sqrt{\tilde{g}_{nn}} \delta \tilde{x}^n \right), \quad (1.2.66)$$

where Eq. (1.2.64) was used to get the length between each \tilde{x}^i and $\tilde{x}^i + \delta \tilde{x}^i$. Given that $\tilde{\mathbf{g}}$ is diagonal we know the i 'th eigenvalue $\tilde{\lambda}_i = \tilde{g}_{ii}$ and therefore $\det(\tilde{\mathbf{g}}) = \prod_i \tilde{g}_{ii}$. Thus the volume δV can be rewritten,

$$\delta V = \sqrt{|\det(\tilde{\mathbf{g}})|} \delta \tilde{x}^1 \delta \tilde{x}^2 \dots \delta \tilde{x}^n, \quad (1.2.67)$$

and the formula for the finite volume of M is,

$$V = \int_M \sqrt{|\det(\tilde{\mathbf{g}})|} d\tilde{x}^1 d\tilde{x}^2 \dots d\tilde{x}^n, \quad (1.2.68)$$

and the form of the weight function in \tilde{x}^μ coordinates is $\tilde{w}(\tilde{x}^\mu) = \sqrt{|\det(\tilde{\mathbf{g}})|}$. We are now free to transform back from $\tilde{x}^\mu \rightarrow x^\mu$, and given that the transformation is orthogonal we know that $\det(\mathbf{g}) = \det(\tilde{\mathbf{g}})$ and the Jacobean matrix \mathbf{J} of the coordinate transformation has $\det(\mathbf{J}) = 1$, therefore

$$V = \int_M \sqrt{|\det(\mathbf{g})|} dx^1 dx^2 \dots dx^n, \quad (1.2.69)$$

which holds for any non-diagonal, real and symmetric metric \mathbf{g} . In general we will now denote the determinant of a metric $\det(\mathbf{g})$ with the lower case letter g . When dealing with a pseudo-Riemannian manifold with a negative determinant, such as spacetime, it is more common to see $\sqrt{-g}$ written rather than $\sqrt{|g|}$ giving

$$V = \int_M \sqrt{-g} dx^1 dx^2 \dots dx^n. \quad (1.2.70)$$

Equation (1.2.69) can also be used to find the volume (or area) of a lower dimensional sub-volume. First cover the new sub-volume A with coordinates z^μ , where $\mu \in \{1, 2, \dots, m\}$ for $m < n$, and then calculate the metric $\tilde{\mathbf{h}}$ which can be done using Eq. (1.2.41). The area V_A of A is then,

$$V_A = \int_A \sqrt{|\tilde{h}|} dz^1 dz^2 \dots dz^m, \quad (1.2.71)$$

which can be seen by mapping to an n -dimensional manifold \mathcal{A} that is diffeomorphic to A and applying Eq. (1.2.69). These volume formulae are very useful in general relativity and have many uses in this thesis, especially throughout chapter 5.

1.2.8 Geodesics

For a manifold equipped with metric (\mathcal{M}, g) the curve with extremised distance between two points $p, q \in \mathcal{M}$ is called a geodesic. As mentioned earlier, the metric defines distance on a manifold and to find the geodesic joining p and q we need to use calculus of variations on the total length Δs from Eq. (1.2.63) of a general curve between two points. Given that the integrand \mathcal{L} of Eq. (1.2.63) is a function $\mathcal{L}(x^\mu, \dot{x}^\mu)$, where the dot denotes differentiation by λ , we can use the Euler-Lagrange equation,

$$\frac{\partial \mathcal{L}}{\partial x^\mu} - \frac{d}{d\lambda} \frac{\partial \mathcal{L}}{\partial \dot{x}^\mu} = 0, \quad (1.2.72)$$

to give a differential equation with solution being a geodesic. Applying the EL equation to the integrand of Eq. (1.2.63) is algebraically messy, it is easier⁶ to square the integrand and start from \mathcal{L}^2 giving the same solution if $d\mathcal{L}/d\lambda = 0$,

$$\frac{\partial \mathcal{L}^2}{\partial x^\alpha} - \frac{d}{d\lambda} \frac{\partial \mathcal{L}^2}{\partial \dot{x}^\alpha} = 0, \quad (1.2.73)$$

$$\frac{\partial}{\partial x^\alpha} (g_{\mu\nu} \dot{x}^\mu \dot{x}^\nu) - \frac{d}{d\lambda} \frac{\partial}{\partial \dot{x}^\alpha} (g_{\mu\nu} \dot{x}^\mu \dot{x}^\nu) = 0, \quad (1.2.74)$$

$$(\partial_\alpha g_{\mu\nu}) \dot{x}^\mu \dot{x}^\nu - 2 \frac{d}{d\lambda} (g_{\alpha\nu} \dot{x}^\nu) = 0, \quad (1.2.75)$$

$$(\partial_\alpha g_{\mu\nu}) \dot{x}^\mu \dot{x}^\nu - 2 (\dot{x}^\rho \partial_\rho (g_{\alpha\nu}) \dot{x}^\nu) - 2 \ddot{x}^\nu g_{\alpha\nu} = 0. \quad (1.2.76)$$

Rearranging and multiplying by $g^{\alpha\beta}$ gives,

$$\ddot{x}^\beta + \frac{1}{2} g^{\alpha\beta} (\partial_\mu g_{\alpha\nu} + \partial_\nu g_{\alpha\mu} - \partial_\alpha g_{\mu\nu}) \dot{x}^\mu \dot{x}^\nu = 0, \quad (1.2.77)$$

$$\ddot{x}^\beta + \Gamma^\beta_{\mu\nu} \dot{x}^\mu \dot{x}^\nu = 0, \quad (1.2.78)$$

where $\Gamma^\beta_{\mu\nu}$ are the components of the connection symbol which will be re-visited in Section (1.3.3). A trivial solution to Eq. (1.2.78) is in flat space using Cartesian coordinates where $\Gamma^\beta_{\mu\nu} = 0$ and therefore $\ddot{x}^\beta = 0$ so \dot{x}^β is a constant; this tells us the shortest distance between two points in flat space is a straight line. In other words, geodesics are straight lines in flat space.

⁶Given that \mathcal{L} is homogeneous to degree k , $\dot{x}^i \partial \mathcal{L} / \partial \dot{x}^i = k\mathcal{L}$ for constant k , one can show that $d\mathcal{L}/d\lambda = 0$ if the Euler-Lagrange equation is assumed.

Non-Affine Geodesics

The equation of a geodesic given above is true for an *affinely* parameterised curve. An affine parameter λ is defined so that the length of a curve δs between two parameter values λ and $\lambda + \delta\lambda$ is given by $\delta s = k(\delta\lambda)$ for constant k ; the arclength along a curve is linearly proportional to the value of the λ . This property was inherent in the derivation of Eq. (1.2.78) is that $d\mathcal{L}/d\lambda = 0$ was assumed along a curve.

A non-affine parameter μ could equally be used to describe the curve. Writing $\mu(\lambda)$ the geodesic equation is transformed as shown,

$$\frac{d^2x^\beta}{d\lambda^2} + \Gamma_{\mu\nu}^\beta \frac{dx^\mu}{d\lambda} \frac{dx^\nu}{d\lambda} = 0, \quad (1.2.79)$$

$$\left(\frac{d^2\mu}{d\lambda^2} \frac{d}{d\mu} + \left(\frac{d\mu}{d\lambda} \right)^2 \frac{d^2}{d\mu^2} \right) x^\beta + \Gamma_{\mu\nu}^\beta \frac{dx^\mu}{d\mu} \frac{dx^\nu}{d\mu} \left(\frac{d\mu}{d\lambda} \right)^2 = 0, \quad (1.2.80)$$

$$\frac{d^2x^\beta}{d\mu^2} + \Gamma_{\mu\nu}^\beta \frac{dx^\mu}{d\mu} \frac{dx^\nu}{d\mu} = - \left(\frac{d\mu}{d\lambda} \right)^{-2} \frac{d^2\mu}{d\lambda^2} \frac{dx^\beta}{d\mu}, \quad (1.2.81)$$

$$\frac{d^2x^\beta}{d\mu^2} + \Gamma_{\mu\nu}^\beta \frac{dx^\mu}{d\mu} \frac{dx^\nu}{d\mu} = -f(\mu) \frac{dx^\beta}{d\mu}, \quad (1.2.82)$$

which is the same as the affine geodesic equation except with an extra non-zero right hand side proportional to $dx^\beta/d\mu$ and some function $f(\mu)$. If μ is a linear function of λ then μ is also an affine parameter; this is reflected in the term $d^2\mu/d\lambda^2 = 0$ and the affine geodesic equation is returned.

The non-affine geodesic equation can be found by re-deriving the Geodesic equation from \mathcal{L} rather than \mathcal{L}^2 . It can be seen that,

$$\frac{\partial \mathcal{L}}{\partial x^\alpha} = \frac{1}{2\mathcal{L}} \dot{x}^\mu \dot{x}^\nu \partial_\alpha g_{\mu\nu}, \quad (1.2.83)$$

$$\frac{d}{d\lambda} \frac{\partial \mathcal{L}}{\partial \dot{x}^\mu} = \frac{d}{d\lambda} \left(\frac{1}{\mathcal{L}} g_{\mu\alpha} \dot{x}^\mu \right), \quad (1.2.84)$$

$$= \frac{1}{\mathcal{L}} g_{\mu\alpha} \ddot{x}^\mu + \frac{1}{\mathcal{L}} \dot{x}^\nu \dot{x}^\mu \partial_\nu g_{\mu\alpha} + g_{\mu\alpha} \dot{x}^\mu \frac{d}{d\lambda} \frac{1}{\mathcal{L}}. \quad (1.2.85)$$

Rearranging and using the Euler-Lagrange equation as in the previous section gives

$$\ddot{x}^\beta + \Gamma_{\mu\nu}^\beta \dot{x}^\mu \dot{x}^\nu = -\mathcal{L} \frac{d\mathcal{L}}{d\lambda} \dot{x}^\alpha, \quad (1.2.86)$$

which is the non-affine geodesic equation.

1.3 Tensor Calculus and Curvature

1.3.1 General Covariance and Coordinate transformations

Many laws of physics can be expressed as tensor field equations where a tensor field is the assignment of a tensor to each point in space; this assignment should be smooth if we want to calculate the derivatives. The power of tensor algebra and tensor calculus is that if a tensor field equation can be written in one coordinate system then it must hold (in index form) in all regular coordinate systems. This is a consequence of the tensor transformation law. Looking back, we can write a generic vector \mathbf{X} as $X^\mu e_\mu = X^\mu \partial_\mu$ and if we choose a coordinate transformation $x^\mu \rightarrow \tilde{x}^\mu$ then we see that in the transformed coordinate system the vector field \mathbf{X} , written $\tilde{\mathbf{X}}$, becomes

$$\tilde{\mathbf{X}} = \tilde{X}^\mu \frac{\partial}{\partial \tilde{x}^\mu}, \quad (1.3.1)$$

$$= \tilde{X}^\mu \frac{\partial x^\nu}{\partial \tilde{x}^\mu} \frac{\partial}{\partial x^\nu}, \quad (1.3.2)$$

$$= X^\nu \frac{\partial}{\partial x^\nu}, \quad (1.3.3)$$

$$= \mathbf{X}, \quad (1.3.4)$$

where the components $X^\nu = \tilde{X}^\mu \frac{\partial x^\nu}{\partial \tilde{x}^\mu}$ are required to transform in order to ensure $\mathbf{X} = \tilde{\mathbf{X}}$. This says that the underlying geometric object (a vector in this case) is independent of the coordinates used to describe them; the tradeoff for this useful property is that the vectors components X^μ have to transform under the tensor transformation law, effectively opposing the transformation of the basis vectors. Working from a co-vector ω we can write it as $\omega_\mu \theta^\mu = \omega_\mu dx^\mu$ in component-basis form and the same coordinate transformation gives

$$\tilde{\omega} = \tilde{\omega}_\mu d\tilde{x}^\mu, \quad (1.3.5)$$

$$= \tilde{\omega}_\mu \frac{\partial \tilde{x}^\mu}{\partial x^\nu} dx^\nu, \quad (1.3.6)$$

$$= \omega_\nu dx^\nu, \quad (1.3.7)$$

where the co-vector components transform like $\omega_\nu = \tilde{\omega}_\mu \frac{\partial \tilde{x}^\mu}{\partial x^\nu}$, the opposite way to the vector components. These transformation laws ensure that a scalar field created from the product of a vector field and a co-vector field, like $\omega : \mathbf{X}$, is a Lorentz scalar not transforming under coordinate transformations. This can be seen from

$$\tilde{\omega} : \tilde{\mathbf{X}} = \tilde{X}^\mu \tilde{\omega}_\mu, \quad (1.3.8)$$

$$= X^\nu \frac{\partial \tilde{x}^\mu}{\partial x^\nu} \frac{\partial x^\rho}{\partial \tilde{x}^\mu} \omega_\rho, \quad (1.3.9)$$

$$= X^\nu \frac{\partial x^\rho}{\partial x^\nu} \omega_\rho, \quad (1.3.10)$$

$$= X^\nu \delta_\nu^\rho \omega_\rho, \quad (1.3.11)$$

$$= X^\nu \omega_\nu, \quad (1.3.12)$$

$$= \omega : \mathbf{X}. \quad (1.3.13)$$

The general tensor transformation law can be derived from chaining multiple of the previous examples together, for example,

$$\tilde{T}^{\mu\nu\dots}_{\rho\sigma\dots} = T^{\alpha\beta\dots}_{\gamma\delta\dots} \left(\frac{\partial \tilde{x}^\mu}{\partial x^\alpha} \frac{\partial \tilde{x}^\nu}{\partial x^\beta} \times \dots \times \frac{\partial x^\gamma}{\partial \tilde{x}^\rho} \frac{\partial x^\delta}{\partial \tilde{x}^\sigma} \times \dots \right), \quad (1.3.14)$$

where each upstairs tensor index on T is contracted with a $\partial \tilde{x}^\mu / \partial x^\nu$ and each downstairs index is contracted with a $\partial x^\rho / \partial \tilde{x}^\sigma$.

Tensor Densities

A tensor density is the generalisation of a tensor field obeying the tensor transformation law in Eq. (1.3.14). One important example of a tensor density is the volume element $\sqrt{-g}$, this is a scalar density. This object does not have any indices so at first glance may pass for a true scalar field. However, when a coordinate transformation $x^\mu \rightarrow \tilde{x}^\mu$ is applied we find that $\sqrt{-g} \rightarrow \sqrt{-\tilde{g}} \neq \sqrt{-g}$, but for a general scalar field ϕ we find $\phi \rightarrow \tilde{\phi} = \phi$; therefore $\sqrt{-g}$ cannot be a scalar field. This can be shown explicitly by looking at the determinant of the metric,

$$\sqrt{-\tilde{g}} = \sqrt{\det(-\tilde{g}_{\mu\nu})}, \quad (1.3.15)$$

$$= \sqrt{\det\left(-g_{\alpha\beta} \frac{\partial x^\alpha}{\partial \tilde{x}^\mu} \frac{\partial x^\beta}{\partial \tilde{x}^\nu}\right)}, \quad (1.3.16)$$

$$= \sqrt{-g} \det\left(\frac{\partial x^\alpha}{\partial \tilde{x}^\mu}\right), \quad (1.3.17)$$

and as can be seen, the volume element picks up a factor of the determinant of the Jacobian. A tensor density \mathcal{T} of weight w can be written in the form,

$$\mathcal{T} = \sqrt{-g}^w \mathbf{T}, \quad (1.3.18)$$

where \mathbf{T} is a tensor obeying the tensor transformation law. It should be noted that a tensor density of weight zero is a regular tensor and the weight of a tensor has nothing to do with the rank of the tensor.

Lie Derivatives of Tensor Densities

To calculate the Lie derivative of a tensor density, first the Lie derivative of $\sqrt{-g}$ should be calculated, and in order to calculate the Lie derivative of the volume element a preliminary result is needed. Following the definition of a Lie derivative in section 1.2.5 and setting $y^\mu = x^\mu + \epsilon \xi^\mu$, the determinant of the Jacobian matrix is,

$$\det\left(\frac{\partial y^\mu}{\partial x^\rho}\right) = \det\left(\delta_\rho^\mu + \epsilon \frac{\partial \xi^\mu}{\partial x^\rho}\right), \quad (1.3.19)$$

$$= \det\begin{pmatrix} 1 + \epsilon \frac{\partial \xi^1}{\partial x^1} & \epsilon \frac{\partial \xi^1}{\partial x^2} & \epsilon \frac{\partial \xi^1}{\partial x^3} & \epsilon \frac{\partial \xi^1}{\partial x^4} \\ \epsilon \frac{\partial \xi^2}{\partial x^1} & 1 + \epsilon \frac{\partial \xi^2}{\partial x^2} & \epsilon \frac{\partial \xi^2}{\partial x^3} & \epsilon \frac{\partial \xi^2}{\partial x^4} \\ \epsilon \frac{\partial \xi^3}{\partial x^1} & \epsilon \frac{\partial \xi^3}{\partial x^2} & 1 + \epsilon \frac{\partial \xi^3}{\partial x^3} & \epsilon \frac{\partial \xi^3}{\partial x^4} \\ \epsilon \frac{\partial \xi^4}{\partial x^1} & \epsilon \frac{\partial \xi^4}{\partial x^2} & \epsilon \frac{\partial \xi^4}{\partial x^3} & 1 + \epsilon \frac{\partial \xi^4}{\partial x^4} \end{pmatrix}, \quad (1.3.20)$$

$$= \left(1 + \epsilon \sum_i \frac{\partial \xi^i}{\partial x^i} + \mathcal{O}(\epsilon^2)\right), \quad (1.3.21)$$

$$= 1 + \epsilon \partial_\mu \xi^\mu + \mathcal{O}(\epsilon^2), \quad (1.3.22)$$

where a four-dimensional spacetime was used for explicitness, but the calculation works exactly the same in any number of dimensions. Using this result and the definition of a Lie derivative, $\mathcal{L}_\xi \sqrt{-g}$ evaluates

to,

$$\mathcal{L}_\xi \sqrt{-g} = \lim_{\epsilon \rightarrow 0} \left(\frac{\Phi^* \sqrt{-\tilde{g}} \Big|_q - \sqrt{-g} \Big|_p}{\epsilon} \right), \quad (1.3.23)$$

$$= \lim_{\epsilon \rightarrow 0} \left(\frac{\sqrt{-\det(g_{\mu\nu}(y^\alpha) \frac{\partial y^\mu}{\partial x^\rho} \frac{\partial y^\nu}{\partial x^\sigma})} - \sqrt{-g}(x^\alpha)}{\epsilon} \right), \quad (1.3.24)$$

$$= \lim_{\epsilon \rightarrow 0} \left(\frac{\sqrt{-g}(y^\alpha) \det\left(\frac{\partial y^\mu}{\partial x^\rho}\right) - \sqrt{-g}(x^\alpha)}{\epsilon} \right), \quad (1.3.25)$$

$$= \lim_{\epsilon \rightarrow 0} \left(\frac{\sqrt{-g}(y^\alpha)(1 + \epsilon \partial_\mu \xi^\mu + \mathcal{O}(\epsilon^2)) - \sqrt{-g}(x^\alpha)}{\epsilon} \right), \quad (1.3.26)$$

$$= \lim_{\epsilon \rightarrow 0} \left(\frac{[\sqrt{-g}(x^\alpha) + \epsilon \xi^\mu \partial_\mu \sqrt{-g}(x^\alpha)](1 + \epsilon \partial_\mu \xi^\mu + \mathcal{O}(\epsilon^2)) - \sqrt{-g}(x^\alpha)}{\epsilon} \right), \quad (1.3.27)$$

$$= \lim_{\epsilon \rightarrow 0} \left(\frac{\epsilon \xi^\mu \partial_\mu \sqrt{-g}(x^\alpha) + \epsilon \sqrt{-g}(x^\alpha) \partial_\mu \xi^\mu + \mathcal{O}(\epsilon^2)}{\epsilon} \right), \quad (1.3.28)$$

$$\mathcal{L}_\xi \sqrt{-g} = \xi^\mu \partial_\mu \sqrt{-g} + \sqrt{-g} \partial_\mu \xi^\mu. \quad (1.3.29)$$

Given that $\mathcal{L}_\xi \sqrt{-g}$ has been calculated, it is straightforward to calculate the Lie derivative of a tensor density $\mathcal{T} = \sqrt{-g}^w \mathbf{T}$ of weight w , where \mathbf{T} is a regular tensor, using the Leibniz rule in Eq. (1.2.45). The Lie derivative is,

$$\mathcal{L}_\xi \mathcal{T} = \sqrt{-g}^w \left(\mathcal{L}_\xi \mathbf{T} + w \mathbf{T} \left(\frac{1}{\sqrt{-g}} \xi^\mu \partial_\mu \sqrt{-g} + \partial_\mu \xi^\mu \right) \right). \quad (1.3.30)$$

As would be expected, setting $w = 0$ returns the regular Lie derivative of a tensor. This can also be written as,

$$\mathcal{L}_\xi \mathcal{T} = \tilde{\mathcal{L}}_\xi \mathcal{T} + w \mathcal{T} \partial_\mu \xi^\mu, \quad (1.3.31)$$

where $\tilde{\mathcal{L}}_\xi$ is the differential operator equivalent to the Lie derivative of the same tensor but with weight zero.

1.3.2 The Covariant Derivative

There are many types of derivative on a manifold that we care about in the context of General Relativity. The simplest is the partial derivative,

$$\partial_\mu = \frac{\partial}{\partial x^\mu}, \quad (1.3.32)$$

which works much the same as always. Two other derivatives are the exterior derivative⁷ and the Lie derivative which is discussed in section 1.2.5.

The purpose of the covariant derivative, denoted ∇_μ , is to generalise the partial derivative to curved spaces (or curvilinear coordinates). The covariant derivative exactly reduces to the partial derivative (∂_μ) in flat space with Cartesian coordinates. As suggested by the name, the covariant derivative of an object is covariant⁸; it obeys the tensor transformation law of section 1.3.1. The covariant derivative

⁷The antisymmetric derivative of a differential n -form (totally antisymmetric co-tensor of rank n) that returns a differential $(n+1)$ -form.

⁸Strictly speaking, the partial derivative ∂_μ is covariant under a coordinate transformation but does not map to the same geometric object as $\partial/\partial \tilde{x}^\mu$ in the new coordinate system. This can also be demonstrated by imagining the basis vector e_μ instead, while this is a perfectly good vector it does not map to \tilde{e}_μ (the basis vector in using coordinates \tilde{x}^μ) under a coordinate transformation.

uses a vector field \mathbf{X} to map a (p, q) tensor field \mathbf{T} to a (p, q) tensor field $\nabla_{\mathbf{X}}\mathbf{T}$. Requiring the covariant derivative of a tensor to return another tensor may sound pedantic but it allows the writing of physical differential equations that are covariant, i.e. that hold in all coordinate systems. Encoding the laws of physics with tensor differential equations is explored in more detail in section 1.4.3.

To be the analogue of the partial derivative, the covariant derivative must be linear in first argument, linear in second argument and obey the Leibniz rule,

$$\nabla_{f\mathbf{X}+g\mathbf{Y}}\mathbf{T} = f\nabla_{\mathbf{X}}\mathbf{T} + g\nabla_{\mathbf{Y}}\mathbf{T}, \quad (1.3.33)$$

$$\nabla_{\mathbf{X}}(a\mathbf{T} + b\mathbf{W}) = a\nabla_{\mathbf{X}}\mathbf{T} + b\nabla_{\mathbf{X}}\mathbf{W}, \quad (1.3.34)$$

$$\nabla_{\mathbf{X}}(f\mathbf{T}) = f\nabla_{\mathbf{X}}\mathbf{T} + \mathbf{T}\nabla_{\mathbf{X}}f, \quad (1.3.35)$$

where a and b are constants, f and g are functions on \mathcal{M} and \mathbf{T} and \mathbf{W} are tensors of equal rank. These are exactly the same as the conditions imposed on Lie derivatives in section 1.2.5. From now on the covariant derivative $\nabla_{\mathbf{e}_\mu}$ with respect to a basis vector \mathbf{e}_μ will be written as ∇_μ .

Let us start by finding the covariant derivative of a scalar field φ . The partial derivative $\partial_\mu\varphi$ obeys the tensor transformation law for a co-vector,

$$\frac{\partial}{\partial\tilde{x}^\mu}\tilde{\varphi} = \frac{\partial}{\partial\tilde{x}^\mu}\varphi, \quad (1.3.36)$$

$$= \frac{\partial x^\nu}{\partial\tilde{x}^\mu}\frac{\partial}{\partial x^\nu}\varphi, \quad (1.3.37)$$

and therefore the $\nabla_\mu\varphi = \partial_\mu\varphi$. Note that $\varphi = \tilde{\varphi}$ for any point p as a scalar remains unchanged in a coordinate transformation. Complications arise when taking the partial derivative of any other higher rank tensor; let's demonstrate this with a vector \mathbf{X} .

$$\frac{\partial}{\partial\tilde{x}^\mu}\tilde{X}^\alpha = \frac{\partial}{\partial\tilde{x}^\mu}\left(\frac{\partial\tilde{x}^\alpha}{\partial x^\beta}X^\beta\right), \quad (1.3.38)$$

$$= \frac{\partial x^\nu}{\partial\tilde{x}^\mu}\frac{\partial}{\partial x^\nu}\left(\frac{\partial\tilde{x}^\alpha}{\partial x^\beta}X^\beta\right), \quad (1.3.39)$$

$$= \underbrace{\frac{\partial\tilde{x}^\alpha}{\partial x^\beta}\frac{\partial x^\nu}{\partial\tilde{x}^\mu}}_{\text{Tensor transformation law}} \frac{\partial}{\partial x^\nu}X^\beta + X^\beta\frac{\partial x^\nu}{\partial\tilde{x}^\mu}\frac{\partial}{\partial x^\nu}\left(\frac{\partial\tilde{x}^\alpha}{\partial x^\beta}\right), \quad (1.3.40)$$

Tensor transformation law

and as can be seen, only the first term on the right hand side should exist if the components $\partial_\mu X^\alpha$ were to obey the tensor transformation law.

The problem with performing differentiation on tensors is that it requires the comparison of tensors at two different (infinitesimally close) tangent spaces. Lie derivatives circumvented this problem by comparing two tangent planes with a pullback defined by a diffeomorphism. Another way of overcoming this problem is to consider how the coordinate basis vectors change over the manifold, not just the components. Defining the covariant derivative of the basis vector as

$$\nabla_{\mathbf{e}_\rho}\mathbf{e}_\nu = \nabla_\rho\mathbf{e}_\nu := \Gamma^\mu{}_{\nu\rho}\mathbf{e}_\mu, \quad (1.3.41)$$

where $\Gamma^\mu{}_{\nu\rho}$ is called the connection symbol⁹ due to it defining a connection between neighbouring tangent spaces. The connection can be used to get the covariant derivative of the vector field $\mathbf{X} = X^\rho\mathbf{e}_\rho$,

$$\nabla_\rho(X^\nu\mathbf{e}_\nu) = (\partial_\rho X^\nu)\mathbf{e}_\nu + X^\nu(\nabla_\rho\mathbf{e}_\nu), \quad (1.3.42)$$

$$= (\partial_\rho X^\nu)\mathbf{e}_\nu + X^\nu\Gamma^\mu{}_{\nu\rho}\mathbf{e}_\mu, \quad (1.3.43)$$

$$= (\partial_\rho X^\mu + \Gamma^\mu{}_{\nu\rho}X^\nu)\mathbf{e}_\mu. \quad (1.3.44)$$

⁹This symbol is also called the *Christoffel symbol* or the *connection coefficients*.

Note that on the first line above we have used $\nabla_\rho X^\nu = \partial_\rho X^\nu$ as the X^ν are being treated as a set of scalar function coefficients multiplying the basis vectors \mathbf{e}_μ . Strictly we should write the covariant derivative of \mathbf{X} as,

$$\nabla \mathbf{X} = (\nabla X)_\sigma^\mu \mathbf{e}_\mu \otimes \boldsymbol{\theta}^\sigma, \quad (1.3.45)$$

but for convenience the coefficients $(\nabla X)_\sigma^\mu$ are usually denoted as,

$$\nabla_\sigma X^\mu = \partial_\sigma X^\mu + \Gamma^\mu_{\nu\sigma} X^\nu. \quad (1.3.46)$$

This is a slight abuse of notation as $\nabla_\sigma X^\mu$ might be understood as the covariant derivative of the components X^μ , but really it denotes the component $\boldsymbol{\theta}^\sigma \cdot (\nabla \mathbf{X}) \cdot \mathbf{e}_\mu$ where $\nabla \mathbf{X}$ is given in Eq. (1.3.45).

Given that the covariant derivative of a scalar reduces to the partial derivative we can see that,

$$\nabla_\rho (\mathbf{e}_\mu : \boldsymbol{\theta}^\nu) = 0, \quad (1.3.47)$$

and using the Leibniz rule (1.3.35),

$$\nabla_\rho (\mathbf{e}_\nu : \boldsymbol{\theta}^\mu) = (\nabla_\rho \mathbf{e}_\nu) : \boldsymbol{\theta}^\mu + \mathbf{e}_\nu : (\nabla_\rho \boldsymbol{\theta}^\mu), \quad (1.3.48)$$

$$= (\Gamma^\sigma_{\nu\rho} \mathbf{e}_\sigma) : \boldsymbol{\theta}^\mu + \mathbf{e}_\nu : (\nabla_\rho \boldsymbol{\theta}^\mu), \quad (1.3.49)$$

$$= \Gamma^\mu_{\nu\rho} + \mathbf{e}_\nu : (\nabla_\rho \boldsymbol{\theta}^\mu). \quad (1.3.50)$$

Combining Eqs. (1.3.47) and (1.3.50) gives

$$\mathbf{e}_\nu : (\nabla_\rho \boldsymbol{\theta}^\mu) = -\Gamma^\mu_{\nu\rho}, \quad (1.3.51)$$

and therefore we must have

$$\nabla_\rho \boldsymbol{\theta}^\mu = -\Gamma^\mu_{\nu\rho} \boldsymbol{\theta}^\nu. \quad (1.3.52)$$

In an identical way, we might ask what is the covariant derivative of a co-vector $\boldsymbol{\omega} = \omega_\alpha \boldsymbol{\theta}^\alpha$. The covariant derivative $\nabla \boldsymbol{\omega}$ can be found from,

$$\nabla_\sigma \boldsymbol{\omega} = \nabla_\sigma (\omega_\alpha \boldsymbol{\theta}^\alpha), \quad (1.3.53)$$

$$= \partial_\sigma (\omega_\alpha) \boldsymbol{\theta}^\alpha + \omega_\alpha \nabla_\sigma \boldsymbol{\theta}^\alpha, \quad (1.3.54)$$

$$= \partial_\sigma (\omega_\alpha) \boldsymbol{\theta}^\alpha - \omega_\alpha \Gamma^\alpha_{\nu\sigma} \boldsymbol{\theta}^\nu, \quad (1.3.55)$$

$$= (\partial_\sigma \omega_\alpha - \omega_\nu \Gamma^\nu_{\alpha\sigma}) \boldsymbol{\theta}^\alpha. \quad (1.3.56)$$

Again, we used have $\nabla_\sigma \omega_\alpha = \partial_\sigma \omega_\alpha$ as the components ω_α are scalar coefficients of the basis co-vectors $\boldsymbol{\theta}^\alpha$. From now on the components $(\nabla \boldsymbol{\omega})_{\sigma\alpha}$ are written as $\nabla_\sigma \omega_\alpha$ even though this is a mild abuse of notation.

The covariant derivative of a general tensor can be found by following the simple rule of adding a connection symbol term for each index, for example,

$$\nabla_\mu T^{\alpha\beta\dots}_{\lambda\nu\dots} = \partial_\mu T^{\alpha\beta\dots}_{\lambda\nu\dots} + \Gamma^\alpha_{\sigma\mu} T^{\sigma\beta\dots}_{\lambda\nu\dots} + \Gamma^\beta_{\sigma\mu} T^{\alpha\sigma\dots}_{\lambda\nu\dots} + \dots - \Gamma^\sigma_{\lambda\mu} T^{\alpha\beta\dots}_{\sigma\nu\dots} - \Gamma^\sigma_{\nu\mu} T^{\alpha\beta\dots}_{\lambda\sigma\dots} - \dots. \quad (1.3.57)$$

1.3.3 The Connection

In flat space we are used to the idea that the partial derivative commutes, i.e. $\partial_\mu \partial_\nu = \partial_\nu \partial_\mu$, and this remains true by definition in curved space¹⁰. However, the covariant derivative does not generally commute, $\nabla_\mu \nabla_\nu \neq \nabla_\nu \nabla_\mu$. Applying $\nabla_\mu \nabla_\nu - \nabla_\nu \nabla_\mu$ to a scalar field φ gives,

¹⁰One could also interpret $\partial_\mu \partial_\nu - \partial_\nu \partial_\mu$ as the commutation of basis vectors $\mathbf{e}_\mu(\mathbf{e}_\nu) - \mathbf{e}_\nu(\mathbf{e}_\mu) = [e_\mu]^\alpha \partial_\alpha([e_\nu]^\beta) \partial_\beta - [e_\nu]^\alpha \partial_\alpha([e_\mu]^\beta) \partial_\beta$. This is only vanishes in the case that all the components $[e_\mu]^\alpha$ of the basis vectors are constant. A special case where $[e_\mu]^\alpha = \delta_\mu^\alpha$ is called the coordinate basis.

$$(\nabla_\mu \nabla_\nu - \nabla_\nu \nabla_\mu)\varphi = \nabla_\mu \nabla_\nu \varphi - \nabla_\nu \nabla_\mu \varphi, \quad (1.3.58)$$

$$= \nabla_\mu \partial_\nu \varphi - \nabla_\nu \partial_\mu \varphi, \quad (1.3.59)$$

$$= (\partial_\mu \partial_\nu - \partial_\nu \partial_\mu)\varphi - \Gamma^\sigma_{\nu\mu} \partial_\sigma \varphi + \Gamma^\sigma_{\mu\nu} \partial_\sigma \varphi, \quad (1.3.60)$$

$$= (\Gamma^\sigma_{\mu\nu} - \Gamma^\sigma_{\nu\mu}) \partial_\sigma \varphi, \quad (1.3.61)$$

where we have used the fact that $\nabla_\mu \varphi = \partial_\mu \varphi$ for a scalar field. This non-commutativity of derivatives of a scalar field is known as torsion.

Torsion

If a connection is torsion free then $(\nabla_\mu \nabla_\nu - \nabla_\nu \nabla_\mu)\varphi = 0$ which implies $\Gamma^\sigma_{\nu\mu} = \Gamma^\sigma_{\mu\nu}$. This leads to two important tensor identities; first the antisymmetric derivative of a co-vector,

$$\nabla_\mu A_\nu - \nabla_\nu A_\mu = \partial_\mu A_\nu - \partial_\nu A_\mu - \underbrace{(\Gamma^\sigma_{\nu\mu} - \Gamma^\sigma_{\mu\nu}) A_\sigma}_{=0}, \quad (1.3.62)$$

$$\nabla_\mu A_\nu - \nabla_\nu A_\mu = \partial_\mu A_\nu - \partial_\nu A_\mu, \quad (1.3.63)$$

and the second identity,

$$\nabla_X Y - \nabla_Y X = (X^\mu \nabla_\mu Y^\nu - Y^\mu \nabla_\mu X^\nu) e_\nu, \quad (1.3.64)$$

$$= (X^\mu \partial_\mu Y^\nu - Y^\mu \partial_\mu X^\nu + \Gamma^\nu_{\sigma\mu} X^\mu Y^\sigma - \Gamma^\nu_{\sigma\mu} Y^\mu X^\sigma) e_\nu, \quad (1.3.65)$$

$$= (X^\mu \partial_\mu Y^\nu - Y^\mu \partial_\mu X^\nu + (\Gamma^\nu_{\sigma\mu} - \Gamma^\nu_{\mu\sigma}) X^\mu Y^\sigma) e_\nu, \quad (1.3.66)$$

$$= (X^\mu \partial_\mu Y^\nu - Y^\mu \partial_\mu X^\nu) e_\nu, \quad (1.3.67)$$

$$\nabla_X Y - \nabla_Y X = [X, Y]. \quad (1.3.68)$$

Here the *commutator bracket* $[X, Y]$ of two vectors X and Y is defined by,

$$[X^\mu \partial_\mu, Y^\nu \partial_\nu] = X^\mu \partial_\mu (Y^\nu \partial_\nu) - Y^\nu \partial_\nu (X^\mu \partial_\mu), \quad (1.3.69)$$

$$= X^\mu \partial_\mu Y^\nu - Y^\nu \partial_\nu (X^\mu) \partial_\mu + X^\mu Y^\nu \partial_\mu \partial_\nu - Y^\nu X^\mu \partial_\nu \partial_\mu, \quad (1.3.70)$$

$$= (X^\mu \partial_\mu Y^\nu - Y^\mu \partial_\mu X^\nu) \partial_\nu, \quad (1.3.71)$$

where the basis vector e_μ has been written as ∂_μ with the intention of acting on a function f over the manifold \mathcal{M} . Note that the components of the commutator bracket are equivalent to the Lie derivative $\mathcal{L}_X Y$.

Metric Compatibility

Another property that can be imposed on the connection is metric compatibility; this is $\nabla_\mu g_{\rho\sigma} = 0$, where g is the metric tensor. This immediately tells us $\nabla_\mu g^{\alpha\beta} = 0$ since,

$$\nabla_\mu \delta_\rho^\alpha = 0, \quad (1.3.72)$$

$$= \nabla_\mu (g^{\alpha\nu} g_{\nu\rho}), \quad (1.3.73)$$

$$= g_{\nu\rho} \nabla_\mu g^{\alpha\nu} + g^{\alpha\nu} \underbrace{\nabla_\mu g_{\nu\rho}}_{=0}, \quad (1.3.74)$$

which implies that $\nabla_\mu g^{\alpha\nu} = 0$. Metric compatibility implies that the raising and lowering of indices with the metric commutes with the covariant derivative,

$$\nabla_\mu T^{\alpha\beta\dots} = \nabla_\mu g^{\alpha\rho} T_\rho^{\beta\dots} = g^{\alpha\rho} \nabla_\mu T_\rho^{\beta\dots}, \quad (1.3.75)$$

and the derivative of the length of a vector X is given by,

$$\nabla_\alpha |\mathbf{X}|^2 = \nabla_\alpha (X^\mu X_\mu) = \nabla_\alpha (g_{\mu\nu} X^\mu X^\nu) = 2X^\mu \nabla_\alpha X_\mu = 2X_\mu \nabla_\alpha X^\mu. \quad (1.3.76)$$

The Levi-Civita Connection

As it turns out, a connection that obeys Eqs. (1.3.33, 1.3.34 & 1.3.35), is both torsion-free and metric-compatible, is uniquely determined. This connection is called the Levi-Civita connection. The Levi-Civita connection will always be assumed from now on and is given by,

$$\Gamma_{\mu\nu}^\rho = \frac{1}{2}g^{\rho\sigma}(\partial_\mu g_{\sigma\nu} + \partial_\nu g_{\mu\sigma} - \partial_\sigma g_{\nu\mu}), \quad (1.3.77)$$

which is also called Christoffel symbol of the second kind. The connection coefficient with lowered indices

$$\Gamma_{\sigma\mu\nu} = \frac{1}{2}(\partial_\mu g_{\sigma\nu} + \partial_\nu g_{\mu\sigma} - \partial_\sigma g_{\nu\mu}), \quad (1.3.78)$$

is called the Christoffel symbol of the first kind. It is very important to note that even though the connection symbols may look like a tensor they are not a tensor. This can be demonstrated by applying the tensor transformation law to the Christoffel symbol of the first kind,

$$2\tilde{\Gamma}_{\sigma\mu\nu} = \tilde{\partial}_\mu \tilde{g}_{\sigma\nu} + \tilde{\partial}_\nu \tilde{g}_{\mu\sigma} - \tilde{\partial}_\sigma \tilde{g}_{\nu\mu}, \quad (1.3.79)$$

$$= \frac{\partial x^\alpha}{\partial \tilde{x}^\mu} \partial_\alpha \left(\frac{\partial x^\beta}{\partial \tilde{x}^\sigma} \frac{\partial x^\gamma}{\partial \tilde{x}^\nu} g_{\beta\gamma} \right) + \frac{\partial x^\gamma}{\partial \tilde{x}^\nu} \partial_\gamma \left(\frac{\partial x^\beta}{\partial \tilde{x}^\sigma} \frac{\partial x^\alpha}{\partial \tilde{x}^\mu} g_{\alpha\beta} \right) - \frac{\partial x^\beta}{\partial \tilde{x}^\sigma} \partial_\beta \left(\frac{\partial x^\alpha}{\partial \tilde{x}^\mu} \frac{\partial x^\gamma}{\partial \tilde{x}^\nu} g_{\gamma\alpha} \right), \quad (1.3.80)$$

$$= \frac{\partial x^\alpha}{\partial \tilde{x}^\mu} \frac{\partial x^\beta}{\partial \tilde{x}^\sigma} \frac{\partial x^\gamma}{\partial \tilde{x}^\nu} (\partial_\alpha g_{\beta\gamma} + \partial_\gamma g_{\alpha\beta} - \partial_\beta g_{\gamma\alpha}) \\ + \frac{\partial x^\alpha}{\partial \tilde{x}^\mu} g_{\beta\gamma} \partial_\alpha \left(\frac{\partial x^\beta}{\partial \tilde{x}^\sigma} \frac{\partial x^\gamma}{\partial \tilde{x}^\nu} \right) + \frac{\partial x^\gamma}{\partial \tilde{x}^\nu} g_{\alpha\beta} \partial_\gamma \left(\frac{\partial x^\beta}{\partial \tilde{x}^\sigma} \frac{\partial x^\alpha}{\partial \tilde{x}^\mu} \right) - \frac{\partial x^\beta}{\partial \tilde{x}^\sigma} g_{\gamma\alpha} \partial_\beta \left(\frac{\partial x^\alpha}{\partial \tilde{x}^\mu} \frac{\partial x^\gamma}{\partial \tilde{x}^\nu} \right), \quad (1.3.81)$$

$$= 2 \frac{\partial x^\alpha}{\partial \tilde{x}^\mu} \frac{\partial x^\beta}{\partial \tilde{x}^\sigma} \frac{\partial x^\gamma}{\partial \tilde{x}^\nu} \Gamma_{\beta\alpha\gamma} \\ + \frac{\partial x^\alpha}{\partial \tilde{x}^\mu} g_{\beta\gamma} \partial_\alpha \left(\frac{\partial x^\beta}{\partial \tilde{x}^\sigma} \frac{\partial x^\gamma}{\partial \tilde{x}^\nu} \right) + \frac{\partial x^\gamma}{\partial \tilde{x}^\nu} g_{\alpha\beta} \partial_\gamma \left(\frac{\partial x^\beta}{\partial \tilde{x}^\sigma} \frac{\partial x^\alpha}{\partial \tilde{x}^\mu} \right) - \frac{\partial x^\beta}{\partial \tilde{x}^\sigma} g_{\gamma\alpha} \partial_\beta \left(\frac{\partial x^\alpha}{\partial \tilde{x}^\mu} \frac{\partial x^\gamma}{\partial \tilde{x}^\nu} \right), \quad (1.3.82)$$

$$= 2 \frac{\partial x^\alpha}{\partial \tilde{x}^\mu} \frac{\partial x^\beta}{\partial \tilde{x}^\sigma} \frac{\partial x^\gamma}{\partial \tilde{x}^\nu} \Gamma_{\beta\alpha\gamma} + \Xi_{\sigma\mu\nu}. \quad (1.3.83)$$

$$(1.3.84)$$

If $\Xi_{\sigma\mu\nu} = 0$ then the $\Gamma_{\sigma\mu\nu}$ would transform as an $(0, 3)$ tensor, however this is not the case in general and the Christoffel symbol of the first kind is not a tensor but instead a *symbol*¹¹. The non-tensorial nature of the Christoffel symbol of first kind is sufficient to prove that the Christoffel symbol of second kind is also not a tensor.

Lie Derivatives in the Levi Civita Connection

The covariant derivative ∇ , described in section 1.3.2 can replace all partial derivatives in a Lie derivative due to the connection symbols $(\Gamma^\mu_{\rho\sigma})$ cancelling out.

A special example of a Lie derivative is of the metric tensor, \mathbf{g} , giving

$$(\mathcal{L}_\xi g)_{\mu\nu} = \xi^\rho \partial_\rho g_{\mu\nu} + g_{\rho\nu} \partial_\mu \xi^\rho + g_{\mu\rho} \partial_\nu \xi^\rho, \quad (1.3.85)$$

$$= \xi^\rho \nabla_\rho g_{\mu\nu} + g_{\rho\nu} \nabla_\mu \xi^\rho + g_{\mu\rho} \nabla_\nu \xi^\rho, \quad (1.3.86)$$

where $\nabla_\rho g_{\mu\nu} = 0$ from metric compatibility, described in section 1.3.3. In the case the Lie derivative vanishes we get Killing's equation

$$\nabla_\mu \xi_\nu + \nabla_\nu \xi_\mu = 0, \quad (1.3.87)$$

and a vector field $\boldsymbol{\xi}$ satisfying Killing's equation is called a Killing vector. Killings equation will be very important in chapter 5.

¹¹Here we use the word symbol to denote an object that looks like the components of a tensor but does not obey the tensor transformation law.

Normal Coordinates

Consider a set of affinely parameterised geodesics, parameterised with λ , passing through the point p on a manifold \mathcal{M} that span a small finite neighbourhood about p . At p , each geodesic has a tangent vector $X^\mu|_p$. For all geodesics, define p to be the origin with $\lambda = 0$ and $x^\mu = 0$. Following a geodesic associated with $X^\mu|_p$ to a parameter value of λ will map to a new point q close to p for small enough λ . Normal coordinates $x^\mu(\lambda)$ at $q(\lambda)$ are defined such that $x^\mu(\lambda) = \lambda X^\mu|_p$. Given that $X^\mu|_p$ is constant, the geodesic equation, from Eq. (1.2.78), becomes

$$\frac{d^2x^\mu(\lambda)}{d\lambda^2} + \Gamma_{\mu\nu}^\alpha \frac{dx^\mu(\lambda)}{d\lambda} \frac{dx^\nu(\lambda)}{d\lambda} = \Gamma_{\mu\nu}^\alpha X^\mu|_p X^\nu|_p = 0. \quad (1.3.88)$$

Using the Levi-Civita connection, the connection symbol is symmetric in the lower two indices and this implies $\Gamma_{\mu\nu}^\alpha = 0$ as the geodesic equation must hold for generic $X^\mu|_p$. From the definition of the covariant derivative,

$$\partial_\alpha g_{\mu\nu} = \nabla_\alpha g_{\mu\nu} + \Gamma_{\alpha\nu}^\beta g_{\mu\beta} + \Gamma_{\alpha\mu}^\beta g_{\beta\nu}, \quad (1.3.89)$$

which must vanish in normal coordinates as $\Gamma_{\mu\nu}^\alpha = 0$ and the Levi-Civita connection demands $\nabla_\alpha g_{\mu\nu} = 0$. Therefore, it is possible to construct a coordinate system such that at one point p both $\partial_\alpha g_{\mu\nu} = 0$ and $\Gamma_{\mu\nu}^\alpha = 0$; importantly $\partial_\alpha \partial_\beta g_{\mu\nu} \neq 0$. As well as the metric's first derivative vanishing at p , it is also possible to demand that $g_{\mu\nu}|_p = \eta_{\mu\nu}$, the Minkowski metric defined in section 1.4.1. This can be done with a set of $(^j)X^\mu|_p$, one for each normal coordinate x^j , that satisfy

$$g((^j)X|_p, (^k)X|_p) = \eta_{jk}. \quad (1.3.90)$$

1.3.4 Curvature Tensors

We have already seen that with the Levi-Civita connection, the antisymmetrised second derivative of a scalar field vanishes; but operating on a vector field \mathbf{X} gives,

$$(\nabla_\mu \nabla_\nu - \nabla_\nu \nabla_\mu) X^\sigma = (\partial_\mu \nabla_\nu - \partial_\nu \nabla_\mu) X^\sigma + (\Gamma_{\mu\rho}^\sigma \nabla_\nu - \Gamma_{\nu\rho}^\sigma \nabla_\mu) X^\rho - \underbrace{(\Gamma_{\nu\mu}^\rho - \Gamma_{\mu\nu}^\rho)}_{=0} \nabla_\rho X^\sigma, \quad (1.3.91)$$

$$= \underbrace{(\partial_\mu \partial_\nu - \partial_\nu \partial_\mu)}_{=0} X^\sigma + (\partial_\mu \Gamma_{\nu\rho}^\sigma - \partial_\nu \Gamma_{\mu\rho}^\sigma) X^\rho + (\Gamma_{\mu\rho}^\sigma \nabla_\nu - \Gamma_{\nu\rho}^\sigma \nabla_\mu) X^\rho, \quad (1.3.92)$$

$$= (\partial_\mu \Gamma_{\nu\rho}^\sigma - \partial_\nu \Gamma_{\mu\rho}^\sigma) X^\rho + (\Gamma_{\mu\rho}^\sigma \partial_\nu - \Gamma_{\nu\rho}^\sigma \partial_\mu) X^\rho + (\Gamma_{\mu\rho}^\sigma \Gamma_{\nu\lambda}^\rho - \Gamma_{\nu\rho}^\sigma \Gamma_{\mu\lambda}^\rho) X^\lambda, \quad (1.3.93)$$

$$= X^\rho (\partial_\mu \Gamma_{\nu\rho}^\sigma - \partial_\nu \Gamma_{\mu\rho}^\sigma) + (\Gamma_{\mu\rho}^\sigma \Gamma_{\nu\lambda}^\rho - \Gamma_{\nu\rho}^\sigma \Gamma_{\mu\lambda}^\rho) X^\lambda, \quad (1.3.94)$$

where one should note that whenever a term appears after a derivative here it is to be differentiated, even if it is outside a bracket. We introduce the Riemann tensor $R^\sigma_{\rho\mu\nu}$ by,

$$(\nabla_\mu \nabla_\nu - \nabla_\nu \nabla_\mu) X^\sigma = R^\sigma_{\rho\mu\nu} X^\rho, \quad (1.3.95)$$

and setting $\mathbf{X} = e_\rho$, the coordinate basis vector associated with the x^ρ coordinate, the Riemann tensor can be written as

$$R^\sigma_{\rho\mu\nu} = \partial_\mu \Gamma_{\nu\rho}^\sigma - \partial_\nu \Gamma_{\mu\rho}^\sigma + \Gamma_{\mu\rho}^\sigma \Gamma_{\nu\lambda}^\lambda - \Gamma_{\nu\rho}^\sigma \Gamma_{\mu\lambda}^\lambda. \quad (1.3.96)$$

Symmetries of the Riemann Tensor

Now we will discuss the symmetries of the Riemann tensor. Firstly, from the definition of the Riemann tensor, it follows that $R^\sigma_{\rho\mu\nu} = -R^\sigma_{\rho\nu\mu}$; this can be written succinctly as $R^\sigma_{\rho[\mu\nu]} = 0$.

The second symmetry of the Riemann tensor is most conveniently derived using normal coordinates (described in section 1.3.3). At a point p where $\Gamma^\mu_{\nu\rho} = 0$ (but $\partial_\alpha \Gamma^\mu_{\nu\rho} \neq 0$) to get

$$R^\sigma_{\rho\mu\nu}|_p = \partial_\mu \Gamma^\sigma_{\nu\rho} - \partial_\nu \Gamma^\sigma_{\mu\rho}, \quad (1.3.97)$$

it is straightforward to show that $R^\sigma_{[\rho\mu\nu]} = 0$ as

$$R^\sigma_{[\rho\mu\nu]}|_p = \partial_{[\mu} \Gamma^\sigma_{\nu\rho]} - \partial_{[\nu} \Gamma^\sigma_{\mu\rho]} = 0, \quad (1.3.98)$$

due to the antisymmetrisation of any connection symbol like $\Gamma^\sigma_{[\nu\rho]} = 0$. Given that the tensor equation $R^\sigma_{[\rho\mu\nu]} = 0$ is true at p in normal coordinates then it is true in any coordinate system; on top of this the point p was arbitrary so therefore $R^\sigma_{[\rho\mu\nu]} = 0$ holds globally.

The next symmetry of the Riemann tensor is $R_{\sigma\rho\mu\nu} = R_{\mu\nu\sigma\rho}$. We can prove this again using normal coordinates at a point p ; here derivatives of the metric and its inverse vanish, but second derivatives do not. The proof of the symmetry follows Eq. (1.3.97) for the Riemann tensor in normal coordinates at a point p ,

$$R_{\sigma\rho\mu\nu}|_p = g_{\lambda\sigma} \partial_\mu \Gamma^\lambda_{\nu\rho} - g_{\lambda\sigma} \partial_\nu \Gamma^\lambda_{\mu\rho}, \quad (1.3.99)$$

$$= \partial_\mu g_{\lambda\sigma} \Gamma^\lambda_{\nu\rho} - \partial_\nu g_{\lambda\sigma} \Gamma^\lambda_{\mu\rho}, \quad (1.3.100)$$

$$= \partial_\mu \Gamma_{\sigma\nu\rho} - \partial_\nu \Gamma_{\sigma\mu\rho}, \quad (1.3.101)$$

$$= \frac{1}{2} (\partial_\mu \partial_\rho g_{\sigma\nu} - \partial_\mu \partial_\sigma g_{\rho\nu} + \partial_\nu \partial_\sigma g_{\rho\mu} - \partial_\nu \partial_\rho g_{\sigma\mu}), \quad (1.3.102)$$

and it is a straightforward to show that this final expression doesn't change under swapping indices $\sigma \leftrightarrow \mu$ and $\rho \leftrightarrow \nu$.

The final symmetry of the Riemann tensor is the Bianchi identity, $\nabla_{[\lambda} R_{\sigma\rho]\mu\nu} = 0$. Using normal coordinates at a point p , we can write

$$\nabla_\lambda R_{\sigma\rho\mu\nu}|_p = \partial_\lambda R_{\sigma\rho\mu\nu}|_p, \quad (1.3.103)$$

as all the Christoffel symbols generated by the covariant derivative cancel and therefore

$$2\nabla_\lambda R_{\sigma\rho\mu\nu}|_p = \partial_\lambda \partial_\mu \partial_\rho g_{\sigma\nu} - \partial_\lambda \partial_\mu \partial_\sigma g_{\rho\nu} + \partial_\lambda \partial_\nu \partial_\sigma g_{\rho\mu} - \partial_\lambda \partial_\nu \partial_\rho g_{\sigma\mu}. \quad (1.3.104)$$

Antisymmetrising over λ, ρ and σ makes each term vanish as the triple partial derivatives always contain two of the antisymmetrised indices and must vanish.

To summarise, we have the following symmetries of the Riemann tensor;

$$R_{\sigma\rho[\mu\nu]} = 0, \quad (1.3.105)$$

$$R_{\sigma\rho\mu\nu} = R_{\mu\nu\sigma\rho}, \quad (1.3.106)$$

$$\nabla_{[\lambda} R_{\sigma\rho]\mu\nu} = 0. \quad (1.3.107)$$

The first two of these can be used together to give another useful relation $R_{[\sigma\rho]\mu\nu} = 0$.

Contractions of the Riemann Tensor

Now that we have explored the Riemann tensor, it is time to introduce the Ricci tensor and Ricci scalar. The Ricci tensor $R_{\mu\nu}$ is simply defined by the unique, non-zero self contraction (or trace) of the Riemann tensor,

$$R_{\rho\mu} := R^\mu_{\rho\mu\nu} = R_{\sigma\rho\mu\nu} g^{\sigma\mu}. \quad (1.3.108)$$

Contracting the the Riemann tensor with $g^{\mu\nu}$ or $g^{\sigma\rho}$ would give zero due to the antisymmetries of those indices in the tensor. Any other contractions, such as with $g^{\rho\mu}$ can be shown to be exactly the same (up

to a minus sign) as contracting with $g^{\sigma\mu}$ using the symmetries of the Riemann tensor. The symmetries of the Riemann tensor guarantee that the Ricci tensor itself is symmetric. We can contract the Ricci tensor with itself (the same as taking the trace with the metric) to give us the Ricci scalar R ,

$$R = g^{\rho\nu} R_{\rho\nu}. \quad (1.3.109)$$

We can also take the trace of the Bianchi identity in Eq. (1.3.107) which gives us

$$g^{\lambda\mu} g^{\rho\nu} (\nabla_\lambda R_{\sigma\rho\mu\nu} + \nabla_\rho R_{\lambda\sigma\mu\nu} + \nabla_\sigma R_{\rho\lambda\mu\nu}) = 0, \quad (1.3.110)$$

$$\nabla^\mu R_{\sigma\mu} + \nabla^\nu R_{\sigma\nu} - \nabla_\sigma R = 0, \quad (1.3.111)$$

$$\nabla^\mu R_{\mu\sigma} - \frac{1}{2} \nabla_\sigma R = 0. \quad (1.3.112)$$

Defining the Einstein tensor \mathbf{G} ,

$$G_{\mu\nu} := R_{\mu\nu} - \frac{1}{2} g_{\mu\nu} R, \quad (1.3.113)$$

and using the contracted Bianchi identity with $\nabla g = 0$ from metric compatibility,

$$\nabla^\mu G_{\mu\nu} = \nabla^\mu R_{\mu\nu} - \frac{1}{2} (g_{\mu\nu} \nabla^\mu R + R \nabla^\mu g_{\mu\nu}), \quad (1.3.114)$$

$$= \nabla^\mu R_{\mu\nu} - \frac{1}{2} \nabla_\nu R, \quad (1.3.115)$$

$$= 0. \quad (1.3.116)$$

The Einstein tensor $G_{\mu\nu}$ therefore has a vanishing divergence $\nabla_\mu G^{\mu\nu} = 0$.

One more useful contraction of the Riemann tensor is with a second Riemann tensor which gives the Kretschmann scalar k ,

$$k := R_{\mu\nu\rho\sigma} R^{\mu\nu\rho\sigma}. \quad (1.3.117)$$

Both k and R are scalar fields so they provide us with a coordinate invariant curvature measure; section 1.4.5 will have use of the Kretschmann scalar in categorising spacetime singularities.

1.3.5 The Divergence Theorem

There is a generalisation of the divergence theorem to curved spaces, using differential geometry, which will have many uses throughout this work; especially section 5. However, before we discuss the divergence theorem, we must derive a preliminary matrix identity for a real symmetric matrix \mathbf{M} with determinant M ,

$$M^{-1} \partial_\mu M = M_{ij}^{-1} \partial_\mu M_{ij} = \text{Tr}(\mathbf{M}^{-1} \partial_\mu \mathbf{M}). \quad (1.3.118)$$

Simplifying the left hand side in terms of the eigenvalues λ_i of \mathbf{M} . Given that $M = \det\{\mathbf{M}\} = \prod_i \lambda_i$ we know

$$M^{-1} \partial_\mu M = \partial_\mu \ln(|M|), \quad (1.3.119)$$

$$= \partial_\mu \ln \left(\left| \prod_i \lambda_i \right| \right), \quad (1.3.120)$$

$$= \partial_\mu \sum_i \ln(|\lambda_i|), \quad (1.3.121)$$

$$= \sum_i \lambda_k^{-1} \partial_\mu \lambda_k. \quad (1.3.122)$$

Now we will show that the right hand side of Eq. (1.3.118) equals this. To do so we start by decomposing \mathbf{M} into a diagonal matrix \mathbf{D} like

$$\mathbf{M} = \mathbf{O}^{-1} \mathbf{D} \mathbf{O}, \quad (1.3.123)$$

$$\mathbf{M}^{-1} = \mathbf{O}^{-1} \mathbf{D}^{-1} \mathbf{O}, \quad (1.3.124)$$

then using the fact that $\text{Tr}(\mathbf{AB} \dots \mathbf{CD}) = \text{Tr}(\mathbf{DAB} \dots \mathbf{C})$ for matrices $\mathbf{A}, \mathbf{B}, \mathbf{C}, \dots$ and \mathbf{D} ,

$$\text{Tr}(\mathbf{M}^{-1} \partial_\mu \mathbf{M}) = \text{Tr}(\mathbf{O}^{-1} \mathbf{D}^{-1} \mathbf{O} \partial_\mu (\mathbf{O}^{-1} \mathbf{D} \mathbf{O})), \quad (1.3.125)$$

$$= \text{Tr}(\mathbf{D}^{-1} \partial_\mu \mathbf{D}) + \text{Tr}(\mathbf{O}^{-1} \partial_\mu \mathbf{O}) + \text{Tr}(\mathbf{O} \partial_\mu \mathbf{O}^{-1}), \quad (1.3.126)$$

$$= \text{Tr}(\mathbf{D}^{-1} \partial_\mu \mathbf{D}) + \text{Tr}(\underbrace{\partial_\mu (\mathbf{O}^{-1} \mathbf{O})}_{=0}), \quad (1.3.127)$$

$$= \text{Tr}(\mathbf{D}^{-1} \partial_\mu \mathbf{D}). \quad (1.3.128)$$

Given that \mathbf{D} is the diagonal matrix composed of the eigenvalues λ_i then it follows that,

$$\mathbf{D} = \text{Diag}\{\lambda_1, \lambda_2, \dots, \lambda_n\}, \quad (1.3.129)$$

$$\partial_\mu \mathbf{D} = \text{Diag}\{\partial_\mu \lambda_1, \partial_\mu \lambda_2, \dots, \partial_\mu \lambda_n\}, \quad (1.3.130)$$

$$\mathbf{D}^{-1} = \text{Diag}\{\lambda_1^{-1}, \lambda_2^{-1}, \dots, \lambda_n^{-1}\}. \quad (1.3.131)$$

Finally $\text{Tr}(\mathbf{D}^{-1} \partial_\mu \mathbf{D})$ can be evaluated in terms of the λ_i as follows,

$$\text{Tr}(\mathbf{D}^{-1} \partial_\mu \mathbf{D}) = \sum_{ij} D_{ij}^{-1} \partial_\mu D_{ij}, \quad (1.3.132)$$

$$= \sum_i D_{ii}^{-1} \partial_\mu D_{ii}, \quad (1.3.133)$$

$$= \sum_i \lambda_i^{-1} \partial_\mu \lambda_i, \quad (1.3.134)$$

which proves that Eq. (1.3.118) is true.

Now we can find a convenient form of the divergence $\nabla_\mu X^\mu$ of a vector \mathbf{X} . Expanding the covariant derivative gives

$$\nabla_\mu X^\mu = \partial_\mu X^\mu + \Gamma_{\mu\nu}^\mu X^\nu, \quad (1.3.135)$$

$$= \partial_\mu X^\mu + \frac{1}{2} g^{\mu\rho} (\partial_\mu g_{\rho\nu} + \partial_\nu g_{\mu\rho} - \partial_\rho g_{\mu\nu}) X^\nu, \quad (1.3.136)$$

$$= \partial_\mu X^\mu + \frac{1}{2} g^{\mu\rho} \partial_\nu g_{\mu\rho} X^\nu. \quad (1.3.137)$$

Applying Eq. (1.3.118) to the metric \mathbf{g} gives,

$$g^{\mu\rho} \partial_\nu g_{\mu\rho} = g^{-1} \partial_\nu g, \quad (1.3.138)$$

and the covariant divergence $\nabla_\mu X^\mu$ of a vector \mathbf{X} simplifies to

$$\nabla_\mu X^\mu = \partial_\mu X^\mu + \frac{1}{2g} \partial_\mu g, \quad (1.3.139)$$

$$= \frac{1}{\sqrt{|g|}} \partial_\mu \left(\sqrt{|g|} X^\mu \right), \quad (1.3.140)$$

which in the standard pseudo-Riemannian spacetime is often written

$$\nabla \cdot \mathbf{X} = \nabla_\mu X^\mu = \frac{1}{\sqrt{-g}} \partial_\mu (\sqrt{-g} X^\mu). \quad (1.3.141)$$

This equation will have much use later in section 5.1.2 where the divergence of a vector will be integrated over a finite n -dimensional volume V in \mathcal{M} . In order to do this, the divergence theorem of curved space is used,

$$\int_V \nabla \cdot \mathbf{X} \sqrt{|{}^{(n)}g|} d^n x = \sum_i \int_{\partial V_i} \mathbf{s}^{(i)} \cdot \mathbf{X} \sqrt{|{}^{(n-1)}g^{(i)}|} d^{n-1} x, \quad (1.3.142)$$

where the surface of V is divided into a set of $(n - 1)$ -dimensional surfaces ∂V_i ; for each of these surfaces there is an $(n - 1)$ -dimensional metric ${}^{(n-1)}g^{(i)}$ with determinant ${}^{(n-1)}g^{(i)}$ and unit normal vector $\mathbf{s}^{(i)}$ with ${}^{(n-1)}g^{(i)}(\mathbf{s}^{(i)}, \mathbf{s}^{(i)}) = \pm 1$. When dealing with a pseudo-Riemannian manifold, we need to take care of the direction of $\mathbf{s}^{(i)}$; in the case that $\mathbf{s}^{(i)}$ is timelike it should be in-directed, and if it's spacelike then it should be out-directed. The correct direction of the $\mathbf{s}^{(i)}$ can be readily checked by computing Eq. (1.3.142) in a non-curved manifold.

1.4 Relativity

1.4.1 Special Relativity

In the nineteenth century, it was widely believed that the universe was permeated by an invisible luminous aether. It was thought that light travels at a fixed speed through this aether; the aether could be thought of as a universal rest frame. Consequently moving towards/away from a light source would cause the speed of oncoming light to vary. With that line of thought one could measure the earth's speed through the aether by setting up an interferometer experiment. An interferometer sends a light beam through a splitter, dividing the beam into two perpendicular paths. The two beams then reach a separate mirror and are reflected to a half-mirror that recombines the two beams after they have travelled identical distance. If the time taken for the two beams to complete their identical length journeys differs then an interference pattern will be seen at a detector placed behind the half-mirror due to the phase change between the two beams. In 1887, Michelson and Morley conducted their famous interferometer experiment to measure the earth's velocity through the aether. They expected to see interference when the different beams made different angles with the earth's velocity through the aether. However, no matter which way they oriented the experiment there was no interference pattern. This implied that light moved at exactly the same speed in any direction; this is only possible if earth is in the rest frame of the aether, but this cannot possibly be true as the planet accelerates round a circular path around the Sun that is following a larger circular path (in the Milky Way) and so on. This famous result demonstrated that the speed of light (in vacuum) is the same in any direction in all inertial (non-accelerating) frames - a result that defied Newtonian physics. This was a crucial hint that a new theory of dynamics was needed.

In 1905, Einstein published “On the Electrodynamics of Moving Bodies” [13] which contained a description of Special Relativity (SR). SR is essentially the idea that the laws of physics (excluding gravity) are the same in any inertial rest frame. A consequence of this is that it is impossible to measure the velocity of your own rest frame and no inertial frame is special. One big problem with SR is that it does not properly describe gravity and thus describes an infinite vacuum universe; this is a problem that will be addressed in the next sections. SR alone contains many interesting results such as time dilation, length contraction and the inclusion of time in distance measures. For a modern textbook on SR that deals with the basics as well as more complicated topics such as acceleration, tensor fields and the incompatibility of gravity with SR see [14]. A more direct, but adequate, account of SR can be found at the beginning of the textbook [10].

Minkowski Space

In Newtonian physics the metric of flat space, using Cartesian coordinates, is,

$$g_{ij} = \delta_{ij} = \begin{pmatrix} 1 & 0 & 0 \\ 0 & 1 & 0 \\ 0 & 0 & 1 \end{pmatrix}, \quad (1.4.1)$$

with the line element,

$$ds^2 = \delta_{ij} dx^i dx^j = dx^2 + dy^2 + dz^2. \quad (1.4.2)$$

In SR, time is promoted to an extra dimension and the metric is over space and time (spacetime); this flat 4-dimensional spacetime is called Minkowski space. The spacetime metric has a single negative eigenvalue and hence negative determinant. In Cartesian coordinates, the flat spacetime metric is,

$$g_{\mu\nu} = \eta_{\mu\nu} = \begin{pmatrix} -1 & 0 & 0 & 0 \\ 0 & 1 & 0 & 0 \\ 0 & 0 & 1 & 0 \\ 0 & 0 & 0 & 1 \end{pmatrix}, \quad (1.4.3)$$

and the line element is,

$$ds^2 = \eta_{\mu\nu} dx^\mu dx^\nu = -dt^2 + dx^2 + dy^2 + dz^2, \quad (1.4.4)$$

where the speed of light has been set to unity again. Having a metric on a 4-dimensional spacetime is a non-intuitive concept where time is included into geometry and paths through spacetime can have negative length.

Transforming between two inertial frames moving at constant velocity with respect to each other is done with a *boost* in special relativity. Boosting from frame S with coordinates x^μ to \tilde{S} with coordinates \tilde{x}^μ we can write,

$$d\tilde{x}^\mu = \frac{\partial \tilde{x}^\mu}{\partial x^\nu} dx^\nu = \Lambda^\mu_\nu dx^\nu, \quad (1.4.5)$$

where we will call Λ the boost matrix. Considering a boost along the x direction with a speed v ,

$$d\tilde{t} = \gamma(dt - vdx), \quad (1.4.6)$$

$$d\tilde{x} = \gamma(dx - vdt), \quad (1.4.7)$$

$$d\tilde{y} = dy, \quad (1.4.8)$$

$$d\tilde{z} = dz, \quad (1.4.9)$$

where $\gamma = 1/\sqrt{1-v^2}$ is the Lorentz factor. This transformation may seem odd at first glance but ensures that every inertial frame agrees on the same speed of light in all directions. For boosts in general directions Λ should be rotated with a spatial rotation matrix using the tensor transformation law.

1.4.2 General Relativity

It is a well known result of Newtonian physics that in a rotating reference frame, with angular velocity ω , a test particle will experience three fictitious forces; the centrifugal force that grows with distance from the origin, the Coriolis force that depends on the velocity of the test particle, and the Euler force depending on $\partial_t \omega$. From the point of view of an observer in the rotating frame a free test particle would appear to accelerate which is a violation of Newton's first law if there is no external force. The curved path followed by the particle in the rotating reference frame is of course a constant-speed straight line in the non-rotating inertial frame, and therefore the particle follows a geodesic. It is possible (but very involved) to do a coordinate transformation from the inertial frame to the rotating frame and find the metric $\tilde{\eta}_{\mu\nu}$ in the rotating frame using the tensor transformation law; it would then be possible to compute the geodesics in the rotating frame using Eq. (1.2.78).

The gravitational force can also be described as a fictitious force. In a non-accelerating frame, the path of a particle moving without external force is seen to accelerate towards massive bodies. The presence of matter density causes geodesics to curve. This is a property also possessed by curved spaces; the path followed by a free particle on a curved background is often curved itself. Einstein's idea to incorporate gravity into relativity was to change the flat spacetime of special relativity to a curved spacetime; this theory is general relativity. In general relativity inertial frames are defined as freely falling frames (under gravity) following geodesics in curved space. The gravitational force is a fictitious force arising from an observer not being in an inertial frame. This explains why an observer standing on earth experiences a reaction force, the frame of the observer is not following a geodesic (not an inertial frame) and therefore to counteract the fictitious gravitational force the ground must push back with a reaction force. In the local inertial frame, the observer standing on the earth is accelerated upwards by the earth's surface.

There are countless textbooks relevant to general relativity. Two noteworthy classics are “*General Relativity*” by R. Wald [15] and “*Gravitation*” by Misner, Thorne and Wheeler [16]. A good modern textbook is “*An Introduction to General Relativity, SPACETIME and GEOMETRY*” by S. Carroll [10]; this is freely available online in lecture note form [17].

Worldlines and Causality

Consider a particle moving through spacetime, the motion can be described with coordinates $x^\mu(\tau)$ which is called a worldline. Here τ denotes *proper time*, the time experienced by the particle following

the worldline. The 4-velocity along a worldline is,

$$v^\mu(\tau) = \frac{dx^\mu}{d\tau}(\tau). \quad (1.4.10)$$

In general relativity, the line element ds elapsed along a coordinate interval dx^μ is,

$$ds^2 = g_{\mu\nu} dx^\mu dx^\nu, \quad (1.4.11)$$

and for a particle with 4-velocity \mathbf{v} is,

$$ds^2 = g_{\mu\nu} \frac{dx^\mu}{d\tau} \frac{dx^\nu}{d\tau} d\tau^2 = g_{\mu\nu} v^\mu v^\nu d\tau^2 = \mathbf{v} \cdot \mathbf{v} d\tau^2. \quad (1.4.12)$$

As shown in section 1.2.8, if a worldline $x^\mu(\lambda)$ parameterised by λ is a geodesic then $g_{\mu\nu} \dot{x}^\mu \dot{x}^\nu$ is constant where the dot denotes a derivative with respect to λ . Equating $\lambda = \tau$ gives $\dot{x}^\mu = v^\mu$ which tells us that $\mathbf{v} \cdot \mathbf{v}$, or $|\mathbf{v}|^2$, is constant along a world line. If $|\mathbf{v}|^2 < 0$ then the geodesic is *timelike*; similarly if $|\mathbf{v}|^2 > 0$ then the geodesic is *spacelike*. In the special case that $|\mathbf{v}|^2 = 0$, the curve is called *null*. Locally, physical massive particles must travel along timelike intervals and massless particles must travel along null ones. Information cannot travel faster than light (which follows null geodesics) and hence all spacelike intervals are locally intraversable. Given that $|\mathbf{v}|^2$ is a scalar, it is unchanged by a coordinate transformation, this means that all observers in all frames (and using any coordinate system) will agree on whether an interval is timelike, spacelike or null.

1.4.3 Physics in Curved Space

General relativity postulates that (locally) the laws of physics in a free falling frame are indistinguishable from special relativity. Any equations of motion that we want to hold in general relativity must agree with special relativity in the flat-space limit. As a general rule, if there is a law of physics expressed as a differential equation in Minkowski space that we want to use in curved space, we must replace all partial derivatives of fields with co-variant derivatives of tensor fields. This process is called the minimal coupling approach and is explored in more detail at the end of section 1.4.6.

The Wave Equation

To derive the curved space wave equation we start with the wave equation for a scalar field ϕ in Minkowski space,

$$\frac{1}{c^2} \frac{\partial^2}{\partial t^2} \phi(x^i, t) - \left(\frac{\partial^2}{\partial x^2} + \frac{\partial^2}{\partial y^2} + \frac{\partial^2}{\partial z^2} \right) \phi(x^i, t) = 0, \quad (1.4.13)$$

using Cartesian coordinates and c as the speed of light which we will set to one. While this equation is Lorentz invariant¹² it is not generally covariant, changing coordinates can change the explicit form of the equation of motion. In SR, using the language of tensor calculus, we can write the wave equation as,

$$\eta^{\mu\nu} \partial_\mu \partial_\nu \phi = 0, \quad (1.4.14)$$

where $\eta^{\mu\nu}$ is the inverse metric of flat space. To adapt this to curved space we follow the minimal coupling procedure and replace $\eta \rightarrow g$ and $\partial_\mu \rightarrow \nabla_\mu$ giving,

$$g^{\mu\nu} \nabla_\mu \nabla_\nu \phi = 0. \quad (1.4.15)$$

This equation is fully covariant as it is a contraction of a tensor with some covariant derivatives; it is a tensor differential equation. Writing the laws of physics as tensor equations is useful as they can

¹²Lorentz invariance is to be invariant under a boost, also called a Lorentz transformation.

be written without reference to an explicit coordinate system. If a coordinate system is then picked, assuming knowledge of $g_{\mu\nu}$, then the wave equation becomes

$$g^{\mu\nu}\nabla_\mu\nabla_\nu\phi = g^{\mu\nu}\nabla_\mu\partial_\nu\phi = 0, \quad (1.4.16)$$

$$= g^{\mu\nu}\partial_\mu\partial_\nu\phi - g^{\mu\nu}\Gamma^\rho_{\mu\nu}\partial_\rho\phi, \quad (1.4.17)$$

in terms of partial derivatives and covariant derivatives.

Equation (1.4.15) is not the only tensor equation that returns Eq. (1.4.13) in the limit of flat space (and Cartesian coordinates). What is to stop us arbitrarily adding terms that vanish in the flat-space limit? For a simple example one is free to choose the wave equation to be,

$$g^{\mu\nu}\nabla_\mu\nabla_\nu\phi + f(\phi)R^n = 0, \quad (1.4.18)$$

for constant n , function f and the Ricci scalar R from section 1.3.4. This equation certainly returns the regular wave equation in the low curvature limit as $R \rightarrow 0$. Following the ideas of minimal coupling, the general rule is to keep things simple and avoid un-necessary terms - especially if these terms contain higher order derivatives of the metric ¹³ which are generally thought to matter only when curvature becomes very large. This procedure can also become more complicated when dealing with tensors of higher ranks. Navigating this minefield of which terms to include in the laws of physics is tricky and leads to the topic of modified gravity as discussed at the end of section 1.4.6.

Electromagnetism

Electromagnetism can also be written in terms of tensor differential equations suitable for use in curved space. Traditionally, Maxwell's equations of electromagnetism (in vacuum) are written as,

$$\boldsymbol{\nabla} \cdot \mathbf{E} = \frac{\rho}{\epsilon_0}, \quad (1.4.19)$$

$$\boldsymbol{\nabla} \cdot \mathbf{B} = 0, \quad (1.4.20)$$

$$\boldsymbol{\nabla} \times \mathbf{E} + \frac{d\mathbf{B}}{dt} = 0, \quad (1.4.21)$$

$$\boldsymbol{\nabla} \times \mathbf{B} - \frac{d\mathbf{E}}{dt} = \mu_0 \mathbf{J} \quad (1.4.22)$$

for charge density ρ , electric field \mathbf{E} , magnetic field \mathbf{B} , current density \mathbf{J} , permittivity of free space ϵ_0 and permeability of free space μ_0 . Note these differential equations are written using vector calculus in flat space, not differential geometry and tensor calculus; the bold faced fields are therefore 3-vectors. In spacetime, the current density and charge are promoted to a single 4-vector $j^\mu = \{\rho, j^i\}$ and the 6 degrees of freedom of the electromagnetic field are encoded in the components $F_{\mu\nu}$ of an antisymmetric tensor \mathbf{F} . The four electromagnetic potentials ϕ and A_i , defined by $E_i = -\partial_i\phi - \partial_t A_i$ and $\mathbf{B} = \boldsymbol{\nabla} \times \mathbf{A}$, are also combined into one 4-vector $A_\mu = \{-\phi, A_i\}$. In Cartesian coordinates, the Electromagnetic field tensor \mathbf{F} is,

$$F_{\mu\nu} = \nabla_\mu A_\nu - \nabla_\nu A_\mu = \partial_\mu A_\nu - \partial_\nu A_\mu, \quad (1.4.23)$$

where the swapping between $\partial_\mu \leftrightarrow \nabla_\mu$ is possible due to the cancellation of Christoffel symbols. To elucidate, in Minkowski space with Cartesian coordinates the field tensor is,

$$F_{\mu\nu} = \partial_\mu A_\nu - \partial_\nu A_\mu = \begin{pmatrix} 0 & E_x & E_y & E_z \\ -E_x & 0 & B_z & -B_y \\ -E_y & -B_z & 0 & B_x \\ -E_z & B_y & -B_x & 0 \end{pmatrix}. \quad (1.4.24)$$

¹³ R contains second derivatives of the metric but $\Gamma^\alpha_{\mu\nu}$ only contains first derivatives.

The vector potential A_μ has a gauge transformation like $A_\mu \rightarrow A_\mu + \partial_\mu f$, for some scalar field f , that leaves the physically measurable field $F_{\mu\nu}$ unchanged,

$$F_{\mu\nu} \rightarrow \partial_\mu(A_\nu + \partial_\nu) - \partial_\nu(A_\mu + \partial_\mu), \quad (1.4.25)$$

$$= \partial_\mu A_\nu - \partial_\nu A_\mu + \underbrace{\partial_\mu \partial_\nu f - \partial_\nu \partial_\mu f}_{=0}, \quad (1.4.26)$$

$$= F_{\mu\nu}. \quad (1.4.27)$$

In curved space, the Maxwell Eqs. (1.4.19) and (1.4.22) in tensor form are,

$$\nabla_\mu F^{\mu\nu} = \mu_0 j^\nu, \quad (1.4.28)$$

as $\mu_0 \epsilon_0 = c^{-2} = 1$ in natural units. The other two Maxwell Eqs. (1.4.20) and (1.4.21) are identically true from computing $\partial_{[\mu} F_{\alpha\beta]}$,

$$\partial_{[\mu} F_{\alpha\beta]} = \partial_\mu \partial_\alpha A_\beta - \partial_\mu \partial_\beta A_\alpha + \partial_\alpha \partial_\beta A_\mu - \partial_\alpha \partial_\mu A_\beta + \partial_\beta \partial_\mu A_\alpha - \partial_\beta \partial_\alpha A_\mu, \quad (1.4.29)$$

$$\partial_{[\mu} F_{\alpha\beta]} = 0, \quad (1.4.30)$$

which is equivalent to $\nabla_{[\mu} F_{\alpha\beta]}$ due to the cancellation of Christoffel symbols.

The Stress-Energy-Momentum Tensor

At the heart of field theory in physics is the stress-energy-momentum tensor \mathbf{T} , also called the energy-momentum tensor or stress tensor for short. The component T^{00} contains the energy density as measured by an observer co-moving with the coordinate system. Similarly, components $T^{0i} = T^{i0}$ contain energy flux or momentum density and components $T^{ij} = T^{ji}$ contain momentum fluxes. The diagonal part of T^{ij} can also be thought of as containing pressure and the off-diagonal terms containing shear stress. In flat space, the conservation of energy and momentum can be written as,

$$\partial_\mu T^{\mu\nu} = 0, \quad (1.4.31)$$

in the absence of external forces. Equation (1.4.31) is also called the continuity equation and can be split into two sets of familiar equations,

$$\partial_0 T^{00} = -\partial_i T^{i0}, \quad (1.4.32)$$

$$\partial_0 T^{0j} = -\partial_i T^{ij}, \quad (1.4.33)$$

where the first equation states “*The rate of change of energy density is equal and opposite to the divergence of energy flux density*” and the second equation states “*The rate of change of momentum density is equal and opposite to the divergence of momentum flux density*”.

The stress tensor plays an important role in curved space and the continuity equation becomes,

$$\nabla_\mu T^{\mu\nu} = \partial_\mu T^{\mu\nu} + \Gamma^\mu_{\mu\rho} T^{\rho\nu} + \Gamma^\nu_{\mu\rho} T^{\mu\rho} = 0, \quad (1.4.34)$$

where the partial derivative has been replaced with a covariant derivative in accordance with minimal coupling. This can be rewritten using Eq. (1.3.141) as,

$$\partial_\mu (\sqrt{-g} T^{\mu\nu}) = -\sqrt{-g} \Gamma^\nu_{\mu\rho} T^{\mu\rho}, \quad (1.4.35)$$

$$\partial_\mu (\mathcal{T}^{\mu\nu}) = -\Gamma^\nu_{\mu\rho} \mathcal{T}^{\mu\rho}, \quad (1.4.36)$$

where the second equation writes the stress tensor as a tensor density $\mathcal{T} = \sqrt{-g} \mathbf{T}$ making the equation resemble the flat space continuity equation more closely. This modification of traditional continuity of energy and momentum to curved spaces will be revisited in chapter 5.

1.4.4 The Einstein Equation

We have already seen how the equations of motion for matter can be promoted to curved space; building on the vague notion of matter causing spacetime curvature it would be helpful to have a mathematical law saying how much curvature is caused by a given matter distribution. The first guess that Einstein arrived at was to write $R_{\mu\nu} = kT_{\mu\nu}$ for some constant k . The problem is that given $\nabla_\mu T^{\mu\nu} = 0$ is the generic equation of continuity for matter, it would imply $\nabla_\mu R^{\mu\nu}$ vanishes which is not generally true. As shown in Eq. (1.3.115), the Einstein tensor $G_{\mu\nu}$ does satisfy $\nabla_\mu G^{\mu\nu} = 0$; the next simplest guess at a physical law for spacetime curvature would be $G_{\mu\nu} = kT_{\mu\nu}$. Remarkably this turns out to be correct and has successfully described many gravitational phenomena. The Einstein equation,

$$R_{\mu\nu} - \frac{1}{2}g_{\mu\nu}R = \frac{8\pi G}{c^4}T_{\mu\nu}, \quad (1.4.37)$$

where $G_{\mu\nu} = R_{\mu\nu} - g_{\mu\nu}R/2$, is at the core of general relativity. This equation relates spacetime curvature, encoded in the Einstein tensor $G_{\mu\nu}$, to the matter distribution described by the stress tensor $T_{\mu\nu}$. This leads nicely to Wheeler's insightful one line summary of general relativity:

"Spacetime tells matter how to move; matter tells spacetime how to curve."

This deceptively simple equation describes an enormous number of vastly diverse spacetime geometries including regular flat Minkowski space, black holes, stars, planets, gravitational waves and even the entire universe; to properly describe the entire universe a small modification (with large consequences on global behaviour) has to be made to this equation as discussed at the end of this section.

General Relativity in Vacuum

In the case of a vacuum spacetime with $T_{\mu\nu} = 0$ the Einstein equation simplifies greatly to

$$G_{\mu\nu} = 0. \quad (1.4.38)$$

Taking the trace of the above equation and the definition of $G_{\mu\nu} = R_{\mu\nu} - g_{\mu\nu}R/2$, we see that,

$$g^{\mu\nu}G_{\mu\nu} = 0 = g^{\mu\nu}\left(R_{\mu\nu} - \frac{1}{2}Rg_{\mu\nu}\right) = R\left(1 - \frac{D}{2}\right), \quad (1.4.39)$$

where D is the number of spacetime dimensions. Clearly for $D \neq 2$ a vanishing Einstein tensor implies a vanishing Ricci scalar R ; if the Ricci scalar vanishes then the Einstein equation in vacuum simplifies to

$$R_{\mu\nu} = 0. \quad (1.4.40)$$

Note that even though $R_{\mu\nu} = 0$, this does not mean there is no spacetime curvature; the Riemann tensor $R^\mu_{\nu\rho\sigma}$ can still be non-zero.

The Cosmological Constant

A discussion of general relativity is incomplete without discussing the cosmological constant Λ . At a geometric level, the cosmological constant encodes the homogeneous spacetime curvature in the absence of matter, and indeed setting $\Lambda \rightarrow 0$ (in vacuum) returns asymptotically flat vacuum general relativity. The cosmological constant is added into Einstein's equation (1.4.37), with $\Lambda g_{\mu\nu}$,

$$R_{\mu\nu} - \frac{1}{2}Rg_{\mu\nu} + \Lambda g_{\mu\nu} = \frac{8\pi G}{c^4}T_{\mu\nu}. \quad (1.4.41)$$

Each term still has a zero-divergence as $\nabla_\mu g_{\alpha\beta} = 0$ due to the Levi-Civita connection defined in section 1.3.3. The traced Einstein equation becomes

$$\left(1 - \frac{D}{2}\right)R + D\Lambda = \frac{8\pi G}{c^4}T \quad (1.4.42)$$

where $T = g^{\mu\nu}T_{\mu\nu}$ is the trace of the stress tensor and D is the number of spacetime dimensions. The traced Einstein equation makes it obvious that Λ has the same effect on curvature as a uniform matter density with constant T . Using geometric units $D\Lambda = 8\pi T$ is a special case which has solution $R = 0$ similarly to vacuum GR. From now on $\Lambda = 0$ will be assumed.

1.4.5 Black Holes

As it turns out, vacuum General Relativity can describe more than just Minkowski space. Arguably the most important family of solutions to Einstein's equations in vacuum are black holes. The first black-hole solution was found by Karl Schwarzschild, whose surname fittingly means “*black shield*” in German. This solution, known as the Schwarzschild solution, was discovered in 1916 with the intention of computing the spacetime curvature in the vacuum about a spherically symmetric mass such as stars and planets. The solution for $g_{\mu\nu}$ was assumed to take the following ansatz,

$$ds^2 = g_{\mu\nu}dx^\mu dx^\nu = -A(r)dt^2 + B(r)dr^2 + r^2(d\theta + \sin^2(\theta)d\phi^2), \quad (1.4.43)$$

which is manifestly spherically symmetric and static; in the case $A(r) = B(r) = 1$ the solution is exactly Minkowski space in spherical polar coordinates. By solving the Einstein equation in vacuum ($R_{\mu\nu} = 0$) the Schwarzschild solution can be found,

$$g_{\mu\nu}dx^\mu dx^\nu = -\left(1 - \frac{2Gm}{rc^2}\right)dt^2 + \left(1 - \frac{2Gm}{rc^2}\right)^{-1}dr^2 + r^2(d\theta + \sin^2(\theta)d\phi^2). \quad (1.4.44)$$

The constants G and c are included for completeness, but are equal to one in geometric units or Planck units. The Schwarzschild solution describes the spacetime around a non-spinning sphere of mass m and as $r \rightarrow \infty$ or $m \rightarrow 0$ we approach the vacuum Minkowski spacetime as desired. What Schwarzschild did not realise before his untimely death was that his solution could in fact be trusted down to vanishing radii and describes the eternal (or static), non-spinning black hole of mass m called the Schwarzschild black hole.

Many other black-hole solutions have been found to date. These solutions include the spinning *Kerr* black hole, non-spinning electromagnetically charged *Reissner-Nordström* black hole and spinning electromagnetically charged *Kerr-Newman* black hole. Non asymptotically flat black holes in cosmological backgrounds have also been found [18]. In modified gravity theories, briefly discussed in section 1.4.6, exotic black-hole solutions (often coupled to other fields such as scalar fields) exist.

Polar-Areal Coordinates

The type of coordinates used in the Schwarzschild solution are called polar-areal coordinates; these are coordinates that assign an area $4\pi r_0^2$ to the 2-surface defined by $r = r_0$ and $t = t_0$. Using Eq. (1.2.71) the surface area of a coordinate sphere with $t = t_0$, $r = r_0$ can be calculated from

$$A = \int_0^\pi \left[\int_0^{2\pi} \sqrt{\sigma} \Big|_{t=t_0, r=r_0} d\phi \right] d\theta, \quad (1.4.45)$$

where σ is the metric determinant on the surface. Evaluating this explicitly for the Schwarzschild metric with $\sqrt{\sigma} = \sqrt{g_{\theta\theta}g_{\phi\phi}} = r^2 \sin(\theta)$ gives

$$A = \int_0^\pi \left[\int_0^{2\pi} \sqrt{g_{\phi\phi}g_{\theta\theta}} \Big|_{t=t_0, r=r_0} d\phi \right] d\theta = r_0^2 \int_0^\pi \left[\int_0^{2\pi} d\phi \right] \sin^2(\theta) d\theta = 4\pi r_0^2, \quad (1.4.46)$$

as expected.

Coordinate Singularities and Physical Singularities

There is obviously some kind problem at radius $r_s = 2m$ (or $r_s = 2mG/c^2$ in S.I. units), known as the Schwarzschild radius, as g_{rr} diverges here. For physical planets and stars observed the radius of the object is much larger than the Schwarzschild radius so the solution should not be trusted inside the object as it has been derived in vacuum. But in order to describe black holes we must consider radii down to $r = 0$. The problem at the Schwarzschild radius is due to the choice of coordinates and is not physically problematic. An easy way to show this is to compute a curvature scalar¹⁴ and show that it is finite and smooth at $r = r_s$. The first choice of curvature scalar might be the Ricci scalar, but this is zero in vacuum so is not useful for this purpose. Vacuum general relativity asserts that $R_{\mu\nu} = 0$, while that guarantees that $R = 0$ it does not guarantee that $R_{\mu\nu\rho\sigma} = 0$. Another curvature scalar is the Kretschmann scalar k , defined in Eq. (1.3.117), which does not generally vanish in vacuum. Calculating the Kretschmann scalar for the Schwarzschild metric gives,

$$k_{sc} = \frac{48m^2}{r^6}, \quad (1.4.47)$$

in polar-areal coordinates. As can be seen, k_{sc} is continuous and infinitely differentiable at $r = 2m$. However, as $r \rightarrow 0$, $k_{sc} \rightarrow \infty$ and there is a real coordinate independent singularity called a physical singularity.

To remove the coordinate singularity at $r = 2m$, new coordinates can be introduced. One example is to use ingoing-Eddington-Finkelstein coordinates $\{v, \tilde{r}, \theta, \phi\}$ defined by

$$\frac{d\tilde{r}}{dr} = \left(1 - \frac{2m}{r}\right), \quad (1.4.48)$$

$$v = t + \tilde{r}, \quad (1.4.49)$$

which transforms the line element to,

$$g_{\mu\nu}dx^\mu dx^\nu = -\left(1 - \frac{2m}{r}\right)dv^2 + 2dvdr + r^2(d\theta + \sin^2(\theta)d\phi^2), \quad (1.4.50)$$

and the metric no longer diverges at $r = 2m$. Bearing in mind that now the metric is not diagonal, the metric determinant can be calculated, giving $\sqrt{-g} = r^2 \sin(\theta)$. Given that the metric is finite for $r > 0$ and the metric determinant is non-zero for $r > 0$, the metric inverse is also guaranteed to be finite for $r > 0$. It has been demonstrated that the coordinate singularity at $r = 2m$ in Schwarzschild polar-areal vanishes when using ingoing-Eddington-Finkelstein coordinates.

Throughout this section we have ignored the fact that the inverse metric also diverges as $\theta \rightarrow 0$ or $\theta \rightarrow \pi$, this is a coordinate singularity that is present in flat space (which is equivalent to the Schwarzschild spacetime with $m = 0$). This coordinate singularity arises in flat space due to the azimuthal angle ϕ being undefined at $\theta = 0$ and $\theta = \pi$. There are no physical singularities in flat space and these coordinate singularities vanish when using Cartesian coordinates.

Isotropic Coordinates

A coordinate system that will be useful later on is the isotropic coordinate system. Isotropic coordinates lead to the line element,

$$g_{\mu\nu}dx^\mu dx^\nu = -\Omega^2(x^\mu)dt^2 + \Psi^2(x^\mu)ds_{\text{flat}}^2, \quad (1.4.51)$$

¹⁴Scalar curvature invariants are useful since if they diverge in one coordinate system then they must diverge in all coordinate systems as they do not transform under coordinate transformations. It should be noted that $\sqrt{-g}$ is a scalar density and not a true scalar so is not a scalar curvature invariant.

where ds_{flat}^2 is the flat space Euclidean line element. For example, in spherical polar and Cartesian spatial coordinates, the isotropic line element in spherical symmetry becomes,

$$g_{\mu\nu}dx^\mu dx^\nu = -\Omega(\rho)^2 dt^2 + \Psi^2(\rho) \left(d\rho^2 + \rho^2 (d\theta^2 + \sin^2(\theta)d\phi^2) \right), \quad (1.4.52)$$

$$= -\Omega(\rho)^2 dt^2 + \Psi^2(\rho) \left(dx^2 + dy^2 + dz^2 \right), \quad (1.4.53)$$

where $\rho^2 = x^2 + y^2 + z^2$.

The Schwarzschild black-hole solution can also be expressed in isotropic coordinates, the line element is

$$g_{\mu\nu}dx^\mu x^\nu = - \left(\frac{1 - \frac{m}{2\rho}}{1 + \frac{m}{2\rho}} \right)^2 dt^2 + \left(1 + \frac{m}{2\rho} \right)^4 ds_{\text{flat}}^2. \quad (1.4.54)$$

As $\rho \rightarrow \infty$ the line element reduces to that of the Minkowski spacetime. At the radius $\rho = m/2$, g_{tt} vanishes (similarly to polar areal coordinates) and this is the Schwarzschild radius in isotropic coordinates. At first glance one might think that there is also the same physical singularity at $\rho = 0$. However, if a new radial coordinate ξ is used, where $\rho = \frac{m^2}{4\xi}$, the line element becomes,

$$g_{\mu\nu}dx^\mu x^\nu = - \left(\frac{1 - \frac{m}{2\xi}}{1 + \frac{m}{2\xi}} \right)^2 dt^2 + \left(1 + \frac{m}{2\xi} \right)^4 \left(d\xi^2 + \xi^2 (d\theta^2 + \sin^2(\theta)d\phi^2) \right). \quad (1.4.55)$$

This is an intriguing result, inverting the radial coordinate about $\rho = 2/m$ has returned an identical metric. Given that at $\rho = \infty$ we have flat space this implies that at $\xi = \infty$ (or $\rho = 0$) there is another separate flat space, not the physical singularity that might have been expected. The black-hole exterior $m/2 < \rho < \infty$ must be identical to the volume $m/2 < \xi < \infty$ (also written as $m/2 > \rho > 0$), hence there are two asymptotically flat universes joined by the surface $\rho = m/2$; this surface is the Einstein-Rosen bridge. The Einstein-Rosen bridge is not traversable, to cross this bridge would require a spacelike worldline or faster than light travel which is forbidden. The geometry of the isotropic black hole is shown in Fig. (1.2).

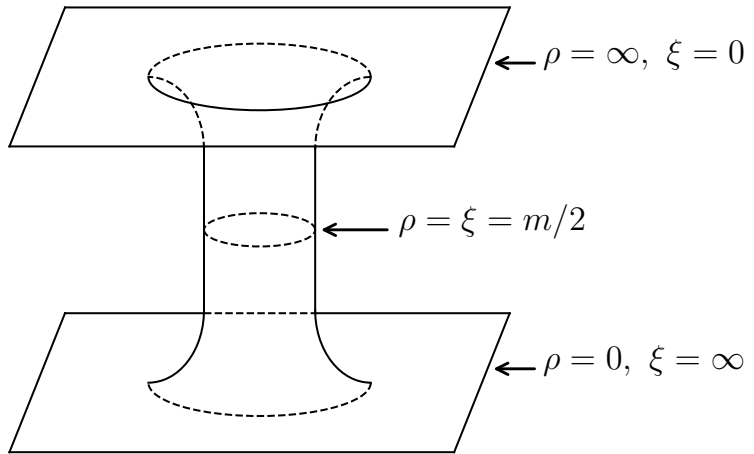


Figure 1.2: This diagram shows the geometry of the spacetime covered by isotropic coordinates. There are two asymptotically flat ends joined by the Einstein-Rosen bridge at $\rho = \xi = m/2$.

The reason that the physical singularity at $\rho = 0$ does not appear in isotropic coordinates is deceptively simple; in isotropic coordinates $\rho = 0$ does not correspond to the same point on the manifold as $r = 0$

does in the polar areal gauge for any value of t , θ or ϕ . Infact, the physical singularity of the black hole is outside of the patch on the manifold covered by isotropic coordinates. This can be illustrated by computing the Kretschmann scalar in isotropic coordinates. Using the isotropic radial coordinate ξ and polar areal radius r we can write,

$$\xi \left(1 + \frac{m}{2\xi}\right)^2 = r, \quad (1.4.56)$$

by comparing the $d\theta^2$ part of the line element. Substituting this into Eq. (1.4.47), the Kretschmann scalar in isotropic coordinates is,

$$k_{\text{iso}} = \frac{48m^2\xi^6}{(\xi + \frac{m}{2})^{12}}. \quad (1.4.57)$$

This is finite for $0 \leq \xi \leq \infty$ and hence there is no physical singularity covered by isotropic coordinates; infact we can make the stronger statement that isotropic coordinates do not penetrate the event horizon. The value of the Kretschmann scalar on the event horizon is,

$$k_{\text{EH}} = \frac{3}{4m^4}. \quad (1.4.58)$$

In isotropic coordinates, the maximum value that k_{iso} can take is found by $\partial k_{\text{iso}}/\partial \xi = 0$ which has a turning point at $\xi = m/2$. At $\xi = m/2$ the value of k_{iso} is $3/(4m^4)$ and given that $k > k_{\text{EH}}$ in the interior of a black hole and $k_{\text{iso}} \leq k_{\text{EH}} \forall \xi$ then isotropic coordinates do not penetrate the event horizon.

1.4.6 The Lagrangian Formulation of General Relativity

A common procedure in theoretical physics is to encapsulate the solution space in an action functional S ,

$$S = \int \mathcal{L} \sqrt{-g} dx^4. \quad (1.4.59)$$

Using the calculus of variation on this action returns differential equations governing the system. As found by Hilbert [19] the following Lagrangian density $\mathcal{L} = R$, equal to the Ricci scalar, returns the vacuum Einstein equation under varying with respect to $g^{\mu\nu}$.

$$\delta S = \int [\sqrt{-g}(\delta R) + R(\delta \sqrt{-g})] dx^4, \quad (1.4.60)$$

$$= \int \left[\sqrt{-g} \delta(g^{\mu\nu} R_{\mu\nu}) - \frac{1}{2} \sqrt{-g} g_{\mu\nu} R (\delta g^{\mu\nu}) \right] dx^4, \quad (1.4.61)$$

$$= \int \left[\sqrt{-g} g^{\mu\nu} (\delta R_{\mu\nu}) + \sqrt{-g} \left(R_{\mu\nu} - \frac{1}{2} R g_{\mu\nu} \right) \delta g^{\mu\nu} \right] dx^4, \quad (1.4.62)$$

where we have used Eq. (1.3.138) to vary $\sqrt{-g}$. Remembering that the difference of two Christoffel symbols such as,

$$\delta \Gamma^\lambda_{\mu\nu} = \Gamma^\lambda_{\mu\nu}|_{g^{\mu\nu} + \delta g^{\mu\nu}} - \Gamma^\lambda_{\mu\nu}|_{g^{\mu\nu}} \quad (1.4.63)$$

is a tensor, and using normal coordinates discussed in section 1.3.3 the left hand term of Eq. (1.4.62) becomes

$$g^{\mu\nu} \delta R_{\mu\nu} = g^{\mu\nu} \left(\partial_\lambda \delta \Gamma^\lambda_{\mu\nu} - \partial_\nu \delta \Gamma^\lambda_{\mu\lambda} \right), \quad (1.4.64)$$

$$= g^{\mu\nu} \left(\nabla_\lambda \delta \Gamma^\lambda_{\mu\nu} - \nabla_\nu \delta \Gamma^\lambda_{\mu\lambda} \right), \quad (1.4.65)$$

$$= \nabla_\lambda \left(g^{\mu\nu} \delta \Gamma^\lambda_{\mu\nu} - g^{\mu\lambda} \delta \Gamma^\nu_{\mu\nu} \right). \quad (1.4.66)$$

$$= \nabla_\lambda X^\lambda. \quad (1.4.67)$$

The first expression follows from contracting Eq. (1.3.97) for the Riemann tensor with normal coordinates and the second line swaps $\nabla_\mu \rightarrow \partial_\mu$ which are equivalent using normal coordinates. Putting everything together, δS becomes

$$\delta S = \int \left[\nabla_\mu X^\mu + \left(R_{\mu\nu} - \frac{1}{2} R g_{\mu\nu} \right) \right] \sqrt{-g} dx^4, \quad (1.4.68)$$

$$= \int_B X^\mu \hat{s}_\mu \sqrt{|{}^{(3)}g|} dx^3 + \int \left[R_{\mu\nu} - \frac{1}{2} R g_{\mu\nu} \right] \sqrt{-g} dx^4, \quad (1.4.69)$$

where the integral over B represents the surface integral over the boundary of our spacetime with metric ${}^{(3)}g_{ij}$ and unit normal \hat{s} ; on B $\delta g^{\mu\nu} \rightarrow 0$ and therefore $X^\mu \rightarrow 0$. Setting $dS = 0$ implies

$$R_{\mu\nu} - \frac{1}{2} R g_{\mu\nu} = 0, \quad (1.4.70)$$

which is the vacuum Einstein equation.

Non-Vacuum Spacetimes

Matter is often added into a spacetime at the level of the Lagrangian with a term $\frac{16\pi G}{c^4} \mathcal{L}_m$. The cosmological constant can be added in exactly the same way with \mathcal{L}_Λ . The total Lagrangian becomes,

$$S = \int \left(R + \frac{16\pi G}{c^4} \mathcal{L}_m + \mathcal{L}_\Lambda \right) \sqrt{-g} dx^4. \quad (1.4.71)$$

As we have already seen earlier in this section, the variation of R with respect to the inverse metric components $g^{\mu\nu}$ returns the vacuum Einstein equation; adding the two new terms from \mathcal{L}_m and \mathcal{L}_Λ , setting $\delta S = 0$ gives the non-vacuum equation

$$R_{\mu\nu} - \frac{1}{2} R g_{\mu\nu} + \frac{16\pi G}{c^4} \frac{1}{\sqrt{-g}} \frac{\delta(\mathcal{L}_m \sqrt{-g})}{\delta g^{\mu\nu}} + \frac{1}{\sqrt{-g}} \frac{\delta(\mathcal{L}_\Lambda \sqrt{-g})}{\delta g^{\mu\nu}} = 0. \quad (1.4.72)$$

Comparing the \mathcal{L}_Λ term to the Einstein equation with cosmological constant in Eq. (1.4.41) we must have

$$g_{\mu\nu} \Lambda = \frac{1}{\sqrt{-g}} \frac{\delta(\mathcal{L}_\Lambda \sqrt{-g})}{\delta g^{\mu\nu}}, \quad (1.4.73)$$

$$= \mathcal{L}_\Lambda \frac{1}{\sqrt{-g}} \frac{\delta(\sqrt{-g})}{\delta g^{\mu\nu}} + \frac{\delta(\mathcal{L}_\Lambda)}{\delta g^{\mu\nu}}, \quad (1.4.74)$$

$$= -\frac{1}{2} g_{\mu\nu} \mathcal{L}_\Lambda + \frac{\delta(\mathcal{L}_\Lambda)}{\delta g^{\mu\nu}}, \quad (1.4.75)$$

$$(1.4.76)$$

which is solved by $\mathcal{L}_\Lambda = -2\Lambda$. Comparing the matter term instead returns another definition of the stress tensor,

$$T_{\mu\nu} := -\frac{2}{\sqrt{-g}} \frac{\delta(\mathcal{L}_m \sqrt{-g})}{\delta g^{\mu\nu}}, \quad (1.4.77)$$

$$= -2 \frac{\delta \mathcal{L}_m}{\delta g^{\mu\nu}} + g_{\mu\nu} \mathcal{L}_m. \quad (1.4.78)$$

Collecting these results, the full Lagrangian is,

$$\mathcal{L} = R + \frac{16\pi G}{c^4} \mathcal{L}_m - 2\Lambda, \quad (1.4.79)$$

or in geometric units (with $c = G = 1$),

$$\mathcal{L} = R + 16\pi\mathcal{L}_m - 2\Lambda. \quad (1.4.80)$$

The form of \mathcal{L}_m is problem specific, depending on the type of matter. The equation of motion of the matter, described by a set of fields ϕ_i , and their partial derivatives with respect to x^μ is,

$$\sqrt{-g} \frac{\delta\mathcal{L}}{\delta\phi_i} - \partial_\mu \left(\sqrt{-g} \frac{\delta\mathcal{L}}{\delta\partial_\mu\phi_i} \right) = 0. \quad (1.4.81)$$

If the ϕ_i are scalar fields then the equation of motion simplifies, using Eq. (1.3.141), to

$$\frac{\delta\mathcal{L}}{\delta\phi_i} - \nabla_\mu \left(\frac{\delta\mathcal{L}}{\delta\nabla_\mu\phi_i} \right) = 0. \quad (1.4.82)$$

Modified Theories of Gravity

At the level of the Lagrangian, minimal coupling means to write down the simplest Lagrangian possible. This avoids higher powers of the curvature tensors¹⁵ as well as coupling between matter fields and curvature where possible. As an example, the action for the minimally coupled scalar field ψ in curved space is,

$$S_\psi = \int (aR - bg^{\mu\nu}\partial_\mu\psi\partial_\nu\psi) \sqrt{-g} d^4x, \quad (1.4.83)$$

for constants a and b . Extra coupling terms between matter and curvature could be added, for instance the action,

$$S_f = \int (aRf(\psi) - bg^{\mu\nu}\partial_\mu\psi\partial_\nu\psi) \sqrt{-g} d^4x, \quad (1.4.84)$$

for some function f ; note that if f is constant then this action reduces to Eq. (1.4.83) for the minimally coupled scalar field. Varying S_f with respect to $g^{\mu\nu}$ gives a modification of the Einstein equation,

$$f(\psi)R_{\mu\nu} - \frac{1}{2}Rf(\psi)g_{\mu\nu} + R\frac{\delta f}{\delta g^{\mu\nu}}(\psi) = \frac{b}{a} \left(\nabla_\mu\psi\nabla_\nu\psi - \frac{1}{2}g_{\mu\nu}g^{\rho\sigma}\nabla_\rho\psi\nabla_\sigma\psi \right), \quad (1.4.85)$$

where a new type of term $R\frac{\delta f}{\delta g^{\mu\nu}}(\psi)$ coupling gravity and matter has arisen; note this becomes the regular Einstein equation for a spacetime with a real massless scalar field ψ if f is constant. Varying S_f with respect to ψ instead gives the modified wave equation,

$$g^{\mu\nu}\nabla_\mu\nabla_\nu\psi + \frac{a}{b}R\frac{\partial f}{\partial\psi} = 0, \quad (1.4.86)$$

which is equivalent to Eq. (1.4.18); note that this returns the regular curved space wave equation if $\partial f/\partial\psi = 0$ and the regular wave equation in the flat-space limit for general f since $R^\mu_{\nu\rho\sigma} = 0$. Other popular methods of modifying gravity include second order curvature terms like R^2 , $R_{\mu\nu}R^{\mu\nu}$, $R_{\mu\nu\rho\sigma}R^{\mu\nu\rho\sigma}$, even higher powers of curvature or different couplings between matter and curvature in the Lagrangian.

The Lagrangian formulation of general relativity is especially useful for the more theoretical aspects of general relativity such as exotic matter and modified gravity. General relativity is not thought of as the correct or final theory of gravity. It is a classical field theory and does not describe particles or quantum mechanics. To date no completely successful quantisation of general relativity has been developed. Another problem with general relativity is that at the centre of black holes there are singularities which are usually viewed as unphysical. A similar singularity exists for the Coulomb force of a point particle

¹⁵The Riemann tensor, Ricci tensor, Ricci scalar and combinations thereof.

and is resolved by quantum field theory (QFT); it is thought a similar thing may happen in a QFT for gravity but it is currently unknown.

Theories such as string theory and loop quantum gravity have attempted to describe a quantum theory of gravity but it is notoriously difficult to derive observable effects from them. Many modified gravity theories aim to describe the first leading-order deviation from general relativity towards quantum gravity. It is thought that deviations from general relativity might be seen in extremely high curvature regimes but there is no conclusive experimental evidence to date.

Chapter 2

Numerical Relativity and Boson Stars

2.1 Numerical Relativity

2.1.1 Spacetime Foliation

Einstein's equation is a classical field equation which, along with an equation of motion for any matter, governs the dynamics of spacetime curvature,

$$R_{\mu\nu} - \frac{1}{2}Rg_{\mu\nu} = \frac{8\pi G}{c^4}T_{\mu\nu}. \quad (2.1.1)$$

The above version is fully covariant, agnostic of the definition of time, and many solutions are known analytically, for instance black-hole geometries. When the system of interest becomes more complicated, such as the case of orbiting objects which will be discussed later, finding an analytic expression becomes impossible. For low energy dynamics, Newtonian theory, post-Newtonian theory and perturbation theory can make more progress; however this work focuses on the highly nonlinear regime where numerical relativity is presently the only hope to solve Einstein's equations. To do this it is common to split the 4-dimensional spacetime into 3+1 dimensions, evolving a 3-dimensional manifold (maybe with matter) on a computer along the final 4th dimension. To do this we need to define a suitable hypersurface $\Sigma \in \mathcal{M}$ where \mathcal{M} is the 4-dimensional manifold representing the entire spacetime. This is usually done by demanding the hypersurface Σ_t be the set of points $p \in \mathcal{M}$ where some scalar function $f : \mathcal{M} \mapsto \mathbb{R}$ satisfies $f(p) = t$. This hypersurface should be a Cauchy surface, intersecting all causal curves only once, or a partial Cauchy surface which intersects all causal curves at most once. Generally we will choose a partial Cauchy surface covering a finite region of Σ_t due to the finite memory of computers. A foliation \mathcal{F} is then the union of a set of Σ_t for some range of the parameter t ,

$$\mathcal{F} = \cup_t(\Sigma_t) \subseteq \mathcal{M}. \quad (2.1.2)$$

This means we should be careful to pick a parameter t such that the foliation is not self intersecting for the parameter range that covers the region of \mathcal{M} that we are interested in simulating. The time coordinate in a suitable coordinate system works in many cases; it also gives the physical interpretation of Σ_t being an instant of time. Now we define the unit normal vector \mathbf{n} to Σ_t ,

$$n^\alpha = -\frac{\nabla^\alpha t}{\sqrt{|g_{\mu\nu}\nabla^\mu t \nabla^\nu t|}} \quad \& \quad n_\alpha = -\frac{dt_\alpha}{\sqrt{|g_{\mu\nu}\nabla^\mu t \nabla^\nu t|}}, \quad (2.1.3)$$

where $dt_\mu = \partial_\mu t$ is the exterior derivative of t . For simplicity we define the lapse function α to be

$$\alpha := \frac{1}{\sqrt{|g_{\mu\nu}\nabla^\mu t \nabla^\nu t|}}. \quad (2.1.4)$$

giving us $n_\mu = -\alpha dt_\mu$ as well as the *normal evolution* vector $m_\mu = \alpha n_\mu$. Defining two infinitesimally close points $p \in \Sigma_t$ and $q \in \Sigma_{t'}$, where $q^\mu = p^\mu + m^\mu \delta t$ and $t' = t + \delta t$, we see,

$$t(q) = t(p^\mu + m^\mu \delta t) = t(p) + \frac{\partial t}{\partial x^\mu} m^\mu \delta t = t(p) + dt_\mu m^\mu \delta t = t(p) + \delta t, \quad (2.1.5)$$

showing that m^μ connects Σ_t and $\Sigma_{t'}$ for any point $p \in \Sigma_t$; therefore when creating evolution equations we should consider Lie derivatives \mathcal{L}_m along m^μ rather than \mathcal{L}_n .

Two very popular books often used as an introduction to numerical relativity are [20] and [21]. For a very detailed account of the 3+1 formalism the reader is directed to [11].

2.1.2 The 3+1 Decomposition

With the notion of a spacetime foliation we should define how to project tensors onto Σ_t ; clearly scalars need no projecting. Following the ideas of section 1.2.4 we can split a vector $X^\mu e_\mu = X_\parallel^\mu e_\mu + X_\perp^\mu e_\mu$ into

components tangent or normal to Σ_t . We then define the orthogonal projector \perp_ν^μ and parallel projector $-n^\mu n_\nu$,

$$X_{\parallel}^\mu = [\delta_\nu^\mu + n^\mu n_\nu] X^\mu = \perp_\nu^\mu X^\nu, \quad (2.1.6)$$

$$X_\perp^\mu = -n^\mu n_\nu X^\nu. \quad (2.1.7)$$

Considering scalars such as $\phi = w_\mu X^\mu$ or $\psi = T^{\mu\nu} w_\mu w_\nu$, and remembering scalars do not vary under projection, it is straightforward to show that any tensor T can be projected by contracting a projection operator \perp on any free index,

$$T_{\parallel}^{ij\dots}_{kl\dots} = \mathcal{T}^{ij\dots}_{kl\dots} = \perp_\mu^i \perp_\nu^j \perp_k^\rho \perp_l^\sigma \dots T^{\mu\nu\dots}_{\rho\sigma\dots}. \quad (2.1.8)$$

We can find the 3-metric $\gamma_{\mu\nu}$ of Σ_t by projecting $g_{\mu\nu}$,

$$\gamma_{ij} = \perp_i^\mu \perp_j^\nu g_{\mu\nu} = g_{\mu\nu} + n_\mu n_\nu \Rightarrow \gamma_j^i = \perp_j^i, \quad (2.1.9)$$

and we find it is equal to the projector \perp ; this has to be the case as $\perp_{ij} dx^i dx^j$ gives the line element along Σ_t . With this machinery we can define the extrinsic curvature tensor \mathcal{K}_{ij} representing curvature due to the choice of spacetime foliation; it could be nonzero for certain foliations of Minkowski space. It is not the same as the 3-Ricci tensor \mathcal{R}_{ij} which is due to spacelike curvature on Σ_t for a single instant in time. The extrinsic curvature tensor is defined the following way,

$$\mathcal{K}_{ij} = \mathcal{K}_{ji} := -\perp_i^\mu \perp_j^\nu \nabla_\mu n_\nu = -\perp_i^\mu \nabla_\mu n_j = -\nabla_i n_j - n_i a_j, \quad (2.1.10)$$

$$\mathcal{K} = \mathcal{K}_i^i = -\nabla \cdot \mathbf{n}, \quad (2.1.11)$$

where $a_i = \mathbf{n} \cdot \nabla n_i$ is called the Eulerian acceleration; it should be noted that \mathcal{K}_{ij} is symmetric. It can also be shown to take the following form,

$$\mathcal{K}_{ij} = -\frac{1}{2} \mathcal{L}_n \gamma_{ij} = -\frac{1}{2\alpha} \mathcal{L}_m \gamma_{ij}, \quad (2.1.12)$$

which gives the intuitive explanation of \mathcal{K}_{ij} being related to the rate of change of the 3-metric γ_{ij} with respect to the foliation.

The next object to discuss is the covariant 3-derivative \mathcal{D}_i . This is the covariant derivative belonging to Σ_t and hence its arguments should be tensors belonging to Σ_t ; it should be noted that $\mathcal{D}_i \neq \perp_i^\mu \nabla_\mu$ for a generic non-scalar tensorial arguments. The covariant 3-derivative is instead found from,

$$\mathcal{T}^{ij\dots}_{kl\dots} = \perp_\mu^i \perp_\nu^j \perp_k^\rho \perp_l^\sigma \dots T^{\mu\nu\dots}_{\rho\sigma\dots}, \quad (2.1.13)$$

$$\mathcal{D}_m \mathcal{T}^{ij\dots}_{kl\dots} := \perp_m^\mu \perp_\mu^i \perp_\nu^j \perp_k^\rho \perp_l^\sigma \dots \nabla_\mu \mathcal{T}^{\mu\nu\dots}_{\rho\sigma\dots} \quad (2.1.14)$$

The covariant 3-derivative in the Levi-Civita connection can be expressed in the same way as section 1.3.3; a simple example is the derivative of a vector $X^i e_i \in \mathcal{T}(\Sigma_t)$,

$$\mathcal{D}_i X^j = \partial_i X^j + \Upsilon^i_{jk} X^k, \quad (2.1.15)$$

$$\Upsilon^i_{jk} = \frac{1}{2} \gamma^{il} [\partial_j \gamma_{lk} + \partial_k \gamma_{lj} - \partial_l \gamma_{jk}], \quad (2.1.16)$$

where Υ^i_{jk} is the 3-dimensional Christoffel symbol of Σ_t . Another useful example is a^μ which can be equated to,

$$a_\mu = \mathbf{n} \cdot \nabla n_\mu = \mathcal{D}_\mu \ln \alpha = \frac{1}{\alpha} \mathcal{D}_\mu \alpha, \quad (2.1.17)$$

and allows us to evaluate the Lie derivative of the projector \perp_j^i ,

$$\mathcal{L}_m \perp_j^i = \alpha n^k \nabla_k \perp_j^i + \perp_k^i \nabla_j \alpha n^k - \perp_j^k \nabla_k \alpha n^i, \quad (2.1.18)$$

$$= \alpha n^k \nabla_k [n^i n_j] + \alpha \nabla_j n^i - [\alpha \mathcal{K}_j^i + n^i \mathcal{D}_j \alpha], \quad (2.1.19)$$

$$= 0. \quad (2.1.20)$$

The result $\mathcal{L}_m \perp_j^i = 0$ is very important, it tells us that the projector commutes with \mathcal{L}_m and as a result any tensor \mathbf{T} which when projected onto Σ_t , written \mathcal{T} , satisfies

$$\mathcal{L}_m \mathcal{T}^{ij\dots}_{\quad kl\dots} = \perp_\mu^i \perp_\nu^j \perp_k^\rho \perp_l^\sigma \mathcal{L}_m T^{\mu\nu\dots}_{\quad \rho\sigma\dots}. \quad (2.1.21)$$

In other words, evolving a projected tensor along integral curves of m leaves the tensor parallel to Σ_t .

2.1.3 Gauss, Codazzi and Ricci Equations

The decomposition of the 4-dimensional curvature tensors into a combination of 3-dimensional curvature tensors and \mathcal{K} is very useful as it captures all the degrees of freedom of the 4-dimensional Riemann tensor in terms of variables on Σ_t . This property is crucial when numerically simulating a single time slice Σ_t as we only have access to variables on Σ_t .

The Gauss Equations

From the definition of the Riemann tensor in section 1.3.4 we know,

$$[\mathcal{D}_i \mathcal{D}_j - \mathcal{D}_j \mathcal{D}_i] v^k = \mathcal{R}^k_{mij} v^m, \quad (2.1.22)$$

$$[\nabla_\alpha \nabla_\beta - \nabla_\beta \nabla_\alpha] X^\gamma = R^\gamma_{\lambda\alpha\beta} X^\lambda, \quad (2.1.23)$$

where $X \in \mathcal{M}$ and $v^m = \perp_\rho^m v^\rho$ is tangent to Σ_t . Expanding the \mathcal{D} 's in terms of ∇ 's gives,

$$\mathcal{D}_i \mathcal{D}_j v^k = \perp_i^\mu \perp_j^\sigma \perp_\xi^k \nabla_\mu (\perp_\sigma^\nu \perp_\rho^\xi \nabla_\nu v^\rho), \quad (2.1.24)$$

and using the following properties; impotence of projections $\perp_\mu^i \perp_j^\mu = \perp_j^i$, null projection of orthogonal vectors $\perp(\mathbf{n}) = 0$, metric compatibility $\nabla_\mu \perp_j^i = n_j \nabla_\mu n^i + n^i \nabla_\mu n_j$ and Eq. (2.1.10) for \mathcal{K}_{ij} we obtain the Gauss relation,

$$\perp_i^\mu \perp_j^\nu \perp_\rho^\sigma R^\rho_{\sigma\mu\nu} = \mathcal{R}^k_{lij} + \mathcal{K}_i^k \mathcal{K}_{lj} - \mathcal{K}_j^k \mathcal{K}_{il}. \quad (2.1.25)$$

Contracting over i, k above and relabelling indices we get the contracted Gauss relation,

$$\perp_i^\mu \perp_j^\nu R_{\mu\nu} + \gamma_{i\mu} n^\nu \perp_j^\rho n^\sigma R^\mu_{\nu\rho\sigma} = \mathcal{R}_{ij} + \mathcal{K}\mathcal{K}_{ij} - \mathcal{K}_j^k \mathcal{K}_{ik}. \quad (2.1.26)$$

Contracting again and realising $R_{\mu\nu\rho\sigma} n^\mu n^\nu n^\rho n^\sigma = 0$ from antisymmetry in indices 0 and 1 or 2 and 3 in the Riemann tensor, gives the scalar Gauss equation,

$$R + 2R_{\mu\nu} n^\mu n^\nu = \mathcal{R} + \mathcal{K}^2 - \mathcal{K}_{ij} \mathcal{K}^{ij}. \quad (2.1.27)$$

The Codazzi Equations

The Codazzi relations are derived from a different start point. Instead of projecting the Riemann tensor fully onto Σ_t with projection operators \perp and a spacelike vector \mathbf{v} , it is now projected with a timelike vector \mathbf{n} ,

$$[\nabla_\alpha \nabla_\beta - \nabla_\beta \nabla_\alpha] n^\gamma = R^\gamma_{\lambda\alpha\beta} n^\lambda, \quad (2.1.28)$$

and again projecting to Σ_t with three projection operators. The following relations are used

$$\nabla_j n^k = -\mathcal{K}_j^k - a^k n_j, \quad (2.1.29)$$

$$\perp_\mu^i \perp_\nu^j \perp_k^\rho \nabla_i \nabla_j n^k = -\mathcal{D}_i \mathcal{K}_j^k + a^k \mathcal{K}_{ij}, \quad (2.1.30)$$

which lead immediately to the Codazzi relation,

$$\perp_i^\mu \perp_j^\nu \perp_\rho^\sigma R^\rho_{\sigma\mu\nu} = \mathcal{D}_j \mathcal{K}_i^k - \mathcal{D}_i \mathcal{K}_j^k, \quad (2.1.31)$$

and the contracted Codazzi relation,

$$\perp_i^\mu n^\nu R_{\mu\nu} = \mathcal{D}_i \mathcal{K} - \mathcal{D}_\mu \mathcal{K}^\mu_i. \quad (2.1.32)$$

The Ricci Equation

Finally we turn our attention to the Ricci equation, the projection of the Riemann tensor twice onto Σ_t and twice contracting with \mathbf{n} . This is done by projecting Eq (2.1.28) with two projectors \perp and one timelike \mathbf{n} . If we contract with n^γ then the antisymmetry in the first two Riemann tensor indices would identically give to zero, therefore the unique choice (up to a minus sign) is to project with n^β ,

$$R_{\gamma\lambda\alpha\beta} n^\lambda n^\beta = n^\beta [\nabla_\alpha \nabla_\beta - \nabla_\beta \nabla_\alpha] n_\gamma, \quad (2.1.33)$$

and project the remaining free indices with \perp like,

$$\perp_i^\gamma \perp_j^\alpha R_{\gamma\lambda\alpha\beta} n^\lambda n^\beta = \perp_i^\gamma \perp_j^\alpha n^\beta [\nabla_\alpha \nabla_\beta - \nabla_\beta \nabla_\alpha] n_\gamma. \quad (2.1.34)$$

Rearranging Eqs. (2.1.10) and (2.1.17) we obtain,

$$\nabla_\sigma n_\mu = -\mathcal{K}_{\mu\sigma} - n_\sigma \mathcal{D}_\mu \ln(\alpha), \quad (2.1.35)$$

which can be used to expand the right hand side of Eq. (2.1.36),

$$\perp_i^\gamma \perp_j^\alpha R_{\gamma\lambda\alpha\beta} n^\lambda n^\beta = \perp_i^\gamma \perp_j^\alpha n^\beta [-\nabla_\alpha \mathcal{K}_{\gamma\beta} + \nabla_\beta \mathcal{K}_{\gamma\alpha}] \quad (2.1.36)$$

$$+ \perp_i^\gamma \perp_j^\alpha n^\beta [-\nabla_\alpha (n_\beta \mathcal{D}_\gamma \ln(\alpha)) + \nabla_\beta (n_\alpha \mathcal{D}_\gamma \ln(\alpha))],$$

$$= \perp_i^\gamma \perp_j^\alpha n^\beta n^\sigma \nabla_\sigma \mathcal{K}_{\gamma\alpha} + \perp_i^\gamma \perp_j^\alpha \mathcal{K}_{\gamma\beta} \nabla_\alpha n^\beta \quad (2.1.37)$$

$$+ \perp_i^\gamma \perp_j^\alpha n^\beta [-n_\beta \nabla_\alpha (\mathcal{D}_\gamma \ln(\alpha)) + n_\alpha \nabla_\beta (\mathcal{D}_\gamma \ln(\alpha)) + (\mathcal{D}_\gamma \ln(\alpha)) \nabla_\beta n_\alpha],$$

$$= \perp_i^\gamma \perp_j^\alpha n^\beta n^\sigma \nabla_\sigma \mathcal{K}_{\gamma\alpha} - \mathcal{K}_{ik} \mathcal{K}_j^k \quad (2.1.38)$$

$$+ \mathcal{D}_j \mathcal{D}_i \ln(\alpha) + \mathcal{D}_i \ln(\alpha) \mathcal{D}_j \ln(\alpha),$$

$$= \perp_i^\gamma \perp_j^\alpha n^\beta n^\sigma \nabla_\sigma \mathcal{K}_{\gamma\alpha} - \mathcal{K}_{ik} \mathcal{K}_j^k + \frac{1}{\alpha} \mathcal{D}_j \mathcal{D}_i \alpha, \quad (2.1.39)$$

where $\mathbf{n}^2 = -1$, $\perp_i^\mu n_\mu = 0$, $\mathcal{D}_\alpha \ln \alpha = n^\beta \nabla_\beta n_\alpha$ from Eq. (2.1.17) and $n^\beta \nabla_\alpha n_\beta = 0$ have been used. This expression can be simplified by calculating the Lie derivative of \mathcal{K} ,

$$\mathcal{L}_m \mathcal{K}_{ij} = \perp_i^\mu \perp_j^\nu \mathcal{L}_m \mathcal{K}_{\mu\nu}, \quad (2.1.40)$$

$$= \alpha \perp_i^\mu \perp_j^\nu \mathcal{L}_n \mathcal{K}_{\mu\nu}, \quad (2.1.41)$$

$$= \alpha \perp_i^\mu \perp_j^\nu [\alpha \mathbf{n} \cdot \nabla \mathcal{K}_{\mu\nu} + 2\mathcal{K}_{k(\nu} \nabla_{\mu)} n^k], \quad (2.1.42)$$

$$= \alpha \perp_i^\mu \perp_j^\nu n^\sigma \nabla_\sigma \mathcal{K}_{\mu\nu} - 2\alpha \mathcal{K}_{ik} \mathcal{K}_j^k, \quad (2.1.43)$$

where the results $\mathcal{L}_m \mathcal{K} = \alpha \mathcal{L}_n \mathcal{K}$ from Eq. (2.1.12), $\mathcal{L}_m \mathcal{K}_{\alpha\beta} \in \Sigma_t$ from Eq. (2.1.21) and Eq. (2.1.10) have been used. Putting everything together we arrive at the Ricci equation,

$$\perp_i^\mu \perp_j^\nu n^\rho n^\sigma R_{\mu\rho\nu\sigma} = \frac{1}{\alpha} \mathcal{L}_m \mathcal{K}_{ij} + \frac{1}{\alpha} \mathcal{D}_j \mathcal{D}_i \alpha + \mathcal{K}_{ik} \mathcal{K}_j^k. \quad (2.1.44)$$

This is the final contraction of the Riemann tensor that can be made with \perp and \mathbf{n} as any projections with three or more contractions with \mathbf{n} would identically give zero due to the symmetries of the Riemann tensor.

2.1.4 Decomposition of Einstein's Equation

To evolve General Relativity numerically we must project the Einstein Equation into 3+1 dimensions. Relations between three and four dimensional geometric objects have been derived above and will be used to decompose the Einstein tensor $G_{\mu\nu} = R_{\mu\nu} - g_{\mu\nu} R/2$ from the left hand side of Eq. (2.1.1). The second component, for simulating non-vacuum spacetimes, is the 3+1 decomposition of the Stress tensor

T_{ab} . We contract twice with \mathbf{n} , then once with \mathbf{n} while projecting onto Σ_t and finally twice projecting onto Σ_t to get an energy, momentum and stress-like split,

$$\rho = \mathbf{T}(\mathbf{n}, \mathbf{n}) = T_{\mu\nu} n^\mu n^\nu, \quad (2.1.45)$$

$$\mathcal{S}_i = -\perp_i^\mu n^\nu T_{\mu\nu}, \quad (2.1.46)$$

$$\mathcal{S}_{ij} = \perp_i^\mu \perp_j^\nu T_{\mu\nu}, \quad (2.1.47)$$

and by construction,

$$T_{\mu\nu} = \rho n_\mu n_\nu + \mathcal{S}_\mu n_\nu + \mathcal{S}_\nu n_\mu + \mathcal{S}_{\mu\nu}. \quad (2.1.48)$$

With this and the Gauss-Codazzi equations of section 2.1.3 we can project the Einstein equation. Let us first look at the scalar equation,

$$G_{\mu\nu} n^\mu n^\nu = R_{\mu\nu} n^\mu n^\nu + \frac{1}{2} R = 8\pi\rho, \quad (2.1.49)$$

and equating the geometric terms to the scalar Gauss equation we get the Hamiltonian constraint, $\mathcal{H} = 0$,

$$\mathcal{H} = \mathcal{K}_{\mu\nu} \mathcal{K}^{\mu\nu} - \mathcal{K}^2 - \mathcal{R} + 16\pi\rho = 0. \quad (2.1.50)$$

Now looking at the mixed space-time projected part we see,

$$\perp_i^\mu n^\nu G_{\mu\nu} = \perp_i^\mu n^\nu R_{\mu\nu} = -8\pi\mathcal{S}_i, \quad (2.1.51)$$

and substituting the geometric terms for the contracted Codazzi relation we get the momentum constraint, $\mathcal{M}_i = 0$,

$$\mathcal{M}_i = \mathcal{D}_i \mathcal{K} - \mathcal{D}_j \mathcal{K}_i^j + 8\pi\mathcal{S}_i = 0. \quad (2.1.52)$$

Finally, the space-space projection gives the 6 evolution PDEs. This time start with the trace reversed Einstein Equation

$$R_{\mu\nu} = 8\pi \left[T_{\mu\nu} - \frac{1}{2} T g_{\mu\nu} \right], \quad (2.1.53)$$

$$\perp_i^\mu \perp_j^\nu R_{\mu\nu} = 8\pi \left[\mathcal{S}_{ij} - \frac{1}{2} (\mathcal{S} - \rho) \gamma_{ij} \right], \quad (2.1.54)$$

where we used $T = [\gamma^{\mu\nu} - n^\mu n^\nu] T_{\mu\nu} = \mathcal{S} - \rho$. When projecting the Ricci tensor, we use the contracted Gauss equation but replace the term with $R^\mu_{\nu\rho\sigma}$ with the Ricci equation (2.1.44). Rearranging gives a normal evolution for the extrinsic curvature,

$$\mathcal{L}_m \mathcal{K}_{ij} = -\mathcal{D}_j \mathcal{D}_i \alpha + \alpha \left[\mathcal{R}_{ij} + \mathcal{K} \mathcal{K}_{ij} - 2\mathcal{K}_i^k \mathcal{K}_{kj} + 4\pi [\gamma_{ij} [\mathcal{S} - \rho] - 2\mathcal{S}_{ij}] \right]. \quad (2.1.55)$$

Along with the definition of \mathcal{K}_{ij} in Eq. (2.1.12),

$$\mathcal{L}_m \gamma_{ij} = -2\alpha \mathcal{K}_{ij}, \quad (2.1.56)$$

this gives the normal evolution equations for γ_{ij} and \mathcal{K}_{ij} . In 4 or n spacetime dimensions the normal evolution equations contain 6 or $\frac{n^2-n}{2}$ differential equations. The Hamiltonian constraint is a single differential equation, the momentum constraint contains 3 or $n-1$ differential equations and the Einstein equation contains 10 or $\frac{n^2+n}{2}$ differential equations. In four spacetime dimensions this corresponds to 6 evolution equations and 4 constraint equations over the surface Σ_t .

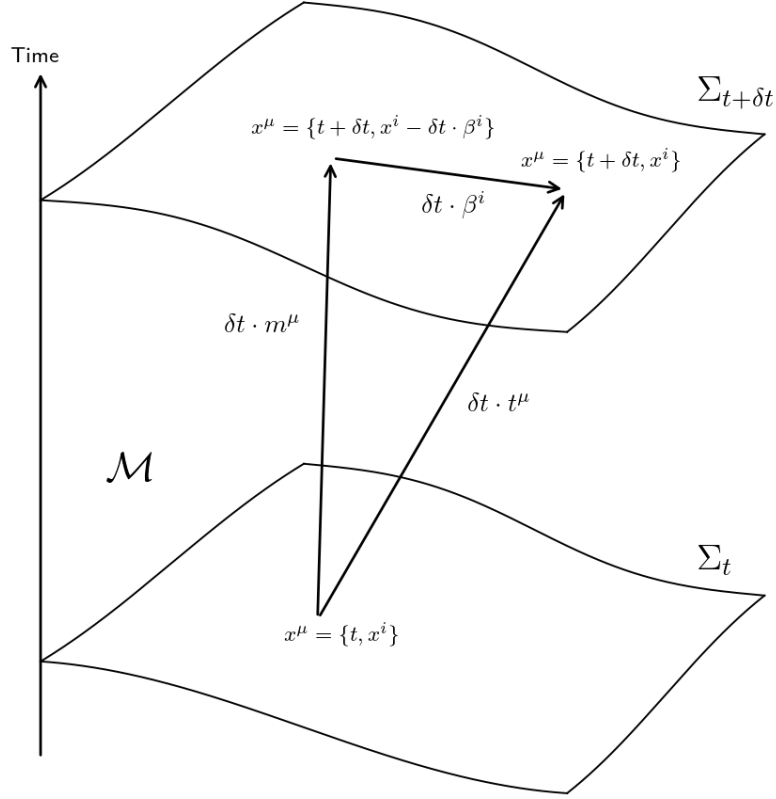


Figure 2.1: An illustration of two hypersurfaces Σ_t and $\Sigma_{t+\delta t}$ and how they are connected by m^μ . As can be seen, integral curves of t^μ have constant spatial coordinates x^i .

2.1.5 Foliation Adapted Coordinates

There is a large gauge freedom associated with picking coordinates in general relativity; we choose to use a level set of the time coordinate $x^0 = t$ to define our foliation hypersurfaces Σ_t . The other three coordinates x^i for $i \in [1, 2, 3]$ can be used to span each hypersurface Σ_t however we define. It is conventional to split the normal evolution vector m^μ into time t^μ and space parts β^μ ,

$$t^\mu = (1, 0, 0, 0), \quad (2.1.57)$$

$$\beta^\mu = (0, \beta^1, \beta^2, \beta^3), \quad (2.1.58)$$

such that,

$$m^\mu = t^\mu - \beta^\mu = (\partial_0)^\mu - \beta^i (\partial_i)^\mu, \quad (2.1.59)$$

$$m^\mu = (1, -\beta^1, -\beta^2, -\beta^3). \quad (2.1.60)$$

We can view t^μ as the (not necessarily causal) worldline for a simulation gridpoint, hence we would like to evolve our PDEs along t^μ on a computer. In other words, integral curves of t^μ must have constant spatial coordinates on Σ_t . Equation (2.1.60), along with the definitions $\mathbf{m} = \alpha \mathbf{n}$ and $\mathbf{n}^2 = -1$, specifies n^μ and n_μ ,

$$n^\mu = \frac{1}{\alpha} (1, -\beta^1, -\beta^2, -\beta^3), \quad (2.1.61)$$

$$n_\mu = -\alpha (1, 0, 0, 0). \quad (2.1.62)$$

The decomposed metric can be calculated, using the property that β is tangent to Σ_t and orthogonal to \mathbf{m} ,

$$g_{00} = \mathbf{g}(\partial_0, \partial_0) = \mathbf{g}(\mathbf{m} + \beta^i \partial_i, \mathbf{m} + \beta^j \partial_j) = \mathbf{g}(\mathbf{m}, \mathbf{m}) + \beta^i \beta_j \langle \partial_i, \mathbf{d}\mathbf{x}^j \rangle = -\alpha^2 + \beta^i \beta_i, \quad (2.1.63)$$

$$g_{0i} = \mathbf{g}(\partial_0, \partial_i) = \mathbf{g}(\mathbf{m} + \beta^j \partial_j, \partial_i) = \beta^j \mathbf{g}(\partial_j, \partial_i) = \beta_i, \quad (2.1.64)$$

$$g_{ij} = \mathbf{g}(\partial_i, \partial_j) = \gamma(\partial_i, \partial_j) = \gamma_{ij}. \quad (2.1.65)$$

This is commonly called the 3 + 1 Arnowitt-Deser-Misner (ADM) metric and α, β^i are referred to as the lapse and shift vector in this context. The line element and metric are commonly written as,

$$ds^2 = -\alpha^2 dt^2 + \gamma_{ij} [dx^i + \beta^i dt] [dx^j + \beta^j dt], \quad (2.1.66)$$

$$g_{\mu\nu} = \begin{pmatrix} -\alpha^2 + \beta^i \beta_i & \beta_i \\ \beta_j & \gamma_{ij} \end{pmatrix}, \quad (2.1.67)$$

$$g^{\mu\nu} = \frac{1}{\alpha^2} \begin{pmatrix} -1 & \beta^i \\ \beta^j & \alpha^2 \gamma^{ij} - \beta^i \beta^j \end{pmatrix}, \quad (2.1.68)$$

and using Cramer's rule for metric determinant,

$$g^{00} = \frac{\det\{\gamma_{ij}\}}{\det\{g_{\mu\nu}\}}, \quad (2.1.69)$$

we get the important relationship,

$$\sqrt{-g} = \alpha \sqrt{\gamma}, \quad (2.1.70)$$

where g and γ are the determinants of $g_{\mu\nu}$ and γ_{ij} respectively.

2.1.6 ADM Equations

Now that we have some coordinates suitable for the spacetime foliation we can find the Arnowitt-Deser-Misner (ADM) evolution equations for \mathcal{K}_{ij} and γ_{ij} . First we simplify the Lie derivative \mathcal{L}_t along t^μ using,

$$\mathcal{L}_t \mathbf{T} = \partial_t \mathbf{T}, \quad (2.1.71)$$

for any tensor \mathbf{T} as $\partial_\nu t^\mu = 0$. This can be used to expand the Lie derivative along m^μ ,

$$\mathcal{L}_m = \mathcal{L}_t - \mathcal{L}_\beta = \partial_t - \mathcal{L}_\beta, \quad (2.1.72)$$

and the ADM equations can be written by substituting $\mathcal{L}_m \rightarrow \partial_t - \mathcal{L}_\beta$ in the normal evolution equations in section 2.1.4 for \mathcal{K} and γ . The ADM equations are,

$$\partial_t \mathcal{K}_{ij} = \mathcal{L}_\beta \mathcal{K}_{ij} - \mathcal{D}_j \mathcal{D}_i \alpha + \alpha \left[\mathcal{R}_{ij} + \mathcal{K} \mathcal{K}_{ij} - 2 \mathcal{K}_i^k \mathcal{K}_{kj} + 4\pi [\gamma_{ij} [\mathcal{S} - \rho] - 2 \mathcal{S}_{ij}] \right], \quad (2.1.73)$$

$$\partial_t \gamma_{ij} = \mathcal{L}_\beta \gamma_{ij} - 2\alpha \mathcal{K}_{ij}. \quad (2.1.74)$$

Unfortunately, these PDEs turn out to be an ill-posed initial value problem with typical gauges [22]; this means that the time evolution of these equations does not generally depend smoothly on the initial data.

2.1.7 BSSN Formalism

To tackle the ill-posedness of the ADM equations in section 2.1.6 we now discuss the Baumgarte-Shapiro-Shibata-Nakamura (BSSN) formalism [23]. The first step in BSSN is to decompose the 3-metric into the conformal metric $\tilde{\gamma}_{ij}$ and the conformal factor χ ,

$$\tilde{\gamma}_{ij} = \chi \gamma_{ij}, \quad (2.1.75)$$

$$\det\{\tilde{\gamma}_{ij}\} = \tilde{\gamma} = \chi^3 \gamma = 1, \quad (2.1.76)$$

with the above being the convention used in GRCHOMBO described in section 3.2.1. Other conventions include factors such as $\tilde{\gamma}_{ij} = \psi^{-4}\gamma_{ij}$ or $\tilde{\gamma}_{ij} = e^{-\phi}\gamma_{ij}$. Along with this the extrinsic curvature \mathcal{K}_{ij} is conformally decomposed with χ and modified to be trace free,

$$\tilde{A}_{ij} = \chi \left[\mathcal{K}_{ij} - \frac{1}{3} \mathcal{K} \tilde{\gamma}_{ij} \right], \quad (2.1.77)$$

so that $\tilde{A}_{ij}\tilde{\gamma}^{ij} = 0$. During an evolution the algebraic constraint $\text{tr } \tilde{A}_{ij} = 0$ (and sometimes $\tilde{\gamma} = 1$) is enforced which avoids the undesirable growth of numerical error [24, 25]. As discussed later in section 2.1.10, the definition of $\chi = \gamma^{-1/3}$ is good for black-hole simulations where $\gamma \rightarrow \infty$ but $\chi \rightarrow 0$. For example the isotropic Schwarzschild metric has,

$$\gamma = \left[1 + \frac{M}{2r} \right]^{12}, \quad (2.1.78)$$

$$\chi = \left[\frac{r}{\frac{M}{2} + r} \right]^4. \quad (2.1.79)$$

The next step is to introduce the conformal connection functions as auxiliary variables,

$$\tilde{\Upsilon}^i{}_{jk} = \frac{1}{2} \tilde{\gamma}^{il} [\partial_j \tilde{\gamma}_{kl} + \partial_k \tilde{\gamma}_{lj} - \partial_l \tilde{\gamma}_{kj}] = \Upsilon^i{}_{jk} + [\delta^i_j \partial_k + \delta^i_k \partial_j - \gamma^{il} \gamma_{jk} \partial_l] \ln \sqrt{\chi}, \quad (2.1.80)$$

$$\tilde{\Upsilon}^i = \tilde{\gamma}^{jk} \tilde{\Upsilon}^i{}_{jk} = -\partial_i \tilde{\gamma}^{ij}, \quad (2.1.81)$$

where $\Gamma^i{}_{jk}$ are the Christoffel symbols of Σ_t as shown in Eq. (2.1.16); this reduces the set of vacuum evolution variables to $\{\chi, \tilde{\gamma}_{ij}, \mathcal{K}, \tilde{A}_{ij}, \tilde{\Upsilon}^i\}$. The idea behind introducing the $\tilde{\Upsilon}^i$ is that their derivatives $(\partial_j \tilde{\Upsilon}^i)$ encode second derivatives of the metric that ruin strong hyperbolicity in the ADM equations; instead these offending terms are encoded as first derivatives of a new evolution variable and are removed from the principal symbol governing the hyperbolicity of the equations. It is conventional to use $-\partial_i \tilde{\gamma}^{ij}$ to evaluate the conformal connection coefficients when they appear in the RHS of an equation, but $\partial_j \tilde{\Upsilon}^i$ is calculated by differentiating the evolution variable $\tilde{\Upsilon}^i$.

One final detail, not mentioned in the Z4 and CCZ4 formulations discussed later, is the addition of multiples of the Hamiltonian and Momentum constraint equations (in section 2.1.4) to the evolution equations to change the characteristic matrix and improve stability. This is not always necessary and can depend on the gauge used, for more information see [26].

The BSSN formalism is not the only way to find a well-posed set of evolution equations for general relativity. Another strongly hyperbolic formalism is the generalised harmonic gauge [27, 28, 29, 30] with,

$$\square x^\mu = H^\mu, \quad (2.1.82)$$

for some functions H^μ .

2.1.8 Z4 Formalism

The Z4 formalism [31] generalises the Einstein equation to include an unphysical field Z_μ , along with damping terms parameterised by κ_1, κ_2 ,

$$R_{\mu\nu} + \nabla_\mu Z_\nu + \nabla_\nu Z_\mu - \kappa_1 [n_\mu Z_\nu + n_\nu Z_\mu - [1 + \kappa_2] g_{\mu\nu} n^\alpha Z_\alpha] = 8\pi G \left[T_{\mu\nu} - \frac{1}{2} T g_{\mu\nu} \right]. \quad (2.1.83)$$

Of course regular General Relativity is recovered by setting $Z_\mu = 0$. It can be shown that achieving $Z_\mu = 0$ whilst dynamically evolving Z_μ is equivalent to solving the constraints. Taking the divergence of the trace reverse of Eq. (2.1.83), and noting that both $G_{\mu\nu}$ and $T_{\mu\nu}$ are divergenceless, gives

$$\nabla^\nu \nabla_\nu Z_\mu + R_{\mu\nu} Z^\nu = -\kappa_1 \nabla^\nu (n_\mu Z_\nu + n_\nu Z_\mu + \kappa_2 g_{\mu\nu} n^\alpha Z_\alpha). \quad (2.1.84)$$

Z_μ is subjected to a wave equation, transporting constraint violation off the computational domain. It can be shown that the system is driven to $Z_\mu = 0$ for $k_1 > 0$ and $k_2 > -1$. It is much cheaper to evolve the variables Z_μ , driven to zero, than to solve four elliptic PDEs for the constraints $\{\mathcal{H}, \mathcal{M}^i\}$ on each timestep.

2.1.9 CCZ4 Formalism

Merging the conformal decomposition of the BSSN formalism with the constraint damping Z4 formalism leads to Z4c formalism [32] and the conformal covariant Z4 (CCZ4) formalism. The purpose of this is to get a formalism combining the strong hyperbolicity of the BSSN equations and the constraint damping effects of the Z4 system. In this thesis we will use the CCZ4 formalism which employs the additional modifications,

$$\Theta = -n \cdot Z = -\alpha Z^0, \quad (2.1.85)$$

$$\hat{Y}^i = \tilde{Y}^i + \frac{2\gamma^{ij} Z_j}{\chi}, \quad (2.1.86)$$

leaving us with the following set of vacuum evolution variables $\{\chi, \tilde{\gamma}_{ij}, \mathcal{K}, \tilde{\mathcal{A}}_{ij}, \hat{Y}^i, \Theta\}$. The evolution equations can now be found in the CCZ4 scheme by applying a 3+1 decomposition to the Z4 modified Einstein equation (2.1.83) and proceeding as in the BSSN formalism. To illustrate this, we derive the equation of motion for χ in the CCZ4 formalism. Using Eqs. (1.3.118) and (2.1.56) with $\chi^{-3} = \gamma$ we obtain,

$$\mathcal{L}_m \gamma = \gamma \gamma^{ij} \mathcal{L}_m \gamma_{ij} = -2\gamma \alpha \gamma^{ij} \mathcal{K}_{ij} = -2\gamma \alpha \mathcal{K}. \quad (2.1.87)$$

This can be used to simplify the Lie derivative of χ ,

$$\mathcal{L}_m \chi = \mathcal{L}_{\partial_t} \chi - \mathcal{L}_\beta \chi, \quad (2.1.88)$$

$$= (\partial_t)^i \partial_i \chi + \omega \chi \partial_i (\partial_t)^i - \beta^i \partial_i \chi - \omega \chi \partial_i \beta^i, \quad (2.1.89)$$

$$= \partial_t \chi - \beta^i \partial_i \chi + \frac{2}{3} \chi \partial_i \beta^i, \quad (2.1.90)$$

$$\mathcal{L}_m \chi = \mathcal{L}_m \gamma^{-\frac{1}{3}}, \quad (2.1.91)$$

$$= -\frac{1}{3} \gamma^{-\frac{4}{3}} \mathcal{L}_m \gamma, \quad (2.1.92)$$

$$= \frac{2}{3} \gamma^{-\frac{1}{3}} \alpha \mathcal{K}, \quad (2.1.93)$$

$$= \frac{2}{3} \chi \alpha \mathcal{K}, \quad (2.1.94)$$

where Eq. (1.3.31) has been used with $\mathcal{T} = \chi$ as χ is a scalar density of weight $\omega = -2/3$. Re-arranging gives the equation of motion for χ ,

$$\partial_t \chi = \beta^i \partial_i \chi + \frac{2\chi}{3} [\alpha \mathcal{K} - \partial_i \beta^i]. \quad (2.1.95)$$

A similar process returns the remaining CCZ4 equations but care should be taken to include the Z4 terms (Θ, \hat{Y}^i) where they are needed. The complete list of CCZ4 equations used in simulations with

GRCHOMBO (section 3.2.1) are given below:

$$\partial_t \chi = \beta^i \partial_i \chi + \frac{2\chi}{3} [\alpha \mathcal{K} - \partial_i \beta^i], \quad (2.1.96)$$

$$\partial_t \tilde{\gamma}_{ij} = \beta^k \partial_k \tilde{\gamma}_{ij} + \tilde{\gamma}_{kj} \partial_k \beta^k + \tilde{\gamma}_{ik} \partial_j \beta^k - \frac{2}{3} \tilde{\gamma}_{ij} \partial_k \beta^k - 2\alpha \tilde{\mathcal{A}}_{ij}, \quad (2.1.97)$$

$$\begin{aligned} \partial_t \mathcal{K} &= \beta^k \partial_k \mathcal{K} + \alpha [\mathcal{R} + 2\mathbf{D} \cdot \mathbf{Z} + \mathcal{K} [\mathcal{K} - 2\Theta]] - 3\alpha \kappa_1 [1 + \kappa_2] \Theta \\ &\quad - \chi \tilde{\gamma}^{kl} \mathcal{D}_k \mathcal{D}_l \alpha + 4\pi G \alpha [\mathcal{S} - 3\rho], \end{aligned} \quad (2.1.98)$$

$$\begin{aligned} \partial_t \tilde{\mathcal{A}}_{ij} &= \beta^k \partial_k \tilde{\mathcal{A}}_{ij} + \chi \left[\alpha [\mathcal{R}_{ij} + 2\mathcal{D}_{(i} Z_{j)}] - \mathcal{D}_i \mathcal{D}_j \alpha \right]^{TF} \\ &\quad + \tilde{\mathcal{A}}_{ij} \left[\alpha [\mathcal{K} - 2\Theta] - \frac{2}{3} \mathcal{K}^2 \right] + 2\tilde{\mathcal{A}}_{k(i} \partial_{j)} \beta^k - 2\alpha \tilde{\gamma}^{kl} \tilde{\mathcal{A}}_{ik} \tilde{\mathcal{A}}_{lj}, \end{aligned} \quad (2.1.99)$$

$$\begin{aligned} \partial_t \Theta &= \beta^k \partial_k \Theta + \frac{1}{2} \alpha \left[\mathcal{R} + 2\mathbf{D} \cdot \mathbf{Z} - \tilde{\mathcal{A}}_{kl} \tilde{\mathcal{A}}^{kl} + \frac{2}{3} \mathcal{K}^2 - 2\Theta \mathcal{K} \right] - \kappa_1 \alpha \Theta [2 + \kappa_2] - Z^k \partial_k \alpha - 8\pi G \alpha \rho, \end{aligned} \quad (2.1.100)$$

$$\begin{aligned} \partial_t \hat{\Upsilon}^i &= \beta^k \partial_k \hat{\Upsilon}^i + \frac{2}{3} \left[\partial_k \beta^k \left[\tilde{\Upsilon}^i + 2\kappa_3 \frac{Z^i}{\chi} \right] - 2\alpha \mathcal{K} \frac{Z^i}{\chi} \right] - 2\alpha \kappa_1 \frac{Z^i}{\chi} \\ &\quad + 2\tilde{\gamma}^{ij} [\alpha \partial_j \Theta - \Theta \partial_j \alpha] - 2\tilde{\mathcal{A}}^{ij} \partial_j \alpha - \alpha \left[\frac{4}{3} \tilde{\gamma}^{ij} \partial_j \mathcal{K} + 3\tilde{\mathcal{A}}^{ij} \frac{\partial_j \chi}{\chi} \right] \\ &\quad - \left[\tilde{\Upsilon}^j + 2\kappa_3 \frac{Z^j}{\chi} \right] \partial_j \beta^i + 2\alpha \tilde{\Upsilon}^i{}_{jk} \tilde{\mathcal{A}}^{jk} + \tilde{\gamma}^{jk} \partial_j \partial_k \beta^i + \frac{1}{3} \tilde{\gamma}^{ij} \partial_k \partial_j \beta^k - 16\pi G \alpha \tilde{\gamma}^{ij} \mathcal{S}_j, \end{aligned} \quad (2.1.101)$$

$$\partial_t \varphi = \beta^k \partial_k \varphi - \alpha \Pi. \quad (2.1.102)$$

In the CCZ4 equations there is an additional parameter κ_3 premultiplying terms in the evolution of $\hat{\Upsilon}^i$ which experimentally were found to lead to instabilities in black-hole simulations [33]; setting $\kappa_3 < 1$ stabilises the simulation but at the cost of covariance. Later on it was realised that setting $\kappa_3 = 1$ and $\alpha \kappa_1 \rightarrow \kappa_1$ retains covariance as well as numerical stability [34]; in this work $\kappa_1 = 0.1$, $\kappa_2 = 0$ and $\kappa_3 = 1$ is used. Notably the pair of variables $\mathcal{R}_{ij} + \mathcal{D}_{(i} Z_{j)}$, and its traced version $\mathcal{R} + \mathbf{D} \cdot \mathbf{Z}$, always appear together; separately they would ruin strong hyperbolicity but together they do not.

The CCZ4 scheme proves several benefits.

- Any initial data that does not satisfy the constraints will generally not do so during evolution when using the BSSN formalism either. Given that superposition of solutions in GR does not generally give a new solution, but does approximate one for separated compact objects, all the simulated binaries considered in this work will have non constraint satisfying initial data.
- Constraint satisfying initial data can also develop constraint violation over time; one reason being that finite resolution imposes some small deviation from the continuum solution. More importantly, the use of adaptive mesh refinement (discussed in section 3.2.1) introduces interpolation errors into the simulation at the boundary of the different grid resolution levels. The use of the CCZ4 scheme can also help to reduce the constraint violation generated in this way.
- Sommerfeld boundary conditions (discussed in section 3.1.3) used are inexact in GR and will introduce errors at the outer boundary that ruin constraint satisfaction and in the worst case scenario cause a simulation to crash. Again, the CCZ4 scheme can be used to help combat this.

In all the cases above, the CCZ4 system forces the evolution towards constraint satisfaction, despite the numerical errors and approximations. There is a caveat, even if a simulation satisfies the constraints, there is no guarantee it is the desired solution to Einstein's equation. Additionally, the damping is more efficient for small amplitude and high frequency errors.

2.1.10 Gauge Conditions

The lapse α and shift β^i are freely specifiable on a hypersurface Σ_t being gauge variables, however they must be chosen carefully along with a suitable initial Cauchy surface Σ_{t_0} and initial data. Σ_{t_0} should be a smooth non-intersecting Cauchy surface as described in section 2.1.1 and contain smooth initial data. It is also wise to avoid singularities (both coordinate and physical) on this surface. As an example, consider the simulation of a single Schwarzschild black hole. Figure 2.2 (left) shows how an initial data surface could extend to the singularity if polar-areal coordinates are used. Figure 2.2 also shows how the physical singularity is avoided when using isotropic coordinates. In this work the isotropic gauge is used; not only does this provide an initial Cauchy surface free of physical singularities but also allows for trivial swapping between spherical polar and Cartesian (used in simulations) coordinates. However, for a poor choice of lapse function, even a well chosen Σ_{t_0} can advance to the physical singularity in finite simulation time. For a comprehensive introduction to gauge conditions the reader is directed to [20, 21, 11].

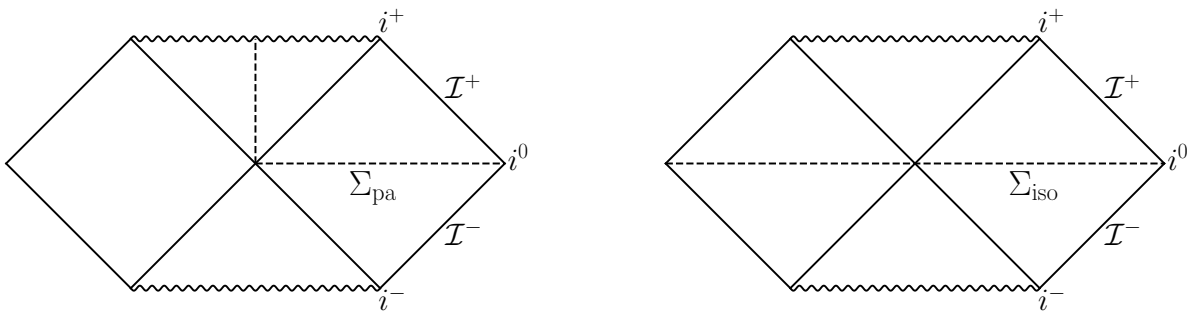


Figure 2.2: Penrose Diagram of the maximally extended Schwarzschild spacetime; the top (future) squiggle represents the spacelike black-hole singularity and the bottom (past) squiggle represents the white-hole singularity. In the right hand diagram, the straight dashed line labelled by Σ_{iso} represent the initial hypersurface Σ_{t_0} for $t = 0$ in isotropic coordinates. In the left hand diagram, the dashed line labelled by Σ_{pa} represent the initial hypersurface Σ_{t_0} for $t = 0$ in polar-areal coordinates. Notably Σ_{pa} initially touches the physical singularity whereas Σ_{t_0} does not; additionally Σ_{pa} is not a Cauchy surface as there exist causal curves which can intersect it multiple times.

Lapse Slicing Conditions

The simplest lapse choice would be to enforce $\alpha = 1$, called geodesic slicing, with the hypersurface following integral curves of n^μ ; given that geodesics can converge this can lead to hypersurface self-intersection which breaks the definition of a Cauchy surface and the simulation will likely fail. Another problem is that a black-hole singularity can be reached in finite simulation time.

An alternative slicing condition is the maximal slicing condition which keeps the volume element $\sqrt{-g}$ constant along geodesics. This means as $\gamma \rightarrow \infty$ nearing a singularity $\alpha \rightarrow 0$ from Eq. (2.1.70), causing the hypersurface to advance more slowly before a singularity is reached as demonstrated in Fig. (2.3). This property is called singularity avoiding and is crucial for numerical stability unless using excision¹. Maximal slicing can be implemented by forcing $\mathcal{K} = \partial_t \mathcal{K} = 0 \forall t$ which requires a slow elliptic solve for α at each timestep. Instead of performing this slow elliptic solve, α is promoted to an evolution variable and is evolved along with every other simulation variable. To do this we can pick an algebraic slicing condition of the Bona-Massó type,

$$\mathcal{L}_m \alpha = \partial_t \alpha - \beta^i \partial_i \alpha = -\alpha^2 f(\alpha) \mathcal{K}. \quad (2.1.103)$$

¹Excision is the practice of cutting singularities out of the computational domain while supplying suitable boundary conditions about the excised region

Using this with $f = 2\alpha^{-1}$ gives,

$$\mathcal{L}_m \alpha = \partial_t \alpha - \beta^i \partial_i \alpha = -2\alpha \mathcal{K}, \quad (2.1.104)$$

which is called 1+log slicing; this is very common in Numerical Relativity codes. In practice 1+log slicing is strongly singularity avoiding reaching $\alpha = 0$ before the singularity. This is modified in the CCZ4 scheme to,

$$\partial_t \alpha = -2\alpha [\mathcal{K} - 2\Theta] + \beta^i \partial_i \alpha. \quad (2.1.105)$$

Using Gaussian normal coordinates $\beta^i = 0$ and provided $\Theta = 0$, the 1+log slicing condition reduces to,

$$\alpha = 1 + \ln \gamma, \quad (2.1.106)$$

giving the slicing condition it's name [21].

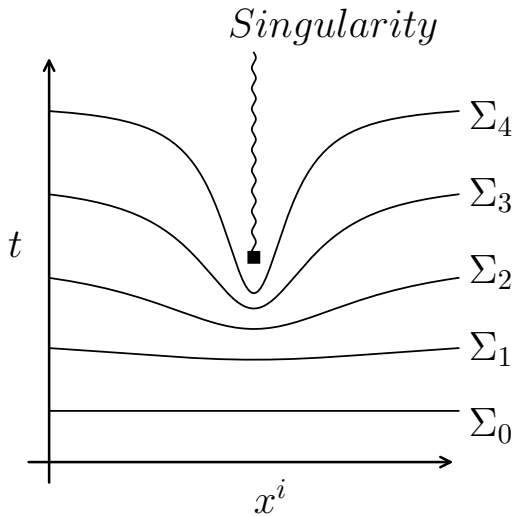


Figure 2.3: Diagram showing the time evolution of a hypersurface using a singularity avoiding slicing condition. The vertical squiggled line represents a physical singularity that is formed at some point in spacetime, potentially from the collapse of matter to a black-hole.

Shift Conditions

The simplest choice for the shift vector would be $\beta^i = 0$ but this can cause great stretching and shearing of integral curves of m^μ in the neighbourhood of a singularity as in Fig. (2.3); the effect of this is that neighbouring gridpoints may have large differences in field values leading to inaccurate and unstable evolutions.

Another negative side effect is that the computational domain can fall inside an event horizon in black-hole simulations. To counteract this we want to employ a shift vector that minimises hypersurface shear σ_{ij} which can be defined as [35],

$$\sigma_{ij} := \perp_i^\mu \perp_j^\nu \left[\nabla_{(\mu} n_{\nu)} - \frac{1}{3} \gamma^{ab} \nabla_{(a} n_{b)} \gamma_{\mu\nu} \right], \quad (2.1.107)$$

where σ_{ij} is tracefree corresponding to shearing rather than inflation or expansion. Minimising the total shear Σ ,

$$\Sigma = \int \sigma_{ij} \sigma^{ij} \sqrt{\gamma} dx^3, \quad (2.1.108)$$

with respect to β^i leads to an elliptic PDE to be solved for each β^i at each time step that minimises shear,

$$\delta\Sigma = 0 \rightarrow \mathcal{D}_i\sigma^{ij} = 0. \quad (2.1.109)$$

This is known as the minimal distortion shift condition. Promoting the β^i to evolution variables is computationally cheaper than solving a set of PDEs at each time step. A very common choice is to promote the elliptic PDE for β^i into a hyperbolic equation via introducing a $\partial_t^2\beta^i$ term and an artificial damping term parameterised by η . This becomes a damped wave equation and is supposed to transport away any part of β^i which does not satisfy $\mathcal{D}_i\sigma^{ij} = 0$. This works well with Sommerfeld (outgoing wave) boundary conditions given in section 3.1.3. The standard Gamma driver shift condition is,

$$\partial_t\beta^i = FB^i, \quad (2.1.110)$$

$$\partial_tB^i = \partial_t\tilde{\Gamma}^i - \eta B^i, \quad (2.1.111)$$

where $F = 3/4$ and $\eta = 1$ are used throughout this work.

Moving Puncture Gauge

The moving puncture gauge (MPG) is the combination of the 1+log slicing lapse condition in Eq. (2.1.104) and the Gamma driver shift condition in Eqs. (2.1.110) and (2.1.111). In 2006, the moving puncture gauge allowed for the first successful simulation of a black-hole binary [36] in the BSSN formalism² without the use of excision. In 2012 the first simulations of black-hole binaries using constraint damping schemes (in the MPG) such as CCZ4 [38] and Z4c [39] were achieved. Although $\chi \rightarrow 0$, or $\gamma \rightarrow \infty$, at the centre of a black hole, as long as a minimum value for χ (such as $\chi = 10^{-4}$) is enforced a simulation can run. Even though it is unphysical to modify a physical variable, the success of the MPG is often attributed to the causal shielding³ provided by the event horizon. Additionally, any extremely sharp field configurations produced will be partially suppressed by a numerical dissipation scheme.

Not only does the MPG safeguard the divergence of fields at the puncture, but it allows the puncture to move; hence the name *moving* puncture gauge. Near the puncture, the lapse α becomes vanishingly small and the 1+log slicing condition in Eq. (2.1.104) becomes,

$$\partial_t\alpha = \beta^i\partial_i\alpha, \quad (2.1.112)$$

which causes the puncture to move. Assigning spatial coordinates $x_{\text{punc}}^i(t)$ to the puncture, we know that

$$\alpha(x_{\text{punc}}^i) = 0, \quad (2.1.113)$$

$$\frac{d}{dt}\alpha(x_{\text{punc}}^i) = \frac{\partial}{\partial t}\alpha + \left(\frac{\partial x^i}{\partial t} \Big|_{x^i=x_{\text{punc}}^i} \right) \frac{\partial}{\partial x^i}\alpha = 0, \quad (2.1.114)$$

which can be compared to Eq. (2.1.112) to show that

$$\beta^i = -\frac{\partial}{\partial t}x_{\text{punc}}^i. \quad (2.1.115)$$

This shows that the puncture must move along integral curves of $-\beta^i$.

²It should be noted that a black-hole binary had been successfully simulated before by [37] in 2003 with co-rotating coordinates and [30] in 2005 using the generalised harmonic gauge.

³Errors that propagate at (or below) light speed will be trapped by the event horizon.

2.2 Mathematical Modelling of Boson Stars

2.2.1 Action and Lagrangian

The Boson Stars considered consist of a complex Klein Gordon Scalar field, φ , minimally coupled to gravity. The action is the Einstein-Hilbert vacuum action plus the matter action for curved space,

$$S = \int_{\mathcal{M}} [\mathcal{L}_{EH} + \mathcal{L}_M] \sqrt{-g} dx^4, \quad (2.2.1)$$

$$\mathcal{L}_{EH} = \frac{c^4}{16\pi G} R, \quad (2.2.2)$$

$$\mathcal{L}_M = -\frac{1}{2} g^{\mu\nu} \nabla_\mu \bar{\varphi} \nabla_\nu \varphi - \frac{1}{2} V(|\varphi|^2), \quad (2.2.3)$$

Here V is the Klein-Gordon potential and its effect on boson stars is discussed in [40] [41]. Some common choices of potentials are,

$$V_{\text{mini}} = \frac{m^2 c^2}{\hbar^2} |\varphi|^2, \quad (2.2.4)$$

$$V_{\text{int}} = \frac{m^2 c^2}{\hbar^2} |\varphi|^2 + \frac{1}{2} \Lambda_4 |\varphi|^4, \quad (2.2.5)$$

$$V_{\text{sol}} = \frac{m^2 c^2}{\hbar^2} |\varphi|^2 \left(1 - \frac{|\varphi|^2}{2\sigma^2}\right)^2, \quad (2.2.6)$$

where \hbar and c are given for completeness but will be set to unity later. Considering only the m^2 term, which corresponds to the squared mass of the particle in the quantum theory, we get a massive wave equation linear in φ , leading to so called *mini* Boson stars. Having $\Lambda_4 \neq 0$ gives *self-interacting* stars which have a nonlinear wave equation corresponding to particle creation and annihilation at the quantum level; self interacting potentials can include higher order terms in φ such as $|\varphi|^6$, $|\varphi|^8$ and more. These self interacting potentials tend to have star solutions with a higher density. Finally, Eq. (2.2.6) describes the *solitonic* potential, giving rise to boson stars with compactness comparable to neutron stars. Solitonic boson stars and their gravitational wave signatures have been studied in [42].

Varying the action with respect to the metric and scalar field return the Einstein field equation and the Klein Gordon equation of curved space respectively,

$$R_{\mu\nu} - \frac{1}{2} R g_{\mu\nu} = \frac{8\pi G}{c^4} T_{\mu\nu}, \quad (2.2.7)$$

$$g^{\mu\nu} \nabla_\mu \nabla_\nu \varphi = \frac{\partial V}{\partial |\varphi|^2} \varphi. \quad (2.2.8)$$

Collectively these are known as the Einstein-Klein-Gordon (EKG) equations. From Eq. (1.4.78), the boson-specific stress energy tensors are,

$$T_{\mu\nu} := -2 \frac{\delta \mathcal{L}_M}{\delta g^{\mu\nu}} + g_{\mu\nu} \mathcal{L}_M, \quad (2.2.9)$$

$$T_{\mu\nu} = \frac{1}{2} \nabla_\mu \bar{\varphi} \nabla_\nu \varphi + \frac{1}{2} \nabla_\nu \bar{\varphi} \nabla_\mu \varphi - \frac{1}{2} g_{\mu\nu} \left[g^{\alpha\beta} \nabla_\alpha \bar{\varphi} \nabla_\beta \varphi + V \right]. \quad (2.2.10)$$

Comparison of Boson Stars to Neutron Stars

Boson stars differ greatly to neutron stars; studying neutron stars requires the fermionic, or ordinary fluid, stress tensor \mathbf{T}_F ;

$$T_F^{\mu\nu} = \left[\rho c^2 + P \right] \frac{u^\mu u^\nu}{c^2} + Pg^{\mu\nu} + 2u^{(\mu} q^{\nu)} + \pi^{\mu\nu} + \dots. \quad (2.2.11)$$

The continuity equation from Eq. (1.4.34), $\nabla_\nu T^{\mu\nu} = 0$, returns the highly nonlinear relativistic Navier-Stokes equations of curved space. The viscosity term $\pi^{\mu\nu}$ and heat flux q^μ are often omitted for simplicity. The remaining variables ρ , P and u^μ are the fluid density, pressure and worldline tangent.

In flat space, the Navier-Stokes equations can develop shockwaves and the use of sophisticated shock capturing schemes is required. In contrast, the flat space Klein-Gordon equation (with the quadratic potential given in Eq. (2.2.4)) is linear and strongly hyperbolic. Moving to curved space, the Klein-Gordon equation (in conjunction with Einstein's equation) can produce divergences in the scalar field φ ; one example is gravitational collapse to a black hole. In practice, boson stars with sensible potential functions are often stable and simple to simulate numerically; for this reason boson stars are a good proxy for compact objects in general relativity.

2.2.2 Solitons

A soliton is a wave packet that exhibits particle-like behaviour. More precisely, in classical field theory, a soliton is a field or set of fields in a localised configuration that travels at constant speed while maintaining its shape. This is a property of solutions to the linear wave equation but many solitonic solutions exist for non-linear differential equations as well. For our purposes, we look for solitons in the Einstein-Klein-Gordon (EKG) system which are self gravitating localised scalar field and metric configurations. In the case of the real scalar field it was shown that there are no long lived solitons [43]; however promoting the field to a complex scalar we can find a spherically symmetric stationary soliton with the following configuration,

$$\varphi = \Phi(r)e^{i\omega t}, \quad (2.2.12)$$

in spherical polar coordinates $x^\mu \in \{t, r, \theta, \phi\}$. Traditionally, the polar areal gauge has been used for the metric's ansatz,

$$g_{\mu\nu}dx^\mu dx^\nu = -a^2(r)dt^2 + b^2(r)dr^2 + r^2[d\theta^2 + \sin^2\theta d\phi^2], \quad (2.2.13)$$

where the boundary condition $b^2(0) = 1$ is demanded to avoid a conical singularity at the origin. However an isotropic gauge is more useful for simulations due to easier conversion to Cartesian space-coordinates, for more information on isotropic coordinates see section 1.4.5. The polar areal solution must then be transformed into an isotropic solution. Alternatively, the approach taken in this report, is to start with an isotropic ansatz,

$$g_{\mu\nu}dx^\mu dx^\nu = -\Omega^2(r)dt^2 + \Psi^2(r)d\mathbf{x}^2, \quad (2.2.14)$$

where $d\mathbf{x}^2$ denotes the euclidean 3D line element; this changes between spherical polar or Cartesian coordinates trivially. This ends up being slightly harder to solve for numerically, but no conversion to isotropic coordinates is needed afterwards. The conformal gauge also lends itself better to constraint solving schemes.

To get a set of ODEs to solve for the functions $\{\Omega(r), \Psi(r), \Phi(r)\}$ we must turn to the Einstein equation and Klein Gordon equation. The Einstein equations for $\{\mu, \nu\} = \{0, 0\}, \{1, 1\}, \{2, 2\}$ are the only components that give unique non-zero equations in spherical symmetry; they are,

$$\frac{\Omega^2[r\Psi'^2 - 2\Psi[r\Psi'' + 2\Psi']]}{r\Psi^4} = 4\pi G \left[\Omega^2 \left[\frac{\Phi'^2}{\Psi^2} + V \right] + \omega^2 \Phi^2 \right], \quad (2.2.15)$$

$$\frac{2\Psi\Psi' [r\Omega' + \Omega] + r\Omega\Psi'^2 + 2\Psi^2\Omega'}{r\Psi^2\Omega} = 4\pi G \left[\Phi'^2 - \Psi^2V + \frac{\omega^2\Phi^2\Psi^2}{\Omega^2} \right], \quad (2.2.16)$$

$$r \left[-\frac{r\Psi'^2}{\Psi^2} + \frac{r\Psi'' + \Psi'}{\Psi} + \frac{r\Omega'' + \Omega'}{\Omega} \right] = -4\pi Gr^2\Psi^2 \left[\frac{\Phi'^2}{\Psi^2} + V - \frac{\omega^2\Phi^2}{\Omega^2} \right], \quad (2.2.17)$$

where the Einstein tensor $G_{\mu\nu} = R_{\mu\nu} - \frac{1}{2}Rg_{\mu\nu}$ and the stress tensor $T_{\mu\nu}$ are on the left and right respectively. Substituting the metric ansatz Eq. (2.2.14) and the field ansatz Eq. (2.2.12) into Eq. (2.2.8),

the Klein Gordon equation becomes,

$$g^{\mu\nu}\nabla_\mu\nabla_\nu\varphi = \frac{\partial V}{\partial|\varphi|^2}\varphi, \quad (2.2.18)$$

$$\frac{1}{\sqrt{-g}}\partial_\mu\left[\sqrt{-g}g^{\mu\nu}\partial_\nu\Phi(r)e^{i\omega t}\right] = \frac{\partial V}{\partial|\varphi|^2}\Phi(r)e^{i\omega t}, \quad (2.2.19)$$

$$\Phi'' = \Phi\Psi^2\left[V' - \frac{\omega^2}{\Omega^2}\right] - \Phi'\left[\frac{\Omega'}{\Omega} + \frac{\Psi'}{\Psi} + \frac{2}{r}\right]. \quad (2.2.20)$$

Simplifying the Einstein Equations and combining with the Klein Gordon equation we get three ODES to solve; the EKG system has been reduced to two second order ODES and a first order ODE,

$$\Omega' = \frac{\Omega}{r\Psi' + \Psi}\left[2\pi Gr\Psi\left[\Phi'^2 - \Psi^2V + \frac{\omega^2\Phi^2\Psi^2}{\Omega^2}\right] - \Psi' - \frac{r\Psi'^2}{2\Psi}\right], \quad (2.2.21)$$

$$\Psi'' = \frac{\Psi'^2}{2\Psi} - \frac{2\Psi'}{r} - 2\pi G\left[V\Psi^3 + \Phi'^2\Psi + \frac{\omega^2\Phi^2\Psi^3}{\Omega^2}\right], \quad (2.2.22)$$

$$\Phi'' = \Phi\Psi^2\left[V' - \frac{\omega^2}{\Omega^2}\right] - \Phi'\left[\frac{\Omega'}{\Omega} + \frac{\Psi'}{\Psi} + \frac{2}{r}\right]. \quad (2.2.23)$$

This is turned into a set of five first order ODES to numerically integrate from $r = 0$ out to large radius. Note that if we had used the polar areal ansatz in Eq. (2.2.13) the equation for Φ would also be first order; reducing the EKG system to four first order ODES.

2.2.3 3+1 Klein Gordon System

Now let us project the Klein Gordon equation in a 3+1 split to get the evolution equations. The first step is to turn the second order Klein-Gordon equation into two first order differential equations (in time),

$$\partial_t\varphi = \dots \quad \text{and} \quad \partial_t\Pi = \dots, \quad (2.2.24)$$

where Π is the foliation dependant definition of conjugate momentum to the complex scalar field defined by,

$$\Pi := -\mathcal{L}_n\varphi. \quad (2.2.25)$$

Above, \mathbf{n} is the unit normal vector to Σ_t . Decomposing the Klein Gordon Equation gives,

$$\nabla^\mu\nabla_\mu\varphi = V'\varphi = \frac{1}{\sqrt{-g}}\partial_\mu\left[\sqrt{-g}\left[\gamma^{\mu\nu} - n^\mu n^\nu\right]\partial_\nu\varphi\right] = \frac{1}{\sqrt{-g}}\partial_\mu\left[\sqrt{-g}\left[\mathcal{D}^\mu\varphi - n^\mu\mathcal{L}_n\varphi\right]\right]. \quad (2.2.26)$$

The term with \mathcal{D}^μ simplifies like,

$$\frac{1}{\sqrt{-g}}\partial_\mu\left[\sqrt{-g}\mathcal{D}^\mu\varphi\right] = \frac{1}{\alpha\sqrt{\gamma}}\partial_\mu\left[\alpha\sqrt{\gamma}\mathcal{D}^\mu\varphi\right] = \mathcal{D}_\mu\mathcal{D}^\mu\varphi + \mathcal{D}^\mu\varphi\frac{1}{\alpha}\partial_\mu\alpha, \quad (2.2.27)$$

and the remainder becomes

$$-\frac{1}{\sqrt{-g}}\partial_\mu\left[\sqrt{-g}n^\mu\mathcal{L}_n\varphi\right] = \nabla_\mu(n^\mu\Pi) = -\mathcal{K}\Pi + \mathcal{L}_n\Pi. \quad (2.2.28)$$

Combining these results, the Klein Gordon equation becomes,

$$\mathcal{L}_m\Pi = -\mathcal{D}^\mu\varphi\partial_\mu\alpha + \alpha\left[\mathcal{K}\Pi - \mathcal{D}_\mu\mathcal{D}^\mu\varphi + V'\varphi\right], \quad (2.2.29)$$

$$\mathcal{L}_m\varphi = -\alpha\Pi. \quad (2.2.30)$$

where $\mathcal{L}_m = \alpha \mathcal{L}_n$ for a scalar field. Using the CCZ4 formalism (covered in section 2.1.9), the equations of motion for the scalar field are

$$\partial_t \varphi = \beta^k \partial_k \varphi - \alpha \Pi, \quad (2.2.31)$$

$$\partial_t \Pi = \beta^k \partial_k \Pi - \chi \tilde{\gamma}^{ij} \partial_i \varphi \partial_j \alpha + \alpha \left[\chi \tilde{\Gamma}^k \partial_k \varphi + \frac{1}{2} \tilde{\gamma}^{lk} \partial_k \chi \partial_l \varphi - \chi \tilde{\gamma}^{ij} \partial_i \partial_j \varphi + \mathcal{K} \Pi + V' \varphi \right]. \quad (2.2.32)$$

The final matter term we must decompose is the Klein-Gordon stress tensor in Eq. (2.2.10) with Eqs. (2.1.45), (2.1.46) and (2.1.47).

$$\rho = n^\mu n^\nu T_{\mu\nu} = \frac{1}{2} |\Pi|^2 + \frac{1}{2} \gamma^{ij} \mathcal{D}_i \bar{\varphi} \mathcal{D}_j \varphi + \frac{1}{2} V(|\varphi|^2), \quad (2.2.33)$$

$$S_i = - \perp_i^\mu n^\nu T_{\mu\nu} = \frac{1}{2} [\bar{\Pi} \mathcal{D}_i \varphi + \Pi \mathcal{D}_i \bar{\varphi}], \quad (2.2.34)$$

$$S_{ij} = \perp_i^\mu \perp_j^\nu T_{\mu\nu} = \mathcal{D}_{(i} \varphi \mathcal{D}_{j)} \bar{\varphi} - \frac{1}{2} [\gamma^{ij} \mathcal{D}_i \varphi \mathcal{D}_j \bar{\varphi} - |\Pi|^2 + V(|\varphi|^2)]. \quad (2.2.35)$$

2.2.4 Klein Gordon's Noether Charge

The complex scalar field has a conserved quantity called the Noether charge. The Noether charge represents the number of particles minus the number of antiparticles described by the field theory. In a numerical simulation a conserved quantity can be used to check the quality of a simulation as with good resolution the total charge should be conserved.

The Noether charge of the complex scalar field is associated with the following U(1) symmetry,

$$\varphi \rightarrow \varphi e^{i\epsilon} \approx \varphi + i\epsilon \varphi, \quad (2.2.36)$$

$$\bar{\varphi} \rightarrow \bar{\varphi} e^{-i\epsilon} \approx \bar{\varphi} - i\epsilon \bar{\varphi}, \quad (2.2.37)$$

which leaves the Lagrangian unchanged and therefore the total action. The associated conserved current \mathbf{j} is then,

$$j^\mu = \frac{\delta \mathcal{L}}{\delta \nabla_\mu \varphi} \delta \varphi + \frac{\delta \mathcal{L}}{\delta \nabla_\mu \bar{\varphi}} \delta \bar{\varphi}, \quad (2.2.38)$$

$$= ig^{\mu\nu} [\varphi \nabla_\nu \bar{\varphi} - \bar{\varphi} \nabla_\nu \varphi], \quad (2.2.39)$$

where the current satisfies the conservation equation,

$$\nabla_\mu j^\mu = 0. \quad (2.2.40)$$

Using Eq. (1.3.141), the conservation equation can be re-written as,

$$\nabla_\mu j^\mu = \frac{1}{\sqrt{-g}} \partial_\mu (\sqrt{-g} j^\mu) = \frac{1}{\sqrt{-g}} \partial_\mu \mathcal{J}^\mu = 0, \quad (2.2.41)$$

where $\mathcal{J}^\mu = \sqrt{-g} j^\mu$ is the current expressed as a tensor density. Therefore,

$$\partial_\mu \mathcal{J}^\mu = 0, \quad (2.2.42)$$

is also true and even in curved space the current \mathcal{J} obeys a conservation equation; this means there must be some conserved charge \mathcal{Q} associated with the current. Integrating Eq. (2.2.42) over a manifold \mathcal{M} gives,

$$\int_{\mathcal{M}} \partial_\mu \mathcal{J}^\mu dx^4 = 0, \quad (2.2.43)$$

$$\int_{t_0}^{t_1} \left[\int_{\Sigma_t} \partial_0 \mathcal{J}^0 dx^3 \right] dt = - \int_{t_0}^{t_1} \left[\int_{\Sigma_t} \partial_i \mathcal{J}^i dx^3 \right] dt, \quad (2.2.44)$$

$$\int_{t_0}^{t_1} \left[\int_{\Sigma_t} \partial_0 \mathcal{J}^0 dx^3 \right] dt = - \int_{t_0}^{t_1} \left[\int_{\partial \Sigma_t} \hat{s}_i \mathcal{J}^i dx^2 \right] dt, \quad (2.2.45)$$

$$\int_{t_0}^{t_1} \left[\int_{\Sigma_t} \partial_0 \mathcal{J}^0 dx^3 \right] dt = 0, \quad (2.2.46)$$

where the flat space divergence theorem was used and $\hat{\mathbf{s}}$ is the flat space normal to $\partial\Sigma_t$, the boundary of Σ_t . The term containing $\hat{s}_i \mathcal{J}^i$ integrates to zero over $\partial\Sigma_t$ due to \mathcal{J} vanishing on $\partial\Sigma_t$. The \mathcal{J}^0 term can be simplified by permuting the time derivative using,

$$\partial_0 \int_{\Sigma_t} \mathcal{J}^0 dx^3 = \int_{\Sigma_t} \partial_0 \mathcal{J}^0 dx^3 + \lim_{\Delta x^0 \rightarrow 0} \left[\frac{1}{\Delta x^0} \int_{\Delta\Sigma_t} [\mathcal{J}^0 + \Delta x^0 \partial_0 \mathcal{J}^0] dx^3 \right], \quad (2.2.47)$$

where the last term vanishes as \mathcal{J} vanishes on $\Delta\Sigma_t$ near $\partial\Sigma$, and Eq. (2.2.46) becomes,

$$\int_{t_0}^{t_1} \left[\partial_0 \int_{\Sigma_t} \mathcal{J}^0 dx^3 \right] dt = 0, \quad (2.2.48)$$

and the formula for the conserved charge Q can be read off as,

$$\partial_0 Q = 0, \quad (2.2.49)$$

$$Q = \int_{\Sigma_t} \mathcal{J}^0 dx^3. \quad (2.2.50)$$

The charge density \mathcal{Q} is defined as,

$$Q := \int_{\Sigma_t} \mathcal{Q} \sqrt{\gamma} dx^3, \quad (2.2.51)$$

$$\mathcal{Q} = \frac{\mathcal{J}^0}{\sqrt{\gamma}} = \frac{\sqrt{-g} j^0}{\sqrt{\gamma}} = \alpha j^0, \quad (2.2.52)$$

where Eq. (2.1.70), saying $\sqrt{-g} = \alpha \sqrt{\gamma}$, was used. Finally we get an expression for the total Noether charge $N = Q$,

$$N = i \int_{\Sigma_t} \sqrt{-g} [\varphi \nabla^0 \bar{\varphi} - \bar{\varphi} \nabla^0 \varphi] dx^3. \quad (2.2.53)$$

Using $\sqrt{-g} = \alpha \sqrt{\gamma}$ again and $\alpha \nabla^0 \varphi = -n_\mu \nabla^\mu \varphi = \Pi$ from Eq. (2.2.25) we get the following neat formula,

$$N = i \int_{\Sigma_t} [\varphi \bar{\Pi} - \bar{\varphi} \Pi] \sqrt{\gamma} dx^3. \quad (2.2.54)$$

Equivalently, the Noether charge density \mathcal{N} is ,

$$\mathcal{N} = i (\varphi \bar{\Pi} - \bar{\varphi} \Pi). \quad (2.2.55)$$

The ideas of this section concerning conserved charges are extended in chapter 5 with applications to continuity equations in energy, momentum, angular momentum and Noether charges for spin-1 Proca fields. The results of this section have all been derived for an infinite volume where only a charge density \mathcal{Q} needs be considered. Chapter 5 considers continuity equations in a finite volume V so must also consider the flux density \mathcal{F} of conserved particles through ∂V (the boundary of V) and the source density \mathcal{S} (creation and destruction of \mathcal{Q}) in V .

2.2.5 Boosted Boson Stars and Black Holes

Let us now consider a moving star, this corresponds to boosting a stationary soliton solution. There is no unique way of doing this as any coordinate transformation that reduces to a Minkowski spacetime boost at large radius is valid. All the degrees of freedom we have can be absorbed into a coordinate gauge choice so it makes sense to choose the trivial, constant valued boost, with rapidity $\chi = \text{arctanh}(v)$ for a velocity v , from Special Relativity. Using Cartesian coordinates, the boost matrix Λ for a boost in the x direction is,

$$\Lambda_\nu^\mu = \exp \begin{pmatrix} 0 & -\chi & 0 & 0 \\ -\chi & 0 & 0 & 0 \\ 0 & 0 & 1 & 0 \\ 0 & 0 & 0 & 1 \end{pmatrix} = \begin{pmatrix} \cosh(\chi) & -\sinh(\chi) & 0 & 0 \\ -\sinh(\chi) & \cosh(\chi) & 0 & 0 \\ 0 & 0 & 1 & 0 \\ 0 & 0 & 0 & 1 \end{pmatrix}, \quad (2.2.56)$$

as discussed in section 1.4.1. Declaring the boosted frame and lab frame (in which the star is moving with a positive speed v) to have coordinates x^μ and \tilde{x}^μ ,

$$\tilde{x}^\mu = [\Lambda^{-1}]^\mu_\nu x^\nu, \quad (2.2.57)$$

where both x^μ and \tilde{x}^μ agree on an origin. The inverse of the boost matrix Λ^{-1} can be found simply by $\Lambda^{-1}(\chi) = \Lambda(-\chi)$ which is equivalent to a boost in the opposite direction. Explicitly, the coordinates transform as,

$$t = \tilde{t} \cosh(\chi) - \tilde{x} \sinh(\chi), \quad (2.2.58)$$

$$x = \tilde{x} \cosh(\chi) - \tilde{t} \sinh(\chi), \quad (2.2.59)$$

$$y = \tilde{y}, \quad (2.2.60)$$

$$z = \tilde{z}. \quad (2.2.61)$$

The metric transforms via the tensor transformation law,

$$\tilde{g}_{\mu\nu}(\tilde{x}^\sigma) = \frac{\partial x^\alpha}{\partial \tilde{x}^\mu} \frac{\partial x^\beta}{\partial \tilde{x}^\nu} g_{\alpha\beta}(x^\sigma) = \Lambda^\alpha_\mu \Lambda^\beta_\nu g_{\alpha\beta}(\tilde{x}^\sigma), \quad (2.2.62)$$

and the metric in the boosted frame and lab frame are,

$$g_{\mu\nu} = \text{diag}\{-\Omega^2, \Psi^2, \Psi^2, \Psi^2\}, \quad (2.2.63)$$

$$\tilde{g}_{\mu\nu} = \begin{pmatrix} -\Omega^2 \cosh^2(\chi) + \Psi^2 \sinh^2(\chi) & \sinh(\chi) \cosh(\chi) [\Omega^2 - \Psi^2] & 0 & 0 \\ \sinh(\chi) \cosh(\chi) [\Omega^2 - \Psi^2] & \Psi^2 \cosh^2(\chi) - \Omega^2 \sinh^2(\chi) & 0 & 0 \\ 0 & 0 & \Psi^2 & 0 \\ 0 & 0 & 0 & \Psi^2 \end{pmatrix}, \quad (2.2.64)$$

respectively. Comparing the boosted metric \tilde{g} to the $3+1$ decomposed metric in Eq. (2.1.67) we can read off the shift vector $\tilde{\beta}_i$, the 3-metric $\tilde{\gamma}_{ij}$ and obtain the lapse and metric determinant,

$$\tilde{\alpha}^2 = \frac{\Psi^2 \Omega^2}{\Psi^2 \cosh^2(\chi) - \Omega^2 \sinh^2(\chi)}, \quad (2.2.65)$$

$$\tilde{\gamma} = \det \tilde{\gamma}_{ij} = \Psi^4 [\Psi^2 \cosh^2(\chi) - \Omega^2 \sinh^2(\chi)]. \quad (2.2.66)$$

The conformal 3-metric, with unit determinant is,

$$\bar{\gamma}_{ij} = \tilde{\gamma}^{-\frac{1}{3}} \begin{pmatrix} \Psi^2 \cosh^2(\chi) - \Omega^2 \sinh^2(\chi) & 0 & 0 \\ 0 & \Psi^2 & 0 \\ 0 & 0 & \Psi^2 \end{pmatrix}, \quad (2.2.67)$$

where normally $\tilde{\gamma}_{ij}$ is the conformal 3-metric, but to avoid confusion it is denoted $\bar{\gamma}_{ij}$ in this section.

Turning our attention to the matter fields now we only need to change the coordinate dependence, like $\varphi(x) \rightarrow \varphi(\tilde{x})$, given that φ and Π are (complex) scalar fields. Given that $\tilde{t} = 0$ describes a time slice in the lab frame (where the star has non-zero velocity), $t = \tilde{x} \sinh(\chi)$ in the rest frame and we get the following boosted complex scalar field,

$$\varphi = \Phi(r) e^{i\omega \tilde{x} \sinh(\chi)}, \quad (2.2.68)$$

where r is the radius in the boosted frame; $r = \sqrt{\tilde{x}^2 \cosh^2(\chi) + \tilde{y}^2 + \tilde{z}^2}$. Note the field is modulated by an oscillatory phase now with wavenumber $k = \omega \tilde{x} \sinh(\chi)$; nodal planes in $\text{Re}(\varphi)$ appear perpendicular to velocity. The conjugate momentum $\tilde{\Pi}$, defined in Eq. (2.2.25), in the rest frame it becomes,

$$\tilde{\Pi}(\tilde{x}^\mu) = -\mathcal{L}_{\tilde{n}} \varphi(\tilde{x}^\mu) = -\frac{1}{\tilde{\alpha}} \tilde{m} \cdot \tilde{\partial} \varphi = -\frac{1}{\tilde{\alpha}} [\tilde{\partial}_t - \tilde{\beta}^i \tilde{\partial}_i] \Phi(r) e^{i\omega t}. \quad (2.2.69)$$

Inconveniently we can not simply evaluate $\tilde{\Pi}$ in the lab frame from Π in the co-moving frame as the two frames have a different spacetime foliation and the normal vector as $\mathbf{n} \neq \tilde{\mathbf{n}}$ and is genuinely changed; not just transforming components under coordinate transformation. Explicitly writing the contra-variant components of the shift vector,

$$\tilde{\beta}^i = \left(\frac{\sinh(\chi) \cosh(\chi) [\Omega^2 - \Psi^2]}{\Psi^2 \cosh^2(\chi) - \Omega^2 \sinh^2(\chi)}, 0, 0 \right), \quad (2.2.70)$$

and using the following derivative formulae,

$$\partial_{\tilde{t}} = \cosh(\chi) \partial_t - \sinh(\chi) \partial_x, \quad (2.2.71)$$

$$\partial_{\tilde{x}} = \cosh(\chi) \partial_x - \sinh(\chi) \partial_t, \quad (2.2.72)$$

$$\partial_t \varphi = \Phi \partial_t e^{i\omega t} = i\omega \Phi e^{i\omega t}, \quad (2.2.73)$$

$$\partial_x \varphi = \frac{\partial r}{\partial x} \frac{\partial \Phi}{\partial r} e^{i\omega t} = \frac{x}{r} \Phi' e^{i\omega t}, \quad (2.2.74)$$

we get an expression for the conjugate momentum of a boosted star. Setting $\tilde{t} = 0$ gives the conjugate momentum on the surface $\tilde{t} = 0$ to be used as initial conditions in the lab frame,

$$\tilde{\Pi} = -\frac{1}{\tilde{\alpha}} \left[i\omega \Phi \left(\cosh(\chi) + \tilde{\beta}^{\tilde{x}} \sinh(\chi) \right) - \frac{\tilde{x} \cosh(\chi)}{r} \Phi' \left(\sinh(\chi) + \tilde{\beta}^{\tilde{x}} \cosh(\chi) \right) \right] e^{i\omega \tilde{x} \sinh(\chi)}. \quad (2.2.75)$$

The penultimate ingredient is the intrinsic curvature $\tilde{\mathcal{K}}$, defined in Eq. (2.1.10). Similarly to the conjugate momentum, the definition of $\tilde{\mathcal{K}}$ depends on the spacetime foliation so using $\mathcal{K}_{ij} = 0$ in the stars rest frame and using the tensor transformation to conclude that $\tilde{\mathcal{K}}_{ij} = 0$ in the lab frame is incorrect. Instead the components $\tilde{\mathcal{K}}_{ij}$ must be calculated from scratch with the correct normal vector \mathbf{n} as follows,

$$\tilde{\mathcal{K}}_{\mu\nu} := -\frac{1}{2} \mathcal{L}_{\tilde{n}} \tilde{\gamma}_{\mu\nu} = -\frac{1}{2\tilde{\alpha}} \mathcal{L}_{\tilde{m}} \tilde{\gamma}_{\mu\nu} = -\frac{1}{2\tilde{\alpha}} \left[\tilde{m} \cdot \tilde{\partial} \tilde{\gamma}_{\mu\nu} + \tilde{\gamma}_{\mu\rho} \tilde{\partial}_\nu \tilde{m}^\rho + \tilde{\gamma}_{\nu\rho} \tilde{\partial}_\mu \tilde{m}^\rho \right]. \quad (2.2.76)$$

The explicit form for the components of $\tilde{\mathcal{K}}_{ij}$ are

$$\tilde{\mathcal{K}}_{xx} = \tilde{\alpha} \cosh^2(\chi) \sinh(\chi) \frac{x}{r} \frac{[2\Psi^2 \Omega' - \tanh^2(\chi) \Omega^2 \Omega' - \Psi \Omega \Psi']}{\Psi^2 \Omega}, \quad (2.2.77)$$

$$\tilde{\mathcal{K}}_{xy} = \tilde{\alpha} \sinh(\chi) \cosh(\chi) \frac{y}{r} \frac{[\Omega' \Psi - \Psi' \Omega]}{\Psi \Omega}, \quad (2.2.78)$$

$$\tilde{\mathcal{K}}_{xz} = \tilde{\alpha} \sinh(\chi) \cosh(\chi) \frac{z}{r} \frac{[\Omega' \Psi - \Psi' \Omega]}{\Psi \Omega}, \quad (2.2.79)$$

$$\tilde{\mathcal{K}}_{yy} = \tilde{\alpha} \sinh(\chi) \frac{x}{r} \frac{\Psi'}{\Psi}, \quad (2.2.80)$$

$$\tilde{\mathcal{K}}_{yz} = 0, \quad (2.2.81)$$

$$\tilde{\mathcal{K}}_{zz} = \tilde{\mathcal{K}}_{yy}, \quad (2.2.82)$$

where the $\{x, y, z\}$ need to be expanded in terms of $\{\tilde{x}, \tilde{y}, \tilde{z}\}$ and $r = \sqrt{x^2 + y^2 + z^2}$.

The final object needed is the three-dimensional connection symbols Υ^i_{jk} , these are calculated numerically after the initial data is loaded in using the definition from Eq. (1.3.77),

$$\Upsilon^i_{jk} = \frac{1}{2} \gamma^{im} (\partial_k \gamma_{jm} + \partial_j \gamma_{mk} - \partial_m \gamma_{jk}). \quad (2.2.83)$$

The boost formalism described here can be applied to a black-hole spacetime by setting,

$$\varphi = 0, \quad (2.2.84)$$

$$\Pi = 0, \quad (2.2.85)$$

$$\Omega = \frac{1 - \frac{M}{2r}}{1 + \frac{M}{2r}}, \quad (2.2.86)$$

$$\Psi = \left[1 + \frac{M}{2r} \right]^2, \quad (2.2.87)$$

corresponding to the isotropic Schwarzschild black hole given in section 1.4.5.

Chapter 3

Numerical Methods and GRChombo

3.1 Numerical Methods

3.1.1 Introduction to Numerical Methods

In classical physics it is common for a system to be described by the solution of a differential equation (or a set of differential equations) subjected to suitable boundary conditions. There exist many cases, where the system is sufficiently simple, in which the differential equation(s) can be solved analytically; some well known examples include Newton's equation of gravity for orbits, the Schrödinger equation for certain potentials (such as the infinite square well and the quadratic potential) and Maxwell's equations for electromagnetic fields.

In four space-time dimensions, general relativity is a set of ten coupled non-linear differential equations. The complexity of general relativity means that analytic solutions are usually restricted to spacetimes with symmetries or simplifying assumptions. Some common examples are single eternal black hole solutions, cosmological solutions for a uniform universe and the flat Minkowski space. In the case of colliding compact objects (such as black holes, neutron stars or boson stars) there is no analytic solution and numerical methods are the only way to solve the differential equations governing the system.

The rest of section 3.1 introduces the reader to the basic concepts in numerical methods such as discretisation, boundary conditions and time evolution. Section 3.2.1 describes GRCHOMBO, the numerical relativity code used throughout this thesis, and is loosely based on the collaboration paper [1]. From section 3.2.2 onward, the rest of the chapter covers the numerical creation of known boson star initial data for use in simulations; the solution is found directly in the isotropic gauge rather than the polar areal gauge used in the literature [40, 41]. Finally numerical simulations of a head-on and grazing boson star collision are presented in Section 3.2.6.

3.1.2 Numerical Discretisation of Spacetime

There are many ways to time evolve a field theory on a spatial surface. Some popular numerical methods include spectral methods, finite element models and finite volume methods. The method used throughout this work is the finite difference framework. This models a continuous spacetime with a discrete lattice of points; usually this lattice is cubic or cuboidal. A field $\phi(x^\mu)$ on a manifold \mathcal{M} is expressed as a set of discrete values ϕ_{ijk}^n , for integer $\{n, i, j, k\}$, on a set of discrete lattice points with coordinates $(x_{ijk}^n)^\mu$. In uniform Cartesian coordinates $(x_{ijk}^n)^\mu = \{n\Delta t, i\Delta x, j\Delta y, k\Delta z\}$ where Δt , Δx , Δy and Δz represent the grid spacing. In the limit that the grid spacing tends to zero, the lattice and discretised fields should converge to the continuum solution. For a detailed introduction to numerical methods the reader is directed to [44].

To calculate gradients on a lattice, we can consider a two dimensional manifold spanned by coordinates $\{t, x\}$. We can no longer employ the traditional definition of df/dx ,

$$\frac{df}{dx} := \lim_{\delta x \rightarrow 0} \left(\frac{f(x + \delta x) - f(x)}{\delta x} \right), \quad (3.1.1)$$

as there no longer exist two points x and $x + \delta x$ that are infinitesimally close to each other. Derivatives are now approximately calculated by comparing gridpoints a finite distance from each other. To elucidate this idea, a formula for the second derivative is calculated. First we pick five lattice points, equally spaced by Δx , with coordinates $\{x_{-2}, x_{-1}, x_0, x_1, x_2\}$, and writing $f(x_i) = f_i$. Then using the well known formula for the Taylor expansion of a function about a point x_0 ,

$$f(x) = f(x_0) + (x - x_0)f'(x_0) + \frac{(x - x_0)^2}{2!}f''(x_0) + \frac{(x - x_0)^3}{3!}f'''(x_0) + \dots, \quad (3.1.2)$$

we can write,

$$f_2 \approx f_0 + 2\Delta x f'_0 + 2(\Delta x)^2 f''_0 + \frac{4}{3}(\Delta x)^3 f'''_0 + \frac{2}{3}(\Delta x)^4 f''''_0, \quad (3.1.3)$$

$$f_1 \approx f_0 + \Delta x f'_0 + \frac{1}{2}(\Delta x)^2 f''_0 + \frac{1}{6}(\Delta x)^3 f'''_0 + \frac{1}{24}(\Delta x)^4 f''''_0, \quad (3.1.4)$$

$$f_0 \approx f_0, \quad (3.1.5)$$

$$f_{-1} \approx f_0 - \Delta x f'_0 + \frac{1}{2}(\Delta x)^2 f''_0 - \frac{1}{6}(\Delta x)^3 f'''_0 + \frac{1}{24}(\Delta x)^4 f''''_0, \quad (3.1.6)$$

$$f_{-2} \approx f_0 - 2\Delta x f'_0 + 2(\Delta x)^2 f''_0 - \frac{4}{3}(\Delta x)^3 f'''_0 + \frac{2}{3}(\Delta x)^4 f''''_0, \quad (3.1.7)$$

where the Taylor expansions are truncated at terms of order $(\Delta x)^4$. The equations above can be inverted to give,

$$\left. \frac{d^2 f}{dx^2} \right|_{x_0} := f''_0 = \frac{-f_2 + 16f_1 - 30f_0 + 16f_{-1} - f_{-2}}{12(\Delta x)^2} + \mathcal{O}(\Delta x^4). \quad (3.1.8)$$

An approximation for the second derivative using a discrete sum of neighbouring points, also called a stencil, has been obtained. Adding terms of order $(\Delta x)^5$ in the Taylor expansion for f_i would not affect the result as the pairs of terms $\{f_2, f_{-2}\}$ and $\{f_1, f_{-1}\}$ appear in equal amounts; therefore Eq. (3.1.8) is correct up to a Taylor expansion of order $(\Delta x)^6$. Given that f''_0 appears with a $(\Delta x)^2$ and Eq. (3.1.8) is correct until terms of order $(\Delta x)^6$, then the expression is accurate up to fourth order. Any other derivative to any order accuracy (in any dimension) can be calculated in a similar fashion. In the limit that the grid spacing $\Delta x \rightarrow 0$ the approximations for the derivatives approach the exact continuum limit while higher order accurate stencils approach the continuum limit more quickly.

3.1.3 Boundary Conditions

Another artefact of evolving field equations over a volume on a computer is that the volume must have finite size; a computer does not have infinite memory to store an infinite amount of gridpoints. The usual way to deal with this problem is to enforce an algebraic condition on the fields on a surface surrounding the region of interest. Alternatively, an infinite volume can be modelled if coordinates are used which compactify the volume to some finite region, this corresponds to the grid spacing Δx diverging or resolution becoming infinitely low towards the boundary.

Common boundary conditions include Dirichlet (fixed value), Von-Neumann (fixed derivative) or some mix of these conditions. It is common to re-categorise boundary conditions into sub-categories with informative names such as reflective, periodic or symmetric.

As an example in one spatial dimension, symmetric boundary conditions for a field ϕ about a point x_n could be implemented by creating extra *ghost cells* beyond the desired simulation domain with coordinates $\{x_{n+1}, x_{n+2}, x_{n+3}, \dots\}$ and setting,

$$\phi_{n+1} = \pm\phi_{n-1}, \quad \phi_{n+2} = \pm\phi_{n-2}, \quad \phi_{n+3} = \pm\phi_{n-3}, \quad \dots, \quad (3.1.9)$$

where the + or - sign is taken for even or odd parity variables and $\phi_i = \phi(x_i) = \phi(i * \Delta x)$. These extra ghost cells allow the calculation of derivatives at x_n using stencils, as shown in section 3.1.2; without these ghost cells the stencil would not be able to access points x_m where $m > n$. The number of ghost cells should be chosen to be the minimum required to allow the calculation of derivative stencils at each point in the simulation domain. The desired location of the boundary condition does not have to coincide with a gridpoint. As an example, modifying the symmetric boundary condition to be centred on $x_n + \Delta x/2$ instead results in,

$$\phi_{n+1} = \pm\phi_n, \quad \phi_{n+2} = \pm\phi_{n-1}, \quad \phi_{n+3} = \pm\phi_{n-2}, \quad \dots. \quad (3.1.10)$$

Generic boundary conditions can be imposed by assigning values to ghost cells similarly to above. Although the examples given in this section are in one dimension, the ideas generalise to arbitrary dimensions.

Sommerfeld Boundary Conditions

A very useful type of boundary condition is the Sommerfeld boundary condition [45], used to approximate an outgoing wave being transmitted through the boundary condition. Sommerfeld boundary conditions can be derived from studying the solution to the wave equation in spherical symmetry in flat space,

$$-\frac{1}{v^2} \partial_t^2 \Psi + \gamma^{ij} \mathcal{D}_i \mathcal{D}_j \Psi = -\frac{1}{v^2} \partial_t^2 \Psi + \frac{1}{\sqrt{-\gamma}} \partial_i (\sqrt{\gamma} \gamma^{ij} \partial_j \Psi) = -\partial_t^2 \Psi + \frac{1}{r^2} \partial_r (r^2 \partial_r \Psi) = 0, \quad (3.1.11)$$

for some field Ψ with wavespeed v . In spherical polar coordinates, $\gamma^{ij} = \text{diag}\{1, r^{-2}, r^{-2} \text{cosec}^2(\theta)\}$, and Eq. (3.1.11) has an outgoing wave solution,

$$\Psi(r, t) = \Psi_\infty + \frac{A}{r} \psi(r - vt), \quad (3.1.12)$$

for an asymptotic value Ψ_∞ and arbitrary constant A . In differential form this can be written as,

$$\frac{1}{v} \partial_t \Psi + \partial_r \Psi + \frac{1}{r} (\Psi - \Psi_\infty) = 0. \quad (3.1.13)$$

The equation of motion for Ψ can be used to write ∂_t in terms of spatial derivatives and field values giving the new boundary condition which can be applied numerically as a regular mixed type boundary condition. Typically one-sided stencils are needed to avoid sampling non-existent gridpoints.

In general relativity, Sommerfeld boundary conditions are commonly used with $v = c = 1$ (the speed of light) to avoid reflections of matter and gravitational waves from the boundary of a simulation. It should be noted that Sommerfeld boundary conditions are approximate in general relativity for a number of reasons.

- Sommerfeld boundary conditions are derived in spherical symmetry and flat space; spacetimes often asymptote to spherically symmetric flat space, but this is only approximately true for finite radii.
- Matter doesn't always obey a wave equation or propagate at the speed of light.
- Gravitational waves only obey a linear wave equation under special circumstances such as small amplitude waves in flat space; again this problem is alleviated at large radius in an asymptotically flat space.

It has been found experimentally in my work that ensuring the boundary conditions are sufficiently far away from any compact objects is very important in maintaining accuracy of the simulation when using Sommerfeld boundary conditions.

3.1.4 The Method of Lines

Assuming adequate boundary conditions are in place, the time evolution of initial data ϕ_{ijk}^n covering a spacelike computational grid can be done by applying a time integration scheme to the PDE governing the field $\phi(x^\mu)$. There are many ways to do this and the reader is directed to [44] for a comprehensive introduction. A common method is the method of lines (MoL).

The MoL reduces the dimensionality of the PDE problem to a set of ODEs in time at each gridpoint (with coordinate \mathbf{x}_{ijk}). Spatial derivatives are treated as a function on each gridpoint; their evaluation is done using the derivative stencils described in section 3.1.2. For example, consider the partial differential equation,

$$\partial_t \phi(\mathbf{x}, t) = \hat{O} \phi(\mathbf{x}, t) + f(\phi, \mathbf{x}, t), \quad (3.1.14)$$

where \hat{O} is some spatial derivative operator, f is a function and \mathbf{x} are spacelike coordinates. Using the MoL, the operator \hat{O} is discretised (in space only) on a grid like,

$$\hat{O}\phi(\mathbf{x}, t) \Rightarrow (\hat{O}\phi)_{ijk}(t), \quad (3.1.15)$$

where $(\hat{O}\phi)_{ijk}(t) \approx \hat{O}\phi(\mathbf{x}_{ijk}, t)$ is a sum of field values at neighbouring gridpoints generated by the method of finite differences. Discretising the function f on the grid gives the following ODE for each gridpoint with spatial indices $\{i, j, k\}$,

$$\partial_t \phi_{ijk}(t) \approx (\hat{O}\phi)_{ijk}(t) + f_{ijk}(\phi, t) := F_{ijk}(\phi, t), \quad (3.1.16)$$

where $F_{ijk}(\phi, t)$ is treated as the discretisation of a continuum function $F(\phi, \mathbf{x}, t)$.

3.1.5 Integration of ODEs

To perform the time evolution of the ODE (3.1.16), we need to pick a time integration method for an ODE. The obvious choice might be to discretise the time integral like,

$$\partial_t \phi_{ijk}^n = \frac{\phi_{ijk}^{n+1} - \phi_{ijk}^n}{\Delta t}, \quad (3.1.17)$$

where Δt is the time-step of evolution. This can be substituted into Eq. (3.1.16) to give,

$$\phi_{ijk}^{n+1} = \phi_{ijk}^n + F_{ijk}^n \Delta t, \quad (3.1.18)$$

which is an explicit scheme; the desired future field values ϕ_{ijk}^{n+1} are given by an explicit formula in terms of the previous values ϕ_{ijk}^n . This is known as the Euler method and is often unstable; it can be shown to be completely unstable no matter how small Δt is taken to be for $F_{ijk}^n = A\phi_{ijk}^n$ for positive constant A . There is nothing stopping us instead writing,

$$\phi_{ijk}^{n+1} - F_{ijk}^{n+1} \Delta t = \phi_{ijk}^n, \quad (3.1.19)$$

which is known as an implicit scheme as the desired future field values ϕ_{ijk}^{n+1} are given by an implicit equation. This is called the backwards Euler method and is often stable, but only first order accurate in time. This can be improved to the second order accurate Crank-Nicolson method,

$$\phi_{ijk}^{n+1} - \frac{1}{2} F_{ijk}^{n+1} \Delta t = \phi_{ijk}^n + \frac{1}{2} F_{ijk}^n \Delta t, \quad (3.1.20)$$

but is still implicit in ϕ_{ijk}^n . The problem with implicit methods is that the F_{ijk}^{n+1} are some combination of the ϕ_{ijk}^{n+1} at \mathbf{x}_{ijk} and multiple other neighbouring gridpoints around \mathbf{x}_{ijk} ; the number of gridpoints increases with higher order accurate derivative stencils. Solving the set of simultaneous equations in Eq. (3.1.20), for example, requires inverting a large (albeit sparse) matrix whose size scales with the number of gridpoints. This can be done in a single step if the F_{ijk}^n are linear in ϕ^n . For non-linear PDEs the F_{ijk}^n are non-linear in ϕ_{ijk}^n ; in the best case one can linearise Eq. (3.1.20) and the ϕ_{ijk}^{n+1} can be solved with an iterative method, in the worst case the implicit scheme is impossible to solve.

A stable and explicit method can be obtained by seeking a higher order accurate time derivative. In a similar fashion to the derivation of Eq. (3.1.8), one can write,

$$\phi_{ijk}^n = \phi_{ijk}^n, \quad (3.1.21)$$

$$\phi_{ijk}^{n-1} = \phi_{ijk}^n - \Delta t \dot{\phi}_{ijk}^n + \frac{1}{2} (\Delta t)^2 \ddot{\phi}_{ijk}^n, \quad (3.1.22)$$

$$\phi_{ijk}^{n-2} = \phi_{ijk}^n - 2\Delta t \dot{\phi}_{ijk}^n + 2(\Delta t)^2 \ddot{\phi}_{ijk}^n, \quad (3.1.23)$$

where the dot represents a time derivative and the Taylor expansion has been given up to $(\Delta t)^2$ terms. Rearranging, these give

$$\partial_t \phi_{ijk}^n = \frac{-3\phi_{ijk}^n + 4\phi_{ijk}^{n-1} - \phi_{ijk}^{n-2}}{6\Delta t}. \quad (3.1.24)$$

Substituting this into Eq. (3.1.16) gives an explicit equation for ϕ_{ijk}^n ,

$$\phi_{ijk}^n = \frac{4}{3}\phi_{ijk}^{n-1} - \frac{1}{3}\phi_{ijk}^{n-2} - 2F_{ijk}\Delta t, \quad (3.1.25)$$

where the index n has been omitted from F_{ijk} as it can be replaced with any combination $aF_{ijk}^n + bF_{ijk}^{n-1} + cF_{ijk}^{n-2}$, provided $a + b + c = 1$, such as $F_{ijk}^n = \frac{4}{3}F_{ijk}^{n-1} - \frac{1}{3}F_{ijk}^{n-2}$. Even though this method is explicit it requires two sets of initial data, ϕ_{ijk}^{n-1} and ϕ_{ijk}^{n-2} and one must take care to check if the choice of F_{ijk} gives a stable scheme.

The Runge Kutta Method

The Runge-Kutta method is an explicit ODE integration scheme that can be made accurate to arbitrary order in Δt . For an ODE of the form,

$$\frac{d\phi}{dt} = F(\phi, t), \quad (3.1.26)$$

the widely used fourth order accurate Runge-Kutta (RK4) method first calculates four intermediate rates of change $\{k_1, k_2, k_3, k_4\}$,

$$k_1 = F(\phi, t), \quad (3.1.27)$$

$$k_2 = F\left(\phi + \frac{1}{2}k_1\Delta t, t + \frac{1}{2}\Delta t\right), \quad (3.1.28)$$

$$k_3 = F\left(\phi + \frac{1}{2}k_2\Delta t, t + \frac{1}{2}\Delta t\right), \quad (3.1.29)$$

$$k_4 = F(\phi + k_3\Delta t, t + \Delta t). \quad (3.1.30)$$

These are then summed in a way that calculates $\phi(t + \Delta t)$ from $\phi(t)$ removing errors up to and including $(\Delta t)^4$ terms,

$$\phi(t + \Delta t) = \phi(t) + \frac{1}{6}(k_1 + 2k_2 + 2k_3 + k_4)\Delta t + \mathcal{O}(\Delta t^5). \quad (3.1.31)$$

A similar procedure can be done for any desired accuracy with higher order methods becoming quite involved. The simplicity of this RK4 scheme along with its robustness has led to it being one of the most popular methods for integrating ODEs. Lower order Runge-Kutta methods also exist, for example the first order RK1 method which is equivalent to the Euler method in Eq. (3.1.18). Another common Runge-Kutta method is the second order accurate RK2 method also called the midpoint method.

3.2 GRCHOMBO

3.2.1 Overview of GRCHOMBO

GRCHOMBO [1] [46] is an open-source fully non-linear Numerical Relativity (NR) code built on top of CHOMBO, a PDE solver with adaptive mesh refinement (AMR). GRCHOMBO is written in C++ making extensive use of templating, classes and object oriented programming. GRCHOMBO also supports vectorisation and parallelisation with OpenMP and MPI for efficient scaling to large problems suitable for use on supercomputer clusters. Current public examples of GRCHOMBO include a black hole binary with separate spins, a single Kerr black hole and a compact real scalar configuration.

The AMR in CHOMBO relies on the Berger-Oliger style AMR [47] with block-structured Berger-Rigoutsos grid generation [48]. The labelling of which regions to regrid, called tagging, is specifiable by the user. A common tagging criterion (used in this work) is to define a gradient sensitive quantity \aleph in terms of a grid variable ψ ,

$$\aleph = \Delta x \sqrt{\frac{|\sum_{ij}(\partial_i \partial_j \psi)(\partial_i \partial_j \psi)|}{|\sum_k(\partial_k \psi)(\partial_k \psi)| + \epsilon}}, \quad (3.2.1)$$

for grid spacing Δx and small positive constant ϵ to avoid division by zero. Some threshold ψ_0 is prespecified and any gridpoint where $\aleph > \psi_0$ is flagged (or tagged) for regridding. If a box¹ has a greater fraction of its cells tagged than a *fill_ratio* parameter then the box will be covered by the next inner AMR level; in this work *fill_ratio* = 0.7. The reason for premultiplying by Δx is so that as the grid spacing gets smaller on deeper levels the tagging criterion is not flagged unless gradients become more extreme.

In order to evolve a spatial hypersurface according to the Einstein equation, GRCHOMBO uses either the BSSN formalism [49] [50] described in section 2.1.7 or the CCZ4 formalism [31] [33]. A summary of the CCZ4 formulation is given in section 2.1.9 along with the equations of motion used in this work. The conformal factor used is $\chi = \gamma^{-\frac{1}{3}}$ where γ is the metric determinant from Eq. (2.1.9) on the three dimensional hypersurface Σ_t . The time evolution scheme is the method of lines (section 3.1.4) using fourth order spatial derivatives (section 3.1.2) and Runge Kutta fourth order time integration (section 3.1.5). While sixth order spatial derivatives have been implemented, they are not used in this work due to the increasing number of ghost cells needed. Kreiss-Oliger dissipation [51] is used to suppress high frequency noise occurring from interpolation, regridding of AMR and high field gradients inside black hole regions. As described in section 2.1.10, the moving puncture gauge with conformal factor χ is used to evolve moving black hole singularities.

The code can use Sommerfeld, periodic, reflective and extrapolating boundary conditions. Simulations in this work all use some combination of Sommerfeld boundary conditions for boundaries far away and symmetric boundary conditions in a plane of symmetry. Headon collisions of identical objects can use *octant* symmetry, three planes of symmetry on the planes $x = 0$, $y = 0$ and $z = 0$. This means one only needs to simulate the region $x > 0$, $y > 0$ and $z > 0$ with symmetric boundary conditions on the symmetry planes; the overall problem size (or number of gridpoints) decreases by a factor of eight. Similarly, some headon collisions of non-similar objects can use *quadrant* symmetry, reducing the problem size by four. The inspiral of two dissimilar compact objects often has one plane of symmetry, the plane of inspiral; *bitant* symmetry can be used to half the problem size. For all the pre-mentioned symmetries, a suitable rest frame must be used aligning with the symmetries of the initial data. In the case that the colliding objects have spin the mentioned symmetries may be broken; in the worst case scenario there are no plane of symmetry for generic orbits with misaligned spins.

A selection of diagnostic tools have been implemented in GRCHOMBO. These include a black hole horizon finder, gravitational wave extraction and the calculation of the ADM mass, ADM momentum, Noether

¹Each AMR level is subdivided into cuboids, often of side lengths 8, 16, or 32 gridpoints, called boxes. These boxes can be evolved forward one time step without sharing memory making them compatible with MPI.

charges and energy-momentum densities and fluxes. The diagnostic for the angular momentum density and flux are derived in chapter 5.

While GRChombo can be used to simulate traditional spacetimes, such as binary black hole inspirals [52], it excels at simulating novel physics due to its adaptable code structure and AMR. The advantage of AMR is that regions needing higher resolution are assigned (and de-assigned) dynamically during run time; this requires no pre-determined grid structure. Other NR codes, such as LEAN [53] or the EINSTEIN-TOOLKIT [54, 55, 56], must either rely on pre-determined grid structures or regrid by tracking BH punctures of the centres of compact objects; while these methods are often very successful², AMR is especially useful for simulations of novel spacetimes that can develop features requiring high resolution in unexpected places. GRChombo has also successfully simulated ring-like configurations [57], inhomogeneous spacetimes [58] and black-hole collisions in higher dimensions³ [59] which would be difficult to accurately resolve with a conventional pre-specified grid structure.

3.2.2 Simulation Units

GRChombo defaults to geometric units with $c = G = 1$, but the value of Newton's gravitational constant G can be changed if desired. Planck's constant does not arise in vacuum General Relativity, but does appear in the Klein Gordon equation for a scalar field as in section 2.2.1. Following the conventions of section 1.1.3, Planck's reduced constant \hbar is also set to unity and Planck units are used.

As given in section 2.2.1, the Lagrangian for a self-interacting boson star is proportional to,

$$g^{\mu\nu}\partial_\mu\varphi\partial_\nu\bar{\varphi} + m^2|\varphi|^2 + \frac{1}{2}\Lambda_4|\varphi|^4, \quad (3.2.2)$$

in natural units; setting $\Lambda_4 = 0$ returns a mini boson star. For a constant κ , Setting $m \rightarrow \kappa m$ with $\varphi \rightarrow \kappa^{-1}\varphi$, $x^\mu \rightarrow \kappa^{-1}x^\mu$ and $\Lambda_4 \rightarrow \kappa^4\Lambda_4$ leaves the Lagrangian unchanged⁴. Similarly for a solitonic boson star with Lagrangian,

$$\mathcal{L}_{\text{soli}} = g^{\mu\nu}\partial_\mu\varphi\partial_\nu\bar{\varphi} + m^2|\varphi|^2 \left(1 - \frac{|\varphi|^2}{2\sigma^2}\right), \quad (3.2.3)$$

the total Lagrangian is unchanged under $m \rightarrow \kappa m$, $x^\mu \rightarrow \kappa^{-1}x^\mu$ and $\sigma \rightarrow \kappa^{-1}\sigma$. This means that changing the boson particle mass m gives a solution of the same equation but with rescaled coordinates, field values and scalar field parameters. To account for this one parameter freedom, from now on the coordinates $\hat{x}^\mu = x^\mu \cdot m$, the scalar field $\hat{\varphi} = \varphi \cdot m$ and the solitonic parameter $\hat{\sigma} = \sigma \cdot m$ will be used; the circumflex over these units will now be dropped for convenience. This is equivalent to setting $m = 1$; if boson stars with particle mass other than $m = 1$ are desired they can be obtained by rescaling the appropriate solution of the $m = 1$ Einstein-Klein-Gordon equation.

3.2.3 Boson Star Initial Data

We now seek to solve the EKG ODEs (2.2.21), (2.2.22) and (2.2.23) numerically to obtain initial data for a single static boson star. The system can be reduced to a set of five first order ODEs with five boundary conditions. For a physical star we would like to impose $\Phi(0) = \Phi_0$, $\Phi'(0) = 0$, $\Phi(r \rightarrow \infty) \rightarrow 0$, $\Omega'(0) = 0$, $\Omega(r \rightarrow \infty) \rightarrow 1$, $\Psi'(0) = 0$ and $\Psi(r \rightarrow \infty) \rightarrow 1$ to obtain regularity at the origin and match the Schwarzschild vacuum solution at large radius; however this implies seven boundary conditions and we can only impose five. The condition $\Omega(0)' = 0$ cannot be specified as Eq. (2.2.21) is first order in derivatives of Ω but given that r and Ψ' both vanish at the origin then Ω' must also vanish at the origin

²For example in simulating binaries.

³In this paper [59] the black-hole collisions form *dumbbell* shaped horizons that pinch off.

⁴It has been assumed that the coordinates x^μ have the dimension of length such as Cartesian coordinates; instead we can demand that $g^{\mu\nu}\partial_\mu\partial_\mu \rightarrow \kappa^2 g^{\mu\nu}\partial_\mu\partial_\mu$ which is generally true even for dimensionless coordinates such as angles.

automatically. One more boundary condition can be removed by asking for the boson star solution to match the isotropic Schwarzschild solution in Eq. (1.4.54) at large radius and therefore,

$$\Omega(\infty) = \Omega_\infty = \left(\frac{1 - \frac{M_{\text{BS}}}{2r}}{1 + \frac{M_{\text{BS}}}{2r}} \right) \quad \text{and} \quad \Psi(\infty) = \Psi_\infty = \left(1 + \frac{M_{\text{BS}}}{2r} \right)^2, \quad (3.2.4)$$

where M_{BS} can be interpreted as the mass of the boson star; this mass will not enter the boundary condition so can be safely ignored. Combining the two equations above gives

$$\sqrt{\Psi_\infty} (1 + \Omega_\infty) = 2 \quad (3.2.5)$$

for a vacuum spacetime. Imposing the single condition $\sqrt{\Psi_\infty} (1 + \Omega_\infty) = 2$, rather than both $\Omega_\infty = 1$ and $\Psi_\infty = 1$, then gives asymptotic flatness in terms of just one boundary condition. One final point of importance is the frequency ω which turns the Klein-Gordon ODE into an eigenvalue problem admitting only discrete values of ω .

The problem has now been reduced to five ODEs with the following five boundary conditions,

$$\{\Phi(0), \Phi'(0), \Psi'(0), \Omega(0), \sqrt{\Psi(\infty)} (1 + \Omega(\infty)) ; \omega\} = \{\Phi_0, 0, 0, \Omega_0, 2; \omega_0\}, \quad (3.2.6)$$

subject to the condition of an eigenvalue $\omega = \omega_0$. The first attempt to find the radial profile $\{\Phi(r), \Omega(r), \Psi(r)\}$ of the boson star was to use a relaxation method as it trivially incorporates the above two-point boundary conditions. In practice this method did not work well for the eigenvalue problem in ω . Unlike with a shooting method, there was no obvious way of telling whether the guess ω was larger or smaller than the correct value. Even if this problem were overcome, a numerical solution with relaxation would be computationally slow, even with Successive Over-Relaxation [60]; perhaps a multigrid method could work here but a simpler method is given by shooting.

Shooting Method

To find the initial data for a single Boson star, a C++ script has been written using the RK4 method of section 3.1.5 to integrate the EKG system taking five initial conditions, and an eigenvalue guess ω_0 ,

$$\{\Phi(0), \Phi'(0), \Psi(0), \Psi'(0), \Omega(0); \omega\} = \{\Phi_0, 0, \Psi_0, 0, \Omega_0; \omega_0\}. \quad (3.2.7)$$

Unfortunately Ω_0 and Ψ_0 are unknown a priori, but guessing any values reasonably close to unity, such as $\Omega_0 = 0.5$ and $\Psi_0 = 2$, still give a boson star. This will generally result in the following asymptotic metric,

$$g_{\mu\nu}(r \rightarrow \infty) \rightarrow \text{diag}(-A^2, B^2, B^2, B^2), \quad (3.2.8)$$

for constant A and B .

Before we discuss how to find the correct value of ω , there is a subtle numerical problem to address. Using spherical polar coordinates in flat space, the Klein-Gordon equation (2.2.8) with $V = m^2|\varphi|^2$ and ansatz $\varphi = \Phi_{\text{flat}}(r)e^{i\omega t}$ reduces to,

$$\frac{1}{\sqrt{-g}} \partial_\mu (\sqrt{-g} g^{\mu\nu} \partial_\nu) \varphi = \frac{\partial V}{\partial |\varphi|^2} \varphi, \quad (3.2.9)$$

$$\partial_t (g^{tt} \partial_t) \Phi_{\text{flat}}(r) e^{i\omega t} + \frac{1}{r^2} \partial_r (r^2 g^{rr} \partial_r) \Phi_{\text{flat}}(r) e^{i\omega t} = m^2 \Phi_{\text{flat}}(r) e^{i\omega t}, \quad (3.2.10)$$

$$\omega^2 \Phi_{\text{flat}}(r) + \frac{1}{r^2} \partial_r (r^2 \partial_r) \Phi_{\text{flat}}(r) = m^2 \Phi_{\text{flat}}(r), \quad (3.2.11)$$

$$(3.2.12)$$

where $\sqrt{-g} = r^2 \sin(\theta)$, $g^{tt} = -1$ and $g^{rr} = 1$. This has general solution,

$$\Phi_{\text{flat}}(r) = \frac{1}{r} \left(C_1 e^{-r\sqrt{m^2 - \omega^2}} + C_2 e^{r\sqrt{m^2 - \omega^2}} \right), \quad (3.2.13)$$

for the amplitude $\Phi_{\text{flat}}(r)$ specified by two constants C_1 and C_2 . Due to finite resolution during numerical integration, at large radius C_2 will never be exactly zero and will eventually grow (along increasing radius) and spoil the numerical integration; even though this behaviour has been derived in flat space it is still present in curved space with spherical symmetry - especially at such large radius that space is approximately flat. In practice, assuming the correct value of ω is used, the scalar field Φ decays to some small⁵ value and is effectively zero within numerical noise. At this point the coefficient C_2 is excited by noise and starts to grow exponentially. At a radius r_* when the growing mode is deemed to be dominating, usually detected by an axis crossing ($\Phi(r_*) = 0$) or a turning point ($\Phi'(r_*) = 0$), the conditions $\Phi(r > r_*) = \Phi'(r > r_*) = 0$ are enforced during integration. This creates a vacuum for $r > r_*$ and the spacetime is equivalent to the Schwarzschild spacetime. After this radius, an exponentially growing stepsize is used to reach radii of order 10^8 to 10^{10} and the values $A = \Omega_\infty = \sqrt{-g_{00}}$ and $B = \Psi_\infty = \sqrt{g_{ii}}$ can be read off.

Interval bisection has been used to find the correct value of ω to machine precision; for the ground state we can tell that $\omega > \omega_0$ if $\Phi(r)$ develops a turning point before an axis crossing and $\omega < \omega_0$ if $\Phi(r)$ develops an axis crossing before a turning point. To find the n 'th excited state, which has n axis crossings for $\Phi(r)$ and $\Phi(r \rightarrow \infty) \rightarrow 0$, a similar scheme is followed to find the eigenvalue ω_n . If $\Phi(r)$ has $n+1$ axis crossings then $\omega > \omega_n$ and if $\Phi(r)$ has n axis crossings followed by a turning point then $\omega < \omega_n$. This method of doing a numerical integration and iteratively restarting to get closer to the target solution is known as a shooting method.

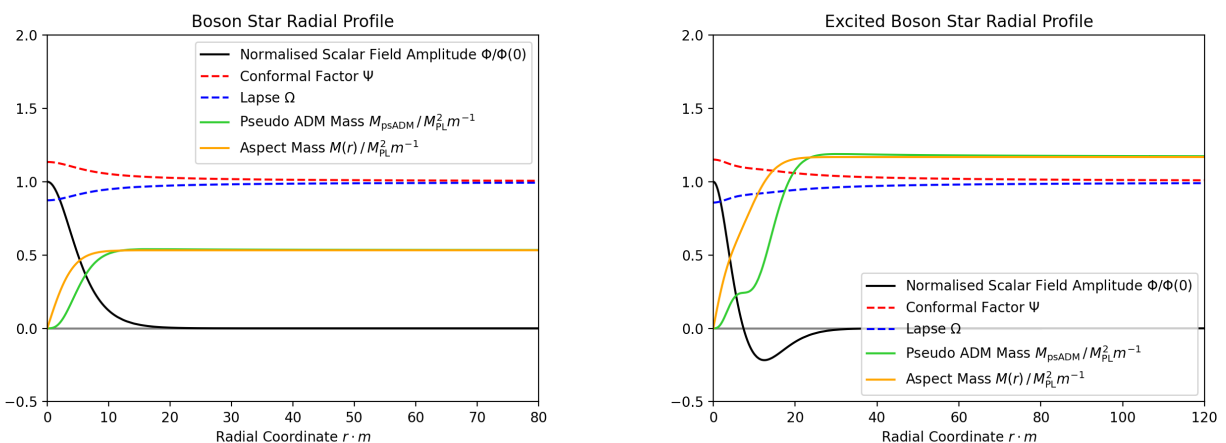


Figure 3.1: Boson Star radial profile, Left: Ground state, Right: 1st Excited state. The ground state has an ADM mass of $M_{\text{ADM}} = 0.532(5) M_{PL}^2 m^{-1}$ and the excited state has an ADM mass of $M_{\text{ADM}} = 1.16(8) M_{PL}^2 m^{-1}$. Both stars have a central amplitude of $\Phi(0) \cdot \sqrt{4\pi G} = 0.1 m^{-1}$. The aspect mass is defined in Eq. (4.1.2) and the pseudo-ADM mass is given by Eq. (3.2.20); in the large radius limit, $M_{\text{psADM}}(\infty) = M_{\text{ADM}}$.

Putting everything together, a boson star solution with eigenvalue ω_0 (or ω_n for excited stars) and asymptotic metric Eq. (3.2.8) can be obtained. To find a star with asymptotic metric $\eta_{\mu\nu}$ of flat space, the initial conditions are iteratively improved according to $\Omega_0 \rightarrow \Omega_0/\Omega_\infty$ and $\Psi_0 \rightarrow \Psi_0/\Psi_\infty$; the interval bisection for ω is then restarted. This is iterated three to five times which leaves $A = \Omega_\infty = 1$ and $B = \Psi_\infty = 1$ to high precision and the isotropic boson star profile has been created. This whole process requires a few seconds runtime for a high resolution 500,000 gridpoint calculation on a regular laptop.

Figure 3.1 shows the numerically obtained radial profile of a mini boson star ($\Lambda = 0$) and an excited

⁵Small meaning roughly twenty orders of magnitude smaller than the central density $\Phi(0)$ for a mini boson star. This gets a little less small for dense solitonic stars but it still a good approximation to zero.

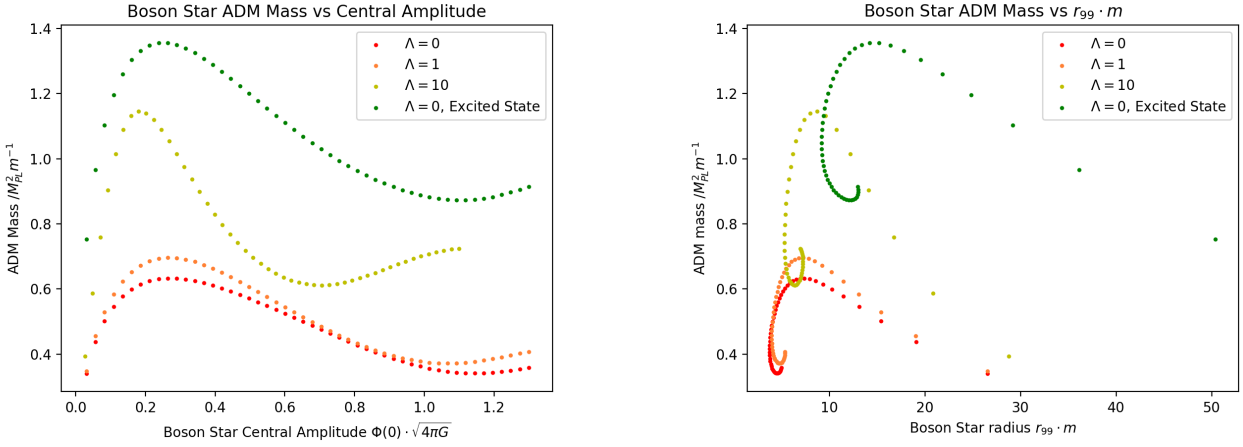


Figure 3.2: Boson star trends, Left: ADM mass vs Φ_0 , Right: ADM mass vs r_{99}

mini boson star. Note two mass definitions are plotted; the aspect mass defined in Eq. (4.1.2) and a pseudo-ADM mass. The conventional ADM mass [61] is defined as

$$M_{\text{ADM}} := \frac{1}{16\pi} \lim_{r \rightarrow \infty} \oint_{s_r} N^i \gamma^{jk} (\partial_j \gamma_{ik} - \partial_i \gamma_{jk}) dA, \quad (3.2.14)$$

for radial coordinate r , 2-sphere s_r of radius r and unit normal vector \mathbf{N} . For an isotropic, diagonal, spherically-symmetric spatial metric γ_{ij} with $\gamma_{rr} = \Psi^2(r)$, $\gamma_{\theta\theta} = \Psi^2(r)r^2$ and $\gamma_{\phi\phi} = \Psi^2(r)r^2 \sin^2 \theta$ (in polar coordinates) this simplifies to,

$$M_{\text{ADM}} = \frac{1}{16\pi} \lim_{r \rightarrow \infty} \oint_{s_r} \left(N^r \gamma^{rr} \partial_r \gamma_{rr} - N^r \gamma^{jk} \partial_r \gamma_{jk} \right) dA, \quad (3.2.15)$$

$$= \frac{1}{16\pi} \lim_{r \rightarrow \infty} \oint_{s_r} N^r \Psi^{-2} \left(\partial_r \Psi^2 - \delta^{jk} \delta_{jk} \partial_r \Psi^2 \right) \sqrt{\gamma_{\theta\theta} \gamma_{\phi\phi}} d\theta d\phi, \quad (3.2.16)$$

$$= \frac{1}{16\pi} \lim_{r \rightarrow \infty} \int_{\theta=0}^{\theta=\pi} \int_{\phi=0}^{\phi=2\pi} -4\Psi^{-2} (\partial_r \Psi) \Psi^2 r^2 \sin^2 \theta d\theta d\phi, \quad (3.2.17)$$

$$= \lim_{r \rightarrow \infty} \left(-r^2 \partial_r \Psi \right), \quad (3.2.18)$$

$$(3.2.19)$$

where we used the fact that $\gamma(\mathbf{N}, \mathbf{N}) = 1$ which gives $N^r = (\gamma_{rr})^{-1/2} = \Psi^{-1}$. Note that for a Schwarzschild black hole with $\Psi = \left(1 + \frac{M}{2r}\right)^2$ the ADM mass formula returns the expected result of M . We define the *pseudo-ADM mass* as

$$M_{\text{psADM}}(r) := -r^2 \partial_r \Psi, \quad (3.2.20)$$

which of course satisfies $M_{\text{ADM}} = M_{\text{psADM}}(\infty)$.

Polytropic fluid star initial data has also been calculated as a preliminary test of the code; they are easier to create as they do not require solving an eigenvalue problem and do not have an asymptotically growing mode. Figure (3.2) shows how the ADM mass of boson stars varies with central amplitude Φ_0 and r_{99} , the radius which $\Phi(r_{99}) = \Phi_0/100$. It should be noted that the mini boson star (with $\Lambda = 0$) case agrees with the known maximum mass, the Kaup limit [62] $M_{\text{max}} \approx 0.633 M_{\text{PL}}^2 m^{-1}$ with the largest mass being $M_{\text{max}} = 0.63299(3) M_{\text{PL}}^2 m^{-1}$ corresponding to a central amplitude of $\sqrt{4\pi G}(\Phi_0)_{\text{max}} = 0.271(0) m^{-1}$.

While many different boson stars have been computed to test the initial data code, all the following evolutions use the same boson star with parameters $\Lambda = 0$, $\sqrt{4\pi G} \Phi_0 = 0.1 m^{-1} \rightarrow \Phi_0 \approx 0.0282 m^{-1}$

and ADM mass $M = 0.532(7) M_{\text{PL}}^2 m^{-1}$. This is as the stars are heavy enough to form black holes under collisions and large deformations, but stable enough to not collapse to a black hole for moderate perturbations.

3.2.4 Single Star Evolution

As a check that the initial data from section 3.2.3 is correct, a mini boson star with central density $\Phi_0 = 0.02820 m^{-1}$ is evolved in time in three spatial dimensions. The simulation has a physical domain size $L = 1024 m^{-1}$ with $N = 320$ gridpoints on AMR level zero with grid spacing $\Delta x = 3.2 m^{-1}$. The AMR is allowed up to six extra levels; the finest level (level six) has a grid spacing of $\Delta x = 0.05 m^{-1}$. The star is supposed to remain in the centre of the grid and not change as it is a rest frame soliton; this is observed through evolution with GRCCHOMBO. Figure (3.3) shows the global maximum value of $|\varphi|$ (left figure) and the total integral of the Noether charge N over the grid (right figure). As can be seen, $|\varphi|_{\max}$ is constant to $\sim 0.7\%$ and N is conserved to the $\sim 0.07\%$ level until time $t = 320 m^{-1}$.

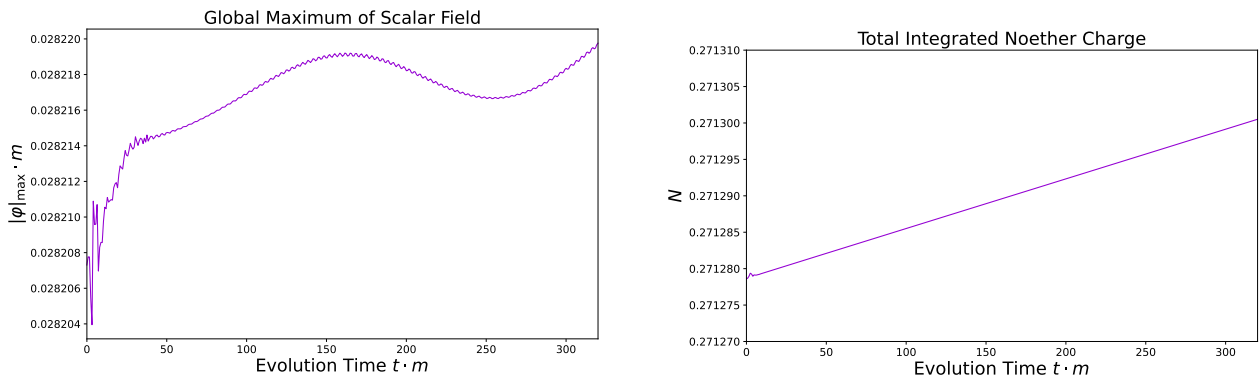


Figure 3.3: Left: Maximum of $|\varphi|$ during the evolution, Right: Total integrated Noether charge N . The initial noise seen in the two figures is attributed to junk radiation from refinement boundaries and is potentially exacerbated by the gauge settling from the initial gauge to the moving puncture gauge used. The lower-amplitude oscillation seen continuously in the left figure is due to finite resolution when calculating the maximum value $\varphi_{\max} = [\text{Re}(\varphi)^2 + \text{Im}(\varphi)^2]_{\max}$ on any gridpoint.

3.2.5 Superposition of Initial Data

In order to simulate a spacetime consisting of two stars (or a star and a black hole) we must choose a way of superposing the initial data of two objects, centred at $x^{(1)}$ and $x^{(2)}$. For some field $\psi^{(j)}$ associated with the compact object at $x^{(j)}$,

$$\psi^{(j)} = \psi(x - x^{(j)}), \quad (3.2.21)$$

where ψ refers to the object centred about the origin. Taking two compact objects with fields φ , Π , γ_{ij} , \mathcal{K}_{ij} , α and β^i , a naive superposition scheme was chosen;

$$\varphi = \varphi^{(1)} + \varphi^{(2)}, \quad (3.2.22)$$

$$\Pi = \Pi^{(1)} + \Pi^{(2)}, \quad (3.2.23)$$

$$\mathcal{K}_j^i = \mathcal{K}_{j\ j}^{(1)i} + \mathcal{K}_{j\ j}^{(2)i}, \quad (3.2.24)$$

$$\gamma_{\mu\nu} = \gamma_{\mu\nu}^{(1)} + \gamma_{\mu\nu}^{(2)} - \delta_{\mu\nu}, \quad (3.2.25)$$

$$\beta_i = \beta_i^{(1)} + \beta_i^{(2)}, \quad (3.2.26)$$

$$\alpha = \sqrt{\alpha_{(1)}^2 + \alpha_{(2)}^2 - 1}, \quad (3.2.27)$$

$$\chi = \det \left(\gamma_{\mu\nu}^{(1)} + \gamma_{\mu\nu}^{(2)} - \delta_{\mu\nu} \right)^{-1/3}, \quad (3.2.28)$$

where the super-scripts ⁽¹⁾ and ⁽²⁾ refer to the separate compact objects. The extrinsic curvature is chosen to be superposed with mixed indices so that it implies the trace \mathcal{K} is also superposed. If one of the compact objects is a black hole the lapse $\alpha \rightarrow 0$ on the horizon; this is circumvented by setting,

$$\alpha = \sqrt{\chi}, \quad (3.2.29)$$

ensuring that the lapse is real and non-negative everywhere on Σ_t .

Superposing two solutions in general relativity usually no longer satisfies the Einstein equation; the Hamiltonian constraint Eq. (2.1.50) and momentum constraints Eq. (2.1.52) are violated. For asymptotically flat compact objects, the constraint violation reduces to zero as the object separation tends to infinity. In the case of finite separations, the CCZ4 scheme in section 2.1.9 aims to drive the constraint violation towards zero and hence a true solution of Einstein's equation; in practice, the CCZ4 scheme is more efficient at damping low amplitude, high-frequency violations and will not fully reduce long-wavelength violations [31]. The collisions of compact objects in section 3.2.6 use this naive superposition scheme. Section 4.2.2 explores a technique to improve the naive superposition of compact objects.

3.2.6 Collisions of Boson Stars

Both a headon collision and a grazing collision of two boson stars are simulated using the superposition scheme given in section 3.2.5. The two stars are identical, each has a central density of $\Phi_0 = 0.02820 \text{ m}^{-1}$ and an ADM mass $M = 0.532(7) M_{\text{PL}}^2 \text{ m}^{-1}$. The stars are placed at positions $x^i = \pm\{40, 0, 0\} \text{ m}^{-1}$ in the headon case and $x^i = \pm\{40, 8, 0\} \text{ m}^{-1}$ in the grazing case and are boosted together with respective velocities $v^i = \mp\{0.1, 0, 0\}$ in both cases. A speed of $v = 0.1$ corresponds to a rapidity of $\psi = 0.1003353$. The simulations have a physical domain size of $L = 512 \text{ m}^{-1}$ with $N = 256$ gridpoints on AMR level zero, this gives a coarse grid resolution of $\Delta x = 2 \text{ m}^{-1}$. There are up to five extra AMR levels giving a finest grid resolution of $\Delta x = 1/16 \text{ m}^{-1}$.

Headon Collision

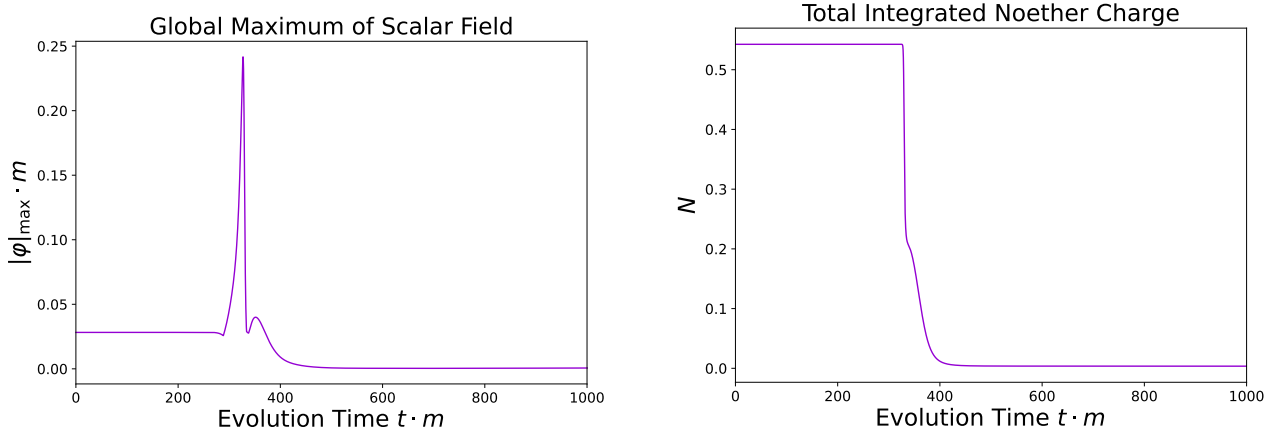


Figure 3.4: Left: Maximum of $|\varphi|$ during evolution, Right: Total integrated Noether charge N .

Figure (3.4) shows $|\varphi|_{\text{max}}$, the global maximum value of $|\varphi|$, and the total Noether charge N as a function of time for the headon collision. At time $t \approx 289 \text{ m}^{-1}$, $|\varphi|_{\text{max}}$ rapidly increases and then drops to zero, signalling the collapse to a black hole. At time $t \approx 327 \text{ m}^{-1}$, there is a temporal maximum in $|\varphi|_{\text{max}}$ as the resolution limit of the simulation is reached and the scalar field is dissipated by the Kreiss-Oliger dissipation and diverging resolution requirements. This dissipation can also be seen in the Noether charge plot at a time of $t \approx 326 \text{ m}^{-1}$ where the total charge that should remain constant but begins to fall. The lack of sufficient resolution inside the black hole is however not problematic for the external simulation;

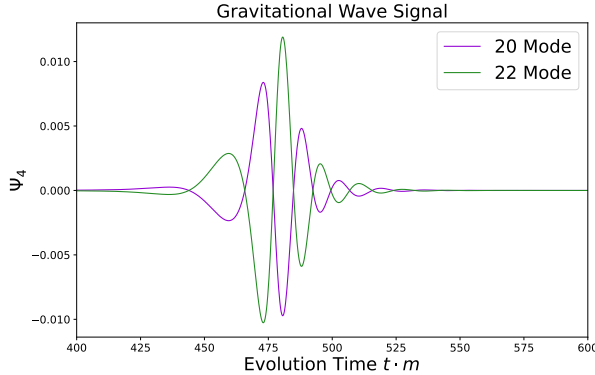


Figure 3.5: Gravitational wave signal of the headon boson star collision. The $l, m = 2, 2$ and $l, m = 2, 0$ spin weighted spherical harmonic modes of the Ψ_4 Newman-Penrose scalar are given.

the errors accumulated are trapped inside the event horizon. Figure (3.4) shows that the total Noether charge rapidly decays to zero at late time as it falls into the black hole and is dissipated.

The gravitational wave extraction at radius $r = 140 \text{ m}^{-1}$ is given in figure 3.5. A spin-weighted spherical harmonic decomposition of the Newman-Penrose scalar Ψ_4 has been done and the $l, m = 2, 0$ and $l, m = 2, 2$ modes are plotted.

The dynamics of the two boson stars are shown in Fig. (3.9) which plots the scalar field modulus $|\varphi|$ in the x, y plane. The stars collide at time $275 \text{ m}^{-1} < t < 300 \text{ m}^{-1}$; which compares well to the Newtonian collision time⁶ $t = 287.6 \text{ m}^{-1}$ of two point masses with the same initial conditions. Soon after collision, an over-density of the scalar field develops which subsequently collapses to a black hole. The black hole then accretes the surrounding scalar field; the scalar field can be seen to be composed of higher order spherical harmonic modes at later times.

Grazing Collision

Figure (3.6) plots $|\varphi|_{\max}$ and the total Noether charge (N) versus time for the grazing collision. At time $t \approx 309 \text{ m}^{-1}$, $|\varphi|_{\max}$ rapidly increases and a black hole is soon formed. The black hole is assumed⁷ to be spinning due to the collapsing matter containing angular momentum. At time $t \approx 356 \text{ m}^{-1}$ there is a temporal maximum in $|\varphi|_{\max}$; similarly to the headon collision, this is caused by diverging resolution requirements near the black hole centre and does not affect the exterior spacetime. Consequently, the Noether charge plot shows a drop in charge at a time of $t \approx 355 \text{ m}^{-1}$.

A simulation of the grazing collision with point masses has been done using Newton's laws. The time taken for closest approach (with separation $s = 2.33 \text{ m}^{-1}$) is $t = 315.8 \text{ m}^{-1}$; at this separation the finite sized stars would collide. Snapshots of the grazing boson star collision using numerical relativity (in full general relativity) are shown in Fig. (3.10) plotting the scalar field modulus $|\varphi|$ in the x, y plane. The stars collide at time $300 \text{ m}^{-1} < t < 350 \text{ m}^{-1}$ which is in good agreement with the Newtonian approximation. Soon after collision, an over-density of the scalar field develops and collapses to a black hole; this black hole is thought to be spinning due to the angular momentum of the collapsing matter. The black hole subsequently accretes most of the surrounding scalar field leaving a quasi-long-lived rotating toroidal scalar field configuration surrounding the black hole. This late time toroidal scalar field configuration will be referred to as a *toroidal wig* due to it being “fake” hair. The late time toroidal wig seems to settle to a rotationally symmetric configuration, with no quadrupole moment, and does not emit a significant

⁶A simulation of point masses in Newtonian physics has been done to extract a collision time.

⁷No horizon measure, or measure of angular momentum of matter falling into the black hole, has been done for this simulation - these measures would be warranted in any future study.

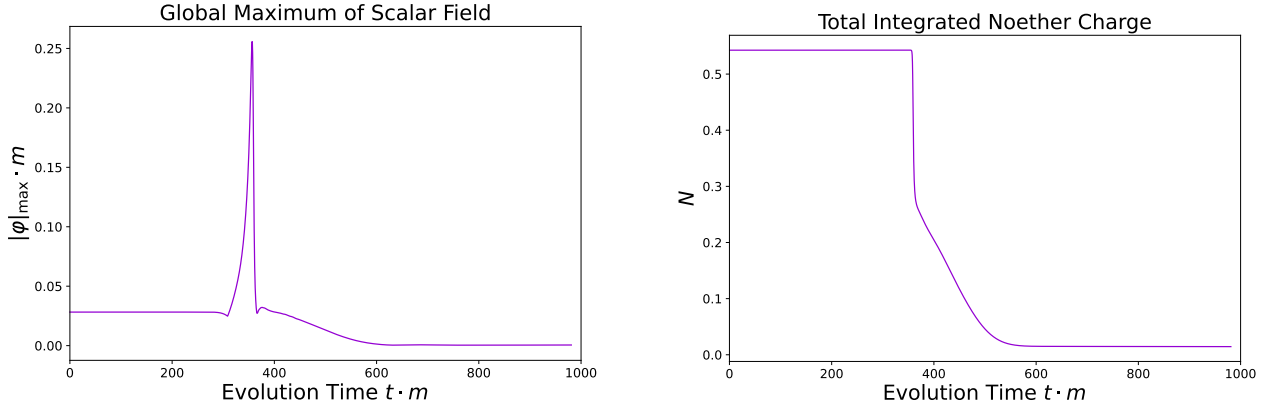


Figure 3.6: Left: Maximum of $|\varphi|$ during evolution, Right: Total integrated Noether charge N .

gravitational wave signal; this can be seen in Fig. (3.7) which plots the $l, m = 2, 2$ and $l, m = 2, 0$ modes of Ψ_4 .

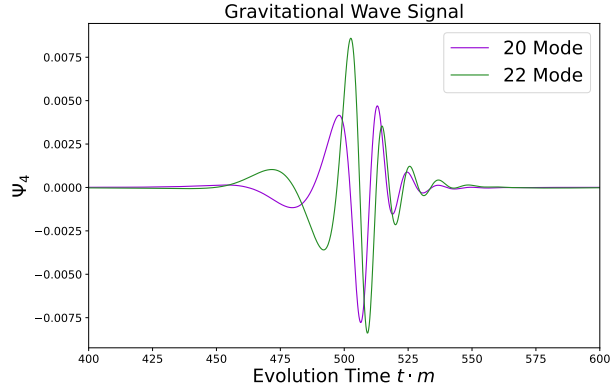


Figure 3.7: Gravitational wave signal of the grazing boson star collision. The $l, m = 2, 2$ and $l, m = 2, 0$ modes of the Ψ_4 Newman-Penrose scalar are given.

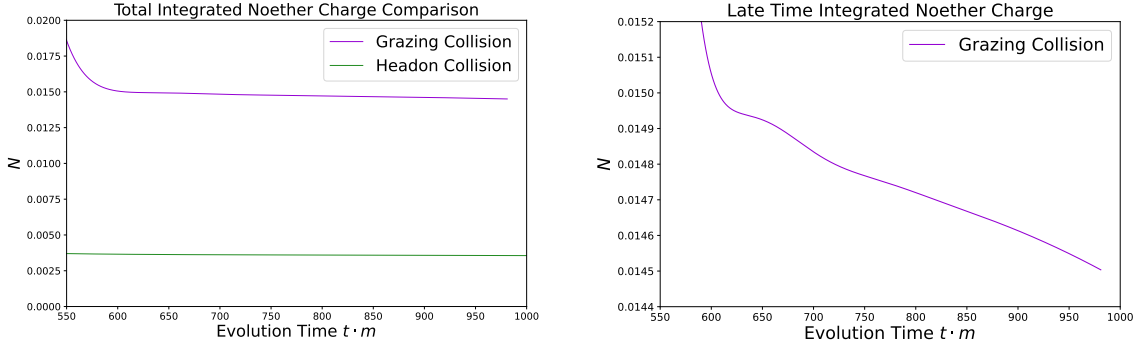


Figure 3.8: Left: Comparison of late time Noether charge N between headon collision and grazing collision of two boson stars. Right: Late time plot of the Noether charge of the grazing collision only.

Figure (3.8) shows the late time Noether charge of the grazing and headon collisions. In contrast to the headon collision, the decay of N in the grazing case is slower and reaches a value approximately 7 times greater. Using linear extrapolation, the Noether charge of the grazing collision decays to zero at time

$t \approx 12500 \text{ m}^{-1}$ and hence the toroidal wig has an approximate lifespan of 12000 m^{-1} .

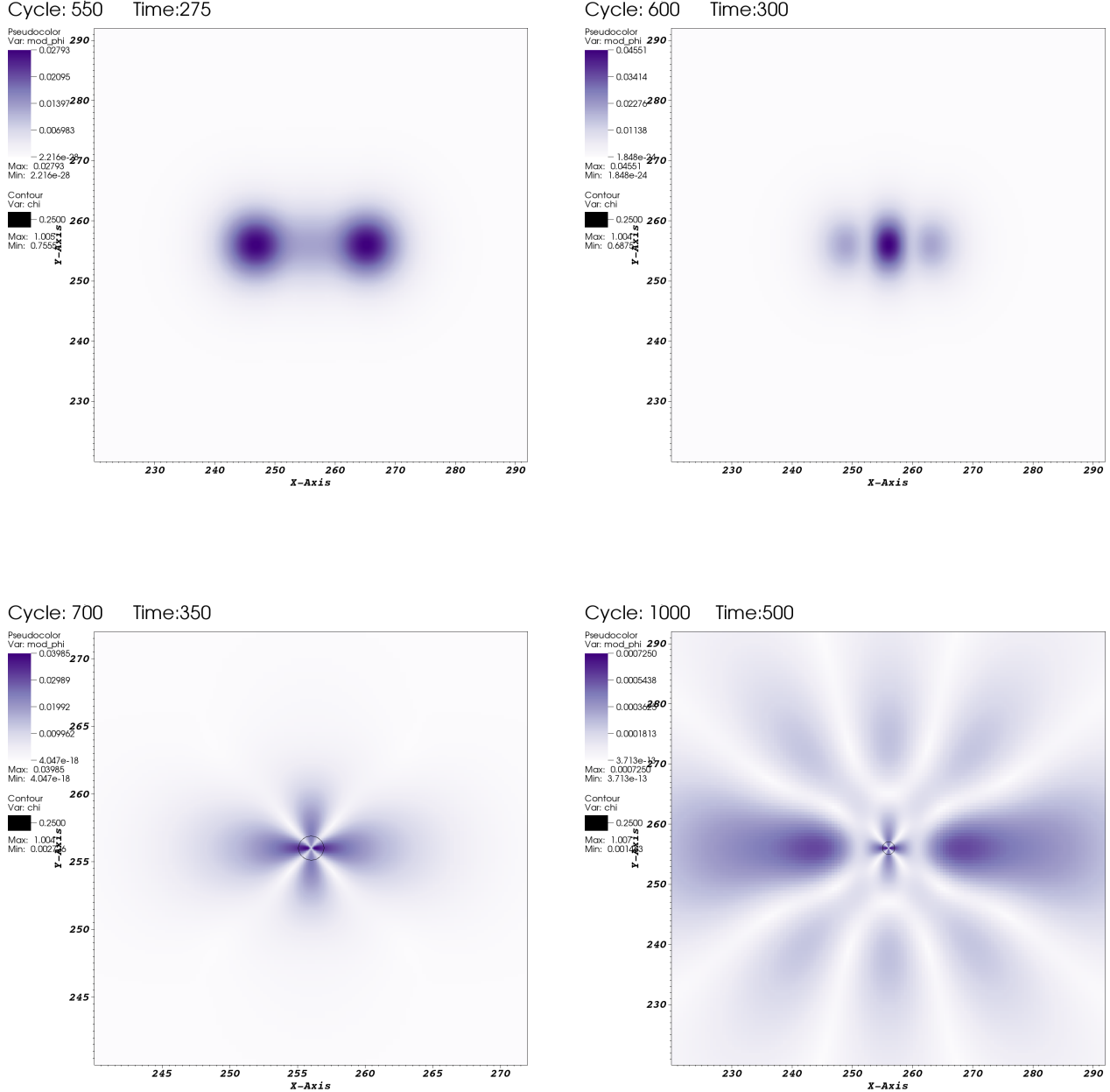


Figure 3.9: Field plots of $|\varphi|$ during evolution at four different times. Time $t = 275 \text{ m}^{-1}$ and $t = 300 \text{ m}^{-1}$ show snapshots momentarily before and after star collision. Time $t = 350 \text{ m}^{-1}$ shows the scalar field accreting into the recently formed black hole. Time $t = 500 \text{ m}^{-1}$ shows the scalar field surrounding the black hole a little later; notably the amplitude is lower. Both the plots of $t = 350 \text{ m}^{-1}$ and $t = 500 \text{ m}^{-1}$ include a contour plot of $\chi = 0.25$ acting as an approximate marker for the event horizon. The Newtonian estimate of collision time is $t = 287.6 \text{ m}^{-1}$.

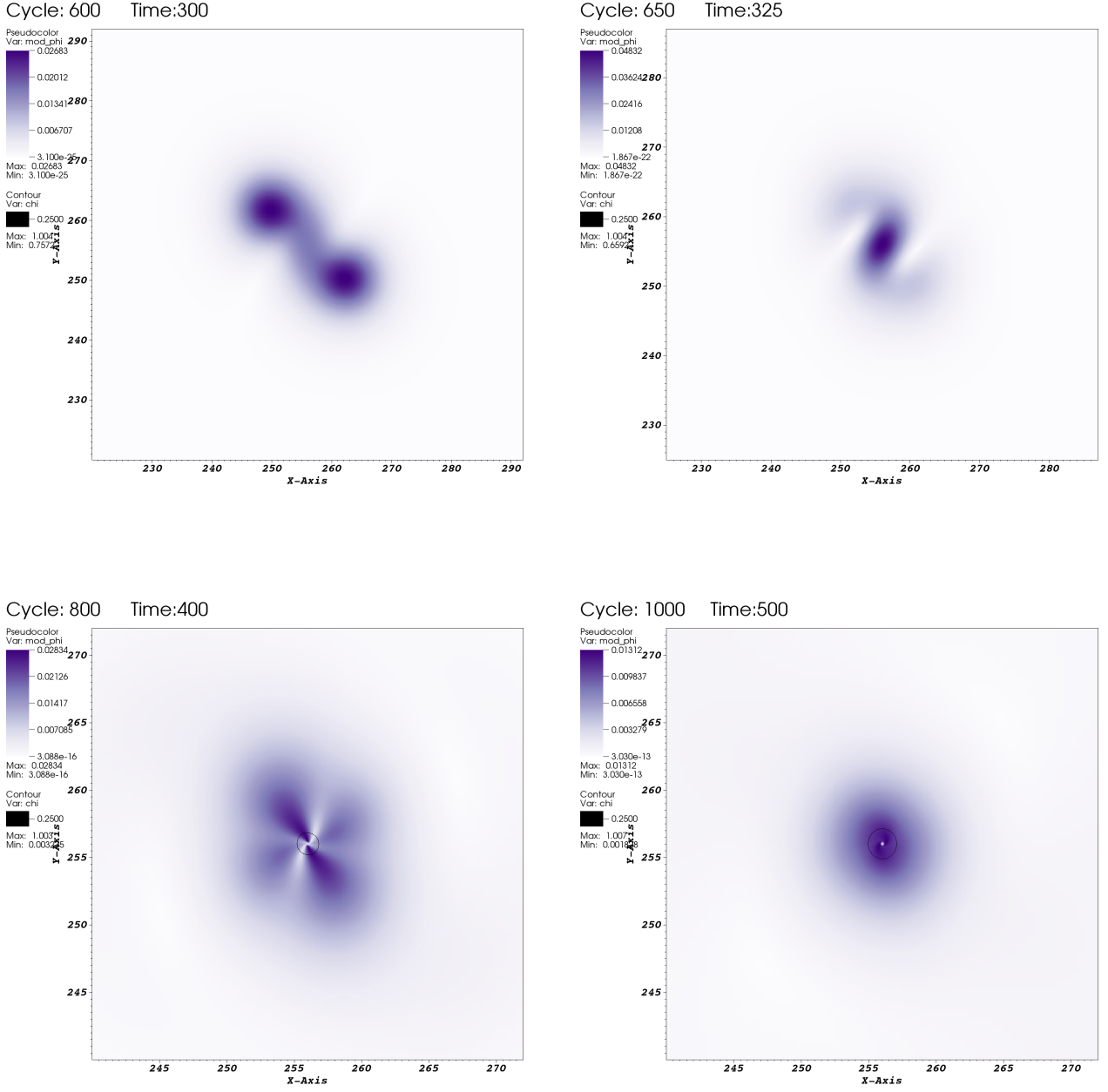


Figure 3.10: Field plots of $|\varphi|$ during evolution at four different times for the grazing boson star collision. Time $t = 300 \text{ m}^{-1}$ and $t = 325 \text{ m}^{-1}$ show snapshots momentarily before and after the collision. The Newtonian estimate of collision time is $t = 315.8 \text{ m}^{-1}$. Time $t = 400 \text{ m}^{-1}$ shows the scalar field accreting into the recently formed black hole. Time $t = 500 \text{ m}^{-1}$ shows the scalar field surrounding the black hole a little later; here this is called a *toroidal wig*. Both the plots of $t = 400 \text{ m}^{-1}$ and $t = 500 \text{ m}^{-1}$ display a contour plot of $\chi = 0.25$ acting as an approximate marker for the event horizon.

Chapter 4

Malaise and Remedy of Binary Boson Star Initial Data

4.1 Introduction

The rise of gravitational-wave (GW) physics as an observational field, marked by the detection of GW150914 [63] and followed by about 50 further compact binary events [64, 65] over the past years, has opened up unprecedented opportunities to explore gravitational phenomena. From tests of general relativity [66, 67, 68, 69, 70, 71] to the exploration of BH populations [72, 73, 74, 75, 76] or charting the universe with independent new methods [77, 78], GW astronomy offers potential for revolutionary insight into long-standing open questions; for a review see [79]. Some answers, such as the association of a soft gamma-ray burst with the neutron star merger GW170817 [80, 81] have already raised our understanding to new levels. GW physics furthermore establishes new concrete links to other fields of research, most notably to particle and high-energy physics and the exploration of the dark sector of the universe [82, 79]. Two important ingredients of this remarkable connection are the characteristic interaction of fundamental fields with compact objects through superradiance [83] and their capacity to form compact objects through an elaborate balance between the intrinsically dispersive character of the fields and their self-gravitation. The latter feature has given rise to the hypothesis of a distinct class of compact objects as early as the 1950s [84]. In contrast to their well known fermionic counterparts – stars, white dwarfs or neutron stars – these compact objects are composed of bosonic particles or fields and, hence, commonly referred to as *Boson Stars* (BS). GW observations provide the first systematic approach to search for populations of these objects or to constrain their abundance. As with all other GW explorations, the success of this exploration is heavily reliant on the availability of accurate theoretical predictions for the anticipated GW signals. This type of calculation, using numerical relativity techniques [85], is the topic of this work.

The idea of bosonic stars dates back to Wheeler’s 1955 study of gravitational-electromagnetic entities or *geons* [84]. By generalising from real to complex-valued fundamental fields, it is even possible to obtain genuinely stationary solutions to the Einstein-matter equations. First established for spin 0 or scalar fields [86, 6, 87], this idea has more recently been extended to spin 1 or vector (aka *Proca*¹) fields [88] as well as wider classes of scalar BSs [89, 90]. In the wake of the dramatic progress of numerical relativity in the simulations of black holes (BHs) [30, 91, 92] (see [93] for a review), the modelling of BSs and binary systems involving BSs has rapidly gathered pace.

The first BS models computed in the 1960s consisted of a massive but non-interacting complex scalar field φ . This class of stationary BSs, commonly referred to as *mini boson stars*, consists of a one parameter family of ground-state solutions characterised by the central scalar-field amplitude that reveals a stability structure analogous to that of Tolman-Oppenheimer-Volkoff [94, 95] stars: a stable and an unstable branch of ground-state solutions are separated by the configuration with maximal mass [96, 97, 98]. For each ground-state model, there furthermore exists a countable hierarchy of excited states with $n > 0$ nodes in the scalar profile [99, 100, 101]. Numerical evolutions of these excited BSs demonstrate their unstable character, but also reveal significant variation in the instability time scales [102].

Whereas mini BS models are limited in terms of their maximum compactness, self-interacting scalar fields can result in significantly more compact stars, even denser than neutron stars [103, 104, 105, 106]. This raises the intriguing question whether compact BS binaries may reveal themselves through characteristic GW emission analogous to that from BHs or NSs [107]. Recent studies conclude that this may well be within the grasp of next-generation GW detectors and, in the case of favourable events, even with advanced LIGO [108, 109, 110].

One of the characteristic properties of BSs is the quantised nature of their spin. The linearised Einstein equations in the slow-rotation limit lead to a two-dimensional Poisson equation that does not admit everywhere regular solutions except for trivial constants; in consequence BSs cannot rotate perturba-

¹Even though the term “boson star” generally applies to compact objects formed of any bosonic fields, it is often used to specifically denote stars made up of a *scalar* field. Stars composed of vector fields, in contrast, are most commonly referred to as *Proca* stars. Unless specified otherwise, we shall accordingly assume the term boson star to imply scalar-field matter.

tively [111]. By relaxing the slow-rotation approximation, Schunck and Mielke [112] computed the first (differentially) rotating BSs and found that these solutions have an integer ratio of angular momentum to particle number. The structure of spinning BS models has been studied extensively over the years [113, 114, 115, 116, 117, 118, 119, 120, 121]. The quantised nature of the angular momentum also applies to Proca and *Dirac* (spin $\frac{1}{2}$) stars [122], but numerical studies of the formation of rotating stars have revealed a striking difference between the scalar and vector case: while collapsing scalar fields shed all their angular momentum through an axisymmetric instability, the collapse of vector fields results in spinning Proca stars with no indication of an instability [123, 109]. This observation is supported by analytic calculations [124], but the instability may be quenched by self-interaction terms in the potential function or in the Newtonian limit [125]. For further reviews of the structure and dynamics of single BSs, we note the reviews [126, 127, 128, 41].

The first simulations of BS binaries have considered the head-on collision of configurations with phase differences between the constituent stars or opposite frequencies [129]; see also [130, 131]. The phase or frequency differences manifest themselves most pronouncedly in the dynamics and GW emission at late times around merger. These collisions result in either a BH, a non-rotating BS or a near-annihilation of the scalar field in the case of opposite frequencies. BS binaries with orbital angular momentum generate a GW signal qualitatively similar to that of BH binaries during the inspiral phase, but exhibit a much more complex structure around merger [132, 42]. In agreement with the above mentioned BS formation studies, the BS inspirals also seem to avoid the formation of spinning BSs, although they may settle down into single nonrotating BSs.

In spite of the rapid progress of this field, the computation of GW templates for BSs still lags considerably behind that of BH binaries, both in terms of precision and coverage of the parameter space. Clearly, the presence of the matter fields adds complexity to this challenge, but also alleviates some of the difficulties through the non-singular character of the BS spacetimes. The first main goal of our study is to highlight the substantial risk of obtaining spurious physical results due to the use of overly simplistic initial data constructed by plain superposition of single-BS spacetimes. Our second main goal is to demonstrate how an astonishingly simple modification of the superposition procedure, first identified by Helfer *et al.* [133] for oscillations, overcomes most of the problems encountered with plain superposition. We summarise our main findings as follows.

1. An adjustment of the superposition procedure, given by Eq. (4.2.3), results in a significant reduction of the constraint violations inherent to the initial data; see Fig. 4.3.
2. In the head-on collision of mini BS binaries with rather low compactness, we observe a significant drop of the radiated GW energy with increasing distance d if we use plain superposition. This physically unexpected dependence on the initial separation levels off only for rather large $d \gtrsim 150 M$, where M denotes the Arnowitt-Deser-Misner (ADM) mass [134]. In contrast, the total radiated energy computed from the evolution of our adjusted initial data displays the expected behaviour over the entire studied range $75.5 m \leq d \leq 176 m$: a very mild increase in the radiated energy with d . In the limit of large $d \gtrsim 150 m$, both types of simulations agree within numerical uncertainties; see upper panel in Fig. 4.6.
3. In collisions of highly compact BSs with solitonic potentials, the radiated energy is largely independent of the initial separations for both initial data types, but for plain superposition we consistently obtain $\sim 10\%$ more radiation than for the adjusted initial data; see bottom panel in Fig. 4.6. Furthermore, we find plain superposition to result in a slightly faster infall. The most dramatic difference, however, is the collapse into individual BHs of both BSs well before merger if we use plain superposition. No such collapse occurs if we use adjusted initial data. Rather, these lead to the expected near-constancy of the central scalar-field amplitude of the BSs throughout most of the infall; see Fig. 4.9.
4. We have verified through evolutions of single boosted BSs that the premature collapse into a BH

is closely related to the spurious metric perturbation (4.2.2) that arises in the plain superposition procedure. Artificially adding the same perturbation to a single BS spacetime induces an unphysical collapse of the BS that is in qualitative and quantitative agreement with that observed in the binary evolution starting with plain superposition; see Fig. 4.9.

We discuss in more detail in Sec. 4.2 the construction of initial data through plain superposition and our modification of this method. In Sec. 4.3, we compare the dynamics of head-on collisions of mini BSs and highly compact solitonic BS binaries starting from both types of initial data. We note the substantial differences in the results thus obtained and argue why we regard the results obtained with our modification to be correct within numerical uncertainties. We summarise our findings and discuss future extensions of this work in Sec. 4.4.

4.1.1 Boson Star Initial Data

The initial data for our time evolution is based on single stationary BS solutions in spherical symmetry as discussed in section 2.2.2. Using spherical polar isotropic coordinates the line element can be written as

$$ds^2 = -e^{2\Phi} dt^2 + \psi^4 \delta_{ij} dx^i dx^j. \quad (4.1.1)$$

where Φ and ψ are functions of r only. The metric can be compared to the metric of the isotropic Schwarzschild metric by setting,

$$\psi(r) = \left(1 + \frac{M(r)}{2r}\right), \quad (4.1.2)$$

and defining the aspect mass function $M(r)$ approximating the mass inside a given radius r . At large radius the boson star spacetime approaches the vacuum black-hole spacetime, $M(r)$ is constant and $M(\infty)$ gives the ADM mass² of an isolated boson star. It turns out convenient to express the complex scalar field in terms of amplitude and frequency,

$$\varphi(t, r) = A(r)e^{i\omega t}, \quad \omega = \text{const} \in \mathbb{R}, \quad (4.1.3)$$

as shown in section 2.2.2. The scalar field potentials used for the stars are,

$$V_{\min} = A^2, \quad (4.1.4)$$

$$V_{\text{sol}} = A^2 \left(1 - 2 \frac{A^2}{\sigma_0^2}\right)^2, \quad (4.1.5)$$

taken from Eqs. (2.2.4) and (2.2.6) for a mini boson star and a solitonic boson star respectively; clearly setting $\sigma_0 \rightarrow \infty$ gives $V_{\min} = V_{\text{sol}}$.

For a given potential, the solutions computed with this method form a one-parameter family characterised by the central scalar field amplitude A_0 . In Fig. 4.1 we display two such families for the potentials (4.1.4) and (4.1.5) with $\sigma_0 = 0.2$ in a mass-radius diagram using the areal radius r_{99} containing 99 % of the BS's total mass. In that figure, we have also marked by circles two specific models, one mini BS and one solitonic BS, which we use in the head-on collisions in Sec. 4.3 below. We have chosen these two models to represent one highly compact and one rather squishy BS; note that both models are located to the right of the maximal $M(r)$ and, hence, stable stars. Their parameters and properties are summarised in Table 4.1.

²It should be noted that the aspect mass is not equivalent to the ADM mass at finite radii, only for large radius in an asymptotically flat spacetime.

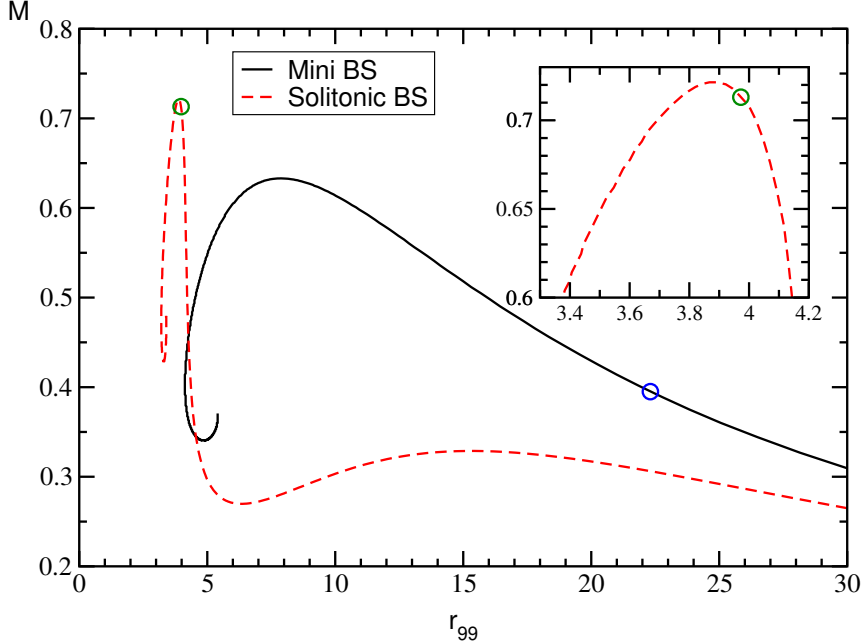


Figure 4.1: One parameter families of mini BSs (black solid) with potential V_{\min} and solitonic BSs (red dashed) with potential V_{sol} and $\sigma_0 = 0.2$ as given in Eqs. (4.1.4) and (4.1.5). In Sec. 4.3 we simulate head-on collisions of two specific models marked by the circles and with parameters listed in Table 4.1.

Model	A_0	σ_0	$m \cdot M_{\text{BS}}$	ω/m	$m \cdot r_{99}$	$\max \frac{m(r)}{r}$
mini	0.0124	∞	0.395	0.971	22.31	0.0249
soli	0.17	0.2	0.713	0.439	3.98	0.222

Table 4.1: Parameters of the two single, spherically symmetric ground state BS models employed for our simulations of head-on collisions. Up to the rescaling with the scalar mass m , each BS is determined by the central amplitude A_0 of the scalar field and the potential parameter σ_0 of Eq. (4.1.5). The mass M_{BS} of the boson star, the scalar field frequency ω , the areal radius r_{99} containing 99 % of the total mass M_{BS} and the compactness, defined here as the maximal ratio of the mass function $m(r)$ to radius, represent the main features of the stellar model.

4.2 Boson Star Binary Initial Data

The single BS models constructed according to the procedure of the previous section are exact solutions of the Einstein equations, affected only by a numerical error that we can control by increasing the resolution, the size of the computational domain and the degree of precision of the floating point variable type employed. The construction of binary initial data is conceptually more challenging due to the non-linear character of the Einstein equations; the superposition of two individual solutions will, in general, not constitute a new solution. Instead, such a superposition incurs some violation of the constraint equations (2.1.50) and (2.1.52). The purpose of this section is to illustrate how we can substantially reduce the degree of constraint violation with a relatively simple adjustment in the superposition. Before introducing this ‘‘trick’’, we first summarise the superposition as it is commonly used in numerical simulations.

4.2.1 Simple Superposition of Boson Stars

The most common configuration involving more than one BS is a binary system, and this is the scenario we will describe here. We note, however, that the method generalises straightforwardly to any number of stars. Recapping the naive superposition procedure given in section 3.2.5, let us then consider two

individual BS solutions with their centres located at x_A^i and x_B^i , velocities v_A^i and v_B^i . The two BS spacetimes are described by the 3+1 (ADM) variables γ_{ij}^A , α_A , β_A^i and \mathcal{K}_{ij}^A , the scalar field variables φ_A and Π_A , and likewise for star B. We can construct from these individual solutions an approximation for a binary BS system via the pointwise superposition,

$$\begin{aligned}\gamma_{ij} &= \gamma_{ij}^A + \gamma_{ij}^B - \delta_{ij}, & \mathcal{K}_{ij} &= \gamma_{m(i} [\mathcal{K}_{j)n}^A \gamma_A^{nm} + \mathcal{K}_{j)n}^B \gamma_B^{nm}] , \\ \varphi &= \varphi_A + \varphi_B, & \Pi &= \Pi_A + \Pi_B.\end{aligned}\tag{4.2.1}$$

One could similarly construct a superposition for the lapse α and shift vector β^i , but their values do not affect the physical content of the initial hypersurface. In our simulations we instead initialise them by $\alpha = \sqrt{\chi}$ and $\beta^i = 0$.

A simple superposition approach along the lines of Eq. (4.2.1) has been used in numerous studies of BS as well as BH binaries including higher-dimensional BHs [129, 132, 135, 136, 42, 137]. For BHs and higher-dimensional spacetimes in particular, this leading-order approximation has proved remarkably successful and in some limits a simple superposition is exact, such as infinite initial separation, in Brill-Lindquist initial data for non-boosted BHs³ [138] or in the superposition of Aichelburg-Sexl shockwaves [139] for head-on collisions of BHs at the speed of light. It has been noted in Helfer *et al.* [133], however, that this simple construction can result in spurious low-frequency amplitude modulations in the time evolution of binary oscillations (real-scalar-field cousins of BSs); cf. their Fig. 7. Furthermore, they have proposed a straightforward remedy that essentially eliminates this spurious modulation. As we will see in the next section, the repercussions of the *simple superposition* according to Eqs. (4.2.1) can be even more dramatic for BS binaries, but they can be cured in the same way as in the oscillation case. We note in this context that BSs may be more vulnerable to superposition artefacts near their centres due to the lack of a horizon and its potentially protective character in the superposition of BHs.

The key problem of the construction (4.2.1) is the equation for the spatial metric γ_{ij} . This is best illustrated by considering the centre x_A^i of star A. In the limit of infinite separation, the metric field of its companion star B becomes $\gamma_{ij}^B \rightarrow \delta_{ij}$. This is, of course, precisely the contribution we subtract in the third term on the right-hand-side and all would be well. In practice, however, the BSs start from initial positions x_A^i and x_B^i with finite separation $d = \|x_A^i - x_B^i\|$ and we consequently perturb the metric at star A's centre by

$$\delta\gamma_{ij} = \gamma_{ij}^B(x_A^i) - \delta_{ij}\tag{4.2.2}$$

away from its equilibrium value $\gamma_{ij}^A(x_A^i)$. This metric perturbation can be interpreted as a distortion of the volume element $\sqrt{\gamma}$ at the centre of star A. More specifically, the volume element at star A's centre is enhanced by $\mathcal{O}(1)\%$ for initial separations $\mathcal{O}(100)\text{ m}$ and likewise for the centre of star B (by symmetry); see appendix A of Ref. [133] for more details.⁴ The energy density ρ , on the other hand, is barely altered by the presence of the other star, because of the exponential fall-off of the scalar field. The leading-order error therefore consists in a small excess mass that has been added to each BS's central region. We graphically illustrate this effect in the upper half of Fig. 4.2 together with some of the possible consequences. As we will see, this qualitative interpretation is fully borne out by the phenomenology we observe in the binaries' time evolutions.

Finally, we would like to emphasise that, while evaluating the constraint violations is in general a good rule of thumb to check whether the field configuration is a solution of the system, it does *not* inform one whether it is *the intended* solution; a system with some constraint violation may have drifted closer to a different, unintended solution. In the present case, in addition to the increased constraint violation, the constructed BS solutions possess significant excitations. Thus, while applying a constraint damping system like conformal Z4 [32, 140] may eventually drive the system to a solution, it may no longer be what was originally intended to be the initial condition of an unexcited BS star.

³Note that for Brill-Lindquist one superposes the conformal factor ψ rather than ψ^4 as in the method discussed here.

⁴Due to the slow decay of this effect $\propto 1/\sqrt{d}$ [133], a simple cure in terms of using larger d is often not practical.

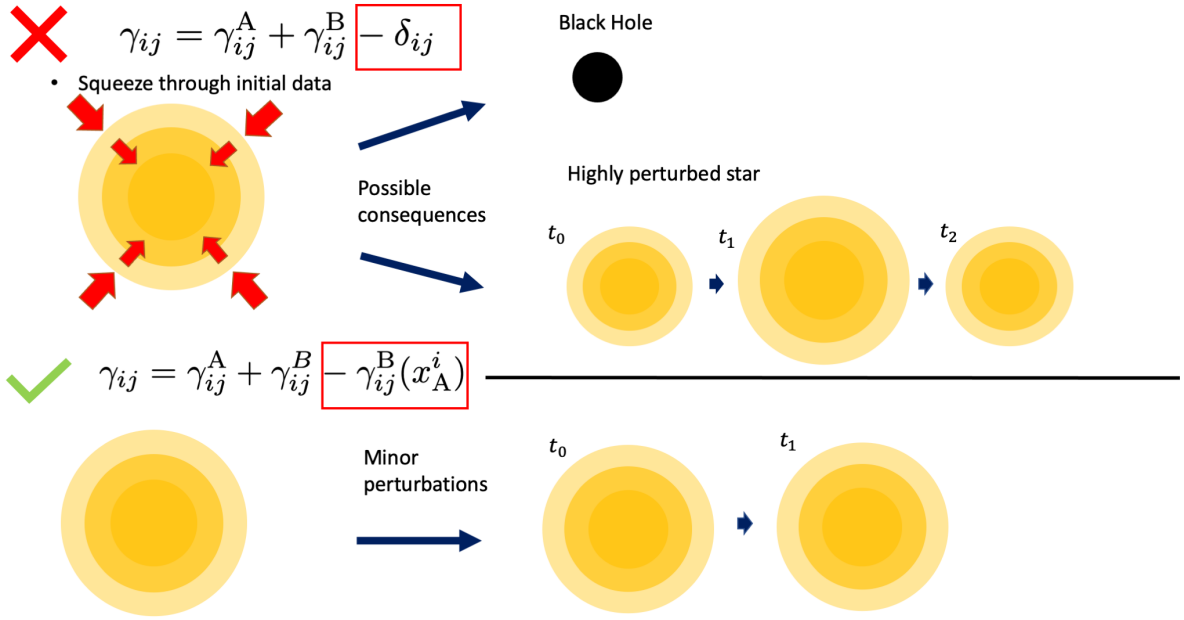


Figure 4.2: Graphical illustration of the spurious dynamics that may be introduced by the simple superposition procedure (4.2.1). *Upper panel:* The spurious increase in the volume element mimics a squeezing of the stellar core that effects a pulsation of the star or may even trigger gravitational collapse to a BH. *Lower panel:* No such squeezing occurs with the adjusted superposition (4.2.3), and the binary evolution starts with approximately unperturbed stars.

4.2.2 Improved Superposition

The problem of the simple superposition is encapsulated by Eq. (4.2.2) and the resulting deviation of the volume elements at the stars' centres away from their equilibrium values. At the same time, the equation presents us with a concrete recipe to mitigate this error: we merely need to replace in the simple superposition (4.2.1) the first relation $\gamma_{ij} = \gamma_{ij}^A + \gamma_{ij}^B - \delta_{ij}$ by

$$\gamma_{ij} = \gamma_{ij}^A + \gamma_{ij}^B - \gamma_{ij}^B(x_A^i) = \gamma_{ij}^A + \gamma_{ij}^B - \gamma_{ij}^A(x_B^i). \quad (4.2.3)$$

The two expressions on the right-hand side are indeed equal thanks to the symmetry of our binary: its constituents have equal mass, no spin and their velocity components satisfy $v_A^i v_A^j = v_B^i v_B^j$ for all $i, j = 1, 2, 3$ in the centre-of-mass frame. Equation (4.2.3) manifestly ensures that at positions x_A^i and x_B^i we now recover the respective star's equilibrium metric and, hence, volume element. We graphically illustrate this improvement in the bottom panel of Fig. 4.2.

A minor complication arises from the fact that the resulting spatial metric does not asymptote towards δ_{ij} as $R \rightarrow \infty$. We accordingly impose outgoing Sommerfeld boundary conditions on the asymptotic background metric $2\delta_{ij} - \gamma_{ij}^A(x_B^i)$; in a set of test runs, however, we find this correction to result in very small changes well below the simulation's discretisation errors.

Finally, we note that the leading-order correction to the superposition as written in Eq. (4.2.3) does not work for asymmetric configurations with unequal masses or spins. Generalising the method to arbitrary binaries requires the subtraction of a spatially varying term rather than a constant $\gamma_{ij}^B(x_A^i) = \gamma_{ij}^A(x_B^i)$ or δ_{ij} . Such a generalisation may consist, for example, of a weighted sum of the terms $\gamma_{ij}^A(x_B^i)$ and $\gamma_{ij}^B(x_A^i)$. Leaving this generalisation for future work, we will focus on equal-mass systems in the remainder of this study and explore the degree of improvement achieved with Eq. (4.2.3).

Label	star A	star B	v	initial data	d/M
<code>mini</code>	mini	mini	0.1	plain	75.5, 101, 126, 151, 176
<code>+mini</code>	mini	mini	0.1	adjusted	75.5, 101, 126, 151, 176
<code>soli</code>	soli	soli	0.1	plain	16.7, 22.3, 27.9, 33.5, 39.1
<code>+soli</code>	soli	soli	0.1	adjusted	16.7, 22.3, 27.9, 33.5, 39.1

Table 4.2: The four types of BS binary head-on collisions simulated in this study. The individual BSs A and B are given either by the mini or solitonic model of Table 4.1, and start with initial velocity v directed towards each other. The initial data is constructed either by plain superposition (4.2.1) or by adjusting the superposed data according to Eq. (4.2.3). For each type of binary, we perform five collisions with initial separations d listed in the final column.

4.3 Models and Results

For our analysis of the two types of superposed initial data, we will now discuss time evolutions of binary BS head-on collisions. A head-on collision is characterised by the two individual BS models and three further parameters, the initial separation in units of the ADM mass, d/M , and the initial velocities v_A and v_B of the BSs. We perform all our simulations in the centre-of-mass frame, so that for equal-mass binaries, $v_A = -v_B =: v$. One additional parameter arises from the type of superposition used for the initial data construction: we either use the “plain” superposition of Eq. (4.2.1) or the “adjusted” method (4.2.3).

For all our simulations, we set $v = 0.1$; this value allows us to cover a wide range of initial separations without the simulations becoming prohibitively long. The BS binary configurations summarised in Table 4.2 then result in four sequences of head-on collisions labelled `mini`, `+mini`, `soli` and `+soli`, depending in the nature of the constituent BSs and the superposition method. For each sequence, we vary the BSs initial separation d (in units of the ADM mass) to estimate the dependence of the outcome on d . First, however, we test our interpretation of the improved superposition (4.2.3) by computing the level of constraint violations in the initial data.

4.3.1 Initial Constraint Violations

As discussed in Sec. 4.2.1 and in Appendix A of Ref. [133], the main shortcoming of the plain superposition procedure consists in the distortion of the volume element near the individual BSs’ centres and the resulting perturbation of the mass-energy inside the stars away from their equilibrium values. If this interpretation is correct, we would expect this effect to manifest itself in an elevated level of violation of the Hamiltonian constraint (2.1.50) which relates the energy density to the spacetime curvature. Put the other way round, we would expect our improved method (4.2.3) to reduce the Hamiltonian constraint violation. This is indeed the case as demonstrated in the upper panels of Fig. 4.3 where we plot the Hamiltonian constraint violation of the initial data along the collision axis for the configurations `mini` and `+mini` with $d = 101 M$ and the configurations `soli` and `+soli` with $d = 22.3 M$.

In the limit of zero boost velocity $v = 0$, this effect is even tractable through an analytic calculation which confirms that the improved superposition (4.2.3) ensures $\mathcal{H} = 0$ at the BS’s centres in isotropic coordinate; see 4.5 for more details.

Our adjustment (4.2.3) also leads to a reduction of the momentum constraint violations of the initial data, although the effect is less dramatic here. The bottom panels of Fig. 4.3 display the momentum constraint \mathcal{M}_x of Eq. (2.1.52) along the collision axis normalised by the momentum density $8\pi\mathcal{S}_x$; we see a reduction by a factor of a few over large parts of the BS interior for the modified data `+mini` and `+soli`.

The overall degree of initial constraint violations is rather small in all cases, well below 0.1 % for our adjusted data. These data should therefore also provide a significantly improved initial guess for a full

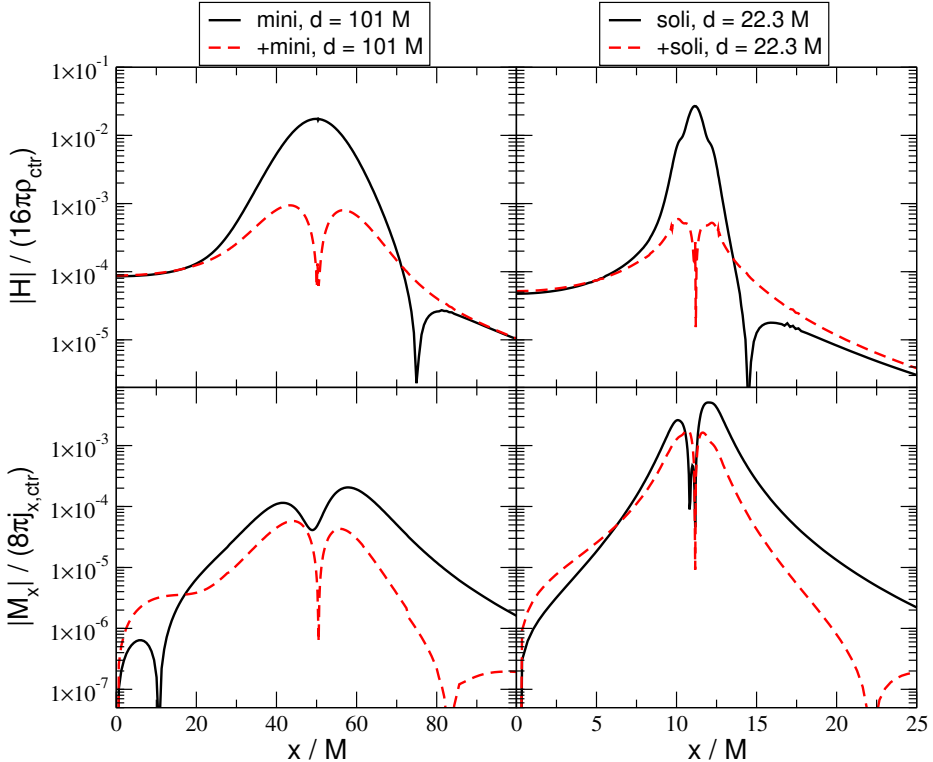


Figure 4.3: Upper row: The Hamiltonian constraint violation \mathcal{H} – Eq. (2.1.50) – normalised by the respective BS's central energy density $16\pi\rho_{\text{ctr}}$ is plotted along the collision axis of the binary configurations **mini**, **+mini** with $d = 101 M$ (left) and **soli**, **+soli** with $d = 22.3 M$ (right). The degree of violations is substantially reduced in the BS interior by using the improved superposition (4.2.3) for **+mini** and **+soli** relative to their plain counterparts; the maxima of \mathcal{H} have dropped by over an order of magnitude in both cases. Bottom row: The same analysis for the momentum constraint \mathcal{M}_x normalised by the central BS's momentum density $8\pi\mathcal{S}_x$. Here the improvement is less dramatic, but still yields a reduction by a factor of a few in the BS core.

constraint solving procedure. We leave such an analysis for future work and in the remainder of the work explore the impact of the adjustment (4.2.3) on the physical results obtained from the initial data’s time evolutions.

4.3.2 Convergence and Numerical Uncertainties

In order to put any differences in the time evolutions into context, we need to understand the uncertainties inherent to our numerical simulations. For this purpose, we have studied the convergence of the GW radiation generated by the head-on collisions of mini and solitonic BSs.

Figure 4.4 displays the convergence of the radiated energy E_{rad} as a function of time for the `+mini` configuration with $d = 101 M$ of Table 4.1 obtained for grid resolutions $h_1 = M/6.35$, $h_2 = M/9.53$ and $h_3 = M/12.70$ on the innermost refinement level and corresponding grid spacings on the other levels. The functions $E_{\text{rad}}(t)$ and their differences are shown in the bottom and top panel, respectively, of Fig. 4.4 together with an amplification of the high-resolution differences by the factor $Q_2 = 2.86$ for second-order convergence. The observation of second-order convergence is compatible with the second-order ingredients of the LEAN code, prolongation in time and the outgoing radiation boundary conditions. We believe that this dominance is mainly due to the smooth behaviour of the BS centre as compared with the case of black holes [141]. By using the second-order Richardson extrapolated result, we determine the discretisation error of our energy estimates as 0.9 % for h_3 which is the resolution employed for all remaining mini BS collisions. We have performed the same convergence analysis for the plain-superposition counterpart `mini` and for the dominant $(\ell, m) = (2, 0)$ multipole of the Newman-Penrose scalar of both configurations and obtained the same convergence and very similar relative errors.

In Fig. 4.5, we show the same convergence analysis for the solitonic collision `+soli` with $d = 22.3 M$ and resolutions $h_1 = M/22.9$, $h_2 = M/45.9$, $h_3 = M/68.8$. We observe second-order convergence during merger and ringdown and slightly higher convergence in the earlier infall phase. For the uncertainty estimate we conservatively use the second-order Richardson extrapolated result and obtain a discretisation error of about 0.07 % for our medium resolution h_2 which is the value we employ in our solitonic production runs. Again, we have repeated this analysis for the plain `soli` counterpart and the $(2, 0)$ GW multipole observing the same order of convergence and similar uncertainties. Our error estimate for the solitonic configurations is rather small in comparison to the mini BS collisions and we cannot entirely rule out a fortuitous cancellation of errors in our simulations. From this point on, we therefore use a conservative discretisation error estimate of 1 % for all our BS simulations.

A second source of uncertainty in our results is due to the extraction of the GW signal at finite radii rather than \mathcal{I}^+ . We determine this error by extracting the signal at multiple radii, fitting the resulting data by the series expansion $f = f_0 + f_1/r$, and comparing the result at our outermost extraction radius with the limit f_0 . This procedure results in errors in E_{rad} ranging between 0.5 % and 3 %. With the upper range, we arrive at a conservative total error budget for discretisation and extraction of about 4 %. As a final test, we have repeated the `mini` and `+mini` collisions for $d = 101 M$ with the independent GRCHOMBO code [142, 143] using the CCZ4 formulation [140] and obtain the same results within $\approx 1.5\%$. Bearing in mind these tests and a 4 % error budget, we next study the dynamics of the BS head-on collisions with and without our adjustment of the initial data.

4.3.3 Radiated Gravitational Wave Energy

For our first test, we compute the total radiated GW energy for all our head-on collisions focusing in particular on its dependence on the initial separation d of the BS centres. In this estimate we exclude any spurious or “junk” radiation content of the initial data⁵ by starting the integration at $t = R_{\text{ex}} + 40 M$.

⁵The non constraint-satisfying initial data of the boson-star binary is thought of as a combination of the “true” boson-star binary solution plus “something else”. This “something else” radiates away at early times and contributes to “junk radiation” - this radiation is unphysical and is omitted from our analysis as we are only interested in astrophysical phenomenology here.

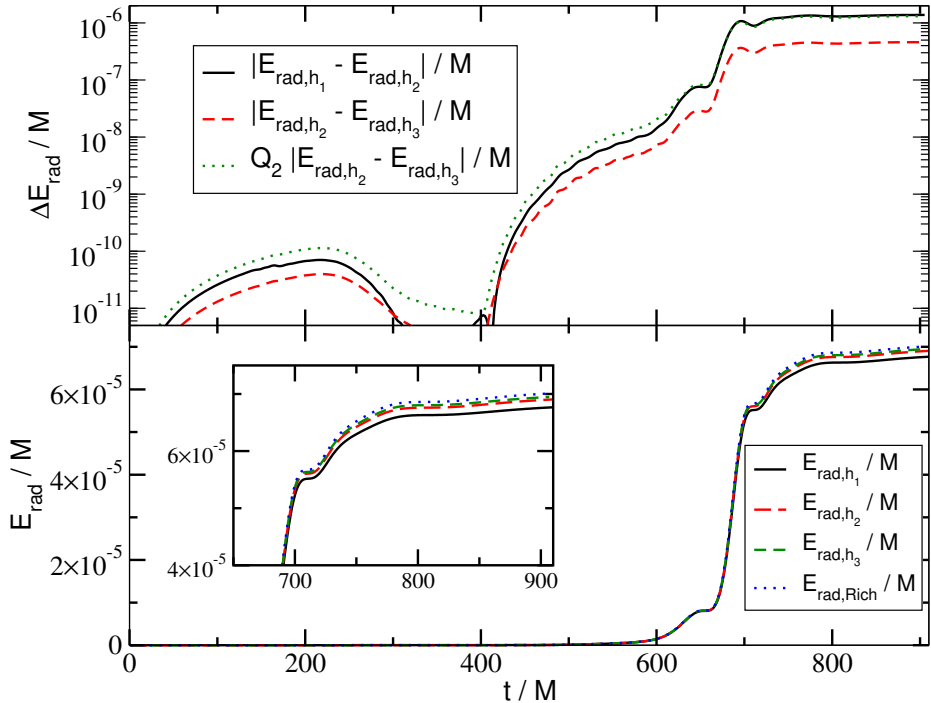


Figure 4.4: Convergence analysis for the GW energy extracted at $R_{\text{ex}} = 252 M$ from the head-on collision `+mini` of Table 4.1 with $d = 101 M$. For the resolutions $h_1 = M/6.35$, $h_2 = M/9.53$ and $h_3 = M/12.70$ (on the innermost refinement level), we obtain convergence close to second order (upper panel). The numerical error, obtained by comparing our results with the second-order Richardson extrapolated values (bottom panel), is 0.9% (1.6%, 3.6%) for our high (medium, coarse) resolutions.

Unless specified otherwise, all our results are extracted at $R_{\text{ex}} = 300 M$ for mini BS collisions and $R_{\text{ex}} = 84 M$ for the solitonic binaries.

The main effect of increasing the initial separation is a reduction of the (negative) binding energy of the binary and a corresponding increase of the collision velocity around merger. In the large d limit, however, this effect becomes negligible. For the comparatively large initial separations chosen in our collisions, we would therefore expect the function E_{rad} to be approximately constant⁶, possibly showing a mild increase with d . The mini BS collisions shown as black \times symbols in the upper panel of Fig. 4.6 exhibit a rather different behaviour: the radiated energy rapidly decreases with d and only levels off for $d \gtrsim 150 M$. We have verified that the excess energy for smaller d is not due to an elevated level of junk radiation which consistently contribute well below 0.1% of E_{rad} in all our mini BS collisions and has been excluded from the results of Fig. 4.6 anyway. The `+mini` BS collisions, in contrast, result in an approximately constant E_{rad} with a total variation approximately at the level of the numerical uncertainties. For $d \gtrsim 150 M$, both types of initial data yield compatible results, as is expected. The key benefit of our adjusted initial data is that they provide reliable results even for smaller initial separations suitable for starting BS inspirals.

The discrepancy is less pronounced for the head-on collisions of (denser) solitonic BSs; both types of initial data result in approximately constant E_{rad} . They differ, however, in the predicted amount of radiation at a level that is significant compared to the numerical uncertainties. As we will see below, this difference is accompanied by drastic differences in the BS's dynamics during the long infall period. We furthermore note that the mild but steady increase obtained for the adjusted `+soli` agrees better with

⁶For the mini boson star collision, the binding energy divided by the ADM mass is $E_{B,2\text{PN}}/M = \{0.010, 0.0049, -0.0017\}$ for the initial radii $r/M = \{\infty, 176, 75.5\}$. Similarly for the solitonic star with $E_{B,2\text{PN}}/M = \{0.010, -0.012, -0.037\}$ for the initial radii $r/M = \{\infty, 39.1, 16.7\}$. In both cases the binding energy was calculated using Equation (2.7) in [144] for the 2PN binding energy of a head-on collision of two point particles.

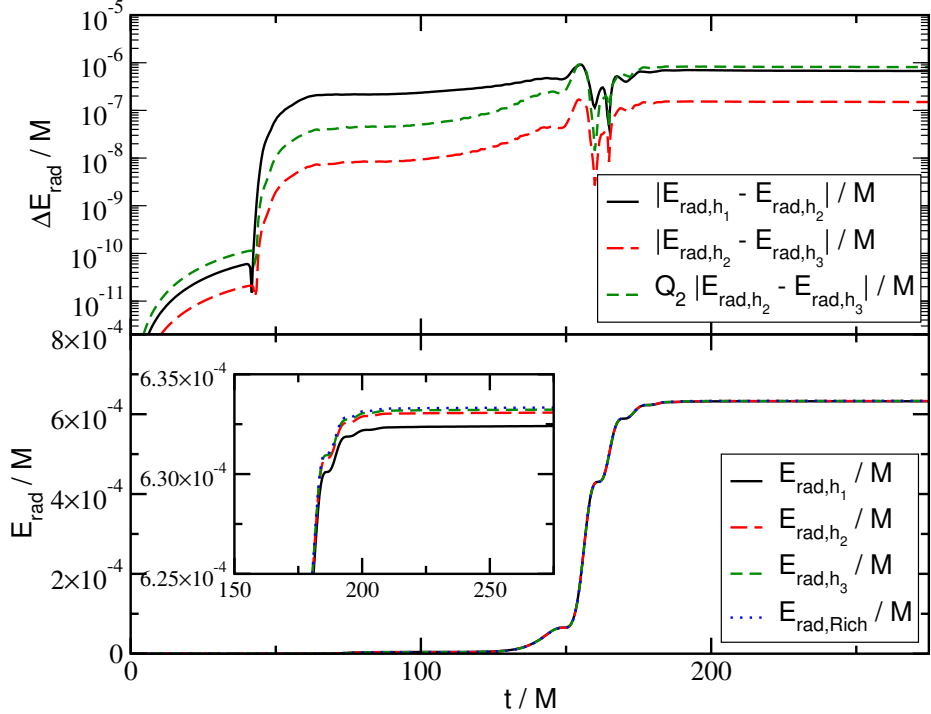


Figure 4.5: Convergence analysis as in Fig. 4.4 but for the configuration `+sol`i of Table 4.1 with $d = 22.3 M$ and resolutions $h_1 = M/22.9$, $h_2 = M/45.9$ and $h_3 = M/68.8$. The numerical error, obtained by comparing our results with the second-order Richardson extrapolated values (bottom panel), is 0.03% (0.07%, 0.6%) for our high (medium, coarse) resolutions.

the physical expectations.

The differences in the total radiated GW energy also manifest themselves in different amplitudes of the $(2, 0)$ multipole of the Newman-Penrose scalar Ψ_4 . This is displayed in Figs. 4.7 and 4.8 where we show the GW modes for the mini and solitonic collisions, respectively. The most prominent difference between the results for plain and adjusted initial data is the significant variation of the amplitude of the $(2, 0)$ mode in the plain mini BS collisions in the upper panel of Fig. 4.7. In contrast, the differences in the amplitudes in Fig. 4.8 for the solitonic collisions are very small. In fact, the differences in the radiated energy of the `sol`i and `+sol`i collisions mostly arise from a minor stretching of the signal for the `sol`i case; this effect is barely perceptible in Fig. 4.8 but is amplified by the integration in time when we calculate the energy. Finally, we note the different times of arrival of the main pulses in Fig. 4.8; especially for larger initial separation, the merger occurs earlier for the `sol`i configurations than for their adjusted counterparts `+sol`i. We will discuss this effect together with the evolution of the scalar field amplitude in the next subsection.

4.3.4 Evolution of the Scalar Amplitude and Gravitational Collapse

The adjustment (4.2.3) in the superposition of oscillations was originally developed in Ref. [133] to reduce spurious modulations in the scalar field amplitude; cf. their Fig. 7. In our simulations, this effect manifests itself most dramatically in the collisions of our solitonic BS configurations `sol`i and `+sol`i. From Fig. 4.1, we recall that the single-BS constituents of these binaries are stable, but highly compact stars, located fairly close to the instability threshold. We would therefore expect them to be more sensitive to spurious modulations in their central energy density. This is exactly what we observe in all time evolutions of the `sol`i configurations starting with plain-superposition initial data. As one example, we show in Fig. 4.9 the scalar amplitude at the individual BS centres and the BS trajectories as functions of time for the `sol`i and `+sol`i configurations starting with initial separation $d = 22.3 M$. Let us first consider the

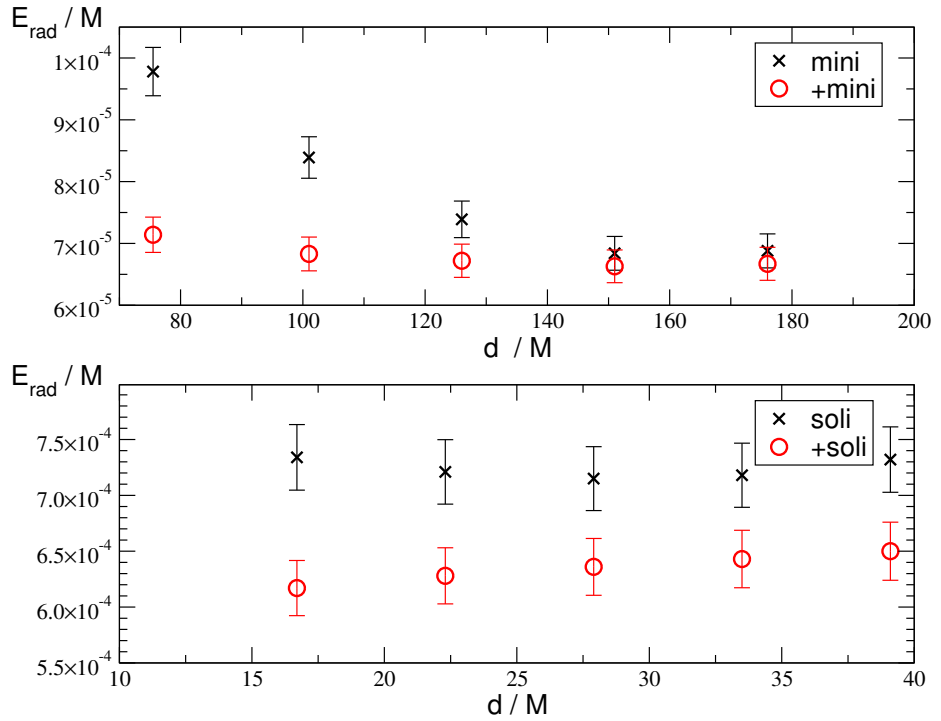


Figure 4.6: The GW energy E_{rad} generated in the head-on collision of mini (upper panel) and solitonic (lower panel) BS binaries starting with initial separation d and velocity $v = 0.1$ towards each other. For comparison, a non-spinning, equal-mass BH binary colliding head-on with the same boost velocity $v = 0.1$ radiates $E_{\text{rad}} = 6.0 \times 10^{-4} M$ [137].

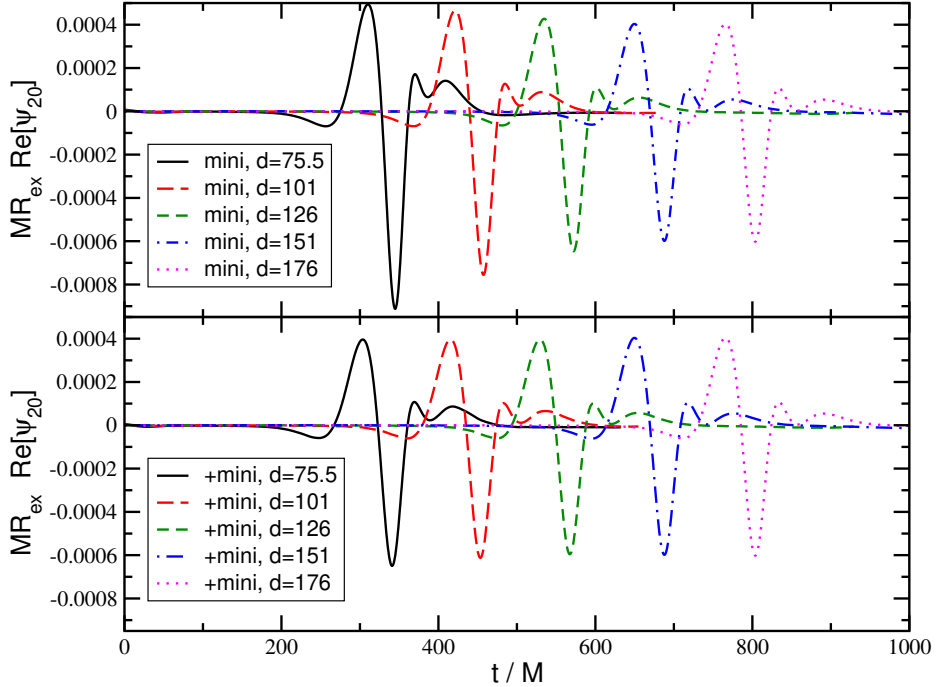


Figure 4.7: The $(2, 0)$ mode of the Newman-Penrose scalar for the mini boson star collisions of Table 4.1.

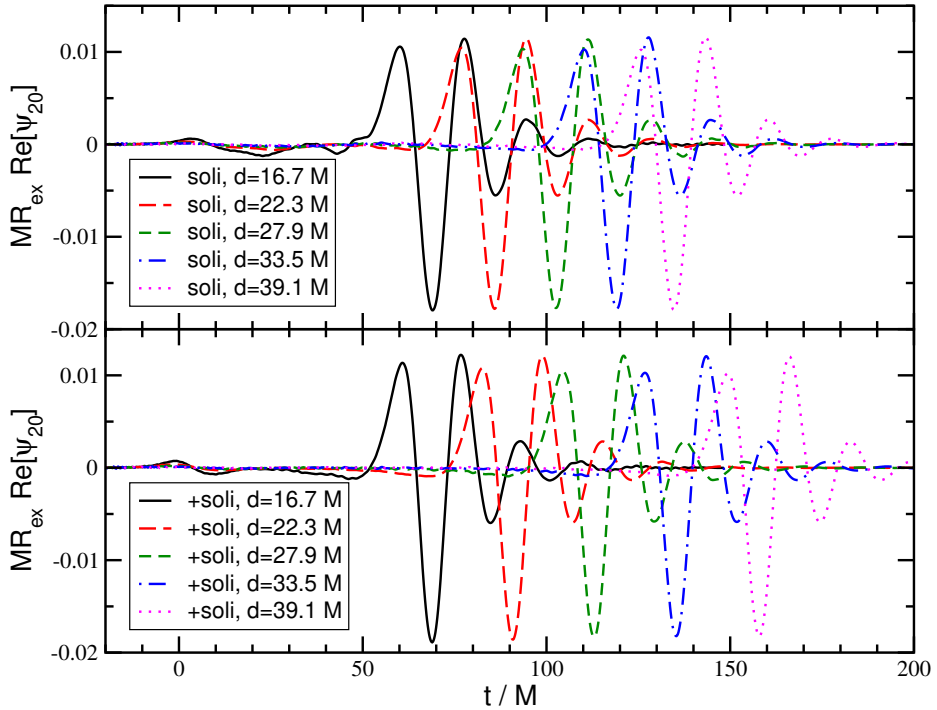


Figure 4.8: The $(2, 0)$ mode of the Newman-Penrose scalar for the solitonic boson star collisions of Table 4.1.

`soli` configuration using plain superposition displayed by the solid (black) curves. In the upper panel of Fig. 4.9, we clearly see that the scalar amplitude steadily increases, reaching a maximum around $t \approx 30 M$ and then rapidly drops to a near-zero level. Our interpretation of this behaviour as a collapse to a BH is confirmed by the horizon finder which reports an apparent horizon of irreducible mass $m_{\text{irr}} = 0.5 M$ just before the scalar field amplitude collapses; the time of the first identification of an apparent horizon is marked by the vertical dotted black line at $t \approx 30 M$. For reference we plot in the bottom panel the trajectory of the BS centres along their collision (here the x) axis. In agreement with the horizon mass $m_{\text{irr}} = 0.5 M$, the trajectory clearly indicates that around $t \approx 30 M$, the BSs are still far away from merging into a single BH; in units of the ADM mass, the individual BS radius is $r_{99} = 2.78 M$. We interpret this early BH collapse as a spurious feature due to the use of plain superposition in the initial data construction. This behaviour is also seen in the case of the real scalar field oscillations in [133].

We have tested this hypothesis with the evolution of the adjusted initial data. These exhibit a drastically different behaviour in the collision `+soli` displayed by the dashed (red) curves in Fig. 4.9. Throughout most of the infall, the central scalar amplitude is constant, it increases mildly when the BS trajectories meet near $x = 0$, and then rapidly drops to zero. Just as the maximum amplitude is reached, the horizon finder first computes an apparent horizon, now with $m_{\text{irr}} = 0.99 M$, as expected for a BH resulting from the merger; see the vertical red line in the figure.

As a final test of our interpretation, we compare the behaviour of the binary constituents with that of single BSs boosted with the same velocity $v = 0.1$. As expected, the scalar field amplitude at the centre of such a single BS remains constant within high precision, about $\mathcal{O}(10^{-5})$, on the timescale of our collisions. We have then repeated the single BS evolution by poisoning the initial data with the very same term (4.2.2) that is also added near a single BS's centre by the plain-superposition procedure. The resulting scalar amplitude at the centre of this poisoned BS is shown as the dash-dotted (blue) curve in Fig. 4.9 and nearly overlaps with the corresponding curve of the `soli` binary. Furthermore, the poisoned single BS collapses into a BH after nearly the same amount of time as indicated by the vertical blue

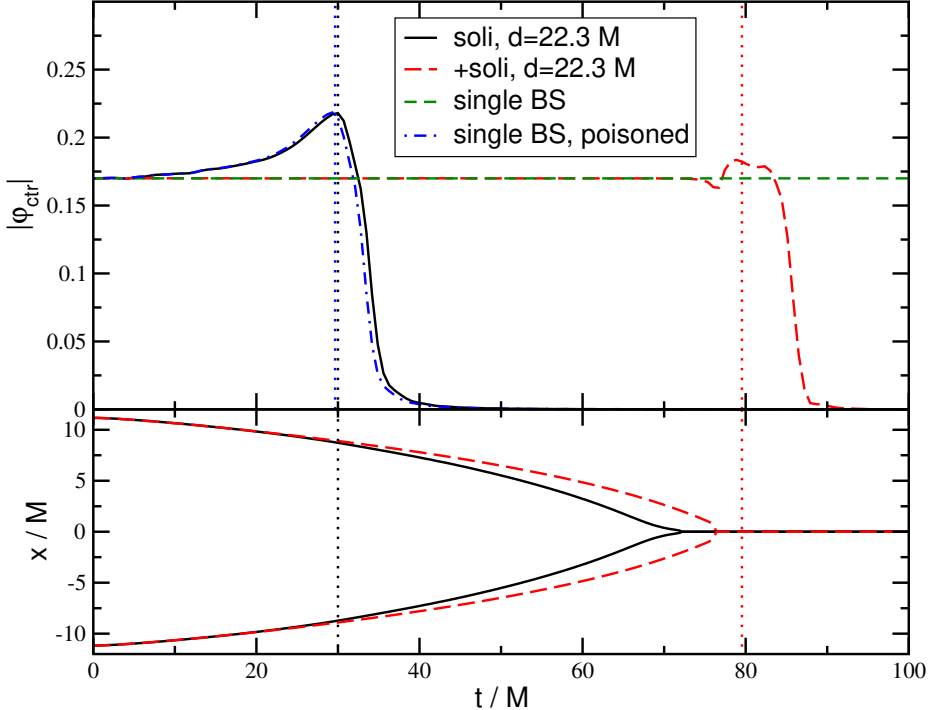


Figure 4.9: The central scalar-field amplitude $|\varphi_{\text{ctr}}|$ as a function of time for one BS in the head-on collisions of solitonic BSs with distance $d = 22.3 M$ (black solid and red long-dashed) as well as a single BS spacetime with the same parameters (green dashed) and the same single BS spacetime “poisoned” with the metric perturbation (4.2.2) that would arise in a simple superposition (see text for details). The dotted vertical lines mark the first location of an apparent horizon in the simulation of the same colour; as expected, no horizon ever forms in the evolution of the unpoisoned single BS. In the bottom panel, we show for reference the coordinate trajectories of the BS centres as obtained from locally Gauss-fitting the scalar profile. Around merger this procedure becomes inaccurate, so that the values around $t \approx 70 M$ should be regarded as qualitative measures, only.

dotted curve in the figure⁵. Clearly this behaviour of the single boosted BS is unphysical, and strongly indicates that the plain superposition of initial data introduces the same unphysical behaviour to our `soli` binary constituents. We have repeated this analysis for our entire sequence of `soli` binaries with very similar results: the individual BSs always collapse to distinct BHs about $\Delta t \approx 50 M$ before the binary merger.

Finally, the trajectories in the bottom panel of Fig. 4.9 indicate that the BS merger occurs a bit later for the `+soli` case than its plain-superposition counterpart `soli`. This is indeed a systematic effect we see for all initial separations d and which agrees with the different arrival times of the peak GW signals that we have already noticed in Fig. 4.8. We do not have a rigorous explanation of this effect, but note that the two trajectories in Fig. 4.9 start diverging right at the time of spurious BH formation in the `soli` binary. Perhaps some of the binding energy in BS collisions is converted into deformation energy rather than simply kinetic energy of the stars' centres of mass, slowing down the infall compared to the BH case⁶. Another explanation may consider the generally repulsive character of the scalar field which endows it with support against gravitational collapse. When the infalling BSs collapse to BHs, the scalar field essentially disappears as a potentially repulsive ingredient and the ensuing collision is sped up. Whatever ultimately generates this effect, the key observation of our study is that even rather mild imperfections in the initial data can drastically affect the physical outcome of the time evolution.

4.4 Conclusions

We have simulated head-on collisions of equal-mass, non-spinning boson stars and the GW radiation generated in the process. The main focus of our study is the construction of BS binary initial data and the ensuing impact of systematic errors on the physical results of the simulations. In particular, we have contrasted the relatively common method of plain superposition according to Eq. (4.2.1) with the adjusted procedure (4.2.3) first identified in Ref. [133] for oscillatons.

Our results demonstrate that the adjustment (4.2.3) in the construction of initial data leads to major improvements in the initial constraint violations and the time evolutions of binary BS collisions. In contrast, we find that the use of plain superposition for BS binary initial data may not only result in quantitatively wrong physical diagnostics but can even result in completely spurious physical behaviour such as premature gravitational collapse. In spite of the great simplicity of the adjustment (4.2.3) and its success in overcoming the most severe errors in the ensuing evolution, it is not free of shortcomings. (i) In its present form, the adjustment only works for a restricted class of binaries, namely equal-mass systems with no spin and velocity vectors satisfying $v_A^i v_A^j = v_B^i v_B^j$. (ii) Even with the adjustment, the initial data contain some residual constraint violations⁷; it should therefore primarily be regarded as an improved initial guess for a constraint solving procedure rather than the “real deal” in its own right. These shortcomings clearly point towards the most urgent generalisations of our work, overcoming the symmetry restrictions and adding a numerical constraint solver.

⁵Recall that this BS model is stable but fairly close to the stability threshold in Fig. 4.1 and therefore does not require a large perturbation to be toppled over the edge.

⁶We note that the relativistic Love numbers (which measure the tidal deformability) of non-rotating BHs are zero [145].

⁷Un-doing the normalisation by the factor $16\pi\rho_{\text{ctrl}} \sim 50$, the maximum constraint violation is approximately $\mathcal{H} \approx 0.01$ near the centre of a star in the improved initial data for a boson-star binary. This is comparable to roughly same value $\mathcal{H} \approx 0.01$ found for a black-hole binary in Figure 3 of [53]. This comparison of a boson-star binary to a black-hole binary should be taken with a pinch of salt as they are different objects and the black-hole example does not have an identical grid structure. In other words it should not be assumed that there are no more improvements that can be made in the Hamiltonian constraint of a boson-star binary. Additionally, the momentum constraint is not as successfully remedied by the modified initial data scheme.

4.5 Analytic Treatment of the Hamiltonian Constraint

For the case of two non-boosted BSs, we can analytically compute the Hamiltonian constraint violation at the stars' centres. Consider the spatial metric

$$\gamma_{ij}^A = \psi_A^4 \delta_{ij}, \quad (4.5.1)$$

for a non-boosted BS at position x_A^i . This metric is time-independent, so that for zero shift vector the extrinsic curvature vanishes, $\mathcal{K}_{ij}^A = 0$. For the second binary member, we likewise obtain a metric γ_{ij}^B and extrinsic curvature $\mathcal{K}_{ij}^B = 0$, now centred at position x_B^i .

For sufficiently large initial separation $d = \|x_B^i - x_A^i\|$, the exponential falloff of the scalar field implies

$$\begin{aligned} \phi_A(x_B) &= \phi_B(x_A) \approx 0, \\ \Pi_A(x_B) &= \Pi_B(x_A) \approx 0. \end{aligned} \quad (4.5.2)$$

The superposition of the two stars' scalar fields results in

$$\varphi = \varphi_A + \varphi_B, \quad \Pi = \Pi_A + \Pi_B, \quad (4.5.3)$$

and, combined with Eqs. (4.5.2),

$$\begin{aligned} \rho(x_A) &= \rho_A(x_A), \\ \rho(x_B) &= \rho_B(x_B). \end{aligned} \quad (4.5.4)$$

The single BS spacetimes are solutions to the Einstein equations; by using Eq. (4.5.1), their individual Hamiltonian constraints (2.1.50) simplify to

$$\mathcal{H}_A = 8\delta^{ij}\partial_i\partial_j\psi_A + 16\pi\psi_A^5\rho_A = 0, \quad (4.5.5)$$

and likewise for star B.

Next, we construct a binary spacetime by superposing the metric which leads to

$$\psi^4 = \psi_A^4 + \psi_B^4 - c^4, \quad (4.5.6)$$

where c is a constant which we keep arbitrary for the moment. For the Hamiltonian constraint of the superposed spacetime at the centre of star A, we find

$$\begin{aligned} \mathcal{H}(x_A^i) &= 8\delta^{ij}\partial_i\partial_j\psi_A(x_A^i) + 8\delta^{ij}\partial_i\partial_j\psi_B(x_A^i) \\ &\quad + 16\pi [\psi_A(x_A^i)^4 + \psi_B(x_A^i)^4 - c^4]^{5/4} \rho(x_A^i). \end{aligned} \quad (4.5.7)$$

We can now choose the constant c in accordance with the “trick” in Eq. (4.2.3), namely

$$c = \psi_B(x_A^i), \quad (4.5.8)$$

and the constraint simplifies to

$$\begin{aligned} \mathcal{H}(x_A^i) &= 8\delta^{ij}\partial_i\partial_j\psi_A(x_A^i) + 8\delta^{ij}\partial_i\partial_j\psi_B(x_A^i) \\ &\quad + 16\pi\psi_A(x_A^i)^4 \rho(x_A^i). \end{aligned} \quad (4.5.9)$$

By Eq. (4.5.5), the derivative of the conformal factor ψ_A cancels out the density ρ_A , so that

$$\mathcal{H}(x_A^i) = 8\delta^{ij}\partial_i\partial_j\psi_B(x_A^i). \quad (4.5.10)$$

Using the analogue of Eq. (4.5.5) for star B, we trade the right-hand side for the energy density,

$$\mathcal{H}(x_A^i) = -16\pi\psi_B(x_A^i)^4 \rho_B(x_A^i). \quad (4.5.11)$$

For sufficiently large separation d of the stars, however, this vanishes by Eq. (4.5.2) which is the result we wished to compute. By symmetry, we likewise obtain $\mathcal{H}(x_B^i) = 0$, which concludes our calculation.

Chapter 5

Local Continuity of Angular Momentum and Noether Charge for Matter in General Relativity

5.1 Local Continuity of Angular Momentum and Noether Charge for Matter in General Relativity

5.1.1 Introduction

Conservation laws play an important role in many areas of physics. For a general Lagrangian density \mathcal{L} , dependent on fields ϕ_i and derivatives $\partial_k \phi_i$ for $i \in \{1, 2, \dots, m\}$ and $k \in \{1, 2, \dots, n\}$, if a field transformation $\phi_i \rightarrow \phi_i + \delta\phi_i$ leaves the Lagrangian constant the Euler-Lagrange equations imply there is a conserved current \mathbf{J} , with zero divergence, given by

$$J^k = \sum_i \frac{\partial \mathcal{L}}{\partial(\partial_k \phi_i)} \delta\phi_i. \quad (5.1.1)$$

In curved space a conserved current \mathbf{J} satisfies $\nabla_\mu J^\mu = 0$. A charge Q within 3-volume V and a flux F through ∂V , the boundary of V , can be associated with \mathbf{J} as described later in Eqs. (5.1.19) and (5.1.20). If \mathbf{J} is conserved then Q is a conserved charge satisfying

$$\partial_t Q = F. \quad (5.1.2)$$

This says the rate of change of a charge in a volume V is equal to the flux across the boundary ∂V of V . In the case that \mathbf{J} has a non-zero divergence, $\nabla_\mu J^\mu \neq 0$, Eq. (5.1.2) generalises to the continuity equation

$$\partial_t Q = F - S, \quad (5.1.3)$$

where S is defined in Eq. (5.1.21); S is the source of \mathbf{J} in V which can be understood as the destruction or creation of charge Q . Eq. (5.1.3) is a simplified version of Eq. (5.1.15), later referred to as the QFS system.

Evaluation of the continuity equations above, and their corresponding charges Q , have many uses in the study of fundamental fields in Numerical Relativity. One such use is the measurement of the Noether current \mathbf{J} of a complex scalar/vector field which arises from a $U(1)$ gauge symmetry of the matter fields ψ_j of the form $\psi_j \rightarrow \psi_j e^{ia} \sim \psi_j + ia\psi_j$ for some small constant a and $j \in \{1, 2, \dots, n\}$. The total charge Q , also called Noether charge in this case, is useful to track during numerical simulations as it gives insight into the numerical quality of a simulation. A violation of Noether charge conservation can arise from insufficient resolution in some region of the simulation or due to boundary conditions in a finite volume simulation. In the case of Sommerfeld (outgoing wave) boundary conditions [45] we might expect charge to be transported out of a finite computational domain and the total charge Q in the simulation should decrease. Monitoring only Q within some volume V , it is impossible to tell whether Noether charge violation is due to a flux F through the surface ∂V or undesirable numerical inaccuracies such as dissipation. It is more useful to check whether the continuity Eq. (5.1.2) (or equivalently Eq. (5.1.3) if there were a non-zero source term) is obeyed for a finite domain V ; if this fails there is likely a problem as the continuity equations should be exactly observed for general spacetimes.

Another use of the continuity equations is to measure the amount of energy-momentum belonging to matter fields within a volume V . This has many possible applications such as calculating the total energy or momentum of compact objects such as boson stars and neutron stars. The energy-momentum of matter obeys a conservation law in General Relativity as given by Penrose [146] where the considered spacetime is assumed to admit a Killing vector. In the case a Killing vector exists then a conserved current \mathbf{J} associated with the energy-momentum tensor \mathbf{T} can be identified. The current is $J^\mu = T_\nu^\mu \xi^\nu$ for some Killing vector ξ and satisfies $\nabla_\mu J^\mu = 0$. If ξ is a Killing vector then Eq. (5.1.2) is the correct continuity equation and the charge Q is conserved. In General Relativity the existence of Killing vectors is rare, reserved for spacetimes with special symmetries. Generic dynamic spacetimes with no symmetries, such as inspirals and grazing collisions of compact objects, have no Killing vector fields. If there is no Killing vector the divergence of \mathbf{J} becomes $\nabla_\mu J^\mu = T^{\mu\nu} \nabla_\mu \xi_\nu$ and the source term S is non-zero. Now

Eq. (5.1.3) is the correct continuity equation and the charge Q is no longer conserved. In section 5.1.5 we will show how the choice of ξ affects the type of current \mathbf{J} , and therefore charge Q , obtained. While measures of energy or momentum are interesting in their own right, the measure of Eq. (5.1.3) within some volume V can be a good measure of numerical quality of a simulation in a similar fashion to the measure of Noether charge mentioned already.

When dealing with black-hole spacetimes resolution requirements typically become very strict towards the singularity and lead to a local violation of Eqs. (5.1.2) and (5.1.3). This might not doom a simulation as for most physical applications in GR singularities are contained by an event horizon and are therefore causally disconnected from the rest of the simulation; a resolution problem in the vicinity of a singularity therefore may not propagate to the exterior. It could be helpful instead to consider a volume \bar{V} equal to V but removing a set of finite volumes \tilde{V}_i which surround any singularities. Testing Eqs. (5.1.2) and (5.1.3) in volume \bar{V} would then give a measure of the simulation resolution untainted by the resolution issues at a singularity.

Currently in Numerical Relativity it is common to measure energy-momentum in a localised region with Eq. (5.1.19) for the charge Q where the charge density \mathcal{Q} is given in section 5.1.5. Examples of this can be seen in [147], [148], [149] and [150]. While this is a good measure it neglects any radiation and the transfer of energy-momentum between matter and spacetime curvature; if the spacetime does not contain the corresponding Killing vector the charge cannot be treated as a conserved quantity. Instead the combination of variables $Q - S$, where S is defined in Eq. (5.1.21) and \mathcal{S} in section 5.1.5, should be treated as a conserved quantity. Other popular methods to obtain the energy-momentum of a system include integrating asymptotic quantities such as the ADM mass and momentum, however these can not be used locally as they are defined in the limit of large radii only.

Recent work by Clough [151] evaluates Q , F and S for energy and linear momentum with the assumption that the approximate Killing vector ξ is a coordinate basis vector satisfying $\partial_i \xi^j = 0$. Successful numerical tests of Eq. (5.1.3) are given for fixed and dynamic background simulations.

This chapter builds on the work of [151] and generalises the system to measure angular momentum conservation and the conservation of Noether charges of complex scalar fields and spin-1 complex Proca fields. The assumption that the approximate Killing vector ξ is a basis vector satisfying $\partial_i \xi^j = 0$ is dropped and leads to a more general source term \mathcal{S} . The QFS system for angular momentum is also tested using fully non-linear numerical Relativity simulations of a spacetime consisting of two boson stars colliding in a grazing fashion.

This chapter is organised as follows. In section 5.1.2 the QFS system for a general non-conserved current is derived and section 5.1.3 explicitly expands the results for use with a spherical extraction surface. Even though no other extraction surfaces are considered, the results of 5.1.3 are easily adaptable to other shapes. Section 5.1.4 is a standalone derivation of the well known Noether charge density from the QFS perspective and goes on to find the flux variable; results for complex scalar fields and complex Proca fields are given. The application of the QFS system to energy momentum currents, angular momentum and energy are given in section 5.1.5. A fully non-linear test of the QFS system for angular momentum, using GRCHOMBO [46] [1] to perform Numerical Relativity simulations, is presented in section 5.1.6 along with a convergence analysis.

5.1.2 Derivation of the QFS System

For a spacetime $(\mathcal{M}, \mathbf{g})$ we start by defining a vector field \mathbf{J} and subjecting it to the following continuity equation,

$$\nabla_\mu J^\mu = S, \quad (5.1.4)$$

where S is a source term and describes the non-conservation of \mathbf{J} . In the case $S = 0$ the current is conserved. We are interested in the charge density \mathcal{Q} and source density \mathcal{S} associated with \mathbf{J} in a spatial

3-volume $V \in_t$. Here Σ_t is the usual 3-dimensional spacelike manifold consisting of the set of all points with constant time coordinate t , equipped with metric γ . We are also interested in the flux density \mathcal{F} through ∂V , the boundary of V with metric σ . Σ_t is spanned by spatial coordinates x^i related to the full spacetime coordinates x^μ by $x^\mu = \{t, x^i\}$. The normal to Σ_t is the unit co-vector \mathbf{n} defined as,

$$n_\mu := \frac{\nabla_\mu t}{\sqrt{g^{\rho\sigma}\nabla_\rho t\nabla_\sigma t}} = -(\alpha, 0, 0, 0), \quad (5.1.5)$$

$$n^\mu = \frac{1}{\alpha} (t^\mu - \beta^\mu) = \frac{1}{\alpha} (1, -\beta^i), \quad (5.1.6)$$

where (α, β^i) are the usual lapse and shift from the ADM 3+1 spacetime decomposition [152]. The reader is directed to section 2.1 or [11] for a comprehensive introduction to the 3 + 1 decomposition. In Eq. (5.1.6), $t^\mu = (1, 0, 0, 0)$ is the future directed vector and is distinct from n^μ . Time vector \mathbf{t} is useful as its integral curves form lines of constant spatial coordinates. With this knowledge we can define the 4-volume M , the spatial 3-volume V evolved along integral curves of \mathbf{t} between times $t_0 \leq t \leq t_0 + \delta t$ in the limit $\delta t \rightarrow 0$. Finally we define the 3-dimensional volume H , with metric \mathbf{h} . H is the evolution of ∂V along integral curves of \mathbf{t} between times $t_0 \leq t \leq t_0 + \delta t$ and is the 3-volume the flux crosses; clearly our definition of H will affect our definition of flux density. There is no reason to choose the timelike vector \mathbf{t} , rather than \mathbf{n} , to evolve V and ∂V in time and both will result in a different definition of flux density. However, it is shown in section 5.1.9 that these two choices result in the same total integrated flux. A diagram summarising the relevant geometry can be found in Fig. 5.1.

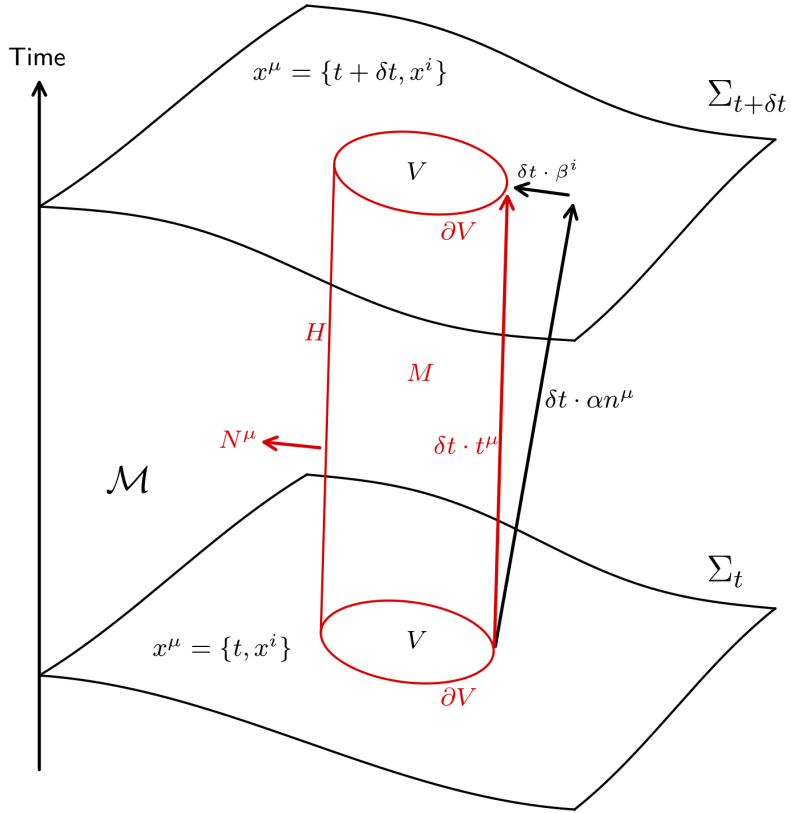


Figure 5.1: Diagram of relevant geometry for derivation of QFS system in section 5.1.2 on manifold \mathcal{M} . Σ_t is the spatial hypersurface at time t and $\Sigma_{t+\delta t}$ is the the spatial hypersurface at a later time $t + \delta t$. V is the coordinate volume, with surface ∂V , that we wish to use as an extraction volume on Σ_t . The sides of the red cylinder are H , defined by ∂V evolved along integral curves of $\mathbf{t} = \partial_t$. The interior of H between times t and $t + \delta t$ is M . Evolving ∂V forward in time with \mathbf{n} , as demonstrated with the long black arrow, gives a different coordinate volume on $\Sigma_{t+\delta t}$ than on Σ_t .

With the relevant geometry discussed we can derive the QFS system, Eq. (5.1.3), by integrating Eq. (5.1.4) over M ;

$$\int_M \nabla \cdot \mathbf{J} \sqrt{-g} dx^4 = \int_M S \sqrt{-g} dx^4. \quad (5.1.7)$$

Let us start by using Gauss' theorem for curved space, discussed in section 1.3.5 or [20], on the left hand side,

$$\int_M \nabla \cdot \mathbf{J} \sqrt{-g} dx^4 = \int_{\partial M} \hat{\mathbf{s}} \cdot \mathbf{J} \sqrt{(3)g} dx^3, \quad (5.1.8)$$

with $\sqrt{(3)g}$ being the volume element of a generic 3-surface and $\hat{\mathbf{s}}$ being the corresponding unit normal. Note that $\hat{\mathbf{s}}$ is outward directed when spacelike and inward directed when timelike. The integral of $\nabla \cdot \mathbf{J}$ over M is now transformed to a surface integral of \mathbf{J} over the compound 3-volume ∂M . This surface is split into an integral over H and two integrals over V at times t_0 and $t_0 + \delta t$. The integrals over V give,

$$\begin{aligned} & \left(\int_V^{(t=t_0)} - \int_V^{(t=t_0+\delta t)} \right) \mathbf{n} \cdot \mathbf{J} \sqrt{\gamma} d^3x, \\ &= - \int_V \left[(\mathbf{n} \cdot \mathbf{J} \sqrt{\gamma})_{t+\delta t} - (\mathbf{n} \cdot \mathbf{J} \sqrt{\gamma})_t \right] d^3x, \end{aligned} \quad (5.1.9)$$

$$= -\delta t \partial_t \int_V \mathbf{n} \cdot \mathbf{J} \sqrt{\gamma} d^3x, \quad (5.1.10)$$

where we made use of the fact that the coordinate volume V is constant for all times due to it evolving in time with t^μ . Here $\sqrt{\gamma}$ is the volume element on the spacelike manifold Σ_t . Now let us evaluate the integral over H , with metric \mathbf{h} of signature $\{-, +, +\}$,

$$\begin{aligned} & \int_H \mathbf{N} \cdot \mathbf{J} \sqrt{-h} d^2x dt, \\ &= \int_{\partial V} \mathbf{N} \cdot \mathbf{J} \sqrt{-h} d^2x \int_t^{t+\delta t} dt, \end{aligned} \quad (5.1.11)$$

$$= \delta t \int_{\partial V} \mathbf{N} \cdot \mathbf{J} \sqrt{-h} d^2x, \quad (5.1.12)$$

where \mathbf{N} is the unit normal to H as shown in Fig. 5.1. Given that \mathbf{n} is not tangent to H (but the time vector \mathbf{t} is) we have $\mathbf{N} \cdot \mathbf{n} \neq 0$ and $\mathbf{N} \cdot \mathbf{t} = 0$. This means we must normalise \mathbf{N} with metric \mathbf{g} and not γ as \mathbf{N} is not tangent to Σ_t and $\mathbf{g}(\mathbf{N}, \mathbf{N}) \neq \gamma(\mathbf{N}, \mathbf{N})$. In other words, \mathbf{N} is a 4-vector in the case we time evolve V with time vector \mathbf{t} but \mathbf{N} is a 3-vector if we time evolve with \mathbf{n} . Finally the right hand side source integral from (5.1.7) becomes,

$$\begin{aligned} & \int_M S \sqrt{-g} dx^4, \\ &= \int_V S \sqrt{-g} dx^3 \int_t^{t+\delta t} dt, \end{aligned} \quad (5.1.13)$$

$$= \delta t \int_V S \alpha \sqrt{\gamma} dx^3. \quad (5.1.14)$$

Combining Eqs. (5.1.10), (5.1.12) and (5.1.14) transforms Eq. (5.1.7) into,

$$\partial_t \int_V \mathcal{Q} \sqrt{\gamma} d^3x = \int_{\partial V} \mathcal{F} \sqrt{\sigma} d^2x - \int_V \mathcal{S} \sqrt{\gamma} d^3x, \quad (5.1.15)$$

where the density, flux density and source density ($\mathcal{Q}, \mathcal{F}, \mathcal{S}$) of angular momentum are defined as,

$$\mathcal{Q} := J^\mu n_\mu, \quad (5.1.16)$$

$$\mathcal{F} := \frac{\sqrt{-h}}{\sqrt{\sigma}} J^\mu N_\mu, \quad (5.1.17)$$

$$\mathcal{S} := \alpha S. \quad (5.1.18)$$

The integrated version of these quantities can be written as

$$Q := \int_V \mathcal{Q} \sqrt{\gamma} d^3x, \quad (5.1.19)$$

$$F := \int_{\partial V} \mathcal{F} \sqrt{\sigma} d^2x, \quad (5.1.20)$$

$$S := \int_V \mathcal{S} \sqrt{\gamma} d^3x. \quad (5.1.21)$$

For later sections it is useful to split the normal vector \mathbf{N} into its spacelike and timelike parts,

$$N_\mu = \perp N_\mu - \mathbf{n} \cdot \mathbf{N} n_\mu, \quad (5.1.22)$$

where $\perp N_\mu = \perp^\nu_\mu N_\nu$ is the projected part of \mathbf{N} onto Σ_t with $\mathbf{n} \cdot \perp \mathbf{N} = 0$ and \perp is the projection operator onto Σ_t ,

$$\perp^\nu_\mu = \delta^\nu_\mu + n^\mu n_\nu. \quad (5.1.23)$$

Using Eqs. (5.1.22) and (5.1.23) the flux term becomes,

$$\mathcal{F} = \frac{\sqrt{-h}}{\sqrt{\sigma}} J^\mu (\perp N_\mu - \mathbf{n} \cdot \mathbf{N} n_\mu), \quad (5.1.24)$$

$$= \frac{\sqrt{-h}}{\sqrt{\sigma}} (\gamma^{\mu\nu} J_\mu N_\nu - \mathbf{n} \cdot \mathbf{N} \mathcal{Q}). \quad (5.1.25)$$

The term on the left arises from flux through the surface ∂V and the term on the right is a consequence of the coordinate volume V moving with respect to a normal observer with worldline traced by \mathbf{n} . Writing the flux term as above makes it obvious how the definition of flux depends on the 3-volume H which determines $\sqrt{-h}$, $\sqrt{\sigma}$ and \mathbf{N} . Equivalently it can be seen that the density (5.1.16) and source (5.1.18) terms do not depend on the extraction surface.

5.1.3 Application to Spherical extraction

The numerical application of the QFS system in section 5.1.6 chooses a spherical coordinate volume V to extract the angular momentum flux. Using standard Cartesian and spherical polar coordinates, $x_{\text{cart}}^i = \{x, y, z\}$ and $x_{\text{polar}}^i = \{r, \theta, \phi\}$ respectively, we can define H as the coordinate volume $r = r_0$, $t_0 \leq t \leq t+\delta t$. Thus, the normal \mathbf{N} to H is proportional to $\nabla(r-r_0) = \nabla(\sqrt{x^2+y^2+z^2}-r_0)$. Explicitly calculating the components N_μ , and normalising to unity, with spherical polar spacelike coordinates gives,

$$N_\mu = \frac{\nabla_\mu r}{\sqrt{g^{\rho\sigma}\nabla_\rho r \nabla_\sigma r}}, \quad (5.1.26)$$

$$= \frac{1}{\sqrt{g^{rr}}}(0, 1, 0, 0). \quad (5.1.27)$$

Note that if we had chosen H , the future evolution of ∂V , to be evolved along the unit vector \mathbf{n} rather than time vector \mathbf{t} then we would have obtained a different definition of \mathbf{N} perpendicular to \mathbf{n} rather than \mathbf{t} . The consequences of the alternate choice of H are explored in section 5.1.9.

The density and source terms \mathcal{Q} and \mathcal{S} do not depend on the integration domain V , but the flux term \mathcal{F} does. The calculation of the Flux term requires the evaluation of the volume element $\sqrt{-h}$ of H . Due to the choice that H is the surface of constant radial coordinate, finding the metric of this surface is straightforward. Here we define spherical polar coordinates $x^\mu = \{t, r, \theta, \phi\}$ on \mathcal{M} and $X^m = \{t, \theta, \phi\}$ spanning H . Projecting the 4-metric \mathbf{g} onto H we can write

$${}^{(4)}h_{\mu\nu} = g_{\mu\nu} - N_\mu N_\nu, \quad (5.1.28)$$

where ${}^4\mathbf{h}$ belongs to \mathcal{M} . The line element of a curve residing in H can be equivalently evaluated in \mathcal{M} or H ; the pullback of ${}^4\mathbf{h}$ from $\mathcal{M}|_{r=r_0}$ to H gives the 3-metric \mathbf{h} belonging to H ,

$$h_{mn} = {}^4h_{\mu\nu} \frac{\partial x^\mu}{\partial X^m} \frac{\partial x^\nu}{\partial X^n}, \quad (5.1.29)$$

$$= \begin{pmatrix} g_{tt} & g_{t\theta} & g_{t\phi} \\ g_{\theta t} & g_{\theta\theta} & g_{\theta\phi} \\ g_{\phi t} & g_{\phi\theta} & g_{\phi\phi} \end{pmatrix}. \quad (5.1.30)$$

A similar argument can be made for ∂V , the set of all points satisfying $r = r_0$ and $t = t_0$, with metric $\boldsymbol{\sigma}$. The metric components and volume element are

$$\sigma_{ab} = \begin{pmatrix} g_{\theta\theta} & g_{\theta\phi} \\ g_{\phi\theta} & g_{\phi\phi} \end{pmatrix}, \quad (5.1.31)$$

$$\sqrt{\sigma} = \sqrt{g_{\theta\theta}g_{\phi\phi} - g_{\phi\theta}g_{\theta\phi}}. \quad (5.1.32)$$

Using Cramer's rule for the inverse of a matrix with Eqs. (5.1.30) and (5.1.31) we get

$$h^{tt} = \frac{\sigma}{h}, \quad (5.1.33)$$

and reading from Eq. (5.1.28) gives

$${}^4h^{tt} = g^{tt} - N^t N^t, \quad (5.1.34)$$

$$= -\frac{1}{\alpha^2} \left(\frac{\gamma^{rr}}{g^{rr}} \right). \quad (5.1.35)$$

Similarly to Eq. (5.1.29), the pushforward of \mathbf{h} on H to ${}^4\mathbf{h}$ on $\mathcal{M}|_{r=r_0}$ gives

$${}^4h^{\mu\nu} = h^{mn} \frac{\partial x^\mu}{\partial X^m} \frac{\partial x^\nu}{\partial X^n}, \quad (5.1.36)$$

$$= \begin{pmatrix} h^{tt} & 0 & h^{t\theta} & h^{t\phi} \\ 0 & 0 & 0 & 0 \\ h^{\theta t} & 0 & h^{\theta\theta} & h^{\theta\phi} \\ h^{\phi t} & 0 & h^{\phi\theta} & h^{\phi\phi} \end{pmatrix}, \quad (5.1.37)$$

which shows that $h^{tt} = {}^4h^{tt}$. Combining Eqs. (5.1.33) and (5.1.35) it can be shown that

$$\sqrt{-h} = \alpha \sqrt{\sigma} \sqrt{\frac{g^{rr}}{\gamma^{rr}}}. \quad (5.1.38)$$

Using this with Eq. (5.1.27) we can expand Eq. (5.1.17) for the flux term \mathcal{F} ,

$$\mathcal{F} = \frac{\sqrt{-h}}{\sqrt{\sigma}} J^\mu N_\mu = \frac{\alpha}{\sqrt{\gamma^{rr}}} J^r, \quad (5.1.39)$$

but for practical purposes it is helpful to decompose this in terms of 3+1 variables as in Eq. (5.1.25),

$$\mathcal{F} = \alpha \frac{\sqrt{g^{rr}}}{\sqrt{\gamma^{rr}}} (\gamma^{\mu\nu} J_\nu N_\mu - \mathbf{n} \cdot \mathbf{N} \mathcal{Q}), \quad (5.1.40)$$

$$= \alpha \frac{\sqrt{g^{rr}}}{\sqrt{\gamma^{rr}}} \left(\gamma^{rr} J_\nu \frac{1}{\sqrt{g^{rr}}} + \alpha^{-1} \beta^r \frac{1}{\sqrt{g^{rr}}} \mathcal{Q} \right), \quad (5.1.41)$$

$$= \frac{1}{\sqrt{\gamma^{rr}}} (\alpha \gamma^{rr} J_\nu + \beta^r \mathcal{Q}). \quad (5.1.42)$$

It is straightforward to re-derive the results of this section for other extraction volume shapes, such as cylinders or cubes/rectangles, with a redefinition of spacelike volume V giving rise to different \mathbf{N} , H and ∂V . It is wise to pick suitable coordinates adapted to the asymptotic symmetry of the problem.

5.1.4 Noether Currents

In this section we apply the previous results of the QFS system Eq. (5.1.15) to the continuity of Noether charge for both a complex scalar and the Proca field. The charge \mathcal{Q} represents the number density of particles. Since the total particle number minus antiparticle number is always conserved the conservation law is exact and the source term \mathcal{S} vanishes.

Globally the total Noether charge should be conserved, however in numerical simulation this might not always be the case. Two common ways for non-conservation to occur are for the matter to interact with the simulation boundary conditions (often unproblematic) or some region of the simulation being insufficiently resolved (often problematic). Without knowledge of the Noether flux it is difficult to know what a change in Noether charge should be attributed to. If a large extraction volume containing the relevant physics shows a violation of Eq. (5.1.15) then the change in total Noether charge being due to boundary conditions can be ruled out and resolution is likely the culprit.

When considering black-hole spacetimes it is common for Noether charge to be dissipated as matter approaches the singularity; this is due to resolution requirements typically becoming very high in this region. The violation of Eq. (5.1.15) inside a black-hole horizon might not cause any resolution problems for the black-hole exterior however due to causal disconnection. If the extraction volume is modified to exclude finite regions containing any black-hole singularities then Eq. (5.1.15) could be used to monitor the conservation of Noether charge away from troublesome singularities. This would be a good way of checking the resolution of a matter field in situations such as boson/Proca stars colliding with black holes or scalar/vector accretion onto a black hole.

Complex Scalar Fields

In this section we consider the conserved Noether current associated with a complex scalar field φ with Lagrangian

$$\mathcal{L} = \left(\frac{1}{16\pi} R - \frac{1}{2} g^{\mu\nu} \nabla_\mu \bar{\varphi} \nabla_\nu \varphi - \frac{1}{2} V(\varphi \bar{\varphi}) \right) \sqrt{-g}, \quad (5.1.43)$$

where V is some real potential function. There is a U(1) symmetry where a complex rotation of the scalar field $\varphi \rightarrow \varphi e^{ia}$, for constant a , leaves the action unchanged. The associated Noether current \mathbf{J} can be found in [153],

$$J^\mu = ig^{\mu\nu}(\varphi \partial_\nu \bar{\varphi} - \bar{\varphi} \partial_\nu \varphi), \quad (5.1.44)$$

and satisfies $\nabla \cdot \mathbf{J} = 0$. The conservation is exact here which tells us the source term vanishes. In this case the Noether charge density (5.1.16) and flux density (5.1.25) are,

$$\mathcal{Q} = n_\mu J^\mu, \quad (5.1.45)$$

$$= i(\varphi n^\mu \partial_\mu \bar{\varphi} - \bar{\varphi} n^\mu \partial_\mu \varphi), \quad (5.1.46)$$

$$= i(\bar{\varphi} \Pi - \bar{\Pi} \varphi), \quad (5.1.47)$$

$$\mathcal{F} = \frac{\sqrt{-h}}{\sqrt{\sigma}} (i\gamma^{\nu\mu} N_\mu (\varphi \partial_\nu \bar{\varphi} - \bar{\varphi} \partial_\nu \varphi) - \mathbf{n} \cdot \mathbf{N} \mathcal{Q}), \quad (5.1.48)$$

where $\Pi = -\mathbf{n} \cdot \nabla \varphi$ is the momentum of the scalar field. This is not quite the same as the canonical conjugate momentum p_φ is defined by,

$$p_\varphi := \frac{\delta \mathcal{L}}{\delta \dot{\varphi}} = -\frac{1}{2} \sqrt{-g} g^{t\mu} \partial_\mu \bar{\varphi} = \frac{1}{2\alpha} \sqrt{-g} n_\nu g^{\nu\mu} \partial_\mu \bar{\varphi} = -\frac{1}{2\alpha} \sqrt{-g} \bar{\Pi} = -\frac{1}{2} \sqrt{\gamma} \bar{\Pi}. \quad (5.1.49)$$

Using Eq. (5.1.42) for a spherical extraction surface, and spherical polar spacelike coordinates $\{r, \theta, \phi\}$, this explicitly becomes

$$\mathcal{F} = \frac{1}{\sqrt{\gamma^{rr}}} (i\alpha \gamma^{\nu r} (\varphi \partial_\nu \bar{\varphi} - \bar{\varphi} \partial_\nu \varphi) + \beta^r \mathcal{Q}). \quad (5.1.50)$$

Complex Vector Fields

The Complex vector field \mathbf{A} , also called a Proca field, has Lagrangian

$$\mathcal{L} = \left(\frac{1}{16\pi} R - \frac{1}{4} F^{\mu\nu} \bar{F}_{\mu\nu} - \frac{1}{2} V(A^\mu \bar{A}_\mu) \right) \sqrt{-g}, \quad (5.1.51)$$

where $F_{\mu\nu} = \nabla_\mu A_\nu - \nabla_\nu A_\mu$. Again V is some real potential function. The action is invariant under a similar $U(1)$ complex rotation of the vector field $A^\mu \rightarrow A^\mu e^{ia}$ for constant a . Following [154] this leads to the following Noether current \mathbf{J} ,

$$J_\mu = i \left(\bar{A}^\nu F_{\mu\nu} - A^\nu \bar{F}_{\mu\nu} \right), \quad (5.1.52)$$

which again satisfies $\nabla \cdot \mathbf{J} = 0$ and the source term vanishes. Defining a 3+1 decomposition compatible with [155] gives,

$$A_\mu := n_\mu \Phi + a_\mu, \quad (5.1.53)$$

$$\Phi = -A_\mu n^\mu, \quad (5.1.54)$$

$$a_\mu = \perp_\mu^\nu A_\nu, \quad (5.1.55)$$

$$F_{\mu\nu} := n_\mu E_\nu - n_\nu E_\mu + B_{\mu\nu}, \quad (5.1.56)$$

$$E_\mu = \perp_\mu^\nu F_{\nu\alpha} n^\alpha, \quad (5.1.57)$$

$$B_{\mu\nu} = \perp_\mu^\alpha \perp_\nu^\beta F_{\alpha\beta} = D_\mu a_\nu - D_\nu a_\mu, \quad (5.1.58)$$

where ϕ , \mathbf{E} , \mathbf{a} and \mathbf{B} all belong to Σ_t . Additionally \mathbf{D} is the covariant 3-derivative of Σ_t . Note that \mathbf{F} has no time-time component as $n_\mu n_\nu F^{\mu\nu} = 0$ from the anti-symmetry of \mathbf{F} . Using these, the Noether charge (5.1.16) becomes,

$$\mathcal{Q} = n_\mu J^\mu, \quad (5.1.59)$$

$$= i \left(n^\mu \bar{A}^\nu F_{\mu\nu} - n^\mu A^\nu \bar{F}_{\mu\nu} \right), \quad (5.1.60)$$

$$= i \left(n^\mu \bar{a}^\nu n_\mu E_\nu - n^\mu a^\nu n_\mu \bar{E}_\nu \right), \quad (5.1.61)$$

$$= i \left(a^\nu \bar{E}_\nu - \bar{a}^\nu E_\nu \right). \quad (5.1.62)$$

Using Eq. (5.1.25), the Noether flux is,

$$\mathcal{F} = \frac{\sqrt{-h}}{\sqrt{\sigma}} (\vec{N}^\mu j_\mu - \mathbf{n} \cdot \mathbf{N} \mathcal{Q}), \quad (5.1.63)$$

$$= \frac{\sqrt{-h}}{\sqrt{\sigma}} (i \vec{N}^\mu (\bar{A}^\nu F_{\mu\nu} - A^\nu \bar{F}_{\mu\nu}) - \mathbf{n} \cdot \mathbf{N} \mathcal{Q}). \quad (5.1.64)$$

Expanding $\vec{N}^\mu \bar{A}^\nu F_{\mu\nu}$ using the 3+1 split,

$$\vec{N}^\mu \bar{A}^\nu F_{\mu\nu} = \vec{N}^\mu \bar{a}^\nu B_{\mu\nu} - \vec{N}^\mu \bar{\Phi} n^\nu n_\nu E_\mu, \quad (5.1.65)$$

$$= \gamma^{\mu\rho} N_\rho (\bar{a}^\nu B_{\mu\nu} + \bar{\Phi} E_\mu), \quad (5.1.66)$$

$$= \gamma^{\mu\rho} N_\rho (\bar{a}^\nu (\partial_\mu a_\nu - \partial_\nu a_\mu) + \bar{\Phi} E_\mu), \quad (5.1.67)$$

where the Christoffel symbols from D_μ in $B_{\mu\nu}$ cancel out. Putting this into the expression for the Proca Noether flux we get,

$$\begin{aligned} \mathcal{F} &= \frac{\sqrt{-h}}{\sqrt{\sigma}} \{ i \gamma^{\mu\rho} N_\rho [\bar{\Phi} E_\mu - \Phi \bar{E}_\mu + \bar{a}^\nu (\partial_\mu a_\nu - \partial_\nu a_\mu) \\ &\quad - a^\nu (\partial_\mu \bar{a}_\nu - \partial_\nu \bar{a}_\mu)] - \mathbf{n} \cdot \mathbf{N} \mathcal{Q} \}, \end{aligned} \quad (5.1.68)$$

and equation (5.1.42) gives the flux term for a spherical extraction surface,

$$\begin{aligned}\mathcal{F} = \frac{1}{\sqrt{\gamma^{rr}}} & (\mathrm{i}\alpha\gamma^{\mu r}(\bar{\Phi}E_\mu - \Phi\bar{E}_\mu + \bar{a}^\nu(\partial_\mu a_\nu - \partial_\nu a_\mu) \\ & - a^\nu(\partial_\mu \bar{a}_\nu - \partial_\nu \bar{a}_\mu)) + \beta^r \mathcal{Q}),\end{aligned}\quad (5.1.69)$$

where spherical polar spacelike coordinates $\{r, \theta, \phi\}$ used.

5.1.5 Energy-Momentum Currents

To find the current associated with energy-momentum we consider a vector field \mathbf{J} defined with respect to a second vector field ξ and the stress tensor \mathbf{T} by

$$J^\mu := T_\nu^\mu \xi^\nu. \quad (5.1.70)$$

Calculating the divergence of this vector leads to the following continuity equation,

$$\nabla_\mu J^\mu = \underbrace{(\nabla_\mu T_\nu^\mu)}_{=0} \xi^\nu + T_\nu^\mu \nabla_\mu \xi_\nu, \quad (5.1.71)$$

$$\nabla_\mu J^\mu = T^{\mu\nu} \nabla_{(\mu} \xi_{\nu)}, \quad (5.1.72)$$

where (5.1.72) shows the divergence vanishes if ξ is a Killing vector of the spacetime; a vanishing divergence corresponds to a conserved current with a zero source term. For more general spacetimes where ξ is not Killing, the right hand side of (5.1.72) leads to a non-zero source term accounting for the transfer of energy-momentum between matter and spacetime curvature [151]. The choice of ξ dictates the type of energy-momentum current retrieved; for instance $\xi = \partial_t$ will correspond to an energy current $J^\mu = T_\nu^\mu (\partial_t)^\nu = T_t^\mu$ and the spatial choice $\xi = \partial_i$ gives a momentum current $J^\mu = T_\nu^\mu (\partial_i)^\nu = T_i^\mu$ corresponding to the coordinate x^i . For an account of energy and linear momentum continuity see [151].

Angular Momentum

The numerical test of the QFS system (5.1.15) in section 5.1.6 measures the conservation of angular momentum. To do this we choose $\xi = \partial_\phi$, used in Eq. (5.1.70), which is the coordinate basis vector of some azimuthal coordinate ϕ . The angular momentum current is

$$J^\mu = T_\nu^\mu (\partial_\phi)^\nu = T_\phi^\mu. \quad (5.1.73)$$

Any spacetime with azimuthal symmetry (e.g. the Kerr spacetime) will have a vanishing source term as ∂_ϕ is a Killing vector. This includes numerical simulations of matter in a fixed background. The example simulation in section 5.1.6 is the fully nonlinear grazing collision of two boson stars and ξ is not a Killing vector for finite distances from the collision centre. In this case the source term is non-zero. Using the standard 3+1 decomposition of the stress tensor [11], [21] and explicitly expanding the density term from Eq. (5.1.16) gives,

$$\mathcal{Q} = T_\nu^\mu n_\mu (\partial_\phi)^\nu, \quad (5.1.74)$$

$$= (S_\nu^\mu + S^\mu n_\nu + S_\nu n^\mu + n_\nu n^\mu) n_\mu (\partial_\phi)^\nu, \quad (5.1.75)$$

$$= S_\nu n^\mu n_\mu (\partial_\phi)^\nu, \quad (5.1.76)$$

$$= -S_\phi, \quad (5.1.77)$$

$$= yS_x - xS_y, \quad (5.1.78)$$

where x and y are Cartesian coordinates related to spherical polar coordinates in the usual way. Combining Eqs. (5.1.25), (5.1.73) and (5.1.77) we can get the angular momentum flux through a spherical

extraction surface,

$$\mathcal{F} = \frac{\sqrt{-h}}{\sqrt{\sigma}} (\gamma^{\mu\nu} T_{\rho\mu} (\partial_\phi)^\rho N_\nu + \mathbf{n} \cdot \mathbf{N} S_\phi), \quad (5.1.79)$$

$$= \frac{\sqrt{-h}}{\sqrt{\sigma}} (\gamma^{\mu\nu} S_{\phi\mu} N_\nu + \mathbf{n} \cdot \mathbf{N} S_\phi). \quad (5.1.80)$$

Using Eq. (5.1.42), for a spherical extraction surface, the flux term becomes,

$$\mathcal{F} = \alpha \frac{\sqrt{g^{rr}}}{\sqrt{\gamma^{rr}}} (\gamma^{\mu r} S_{\phi\mu} N_r - \frac{\beta^r}{\alpha} N_r S_\phi), \quad (5.1.81)$$

$$= \alpha \frac{\sqrt{g^{rr}}}{\sqrt{\gamma^{rr}}} (\gamma^{\mu r} S_{\phi\mu} N_r - \frac{\beta^r}{\alpha} N_r S_\phi), \quad (5.1.82)$$

$$= \frac{1}{\sqrt{\gamma^{rr}}} (\alpha \gamma^{\mu r} S_{\phi\mu} - \beta^r S_\phi) \quad (5.1.83)$$

in spherical polar coordinates. The explicit expansion of the source term \mathcal{S} is left for the section 5.1.8, but the result is given here,

$$\begin{aligned} \mathcal{S} = & \alpha S_\nu^{\mu(3)} \partial_\mu \xi^\nu + \alpha S_\nu^{\mu(3)} \Gamma_{\mu\sigma}^\nu \xi^\sigma \\ & - S_\nu \beta^i \partial_i \xi^\nu + S_\nu \xi^\mu \partial_\mu \beta^\nu - \rho \xi^\mu \partial_\mu \alpha. \end{aligned} \quad (5.1.84)$$

As noted in section 5.1.8, when choosing a coordinate system to evaluate \mathcal{S} , if ξ is a coordinate basis vector then the $\partial_i \xi^j$ terms vanish.

It would be simple to re-derive these results for linear momentum, by using $\xi = \partial_i$ for momentum in the x^i direction for example, where x^i is some Cartesian spatial coordinate. Results for linear momentum can be found in [151].

Energy

A local conservation system can also be applied to energy with the choice of an approximate Killing vector ξ , $\xi^\mu = (\partial_t)^\mu = t^\mu = (1, 0, 0, 0)$, and energy current

$$J^\mu = T_\nu^\mu t^\nu = T_t^\mu. \quad (5.1.85)$$

Using the standard 3+1 decomposition of the stress-energy tensor from [11] or [21] the energy density \mathcal{Q} is,

$$\mathcal{Q} = T_\nu^\mu n_\mu \xi^\nu, \quad (5.1.86)$$

$$= T_\nu^\mu n_\mu (\alpha n^\nu + \beta^\nu), \quad (5.1.87)$$

$$= \alpha \rho - S_\mu \beta^\mu, \quad (5.1.88)$$

from Eq. (5.1.16). Similarly, combining Eqs. (5.1.17) and (5.1.22), the energy flux is,

$$\mathcal{F} = \frac{\sqrt{-h}}{\sqrt{\sigma}} T_\nu^\mu N_\mu \xi^\nu, \quad (5.1.89)$$

$$= \frac{\sqrt{-h}}{\sqrt{\sigma}} T_\nu^\mu (\perp N_\mu - \mathbf{n} \cdot \mathbf{N} n_\mu) (\alpha n^\nu + \beta^\nu), \quad (5.1.90)$$

$$\begin{aligned} = & \frac{\sqrt{-h}}{\sqrt{\sigma}} (-\mathbf{n} \cdot \mathbf{N} \alpha \rho - \perp N_\mu S^\mu \alpha \\ & + \mathbf{n} \cdot \mathbf{N} S_\mu \beta^\mu + \perp N^\mu \beta^\nu S_{\mu\nu}), \end{aligned} \quad (5.1.91)$$

and Eqs. (5.1.27) and (5.1.38) can be used for a spherical extraction surface,

$$\mathcal{F} = \frac{1}{\sqrt{\gamma^{rr}}} (\alpha\rho\beta^r - \alpha^2 S^r + \alpha S_\mu^r \beta^\mu - \beta^\mu S_\mu \beta^r). \quad (5.1.92)$$

The source term is omitted here as the expression derived in section 5.1.8 assumes that ξ is spatial. For energy continuity a timelike approximate Killing vector ξ is used and leads to a different expression for the source term that can be found in [151] along with the above density \mathcal{Q} and flux term \mathcal{F} .

5.1.6 Numerical Application

To numerically test the QFS system, given in Eq. (5.1.15), for angular momentum an example spacetime consisting of colliding boson stars is simulated in 3D using GRCHOMBO [46] [1]. GRCHOMBO is a modern, open source, Numerical Relativity code with fully Adaptive Mesh Refinement (AMR) using the Berger-Rigoutsos block-structured adaptive mesh algorithm [156]. The CCZ4 constraint damping formulation [156, 33] is used with the moving puncture gauge [36, 157]. Time integration is done with 4th order Runge-Kutta method of lines.

Numerical Setup of Simulations

Boson stars are self-gravitating solutions of the Einstein-Klein-Gordon system in curved space with the Lagrangian given in Eq. (5.1.43); for a detailed review of boson stars see [153]. The boson stars considered in this work are stable and spherically symmetric with the Klein-Gordon potential chosen to be $V = m^2 \varphi \bar{\varphi}$, where m is the mass of a bosonic particle, leading to so called *mini boson stars*. The Kaup limit for the maximum stable mass of a mini boson star can be found numerically as approximately

$$M_{\text{Kaup}} \sim 0.633 \frac{\hbar c}{Gm} = 0.633 M_{pl}^2 m^{-1}, \quad (5.1.93)$$

where the physical constants are included for completeness, but have numerical value 1 in Planck units. Notably, the maximum mass of a mini boson star scales inversely with the boson particle mass m .

The Lagrangian in Eq. (5.1.43) with potential $V = m^2 \varphi \bar{\varphi}$ is unchanged up to an overall constant under a rescaling of the boson mass like $m \rightarrow bm$, for some dimensionless constant b , while simultaneously rescaling $x^\mu \rightarrow b^{-1}x^\mu$ for coordinates with dimension length/time. Consequently a mini boson star solution, categorised by the central scalar field amplitude φ_c , represents a one parameter family of solutions with ADM mass and radius inversely proportional to m . To keep the choice of m arbitrary the coordinates used in the simulation are mx^μ , which are exactly Planck units in the case $m = 1$ (i.e. the Planck mass).

To measure the charge associated with angular momentum, the following angular momentum measures are considered,

$$Q := \int_V \mathcal{Q} \sqrt{\gamma} d^3x, \quad (5.1.94)$$

$$F := \int_{\partial V} \mathcal{F} \sqrt{\gamma} d^2x, \quad (5.1.95)$$

$$S := \int_V \mathcal{S} \sqrt{\gamma} d^3x, \quad (5.1.96)$$

$$\tilde{Q} := Q(t=0) + \int_0^t F dt, \quad (5.1.97)$$

$$\delta Q_S := \int_0^t S dt, \quad (5.1.98)$$

$$\hat{Q} := Q + \delta Q_S, \quad (5.1.99)$$

$$\bar{Q} := \tilde{Q} - \delta Q_S, \quad (5.1.100)$$

where \mathcal{Q} , \mathcal{F} and \mathcal{S} are defined in Eqs. (5.1.74), (5.1.83) and (5.1.84) respectively. $\hat{\mathcal{Q}}$ is the angular momentum modified by δQ_S ; this is equivalent to absorbing the source term into \mathcal{Q} . $\tilde{\mathcal{Q}}$ is the initial angular momentum modified by the time integrated total flux. Equation (5.1.15) implies $\hat{\mathcal{Q}} = \tilde{\mathcal{Q}}$ exactly, and we define the relative numerical error measure e_1 by

$$e_1 := \frac{\hat{\mathcal{Q}} - \tilde{\mathcal{Q}}}{\hat{\mathcal{Q}}}, \quad (5.1.101)$$

which converges to zero in the continuum limit. We can alternatively define a different relative error

$$e_2 := \frac{\mathcal{Q} - \bar{\mathcal{Q}}}{\mathcal{Q}}, \quad (5.1.102)$$

where the source term is not absorbed into \mathcal{Q} . Again, Eq. (5.1.15) implies that $\mathcal{Q} = \bar{\mathcal{Q}}$, or $e_2 = 0$, in the continuum limit.

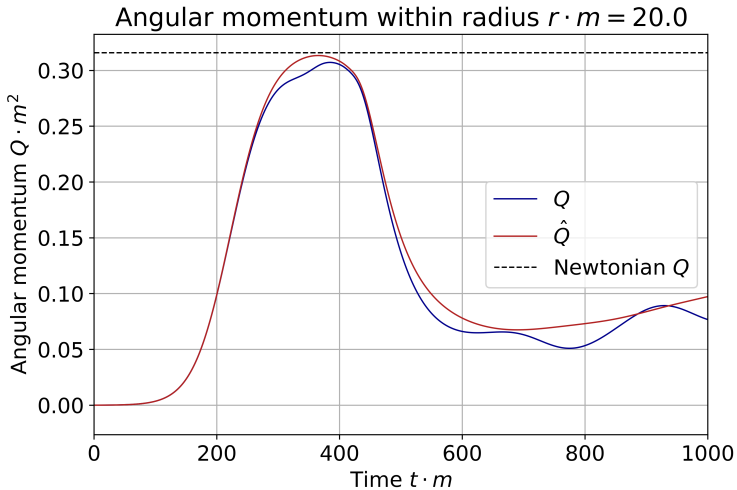


Figure 5.2: Integrated angular momentum within radius $r < 20 \text{ m}^{-1}$. \mathcal{Q} is the angular momentum integral in Eq. (5.1.94) and $\hat{\mathcal{Q}}$ includes the source term as in Eq. (5.1.99). The black dashed line indicates the Newtonian calculation for the angular momentum given in Eq. (5.1.103). The boson stars initially start outside the extraction radius.

The initial data of the numerical simulations consists of two boson stars, each with mass $M = 0.395(0) \text{ m}^{-1}$, boosted towards each other in a grazing configuration. The data for two single boosted stars are superposed as in Ref. [158] to minimise errors in the Hamiltonian and momentum constraints and spurious oscillations in the scalar field amplitudes of the stars. The physical domain is a cube of size $L = 1024 \text{ m}^{-1}$, the centre of this domain locates the origin of the Cartesian coordinates x , y and z . The stars are placed at $x_0^i = \pm(40, 4, 0) \text{ m}^{-1}$ with respect to the centre of the physical domain, giving an initial impact parameter $d = 8 \text{ m}^{-1}$, and the boost velocity is $v^i = \mp(0.1, 0, 0)$ along the x axis. The stars travel towards each other and undergo a grazing collision to form a short lived dense object at time $t \sim 375 \text{ m}^{-1}$. Afterwards, much of the scalar field (and angular momentum) leaves the extraction radii as it is ejected to spatial infinity. Figures. 5.2, 5.3 and 5.4 show the angular momentum within radii $r = \{20, 40, 60\} \text{ m}^{-1}$. The Newtonian angular momentum for this configuration is

$$Md v = 0.316(0) \text{ m}^{-2} \quad (5.1.103)$$

which is in close agreement with \mathcal{Q} and $\hat{\mathcal{Q}}$ in Figs. 5.2, 5.3 and 5.4 while the matter is contained by the extraction radii. Given that we are dealing with a fully non-linear spacetime in general relativity there is no reason why the naive Newtonian angular momentum should agree so well with the numerically

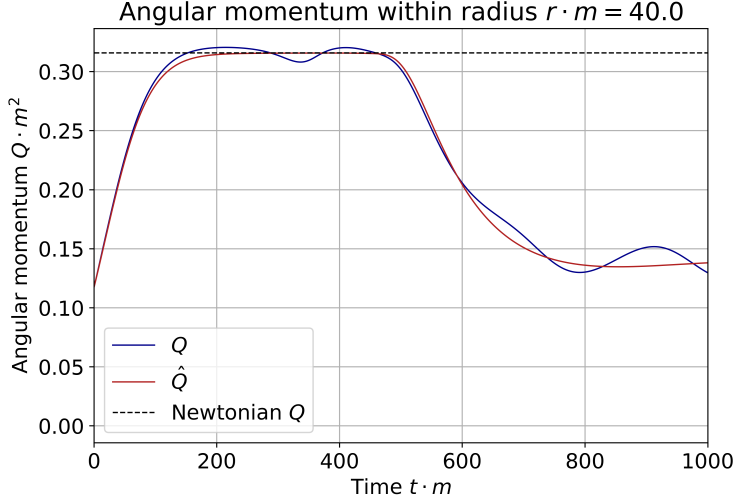


Figure 5.3: Integrated angular momentum within radius $r < 40 \text{ m}^{-1}$. Quantities plotted are identical to Fig. 5.2. The boson stars initially start intersecting the extraction radius.

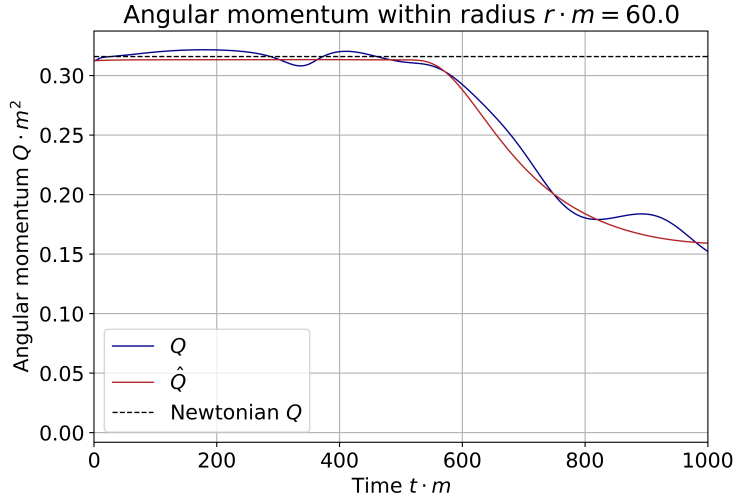


Figure 5.4: Integrated angular momentum within radius $r < 60 \text{ m}^{-1}$. Quantities plotted are identical to Figs. 5.2 and 5.3. The boson stars initially start inside the extraction radius.

integrated values Q or \hat{Q} ; this could be due to the mass of the stars being $M = 0.395(0) \text{ m}^{-1}$, well below the Kaup limit $M_{\text{Kaup}} \sim 0.633 \text{ m}^{-1}$ and the mild boost velocities $v = 0.1$. In the case that the star masses/densities and velocities tend to zero we expect general relativity to approach the Newtonian limit; conversely for large masses/densities and boost velocities the Newtonian estimate likely becomes less accurate.

Finally we note in Figs. 5.2, 5.3 and 5.4 that the source-corrected density variable \hat{Q} is less prone to oscillations than Q and is closer to being constant at early times when no angular momentum flux is radiated. \hat{Q} has another advantage over Q ; at extraction radii sufficiently far from any matter \hat{Q} will remain constant due to the flux \mathcal{F} vanishing. Q will only remain constant if the source term integral δQ_S also remains constant which does not happen in general dynamic spacetimes, even for large extraction radii.

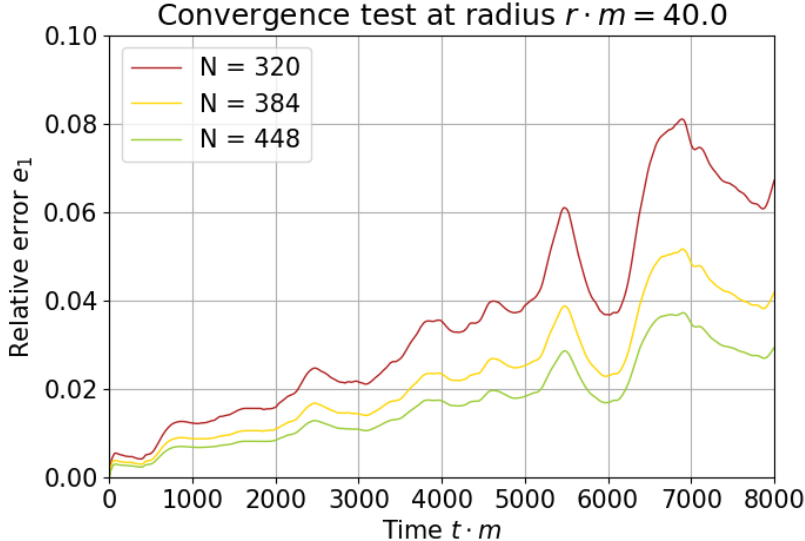


Figure 5.5: Relative error e_1 , from Eq. (5.1.101), for the modified total angular momentum at extraction radius $r = 40 \text{ m}^{-1}$; the modified total angular momentum \hat{Q} includes the source term. Figure includes four convergence simulations with $N \in \{320, 384, 448\}$ gridpoints along the coarse grid.

Convergence Analysis

Three numerical simulations are used to test the convergence of the angular momentum measures as the continuum limit is approached. They have $N \in \{320, 384, 448\}$ gridpoints on the coarsest level, named level 0 with grid spacing $\Delta x_0 = L/N$. Each finer level, named level n , has grid spacing $\Delta x_n = 2^{-n}\Delta x_0$. Any gridpoints that fall inside radius $r = 200 \text{ m}^{-1}$ are forced to be resolved by at least AMR level 1. Similarly, any points within radius $r < 60 \text{ m}^{-1}$ are resolved by at least AMR level 3; this modification quadruples the default resolution for $r < 60 \text{ m}^{-1}$ compared to level 1. These two radii have a 20% extra buffer zone to ensure that AMR boundaries are outside and away from the desired radii. On top of this the AMR is triggered to regrid when a tagging criterion is exceeded; a description of the algorithm can be found in section 3.2.1 or 2.2.2 of [159]. The tagging criteria used in this chapter involve gradients of the scalar field and spatial metric determinant; this loosely means as a region of spacetime becomes more curved, or matter becomes denser, the region is resolved with higher resolution. Figs. 5.5 and 5.6 show the relative errors e_1 and e_2 for the convergence sequence; it can be seen that e_1 , the relative error of \hat{Q} , is less prone to oscillations than e_2 , the relative error of Q . The choice of enforcing AMR regridding to level 3 within $r < 60 \text{ m}^{-1}$ is very problem specific and the grid structure has been chosen carefully for the particular physical scenario to give higher resolution around the late time scalar field configuration at the origin; this enables accurate simulation of the extended object after merger. Simulations prior to this modification showed approximately five times higher relative error e_1 and much worse Noether charge conservation. The highest resolution simulation, with $N = 448$, shows that the relative error e_1 is 3% after 8000 m^{-1} time units.

We now obtain the order of convergence ω of e_1 . It is convenient to express e_1 as three functions $\{f_1, f_2, f_3\}$ corresponding to the three different resolution simulations with $N = \{320, 384, 448\}$ and f_∞ to denote the continuum limit solution. A traditional convergence analysis, as in [160], assumes that the numerical error of a function (i.e. difference from f_∞) is dominated by a term proportional to Δx_i^ω for an order of convergence ω ; thus we can write

$$f_i + E(\Delta x_i)^\omega = f_\infty \quad (5.1.104)$$

for some constant coefficient E for all resolutions i . Equation (5.1.104) with $i = \{1, 2, 3\}$ can be used to

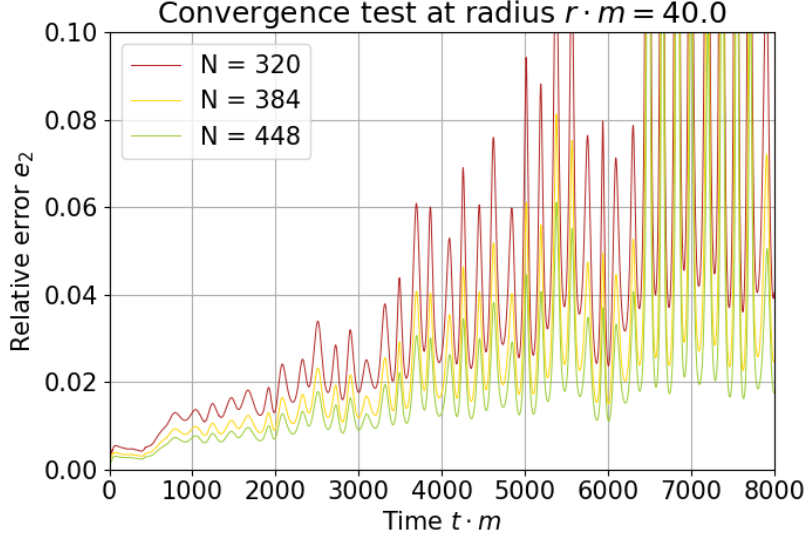


Figure 5.6: Relative error e_2 , from Eq. (5.1.102), for the total angular momentum at extraction radius $r = 40 \text{ m}^{-1}$; the total angular momentum Q excludes the source term. Figure includes four convergence simulations with $N \in \{320, 384, 448\}$ gridpoints along the coarse grid.

eliminate both E and f_∞ giving the well known result

$$\frac{f_3 - f_2}{f_2 - f_1} = \frac{\Delta x_3^\omega - \Delta x_2^\omega}{\Delta x_2^\omega - \Delta x_1^\omega} \quad (5.1.105)$$

for ideal convergence. Figure 5.7 shows $f_3 - f_2$ and $(f_2 - f_1)(\Delta x_3^\omega - \Delta x_2^\omega)/(\Delta x_2^\omega - \Delta x_1^\omega)$ for three orders of convergence $\omega = \{2, 3, 4\}$; the two expressions should be equal for an ideal order of convergence ω . It can be seen by eye that $\omega = 3$ ¹ is approximately² true.

To quantify the order of convergence, rather than guessing, we define the deviation factor \mathcal{D} as

$$\mathcal{D}(\omega) = \int_{t_0}^{t_1} \left(\frac{f_3 - f_2}{f_2 - f_1} - \frac{\Delta x_3^\omega - \Delta x_2^\omega}{\Delta x_2^\omega - \Delta x_1^\omega} \right)^2 dt, \quad (5.1.106)$$

which averages the violation of Eq. (5.1.105) between times $t_0 \leq t \leq t_1$. Figure 5.8 plots \mathcal{D} versus ω with a red curve and the order of convergence can be estimated by minimising $\mathcal{D}(\omega)$ with respect to ω . As can be seen in Fig. 5.8, the traditional order of convergence is approximately 3.2.

Given that e_1 vanishes in the continuum limit we can set $f_\infty = 0$ to find the order of convergence to zero. Using Eq. (5.1.104) with the two highest resolutions $i = \{2, 3\}$, and setting $f_\infty = 0$, E can be eliminated to give

$$\frac{f_3}{f_2} = \frac{\Delta x_3^\omega}{\Delta x_2^\omega}. \quad (5.1.107)$$

Similarly to before, we can define a deviation factor $\tilde{\mathcal{D}}$,

$$\tilde{\mathcal{D}}(\omega) = \int_{t_0}^{t_1} \left(\frac{f_3}{f_2} - \frac{\Delta x_3^\omega}{\Delta x_2^\omega} \right)^2 dt, \quad (5.1.108)$$

¹The code uses a mix of 4th order accurate operations such as spatial derivatives and time evolution schemes along with 3rd order accurate interpolation methods at AMR boundaries.

²Obtaining a strict convergence series with AMR is difficult as the regions chosen for extra refinement by the tagging criterion are chosen dynamically at runtime. This means the grid structure of different resolution runs will typically not be identical. Care was taken when choosing a tagging criterion to match this grid structure as much as possible. Due to the fact that regridding is done using cuboidal boxes of sidelengths 16 or 32 gridpoints it is impossible to match perfectly at different resolutions.

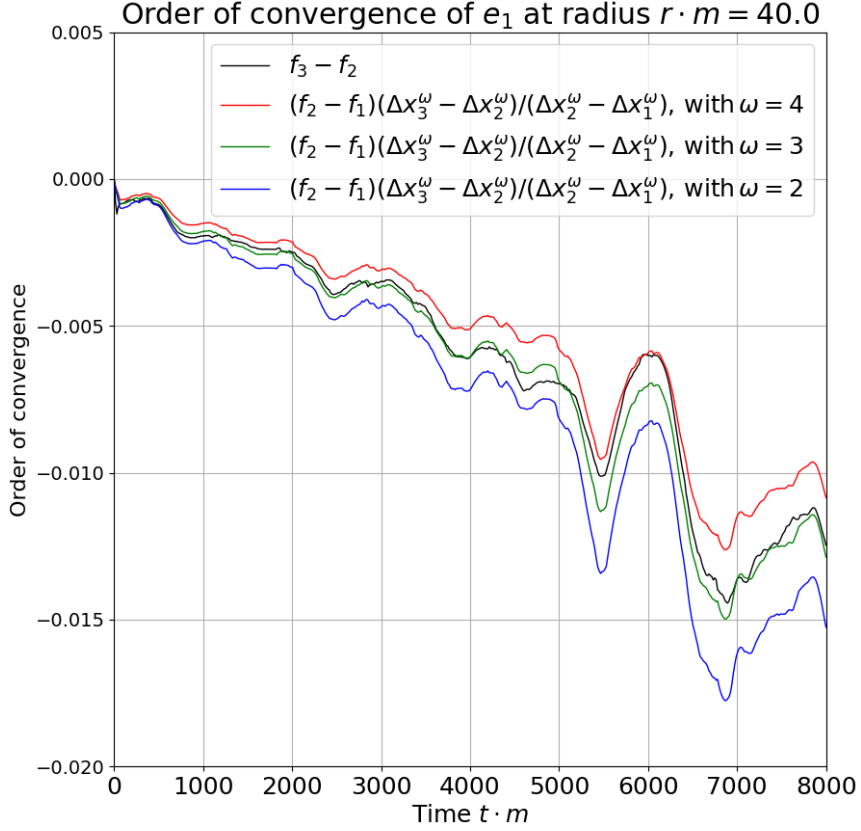


Figure 5.7: Estimating the order of convergence ω of the angular momentum error e_1 in Fig. 5.5 at extraction radius $r = 40 \text{ m}^{-1}$. The black curve shows the difference between f_3 and f_2 ; the relative error e_1 of the two highest resolution simulations in Section 5.1.6. The three coloured curves show the difference between the two lowest resolution simulations f_2 and f_1 , but modified by $(\Delta x_3^\omega - \Delta x_2^\omega)/(\Delta x_2^\omega - \Delta x_1^\omega)$ in accordance with Eq. (5.1.105), for three idealised orders of convergence $\omega = \{2, 3, 4\}$. The black curve is in best agreement with the green curve giving an estimate of $\omega = 3$ for the order of convergence.

which time averages the violation of Eq. (5.1.107). The black curve in Fig. 5.8 plots Eq. (5.1.108) versus ω and the order of convergence to zero can be estimated by minimising $\tilde{\mathcal{D}}(\omega)$ with respect to ω . As can be seen in Fig. 5.8, the order of convergence convergence to zero is approximately 1.9.

5.1.7 Conclusion

A derivation of the QFS system (5.1.15) for continuity equations, valid locally for general spacetimes, is derived and applied to spherical integration surfaces. Although spherical extraction surfaces are used, the methods of section 5.1.3 can be applied to general extraction surfaces with minor adjustments. The QFS system is used to calculate the well known Noether charge densities for complex scalar and complex vector (Proca) fields along with novel expressions for the flux variable \mathcal{F} in section 5.1.4. Next the QFS system for energy momentum currents associated with matter are found and the main result of this chapter is the explicit derivation of the angular momentum QFS variables \mathcal{Q} , \mathcal{F} and \mathcal{S} . The three variables can be used to measure the angular momentum of matter within a region, the flux of angular momentum of matter through the boundary of that region and the transfer of angular momentum between matter and curvature; they can also be used with Eq. (5.1.15) to determine the numerical quality of a simulation as the QFS system is exactly satisfied in the continuum limit. In section 5.1.6 the combination of variables \mathcal{Q} and \mathcal{S} is shown to be a superior measure of angular momentum than integrals of only the charge density \mathcal{Q} in two ways; firstly its measurement is less prone to oscillations and secondly it is conserved in the large radius limit.

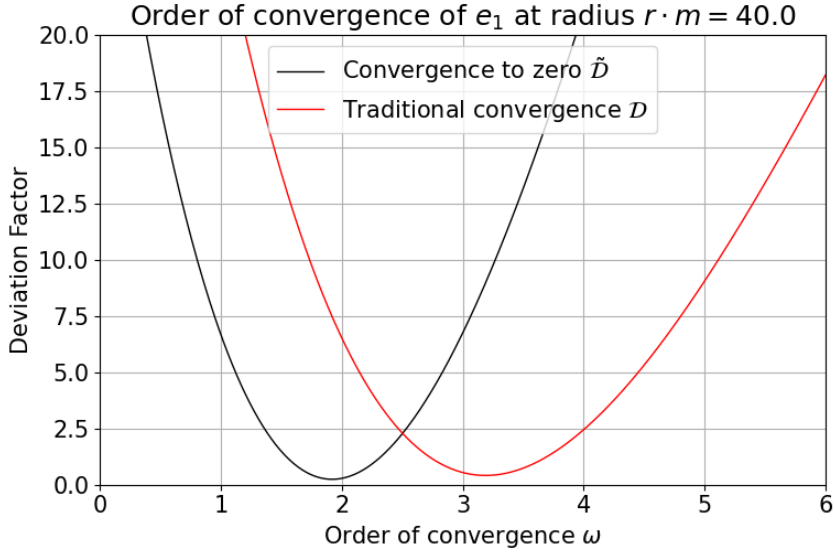


Figure 5.8: Estimating the order of convergence ω of the angular momentum error e_1 in Fig. 5.5 at extraction radius $r = 40 \text{ m}^{-1}$. The red curve gives the deviation from ideal traditional convergence \mathcal{D} , defined by Eq. (5.1.106), as a function of ω . The black curve shows the deviation from ideal convergence to zero $\tilde{\mathcal{D}}$, using the definition given in Eq. (5.1.108), as a function of ω . For both curves the estimated order of convergence is found by minimisation with respect to ω ; this gives $\omega = 3.2$ for traditional convergence and $\omega = 1.9$ for convergence to zero.

The QFS system for angular momentum is numerically tested on a dynamic non-linear spacetime consisting of two colliding boson stars; the collision has a small impact parameter giving rise to a non-zero total angular momentum. The stars promptly collide and form a highly perturbed, localised scalar field configuration partially retaining angular momentum. The total angular momentum of the spacetime is measured using the QFS variables (Eqs. (5.1.77), (5.1.83) and (5.1.84)) and is shown to agree well with the Newtonian approximation. This is a good check on the normalisation of the QFS variables as they should return the Newtonian calculation in the low energy limit; even though we simulate a fully non-linear spacetime the density and boost velocity of the stars are mild. The final numerical result is the convergence test of the QFS system which measures the relative error described in 5.1.6. The relative error converges to zero with order $\omega \approx 1.9$ in the continuum limit and the highest resolution simulation gives a fractional error of approximately 3% in the total angular momentum after 8000 time units.

The QFS system is straightforward to implement and it is hoped these results will be useful to the Numerical Relativity community for better measurement of local energy-momentum of matter and Noether charge as well as powerful check on simulation resolution.

5.1.8 Source Term Calculation

Here we expand the source term \mathcal{S} from section 5.1.2,

$$\mathcal{S} = \alpha T_{\mu\nu} \nabla^\mu \xi^\nu. \quad (5.1.109)$$

Note that ξ is assumed spatial, $\xi^\mu n_\mu = 0 \rightarrow \xi^0 = 0$. If the reader is interested in a timelike ξ , for calculating the source term of energy, it can be found in [151]. Expanding the stress tensor with the usual 3+1 components [11], [21] ($S_{\mu\nu}, S_\mu, \rho$), gives

$$\frac{1}{\alpha} \mathcal{S} = S_{\mu\nu} \nabla^\mu \xi^\nu + S_\mu n_\nu \nabla^\mu \xi^\nu + S_\nu n_\mu \nabla^\mu \xi^\nu + \rho n_\mu n_\nu \nabla^\mu \xi^\nu. \quad (5.1.110)$$

Let us decompose each piece separately. Starting with the spatial tensor $S_{\mu\nu}$ term,

$$S_{\mu\nu}\nabla^\mu\xi^\nu = (S_{\rho\sigma}\perp_\mu^\rho\perp_\nu^\sigma)\nabla^\mu(\perp_n^\nu\xi^n), \quad (5.1.111)$$

$$= S_{\rho\sigma}(\perp_\mu^\rho\perp_\nu^b\nabla^\mu(\perp_n^\nu\xi^n)), \quad (5.1.112)$$

$$= S_{\mu\nu}D^\mu\xi^\nu, \quad (5.1.113)$$

$$= S_j^i\partial_i\xi^j + S_j^{i(3)}\Gamma_{ik}^j\xi^k, \quad (5.1.114)$$

where we used the idempotence of the projector \perp on components $S_{\mu\nu}$ and ξ^μ which are already projected onto Σ_t . Here D and ${}^{(3)}\Gamma_{ik}^j$ are the covariant derivative and Christoffel symbol components of Σ_t . Some algebra shows that the terms containing S_μ become

$$S_\nu n^\mu\nabla_\mu\xi^\nu + S^\mu n_\nu\nabla_\mu\xi^\nu = S_\nu\mathcal{L}_n\xi^\nu, \quad (5.1.115)$$

where we used the fact that $S^0 = 0$, $n_{i\neq 0} = 0$ and that we are free to swap between $\partial_\mu \leftrightarrow \nabla_\mu$ derivatives in a Lie derivative. Finally the ρ term simplifies, using $\nabla_\mu(n^\nu n_\nu) = 0$, to

$$\rho n_\mu n_\nu\nabla^\mu\xi^\nu = \rho n_\nu\mathcal{L}_n\xi^\nu. \quad (5.1.116)$$

Combining Eqs. (5.1.114), (5.1.115) and (5.1.116) we can write the source term as,

$$\frac{1}{\alpha}\mathcal{S} = S_j^i\partial_i\xi^j + S_j^{i(3)}\Gamma_{ik}^j\xi^k + S_\nu\mathcal{L}_n\xi^\nu + \rho n_\nu\mathcal{L}_n\xi^\nu, \quad (5.1.117)$$

We can expand the Lie derivatives to partial derivatives, for ease of numerical implementation, with the following assumptions $n_\mu S^\mu = 0$, $\xi^0 = 0$, $n_{i\neq 0} = 0$ and $\partial\xi^0 = 0$.

$$S_\nu\mathcal{L}_n\xi^\nu = -\frac{1}{\alpha}S_\nu\beta^i\partial_i\xi^\nu + \frac{1}{\alpha}S_\nu\xi^\mu\partial_\mu\beta^\nu \quad (5.1.118)$$

$$\rho n_\nu\mathcal{L}_n\xi^\nu = -\frac{1}{\alpha}\rho\xi^\mu\partial_\mu\alpha \quad (5.1.119)$$

This gives us our final form for the angular momentum source density,

$$\begin{aligned} \mathcal{S} = & \alpha S_\nu^{(3)}\partial_\mu\xi^\nu + \alpha S_\nu^{(3)}\Gamma_{\mu\sigma}^\nu\xi^\sigma \\ & - S_\nu\beta^i\partial_i\xi^\nu + S_\nu\xi^\mu\partial_\mu\beta^\nu - \rho\xi^\mu\partial_\mu\alpha. \end{aligned} \quad (5.1.120)$$

If we pick a coordinate basis vector as our approximate Killing vector, for example with components $\xi^\mu = (\partial_\phi)^\mu = (0, 0, 0, 1)^\mu$ in polar coordinates, then the $\partial_\mu\xi^\nu$ terms will vanish. However if we wish to work in Cartesian coordinates, which is very common for numerical codes, then the vector components $\tilde{\xi}^\mu$ become,

$$\tilde{\xi}^\mu = (\partial_\phi)^\nu\frac{\partial\tilde{x}^\mu}{\partial x^\nu} = (0, -y, x, 0), \quad (5.1.121)$$

where \tilde{x}^μ are Cartesian coordinates and x^μ are spherical polar coordinates.

5.1.9 Generality of Result

Here we demonstrate that the choice of 4-volume M integrated in Eq. (5.1.7) does not change the resulting QFS system (5.1.3). We start by defining the extraction 3-volume $V_1 \in \Sigma_t$ at time $t = t_0$. The boundary of V_1 is the 2-volume ∂V_1 with metric $\boldsymbol{\sigma}$. As in section 5.1.2, Σ_t is the 3-manifold defined by the set of all points with constant time coordinate t , equipped with metric $\boldsymbol{\gamma}$ and unit normal \mathbf{n} like Eq. (5.1.5). We now choose to define a 4-volume \tilde{M} , different to M , as the evolution of V_1 along integral curves of \mathbf{n} between times $t_0 \leq t \leq t_0 + \delta t$ in the limit $\delta t \rightarrow 0$. The boundary of \tilde{M} , $\partial\tilde{M}$, is composed of three coordinate 3-volumes, $V_1 \in \Sigma_t$, $V_2 \in \Sigma_{t+\delta t}$ and \tilde{H} . Here $V_2 = V_1 + \delta V$ and is the future of V_1 , at time

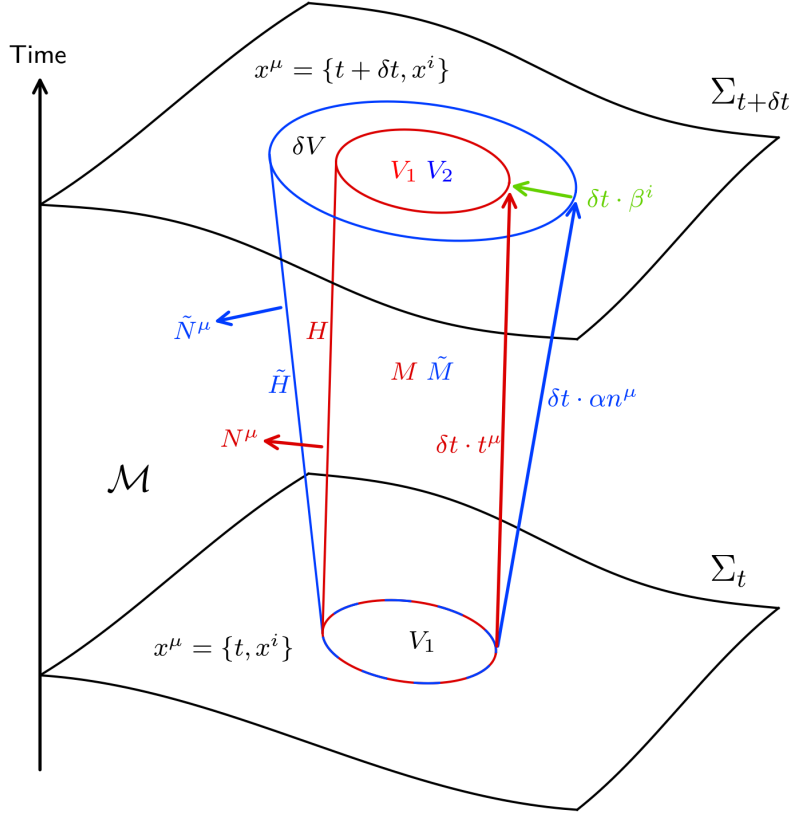


Figure 5.9: Comparison of two possible geometries for derivation of QFS system in section 5.1.2 on manifold \mathcal{M} . Σ_t is the spatial hypersurface at time t and $\Sigma_{t+\delta t}$ is the the spatial hypersurface at a later time $t + \delta t$. V_1 is the coordinate volume, with surface ∂V_1 (not labelled), that we wish to use as an extraction volume on Σ_t . The red cylinder, defined by ∂V_1 evolved along integral curves of $\mathbf{t} = \partial_t$, is the same as in Fig. 5.1. Evolving ∂V_1 forward in time with \mathbf{n} , as demonstrated with the blue cylinder, gives a different coordinate volume ∂V_2 (not labelled) on $\Sigma_{t+\delta t}$. Similarly to the red cylinder, the blue cylinder has sides labelled by \tilde{H} and an interior \tilde{M} . The difference in the volumes V_1 and V_2 on $\Sigma_{t+\delta t}$ is denoted by δV .

$t = t_0 + \delta t$, found by following integral curves of \mathbf{n} . \tilde{H} is the 3-volume defined by the time evolution of 2-volume ∂V_1 with \mathbf{n} . A diagram showing the differences between the choices of time evolution vectors \mathbf{n} and \mathbf{t} is given in Fig. 5.9.

We start again by using Gauss' theorem like in Eq. (5.1.8) which results in three surface integrals over $V_1 \in \Sigma_t$, $V_2 \in \Sigma_{t+\delta t}$, and \tilde{H} ,

$$\begin{aligned} \int_{\tilde{M}} \nabla \cdot \mathbf{J} \sqrt{-g} d^4x &= - \int_{V_2}^{t=t_0+\delta t} \mathbf{n} \cdot \mathbf{J} \sqrt{\gamma} d^3x \\ &\quad + \int_{V_1}^{t=t_0} \mathbf{n} \cdot \mathbf{J} \sqrt{\gamma} d^3x \\ &\quad + \int_{\tilde{H}} \tilde{\mathbf{N}} \cdot \mathbf{J} \sqrt{-\tilde{h}} dx^2 dt, \end{aligned} \quad (5.1.122)$$

where $\tilde{\mathbf{N}}$ is the unit normal to \tilde{H} . Starting with the integrals over V_1 and $V_2 = V_1 + \delta V$ we get,

$$- \int_{V_2}^{t=t_0+\delta t} \mathbf{n} \cdot \mathbf{J} \sqrt{\gamma} d^3x + \int_{V_1}^{t=t_0} \mathbf{n} \cdot \mathbf{J} \sqrt{\gamma} d^3x, \quad (5.1.123)$$

$$= -\delta t \partial_t \int_{V_1} \mathbf{n} \cdot \mathbf{J} \sqrt{\gamma} d^3x - \int_{\delta V} \mathbf{n} \cdot \mathbf{J} \sqrt{\gamma} d^3x, \quad (5.1.124)$$

with the new integral over δV appearing because $V_1 \neq V_2$ as V_1 is evolved along integral curves of \mathbf{n} rather than time basis vector $\mathbf{t} = \partial_t$; this is demonstrated in Fig. 5.9. In the limit that $\delta t \rightarrow 0$ it can be seen that,

$$\int_{\delta V} \mathbf{n} \cdot \mathbf{J} \sqrt{\gamma} d^3x = -\delta t \int_{\partial V_1} \beta^i s_i \mathbf{n} \cdot \mathbf{J} \sqrt{\gamma} d^2x, \quad (5.1.125)$$

where s_i are the components of the unit normal to the coordinate surface ∂V_1 in \mathbb{R}^3 rather than Σ_t . The overall negative sign in Eq. (5.1.125) comes from the defined direction of the shift vector β as seen Fig. 5.9. Addressing the integral over \tilde{H} gives,

$$\begin{aligned} & \int_{\partial V_1} \int_{t_0}^{t_0 + \delta t} \tilde{\mathbf{N}} \cdot \mathbf{J} \sqrt{-\tilde{h}} dx^2 dt, \\ &= \delta t \int_{\partial V_1} \tilde{\mathbf{N}} \cdot \mathbf{J} \sqrt{-\tilde{h}} dx^2. \end{aligned} \quad (5.1.126)$$

Combining Eqs. (5.1.124), (5.1.125) and (5.1.126) and a source term like in (5.1.7) we get,

$$\begin{aligned} \partial_t \int_{V_1} \mathbf{n} \cdot \mathbf{J} \sqrt{\gamma} d^3x = & \\ & \int_{\partial V_1} \left(\beta^i s_i \mathbf{n} \cdot \mathbf{J} \sqrt{\gamma} + \tilde{\mathbf{N}} \cdot \mathbf{J} \sqrt{-\tilde{h}} \right) dx^2 \\ & - \int_{V_1} S \alpha \sqrt{\gamma} d^3x, \end{aligned} \quad (5.1.127)$$

which is in the same form as Eq. (5.1.15) with definitions,

$$\mathcal{Q} := J^\mu n_\mu, \quad (5.1.128)$$

$$\mathcal{F} := \frac{\sqrt{-\tilde{h}}}{\sqrt{\sigma}} J^\mu \tilde{N}_\mu + \frac{\sqrt{\gamma}}{\sqrt{\sigma}} \beta^i s_i \mathcal{Q}, \quad (5.1.129)$$

$$\mathcal{S} := \alpha S, \quad (5.1.130)$$

where we used $\mathbf{n} \cdot \mathbf{J} = \mathcal{Q}$ for the flux term. The density term \mathcal{Q} and source term \mathcal{S} are agnostic to our choice of extraction surface and its time evolution so have turned out the same as Eqs. (5.1.16) and (5.1.18). At first glance the flux term \mathcal{F} seems different to Eq. (5.1.25) but evaluating this term in a coordinate basis will show otherwise.

Choosing a spherical extraction surface as in Section 5.1.3 and using spherical polar coordinates, $x^\mu = \{t, r, \theta, \phi\}$, V_1 becomes the coordinate 3-volume $r \leq r_0$, $t = t_0$. The unit normal $\tilde{\mathbf{N}}$ satisfies $\tilde{\mathbf{N}} \cdot \mathbf{n} = 0$ so $\tilde{N}^\mu = (0, \tilde{N}^i)$ where,

$$\tilde{N}_i = \frac{\nabla_i(r - r_0)}{\sqrt{\gamma^{jk} \nabla_j(r - r_0) \nabla_k(r - r_0)}}, \quad (5.1.131)$$

$$= \left(\frac{1}{\sqrt{\gamma^{rr}}}, 0, 0 \right), \quad (5.1.132)$$

and the flat space normal has components is $s^i = s_i = (1, 0, 0)$ with respect to spherical polar coordinates over a different flat manifold. Using Eqs. (5.1.31) and (5.1.32) with Cramer's rule for matrix inverse, it can be shown that,

$$\gamma^{rr} = \frac{\det \sigma_{ab}}{\det \gamma_{ij}} = \frac{\sqrt{\sigma}^2}{\sqrt{\gamma}^2}, \quad (5.1.133)$$

$$\tilde{h}^{tt} = \frac{\det \sigma_{ab}}{\det \tilde{h}_{ij}} = -\frac{\sqrt{\sigma}^2}{\sqrt{-\tilde{h}}^2}, \quad (5.1.134)$$

where it should be noted that $\tilde{h} < 0$ and $\sigma > 0$. Deriving Eq. (5.1.134) uses the fact that \tilde{H} intersects Σ_t on ∂V_1 and therefore must have the same line element for variations in angular coordinates; hence $g_{\theta\theta} = \tilde{h}_{\theta\theta}$, $g_{\theta\phi} = \tilde{h}_{\theta\phi}$ and $g_{\phi\phi} = \tilde{h}_{\phi\phi}$. The final component we need is to calculate \tilde{h}^{tt} which can be done by projecting the 4-metric \mathbf{g} onto \tilde{H} as,

$${}^{(4)}\tilde{h}^{\mu\nu} = g^{\mu\nu} - \tilde{N}^\mu \tilde{N}^\nu, \quad (5.1.135)$$

$${}^{(4)}\tilde{h}^{tt} = g^{tt} - \tilde{N}^t \tilde{N}^t, \quad (5.1.136)$$

$$= -\alpha^{-2}, \quad (5.1.137)$$

where ${}^{(4)}\tilde{\mathbf{h}}$ is a 4-tensor belonging to \mathcal{M} and $\tilde{N}^t = 0$. Using the pushforward of $\tilde{\mathbf{h}}$ on \tilde{H} to ${}^{(4)}\tilde{\mathbf{h}}$ on $\mathcal{M}|_{p \in \tilde{H}}$, similarly to Sec. 5.1.3, it can be shown that ${}^{(4)}h^{tt} = h^{tt}$. Equations (5.1.134) and (5.1.137) combine to give,

$$\sqrt{-\tilde{h}} = \alpha\sqrt{\sigma}, \quad (5.1.138)$$

again noting $\tilde{h} < 0$. Now we can re-write the flux (5.1.129) term as,

$$\mathcal{F} = \alpha J_\mu \tilde{N}^\mu + \frac{1}{\sqrt{\gamma^{rr}}} \beta^i s_i \mathcal{Q}, \quad (5.1.139)$$

$$\mathcal{F} = \alpha \gamma^{r\nu} J_\nu \tilde{N}_r + \frac{1}{\sqrt{\gamma^{rr}}} \beta^r \mathcal{Q}, \quad (5.1.140)$$

$$= \frac{1}{\sqrt{\gamma^{rr}}} (\alpha \gamma^{r\nu} J_\nu + \beta^r \mathcal{Q}), \quad (5.1.141)$$

and this is identical to Eq. (5.1.42) found earlier.

Chapter 6

The Gravitational Afterglow of Boson Stars

6.1 The Gravitational Afterglow of Boson Stars

6.1.1 Introduction

Gravitational waves (GWs) were first predicted by Einstein in 1916 as a consequence of general relativity. Their recent detection by the LIGO and Virgo observatories has opened up a new window on the Universe. This window has led to new probes of the nature of black holes (BHs) and to a wealth of astrophysical findings, challenging our understanding of stellar evolution and binary population models [161, 162, 74, 163]. However, one of the most exciting and as yet unrealised prospects is to use GWs to shed light on the nature of the dark matter (DM) component of the Universe’s energy budget. In the absence of direct couplings between dark and baryonic matter, gravitational interactions will be the only way to probe fundamental characteristics of DM - i.e. mass, spin and strength of self-interactions. With weakly interacting massive particles (WIMPs) proving elusive in direct detection experiments, there has been a resurgence in the interest of other DM candidates, particularly those with low masses ($m \leq \text{eV}$) and bosonic in nature. Promising alternatives of this type include the QCD axion, axion-like particles (ALPs) motivated by string theory compactifications, and “dark photons” [164, 165, 166, 167, 168, 169, 170, 171, 172, 173].

These bosonic distributions may condense, for example from localised overdensities [174], into gravitationally bound compact objects, which are referred to as boson stars (BS) [175, 62, 176, 177, 178, 41, 40, 179, 180, 181, 182, 183]. Stationary equilibrium solutions of this type have been found for different types of bosons, including scalars [184, 185, 186, 187, 6, 87, 103, 104, 188, 105, 189, 190, 191, 192, 193, 194, 89, 195, 179, 118, 120, 196, 197, 198, 199], vector fields [88, 200, 201, 202, 203, 204, 205, 206, 107, 207, 208, 209, 210, 211] or higher-spin fields [212].

Binary coalescences involving BSs represent a promising channel to observationally identify or constrain their populations. Their potentially high compactness implies that mergers can generate GWs detectable with present GW observatories. Most present work in the literature on BSs focuses on the GW signatures generated during the pre-merger infall or inspiral [213, 214, 108, 215, 216] and during the merger phase itself [217, 218, 184, 147, 219, 133, 42, 220, 41, 130, 132, 131, 129, 221, 222, 223, 224, 225]; these are, of course, the regimes of most notable interest in the GW observation of neutron-star and black-hole binary coalescences. The main focus of our work, however, is the long-lived post-merger GW emission or *afterglow* resulting from the merger of two BSs into a single compact but horizon-free remnant (see 6.4). First indications of such an afterglow were noted in Ref. [133] in the case of a head-on collision resulting in a highly perturbed BS. Here, we demonstrate that this afterglow can be very long lived, with barely any decay in amplitude following a transient burst during the merger phase itself. The characteristics of this post-merger afterglow contrast sharply with the corresponding GW signatures of most BH or NS mergers, which, if resulting in BH formation, are dominated by the exponential quasi-normal ringdown.

We illustrate and explore in detail the gravitational afterglow of BSs for the case of the inspiral and merger of two equal-mass BSs in a collision with a non-zero impact parameter. For the moderate compactness of the initial binary constituents chosen in our simulations, the final state of the collision is a highly perturbed BS with decreasing spin. Crucially, this spin-down occurs on a time scale *much longer* than a single GW oscillation time period. The associated long-lived GW afterglow may exhibit information about the post-merger dynamics of such systems. In particular, we find an intriguing correlation between the phases of different GW multipoles and the dynamical spin amplitude.

The results of this work suggest that using standard merger templates consisting mostly of the inspiral and merger contributions may be insufficient to capture fundamental dynamics of a boson-star merger event. Rather, comprehensive BS searches likely require extended waveform templates which also capture the rich post-merger GW afterglow phenomenology.

In 6.1.2 we briefly summarise our computational framework, list the parameters of our initial configurations and the grid setups employed in their time evolution, and introduce the diagnostics specific to our

simulations. In Sec. 6.1.3, we list the key features of the post-merger remnant. The corresponding GW signal is discussed in more detail in Sec. 6.1.4 and we conclude in Sec. 6.1.5. Technical details of the calculation of angular momentum, and the estimate of numerical uncertainties are relegated to Sec. 6.1.6 and Sec. 6.1.7.

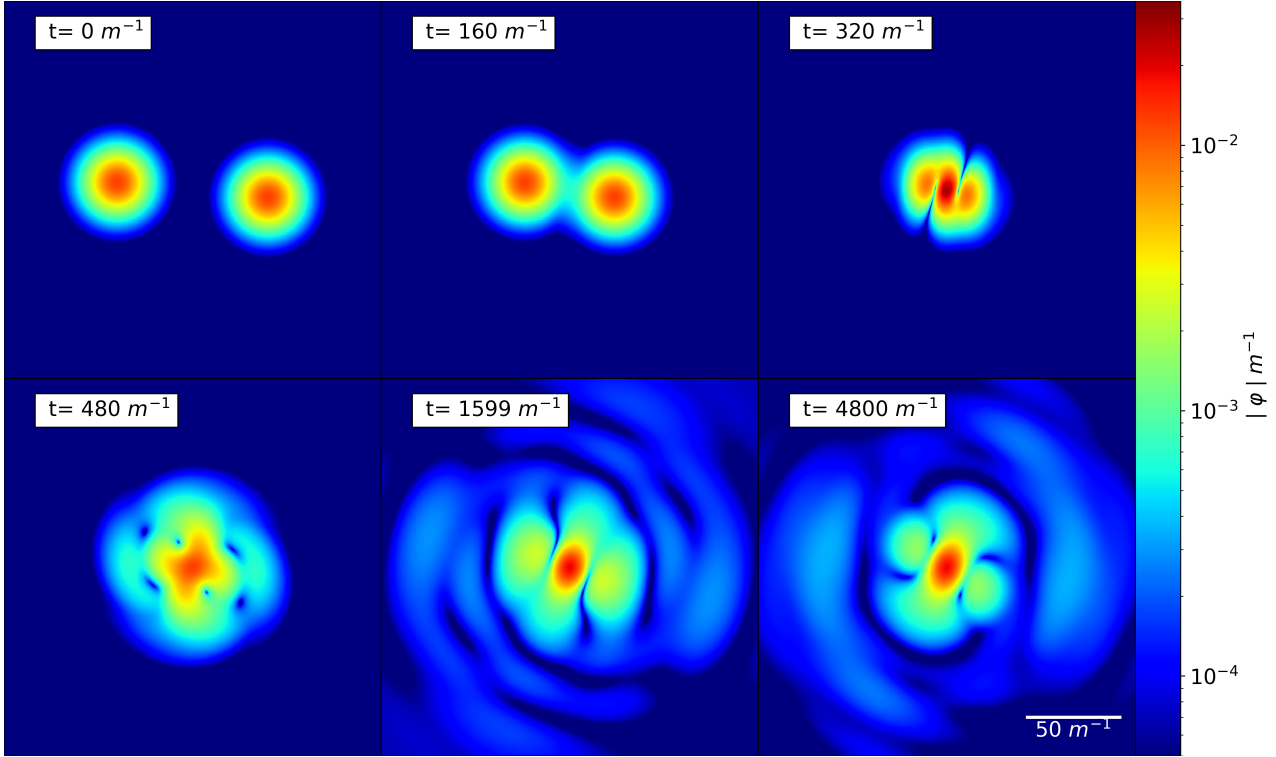


Figure 6.1: Snapshots of the scalar field amplitude $|\varphi|$ in the orbital plane for a grazing collision of two boson stars of equal mass $M = 0.395 M_{\text{pl}}^2 m^{-1}$ starting with initial horizontal distance $80 m^{-1}$, impact parameter $b = 8 m^{-1}$ (vertical centre to centre distance) and initial velocity $v = \pm 0.1$ in the x (horizontal) direction. A video of the merger can be found at <https://youtu.be/JE5FRG7kgvU>.

6.1.2 Simulation Setup

Throughout this work, we model BSs as a complex scalar field minimally coupled to the gravitational sector of a Lorentzian manifold with metric $g_{\alpha\beta}$. The corresponding Lagrangian is given by the Einstein-Hilbert action plus a matter term for a complex scalar field, as in section 2.2.1,

$$\mathcal{L} = \frac{1}{16\pi} R + \mathcal{L}_m, \quad (6.1.1)$$

$$\mathcal{L}_m = -\frac{1}{2} g^{\mu\nu} \nabla_\mu \bar{\varphi} \nabla_\nu \varphi - \frac{1}{2} V(\varphi). \quad (6.1.2)$$

The potential function for a non-interacting scalar of mass m ,

$$V(\varphi) = m^2 \bar{\varphi} \varphi; \quad (6.1.3)$$

this choice of potential results in BS solutions that are referred to as *mini-boson stars* [6, 226, 227].

Our construction of boson-star binary initial data can loosely be summarised in the following three steps.

1. Generate a stationary, non-rotating solution for a single boson star (2.2.2).
2. Apply a Lorentz boost to obtain a single star with linear momentum (2.2.5).

3. Superpose two such solutions according to the procedure described in section 4.2.2, or Refs. [133, 2], which substantially reduces spurious initial oscillations of the individual BSs as compared to the more common procedure of plain superposition.

Most of our results are obtained from simulating a grazing collision of two stable BSs, each with mass¹ $M = 0.3950 M_{\text{pl}}^2 m^{-1}$ and initial velocity $v = \mp(0.1, 0, 0)$.

The stars are initially located $d_{\text{init}} = 80 m^{-1}$ apart in the x direction and also offset by an impact parameter $b = 8 m^{-1}$ perpendicular to this axis; it is through this offset (rather than a velocity component off the x direction) that the binary is endowed with initial orbital angular momentum. The Newtonian point-particle estimate for the angular momentum of this configuration,

$$L_N = Mbv_x = 0.316 M_{\text{pl}}^2 / m^2, \quad (6.1.4)$$

agrees remarkably well with the relativistic measurement which only deviates by 1.1 %. A summary of this binary's initial data together with the main parameters of the numerical setup are given in Table 6.1. We have simulated numerous other binary configurations – different boson star masses, initial velocities v and impact parameters b – that display qualitatively the same behaviour. The main features of the binary dynamics that we will report in the following are thus *not* a consequence of any fine tuning of initial data.

	Run	N	$d_{\text{init}} [m^{-1}]$	$b [m^{-1}]$	v_x	$M [M_{\text{pl}}^2 m^{-1}]$
low	1	256	80	8	0.1	0.395(0)
medium	2	320	80	8	0.1	0.395(0)
high	3	384	80	8	0.1	0.395(0)
ultra-high	4	448	80	8	0.1	0.395(0)

Table 6.1: **Overview** of the simulations. Here, M is the individual mass of each boson star, v_x the initial velocity, b the impact parameter, d_{init} the initial distance in the x direction, b the vertical offset or *impact parameter* and N is the number of cells on the coarsest AMR Level (which sets the resolution of the respective runs). We allow for seven extra refinement levels.

For all simulations, we use a square box of width $D = 1024 m^{-1}$, employing the adaptive mesh refinement (AMR) capabilities of GRChombo [228, 229, 142]. Besides the standard computation of the Newman-Penrose scalar whose implementation in GRChombo is described in detail in Ref. [228], we compute in our simulations two diagnostic quantities specific to the BS systems under study.

First, we introduce the mass measure

$$M = \int_{\Omega} \rho \sqrt{\gamma} dV, \quad (6.1.5)$$

where $\rho = T_{\mu\nu} n^\mu n^\nu$ is the energy density as measured by observers moving along the normal vector n^μ to the spatial hypersurfaces. The second is a time dependent measure \tilde{L} , defined in Eq. (6.1.17), for the angular momentum contained inside a specified volume V . This quantity is obtained by adding to the initial angular momentum the time integrated rate of change due to the source of momentum that crucially includes contributions from the spacetime dynamics; the details for computing this quantity \tilde{L} are given in section 6.1.6.

6.1.3 The Merger Remnant

When colliding two BSs with angular momentum, we expect one of the following outcomes:

¹This mass is obtained for a central scalar-field amplitude $|\varphi(0)|/M_{\text{pl}} = 0.0124$ and results in a compactness estimate $\mathcal{C} := \max(m(r)/r) = 0.024$ in radial gauge. For comparison the Kaup limit configuration has $M = 0.633 M_{\text{pl}}^2 m^{-1}$ and $\mathcal{C} = 0.12$.

1. A toroidal spinning BS [230, 115, 231, 125],
2. A non-spinning BS with perturbations carrying away the angular momentum [225, 232, 233, 234],
3. A black hole [133, 42, 220], or,
4. Total dispersion of all matter.

For sufficiently small compactness of the progenitors the merger does not form a black hole. While we have observed black-hole formation in some of our calibration runs starting with more compact BSs (for example in section 3.2.6), in the remainder of this chapter we focus on the scenario where the merger results in a compact bosonic configuration without a horizon as shown in Fig. 6.1. The scalar-amplitude profiles in this figure (nor at any other times during the evolution) display no signs of a toroidal structure and we therefore interpret the merger outcome as a perturbed non-spinning BS corresponding to the second item in the above list; cf. also Refs. [42, 220].

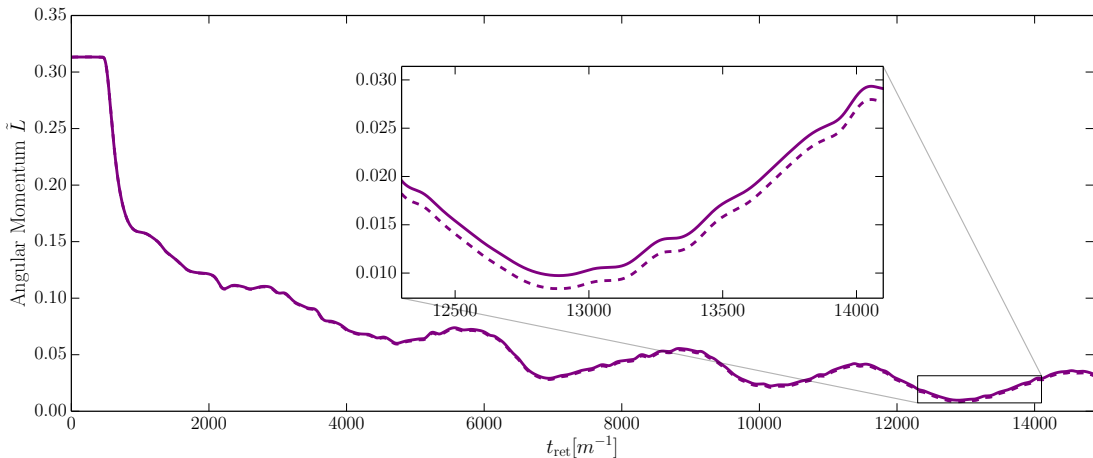


Figure 6.2: Angular momentum of the scalar field: We show the angular momentum \tilde{L} (see definition in 6.1.17) inside a coordinate sphere of radius 60 m^{-1} as a function of time. We compute \tilde{L} in two ways, (i) via integrating the outgoing flux – solid lines (see 6.1.11) – and (ii) as a volume-integral – dotted lines. This was plotted using run 2 of Table 6.1.

In Fig. 6.2, we display the angular momentum \tilde{L} of the BS configuration inside a coordinate sphere of radius 60 m^{-1} throughout inspiral, merger and the afterglow phase. Up to the time of merger around $t \approx 300 \text{ m}^{-1}$, the angular momentum remains approximately constant before rapidly decreasing in the post-merger phase. To leading order, the tail of the resulting curve $\tilde{L}(t)$ is approximated by an exponential decay with half-life $4 \times 10^3 \text{ m}^{-1}$, as obtained from an exponential fit to the data of Run 2 (of Table 6.1) starting at $t = 2000 \text{ m}^{-1}$. Translated into SI units, the half-life is

$$t_{\text{half}} = 83 \text{ years} \left(\frac{10^{-21} \text{ eV}}{m} \right). \quad (6.1.6)$$

For a scalar mass $m = 10^{-14} \text{ eV}$, for example, the dominant frequency of the $\ell = 2, m = 0$ signal falls into the most sensitive region of the LISA noise curve (see Eq. 6.1.7) and we obtain a half-life of $\sim 4 \text{ min}$. For scalar masses in or above this regime, this implies that a delayed formation of a black hole, should it occur, will result in a black hole with negligible spin. With regard to the possibility of the formation of a black-hole population through isolated BS progenitors [194, 193], this implies that spinning black holes are unlikely to have formed this way unless the BS progenitors are composed of ultra light scalar particles. More quantitatively, we see from Eq. (6.1.6), that astrophysically large decay times for the

angular momentum of order $\mathcal{O}(\text{Myr})$ require ultra light scalars with mass² $m \lesssim 10^{-25} \text{ eV}$.

The rapid drop in the angular momentum of rotating scalar soliton stars has been noticed as early as the mid 1980s [104, 188], but we note that the post-merger evolution of our \tilde{L} , besides an approximately exponential drop, also exhibits significant oscillations on a time scale of about 2000 m^{-1} . We conjecture that these oscillations arise from the complex dynamics of the post-merger remnant and may carry memory of its formation process.

We also observe significant oscillations in the time evolution of the merger remnant's mass M as defined in Eq. (6.1.5). As demonstrated in Fig. 6.3, however, the mass evolution differs significantly from that of the angular momentum. First, the mass gradually levels off at $M \sim 0.57 M_{\text{Pl}}^2 m^{-1}$ or $\sim 72\%$ of the initial mass instead of decaying over time. Second, the oscillations occur on a much shorter time scale. The fluctuations after merger are attributed to the fact that the estimated mass is calculated as in section 5.1.5 by volume integrating only the energy density term whereas the angular momentum measure (which does not see similar fluctuations) includes the source term as well. The inclusion of this source term smooths out the fluctuations in the integrated quantity as mentioned in section 5.1.6.

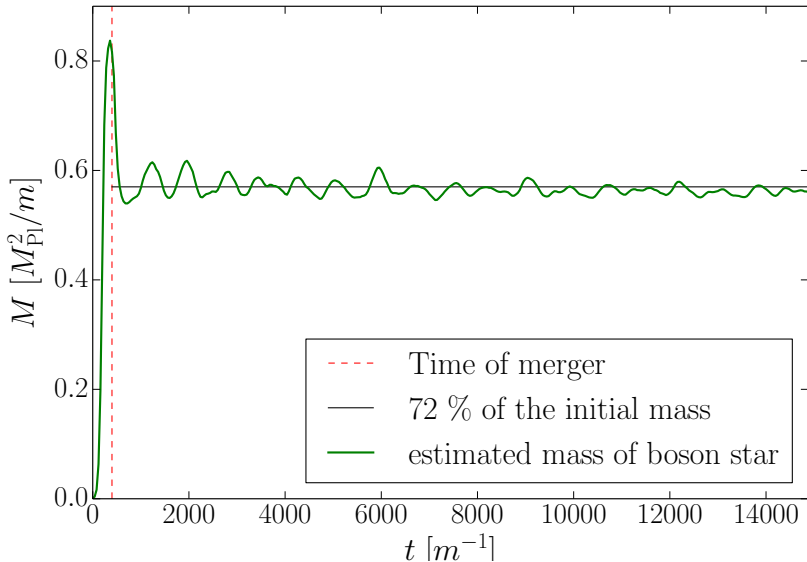


Figure 6.3: **The estimated mass** using 6.1.5 contained inside a box Ω with side length 40 m^{-1} as computed for the “medium” resolution run 2 of Table 6.1. Since the BSs are not initially inside this box, the mass at $t = 0$ is close to zero.

6.1.4 Gravitational Wave Signal

We now turn our attention to the GW signal generated by the BS coalescence. We find this signal to be dominated by the $(l, m) = (2, \pm 2)$ and $(2, 0)$ quadrupole modes which are displayed in Fig. 6.4 for Run 2 in Table 6.1) using an extraction radius 220 m^{-1} . The large burst around merger at $t \approx 300 \text{ m}^{-1}$ (see the upper left inset of the figure) closely resembles the corresponding features regularly seen in the merger of black-hole binaries. The ensuing long-lived, semi-regular radiation clearly visible with barely any signs of diminution up to the end of our simulation, however, drastically differs from the familiar ringdown of a merged black hole. This *afterglow* signal is the main result of our study. We emphasise that this signal is well resolved (rather than merely displaying numerical noise), and also persists with negligible variation under changes in the numerical resolution of our grid. As discussed in more detail in 6.1.7, we

²Note that candidates below $m \lesssim 10^{-22} \text{ eV}$ are ruled out as constituting 100% of the DM by structure formation constraints but may still form some proportion of the DM [166]

estimate the numerical uncertainty of the $r\Psi_4$ signal at about 7% during the afterglow phase with most of this error budget being due to the finite extraction radius. The GW signals of the higher-resolution Runs 3 and 4, if added to Fig. 6.4, would almost overlap with that shown in the figure for Run³ 2; cf. also Fig. 6.5 below.

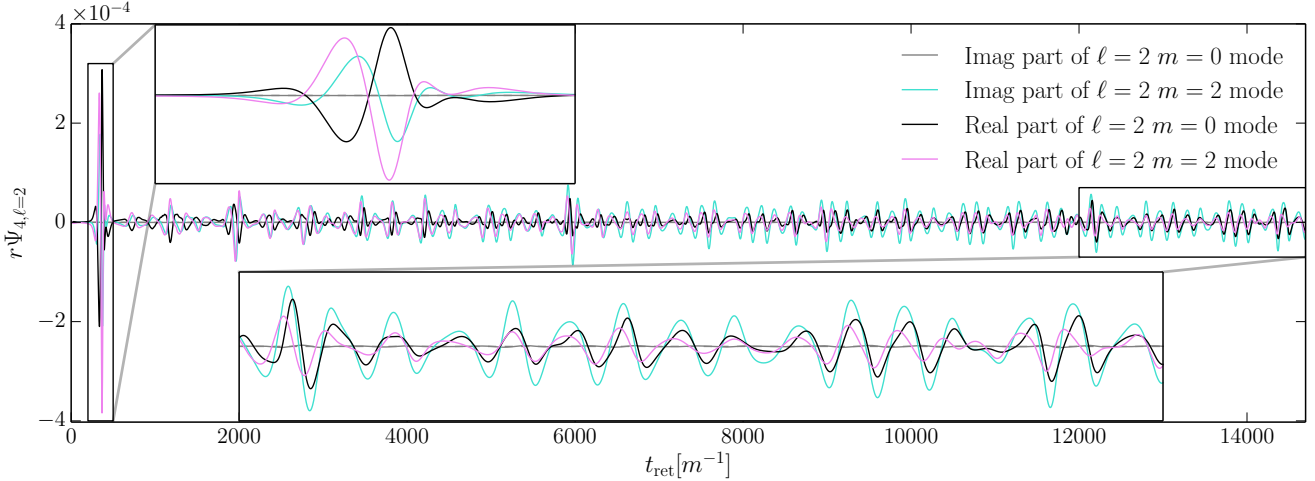


Figure 6.4: **Gravitational wave afterglow** emission from the collision of two boson stars with non-zero impact parameter (Run 2 in Table 6.1). The Weyl scalar Ψ_4 is extracted at $r = 220 \text{ m}^{-1}$ and we only show the dominant $(\ell, m) = (2, 2), (2, 0)$ modes. The $(\ell, m) = (2, \pm 1)$ vanishes identically due to symmetry. There is a large initial burst at merger (first zoom-in box), followed by a long, but irregular signal produced by the excited remnant boson star. A video of the merger can be found at <https://youtu.be/JE5FRG7kgvU>.

The afterglow signal (without the prodigious merger burst) is also shown in Fig. 6.6 together with its Fourier spectrum. The frequency spectrum demonstrates contributions on many time scales, but also reveals a narrow dominant peak at $f_{\text{dom}} \approx 0.6 \times 10^{-2} \text{ m}$ which, translated into SI units, can be written as

$$f_{\text{dom}} \sim 9.0 \cdot 10^{-2} \text{ Hz} \left(\frac{m}{10^{-14} \text{ eV}} \right). \quad (6.1.7)$$

Both the time- and frequency-domain signals exhibit signature of beating effects: the amplitude of the rapid oscillations itself undergoes a modulation at lower frequency.

The prolonged afterglow furthermore accumulates a non-negligible amount of energy emitted in GWs. By the end of our simulation at $t \approx 15\,000 \text{ m}^{-1}$, the radiated energy computed according to Eq. (6.1.20) including infall and merger has reached $(0.04 \pm 0.0014)\%$ of the initial mass, corresponding to an average rate of $2.5 \times 10^{-8} M_{\text{init}} \text{ m}$ (see dotted line in 6.7). The radiated energy and power are shown as functions of time in Fig. 6.7 and clearly show an approximately linear increase in E_{GW} during the afterglow phase. This significant amount of post-merger GW emission in itself is a striking signature of exotic binary merger progenitors that distinguishes them from BH binaries devoid of significant post-merger radiation beyond the quasi-normal ringdown. A crude comparison of the radiated energy of the boson-star collision to a black-hole collision can be made with the data in [235]; an equivalent black-hole collision could potentially radiate $\sim 2\%$ of the initial mass⁴. By using windowing of the GW signal, we

³Run 2 is our second longest simulation, run for nearly as long as the low resolution Run 1, and used for most of our analysis.

⁴This comparison is not perfect as the black-hole collision data in [235] has initial boosts perpendicular to the initial separation only. The boson-star collision has a perpendicular momentum per star mass of $P/M = 0.00995$, a parallel separation per star mass of $D/M = 203.5$ and an angular momentum per star mass squared of $L/M^2 = 2.03$ which, ignoring the large component of velocity parallel to the initial separation, can be compared to the black-hole collision. Extrapolating

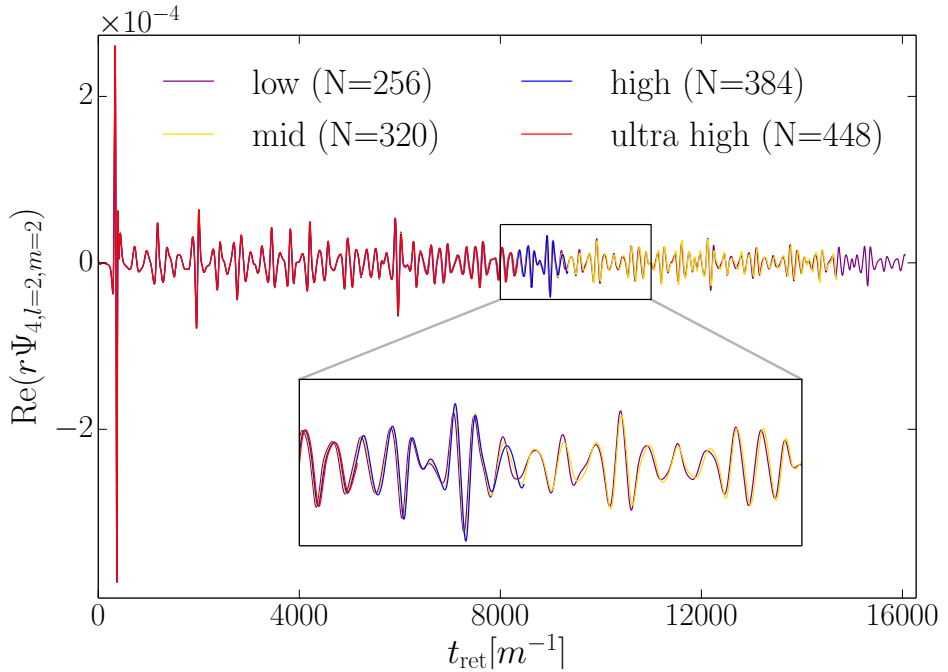


Figure 6.5: **Convergence:** We display the $(2, 2)$ multipole of the GW signal obtained for four different resolutions corresponding to runs 1 to 4 in 6.1. A quantitative analysis yields overall convergence at first order.

find that the rate of radiation in the afterglow (excluding the merger peak) decreases by about 20% over the course of the simulation. Note that the decay in GWs is much more protracted than the drop in the angular momentum displayed in Fig. 6.2. Clearly, the system loses angular momentum much more rapidly than energy.

A more subtle feature in the post-merger signal is revealed in the multi-polar decomposition of the quadrupole signal; more specifically in the relative position of the local extrema in the $(\ell, m) = (2, 2)$ and $(2, 0)$ modes. As exhibited by the upper left inset of Fig. 6.4, the amplitudes of the $(2, 2)$ and $(2, 0)$ modes are almost exactly in anti-phase around merger and remain so in the early afterglow around $t \sim 1000 \text{ } m^{-1}$. At late times $t \gtrsim 3000 \text{ } m^{-1}$, however, the two modes are almost synchronised with their extrema in good overlap. The timing of this synchronisation coincides remarkably well with the drop in angular momentum shown in Fig. 6.2 and we hypothesise the two effects are causally related. This would imply a concrete observational signature of the BS angular momentum in the emitted GW afterglow signal.

In physical terms, the GW afterglow is a direct consequence of the presence of matter around the compact merger remnant and the resulting complex matter dynamics following the violent merger. A qualitatively similar behaviour may arise in the merger of neutron stars provided these do not promptly merge into a black hole. Two key differences between neutron-star and BS signals, however, may aid considerably in the distinction between neutron-star and BS signals. The first consists in the extremely long-lived nature of the BS afterglow which we anticipate will last for much longer times than are presently within grasp of our numerical studies; cf. again Fig. 6.4 and the barely perceptible drop in the GW signal. The second fundamental discriminator arises from the scale-free nature of the BS spacetimes; the scalar mass parameter m appears as a characteristic scale in all dimensional variables of the GW analysis. While NS masses are restricted to be below the Chandrasekhar limit of about $2M_\odot$,

outside of the given data in Table 1 of [235] gives a crude estimate of for a similar black-hole collision radiating $\sim 2\%$ of the initial mass. It is unclear what effect the ignored component of momentum parallel to initial boost in the boson-star binary has.

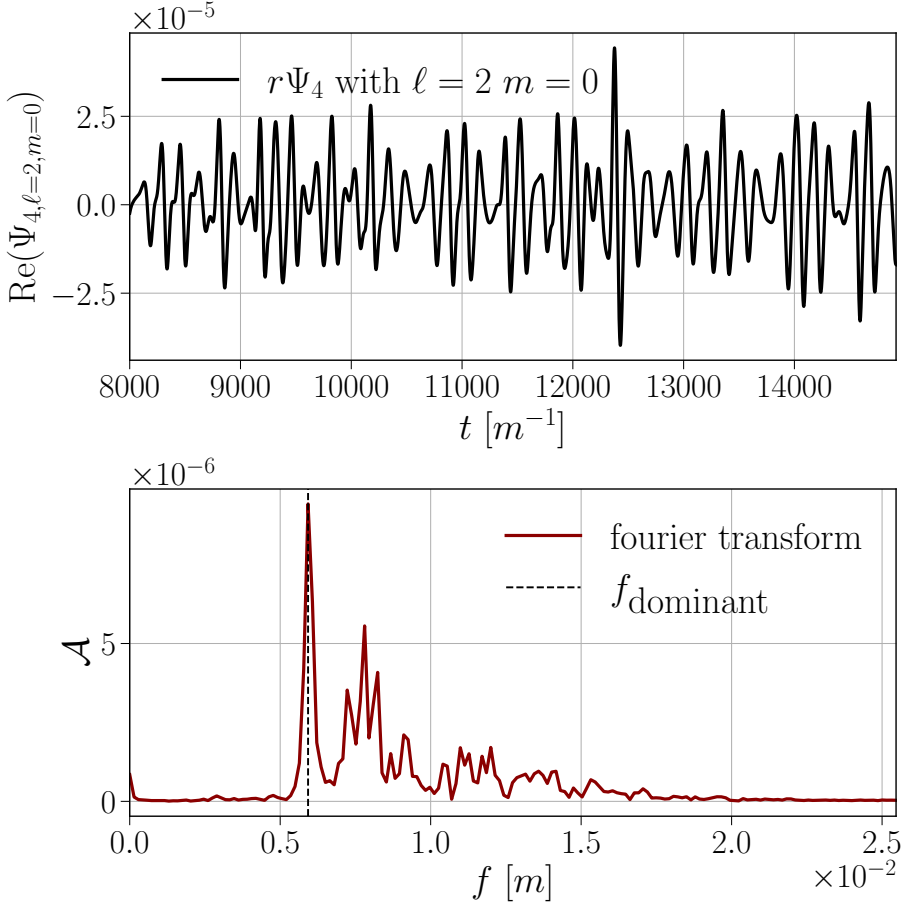


Figure 6.6: **Time domain signal and Fourier transform of the (2, 0) mode of $r\Psi_4$:** We perform a Fourier transformation of the tail of the gravitational wave signal of Run 2 in Table 6.1. We find excellent agreement between the displayed spectrum for the (2, 0) mode and the corresponding Fourier transform of the (2, 2) mode; in particular, both yield the same peak frequency.

BSs may theoretically exist across the entire mass spectrum and barring for a remarkable coincidence in the scalar mass value, will be distinguishable from their neutron-star counter parts by the frequency regime of their GW emission. Put the other way round, comprehensive observational searches for GW signatures from BSs require scanning over a wide range of frequencies using vastly different detectors such as LIGO-Virgo-KAGRA, LISA, third-generation detectors but also high frequency GW observatories presently under development [236, 237].

6.1.5 Conclusion

We have shown that the inspiral and coalescence of BS binaries into a non-BH remnant can produce a long-lasting GW *afterglow*. This signature is salient, and markedly differs in duration and – possibly – also frequency from the GW signatures of more traditional astrophysical compact object mergers; it thus represents a distinct detection channel for exotic compact objects in compact-binary-coalescence and continuous-GW searches [238, 239, 240, 241, 242, 243, 244, 245]. Notably the late time scalar field configuration radiates angular momentum a few orders of magnitude slower than suggested by perturbation theory; the dramatic failure of perturbation theory in this case is a consequence of the highly nonlinear nature of the object in question.

There are several implications resulting from our findings. In terms of search strategies, as mentioned in the introduction, these signatures are likely to be missed if we focus exclusively on constructing pre-

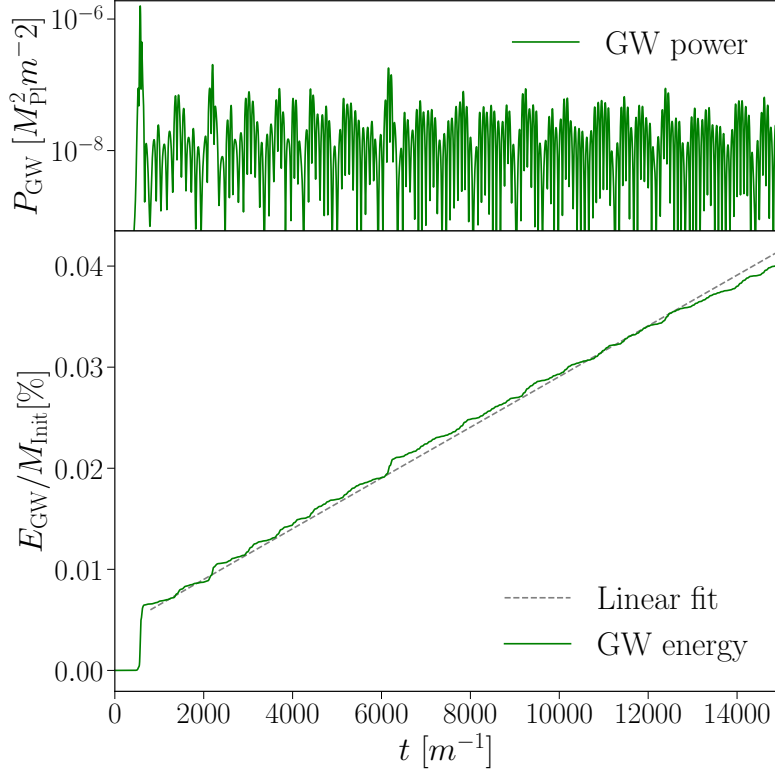


Figure 6.7: **Radiated GW energy over time:** We calculate the energy and power radiated in gravitational waves from Run 2 of Table 6.1. We observe no significant reduction in the GW radiation over the simulation time, allowing us to estimate a lower bound on the half-life of the signal.

merger inspiral and merger waveform templates. The systematic construction of waveform templates for post-merger signatures of this type of binaries is in its infancy at present and an immediate challenge for further work consists in identifying an effective parameterisation of the GW signatures. Our results furthermore demonstrate an efficient loss of angular momentum in BS mergers resulting in a horizon-less remnant, consistent with previous studies noticing that the spin of rotating BSs decays with a fairly short half-life of $4 \times 10^3 \text{ m}^{-1}$ [123]. We also observe a remarkable correlation between the BS remnant's spin-down in Fig. 6.2 with a gradual synchronisation of the local extrema in the GW amplitudes of the (2, 2) and (2, 0) modes; from near anti-alignment of the peaks around merger and shortly thereafter, the extrema gradually shift into approximate overlap over a time interval $\Delta t \approx 2000 \text{ m}^{-1}$ (see Fig. 6.4), coinciding exactly with the time during which the angular momentum drops to a negligible level. We tentatively conclude that through this synchronisation, the GW afterglow carries important information about the remnant's dynamical evolution.

Given the extraordinary length of the afterglow signal, one would expect the radiation from numerous BS merger events – if they occur – to result in a stochastic background. Such a background could be searched for additionally to that expected from more traditional binary mergers [246]. Evidently, more exploration of the underlying BS parameter space and the resulting afterglow phenomenology will be required to relate theoretical estimates of the GW background to hypothesised BS populations. We reiterate, however, that nothing about our BS configurations has been fine-tuned, so that we expect the afterglow to be a rather generic feature of BS coalescences as long as these do not promptly form a black hole.

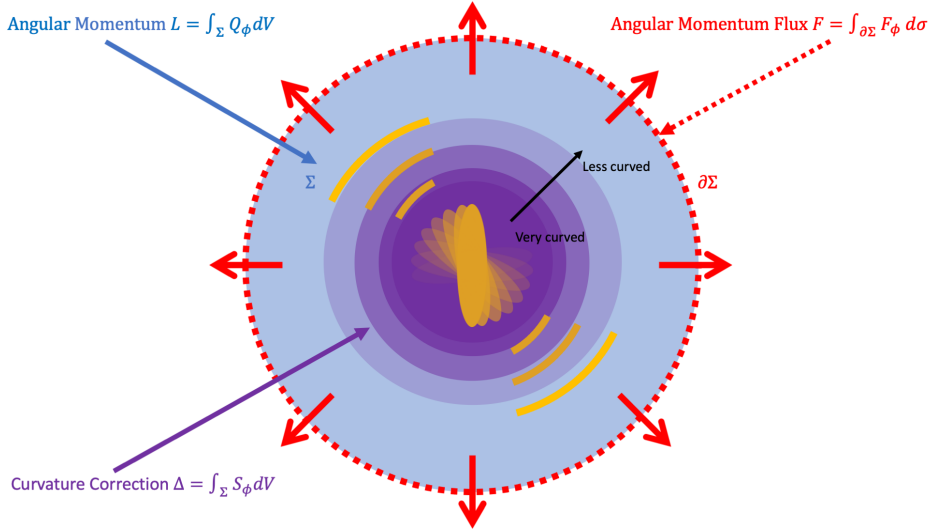


Figure 6.8: **Schematic representation of the angular momentum measure:** We illustrate the origin of the different quantities appearing in the conservation equation (6.1.16): The angular momentum L , the angular momentum flux F and the curvature correction Δ . Recall that the post-merger configuration does not have a toroidal structure as would be expected for the spinning BS model of Ref. [230, 115], but is more bar-like in shape.

6.1.6 Angular Momentum Measure

In general relativity isometries of the spacetime manifold lead to conserved quantities. In particular, if a spacetime conserves energy, then there must exist a time-like Killing vector field ξ . A classic example is that of the Kerr vacuum solution. On the other hand, in a less symmetric spacetime like that of a black-hole merger, such a Killing vector field does not usually exist except in the asymptotically flat region. In this section we define a diagnostic quantity for the angular momentum that does not require a Killing vector, but merely a vector field to generate a measure that converges to the classical angular momentum definition in the flat-spacetime limit.

In order to define such a measure in a precise manner we will follow the results of chapter 5 or [3, 247].

We start by defining, based on our Cartesian coordinates, the azimuthal vector

$$\xi^\mu = (\partial_\phi)^\mu = y(\partial_x)^\mu - x(\partial_y)^\mu . \quad (6.1.8)$$

We next define the angular angular momentum

$$L = \int_\Sigma \mathcal{Q} \sqrt{\gamma} d^3x , \quad (6.1.9)$$

with the volume element $\sqrt{\gamma}$ on the spatial hypersurface Σ , which in our case is a sphere of finite radius, and

$$\mathcal{Q} = -S_\phi , \quad (6.1.10)$$

where $S_\phi = S_i(\partial_\phi)^i$ is the azimuthal component of the mixed space-time projection S_i given by Eq. (??). We also integrate the angular momentum flux density \mathcal{F} through $\partial\Sigma$, to get the total angular momentum flux

$$F = \int_{\partial\Sigma} \mathcal{F} \sqrt{\sigma} d^2x . \quad (6.1.11)$$

Here $\sqrt{\sigma}$ is the induced volume element on $\partial\Sigma$ and the flux density is

$$\mathcal{F} = \frac{1}{\sqrt{\gamma^{rr}}} (\alpha S_\phi^r - \beta^r S_\phi) . \quad (6.1.12)$$

where $\boldsymbol{\beta}$ is the shift vector where $S_\phi^r = S^\mu_\nu (\partial_r)_\mu (\partial_\phi)^\nu$ and with $\boldsymbol{\partial}_r$ the radial unit vector.

If $\boldsymbol{\xi} = \boldsymbol{\partial}_\phi$ is a Killing vector the rate of change of the momentum within a given volume Σ will be equal to the momentum flux through the boundary, i.e.

$$\partial_t L = F. \quad (6.1.13)$$

However, in general dynamical spacetimes, we do not have such a Killing vector and angular momentum is not conserved in this simple manner. Instead, we obtain a further term representing curvature contributions on the right-hand side of Eq. (6.1.13) which effectively acts as a further source or sink of momentum for the matter [3, 247]. This term is given by

$$\Delta = \int_V \mathcal{S} \sqrt{\gamma} d^3x , \quad (6.1.14)$$

where the momentum source density $\mathcal{S} = \alpha \nabla_\mu \xi^\mu$ expressed in terms of the 3+1 variables is

$$\begin{aligned} \mathcal{S} = & \alpha S_\nu^{\mu(3)} \partial_\mu \xi^\nu + \alpha S_\nu^{\mu(3)} \Gamma_{\mu\sigma}^\nu \xi^\sigma \\ & - S_\nu \beta^i \partial_i \xi^\nu + S_\nu \xi^\mu \partial_\mu \beta^\nu - \rho \xi^\mu \partial_\mu \alpha , \end{aligned} \quad (6.1.15)$$

for a spacelike vector $\boldsymbol{\xi}$. The corresponding term for a timelike vector $\boldsymbol{\xi}$ is given (see Eq. (19) in [247]). We can thus generalise 6.1.13 to the exact conservation law

$$\partial_t L + \Delta = F ; \quad (6.1.16)$$

a schematic overview of the different contributions to this balance law is shown in Fig. 6.8. In the flat-space limit $\gamma_{ij} \rightarrow \delta_{ij}$, so that find that $\Delta \rightarrow 0$ and we recover Eq. 6.1.13 as expected given the symmetry of flat spacetime.

In our simulations we introduce the adjusted angular momentum defined as

$$\tilde{L} = L + \int_0^t \Delta dt , \quad (6.1.17)$$

which obeys the equation

$$\partial_t \tilde{L} = F. \quad (6.1.18)$$

We can then define a relative measure for the error in the conservation of angular momentum as

$$\text{err}_{\tilde{L}} = \frac{\tilde{L} - \int F dt}{L(t=0)} . \quad (6.1.19)$$

The resulting error measured for our BS binary using the four different resolutions is shown in Fig. 6.9 and exhibits clear convergence towards the expected limit of zero.

We reiterate that this angular momentum measure is a quasi-local quantity that obeys a rigorous conservation law given by Eq. (6.1.18) for any chosen volume. Its calculation does therefore not require extrapolation to infinity (as is needed, for example, for the calculation of the GW signal) nor even asymptotic flatness of the underlying spacetime. Also note that for matter fields decaying to zero on the surface of Σ the quantity \tilde{L} (but not L) is constant in time for a general spacetime.

In practice, we monitor the conservation of \tilde{L} as follows. We calculate our angular momentum measure by integrating (i) the angular momentum (see 6.1.17), and (ii) integrating the flux F (see 6.1.11) over time; we set the integration constant equal to $L(t=0)$. Having thus obtained two measures for the same quantity allows us to estimate the uncertainty by taking the difference between the two; see 6.9 for the evolution of the error. Using the final value of \tilde{L} obtained for Run 2 (see Table 6.1) inside the volume of a coordinate sphere of coordinate radius $60 m^{-1}$, we estimate the final spin of the merged BS as $0.0321 \pm 0.0007 M_{\text{pl}}^2 m^{-2}$.

6.1.7 Numerical Accuracy

To assess the accuracy of our results we have performed simulations with four different resolution given, in terms of the number of points in each direction on the coarsest level, by $N = \{256, 320, 384, 448\}$, all for a box width of 1024 m^{-1} . As demonstrated in Fig. 6.5, the individual wave signals obtained for this range of resolution are in excellent agreement. More quantitatively, we observe convergence at about 1st order convergence using the four resolutions for the $\ell = 2 m = 2$ mode of $r\Psi_4$. Additionally, we estimate the discretisation and error from the finite extraction region in $r\Psi_4$ and we find that the latter dominates, causing a $\sim 7\%$ error.

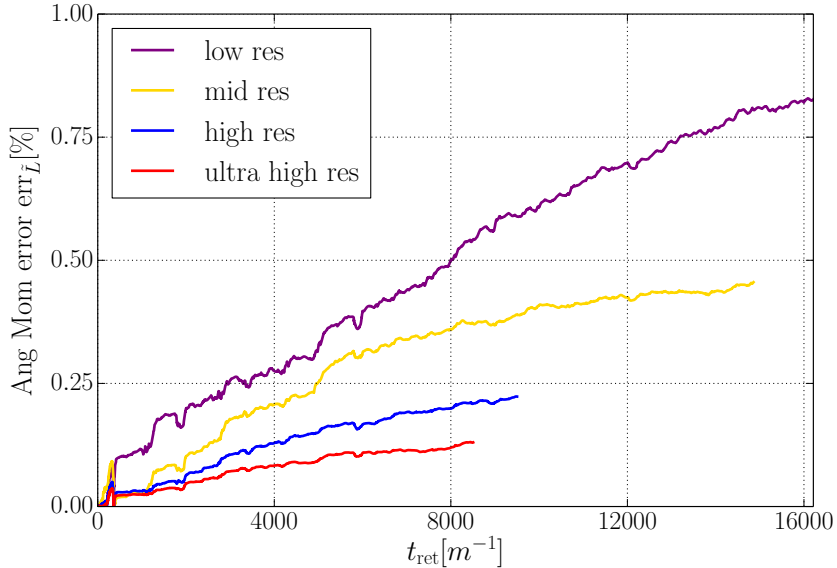


Figure 6.9: **Angular momentum error** : We numerically verify the conservation Eq. 6.1.16 for the simulations with parameters given in Table 6.1. In the continuum limit this quantity becomes zero. The coloured curves obtained for different resolutions demonstrate conservation with excellent accuracy of about $\sim 0.8\%$ error after 16000 m^{-1} and exhibit convergence to the zero continuum limit.

To calculate the energy (see Fig. 6.7) we used the the $\ell = 2$ modes and using the equation for the power

$$\frac{dE}{dt} = \lim_{r \rightarrow \infty} \frac{1}{16\pi} \sum_{\ell=2,m} \left| \int_{t_0}^t r\Psi_{4,\ell m} dt' \right|^2, \quad (6.1.20)$$

where we apply an 5th order Butterworth high-pass filter (using the scipy implementation [248]) on the integral $r\Psi_{4,\ell m}$. As otherwise accumulating numerical error causes a drift in the Energy over time. We estimate the error, similarly as for $r\Psi_4$, using both the discretisation error as well as the error from the finite extraction radius. For the discretisation error we use Richardson extrapolation assuming 1st order convergence to estimate the error. Similarly to before, we find that the error in the finite extraction radius dominates, giving us the value $0.04 \% \pm 0.0014 \%$.

Lastly to calculate the average rate of emission, we simply perform a linear fit over the whole energy over time signal of the largest radius of the “medium” run (see Fig. 6.7). We also perform this fit on a rolling window of 3000 m^{-1} to determine any reduction of radiation over time. Excluding the merger, we find the rate roughly declines by 20% over the simulation time.

Chapter 7

Anomalies in the Gravitational Recoil of Eccentric Black-Hole Mergers with Unequal Mass Ratios

7.1 Introduction

Gravitational waves (GWs) carry energy, angular momentum and linear momentum away from the source with potentially observable consequences. The radiated energy corresponds to an often enormous mass deficit in the source; for example the first ever detected black-hole (BH) binary merger, GW150914 [63], radiated $\Delta M \approx 3 M_\odot$, or about 4.6 % of the total mass of the source. A tiny fraction of this energy is deposited into GW interferometers, thus enabling us to detect and characterise the signal [249]. The angular momentum radiated in GWs reduces the rotation rate of possible merger remnants and—at least in four spacetime dimensions—plays a critical role in avoiding the formation of naked singularities in the form of BHs spinning above the Kerr limit; see e.g. Refs. [250, 251]. Therefore, GW emission is a necessary ingredient of the theory of general relativity, in the sense that it avoids the formation of naked spacetime singularities and preserves its predictive power.

In this chapter, we focus on the radiated linear momentum, which imparts a recoil (commonly referred to as a *kick*) on the centre of mass of the emitting system [252, 253, 254].

Whereas GWs inevitably carry energy and angular momentum—provided their sources do—the radiation of linear momentum requires some degree of asymmetry, as realised in nonspherical supernova explosions or unequal-mass ratios and/or spin misalignments in binary BH mergers. The inspiral of two equal-mass, nonspinning BHs, for example, radiates energy and angular momentum, whereas the emitted linear momentum is zero by symmetry. By turning these considerations around, we may also regard the study of recoiling GW emitters as a guided search for characteristic (in some loose sense “asymmetric”) features in their orbital dynamics which, in turn, might help us to better understand astrophysical sources through GW observations. A recoiling postmerger BH, for example, can induce a blue (or red) shift in parts of its GW signal that may be exploited in future GW observations to directly measure BH kicks [255, 256, 257], and the effect of kicks should be taken into account in future ringdown tests of general relativity with third-generation GW detectors to avoid systematic biases [258]. The asymmetric emission of GWs is not the only mechanism that can contribute to recoils; if there is an accretion disk or some other astrophysical background, this can also impart a kick on the remnant BH that can be $\mathcal{O}(100)$ km/s [259].

For binary BH mergers, early estimates of the recoil speeds of the remnant BH relied on a variety of approximations, including post-Newtonian (PN) theory [260, 261], BH perturbation theory [262], the effective-one-body formalism [263], the close-limit approximation [264, 265], and combinations thereof [266]. Not long afterwards, during the numerical relativity (NR) gold rush, several groups obtained more accurate results for the kick velocity from the merger of nonspinning BHs along quasicircular orbits [267, 268, 269]. These calculations were followed by the discovery that the merger of spinning BHs can lead to kick velocities of ~ 3000 km/s when the spins lie in the orbital plane and point in opposite directions (“superkick” configurations [270, 271, 272]), and to even larger kicks of order ~ 5000 km/s when the spins are partially aligned with the orbital angular momentum (“hang-up kick” configurations [273]). The probability of such large recoils occurring in nature depends therefore on spin alignment, and this has been studied by several authors (see, e.g., Refs. [274, 275, 276, 277, 278, 277]).

The possible occurrence of superkicks has important consequences for astrophysical BHs and their environments [279, 280, 281, 79]. It is pertinent to compare the recoil velocities obtained from NR simulations with the escape velocities of various astrophysical environments [282]. For example, stellar-mass BH binaries are believed to form dynamically in globular clusters [283]. In this case the escape velocities are generally $\mathcal{O}(10)$ km/s, smaller than the $\mathcal{O}(100)$ km/s kicks predicted for quasicircular, nonspinning binaries [268]. Then relativistic recoils can affect the proportion of BH merger remnants that are retained by globular clusters even if the BHs are nonspinning [284]. At the other end of the scale, the recoil velocities of supermassive BHs can be used to constrain theories of their growth at the centre of dark matter halos [285]. Kicked remnants in the accretion disk of an active galactic nucleus may also lead to detectable electromagnetic counterparts for stellar-origin BH mergers [286, 287].

As mentioned above, a net gravitational recoil requires some asymmetry in the system, so that the GW emission is anisotropic. A natural way to accentuate the asymmetry is through the addition of orbital eccentricity. Early calculations in the close-limit approximation [265] predicted a kick proportional to $1+e$ for small eccentricities, $e \lesssim 0.1$. More recently, numerical relativity calculations led to the conclusion that eccentricity can lead to an approximate 25% increase in recoil velocities for superkick configurations with moderate eccentricities [288].

The main goal of this study is to investigate the impact of nonzero eccentricity on the kick magnitude and the corresponding GW emission of nonspinning, unequal-mass BH binaries. As we shall see, the eccentricity has a subtle but significant effect on the kick magnitude, which manifests itself in corresponding patterns in the GW signal, especially in subdominant multipoles.

For isolated binary systems with large initial separations, the emission of GWs acts to circularise the orbit by the time the signal enters the frequency band of ground-based detectors. However, viable dynamical formation channels of stellar-origin BH binaries could result in a non-negligible population of merging BHs that still retain moderate eccentricities at frequencies relevant for ground-based GW detection (see, e.g., Refs. [289, 290, 291, 292, 293, 294]). Furthermore, the presence of astrophysical media such as accretion disks may increase the eccentricity during the inspiral [295]. Most of the events observed by the LIGO/Virgo Collaboration show no evidence of significant eccentricities [296] but the extraordinary GW190521 event [297] is potentially consistent with an eccentricity as high as $e \approx 0.7$ [298, 299].

Orbital eccentricity is expected to be a distinguishing feature of stellar-origin BH binaries that form dynamically, but a nonzero eccentricity is more likely at the low frequencies accessible by LISA, where gravitational radiation reaction has less time to circularise the binary [300, 301, 302]. If confirmed, a nonzero eccentricity would hint at a possible dynamical origin for this event [298].

Eccentricity is expected to play an even more prominent role for massive BH binaries: the dynamics of these binaries in stellar and gaseous environments may lead to nonzero orbital eccentricities by the time the binaries enter the LISA sensitivity window (see Ref. [303] and references therein). Even larger eccentricities are possible if BH binary coalescence occurs through the interaction with a third BH [304].

Our work is an exploration of the effect of large eccentricities near merger, and it differs in several ways from the catalogue of eccentric, unequal-mass simulations presented in Ref. [305]. While their study considered a larger range of mass ratios (in our notation, $1/10 \leq q \leq 1$), they carried out fewer simulations for each value of q . The binaries in their simulations have initial eccentricities smaller than $e_0 = 0.18$ 15 cycles before merger, and since they start at larger orbital separations, their eccentricity will have further decreased by the time of merger. As we will see below, the larger initial eccentricities in our simulations allow us to highlight interesting periodicities in the emission of gravitational radiation and the behaviour of the recoil velocity.

The remainder of this chapter is organised as follows. In Sec. 7.2 we discuss our two numerical codes (LEAN and GRCHOMBO), the computational framework, and the catalogue of simulations we produced for this study. In Sec. 7.3 we present the main results of our simulations. In Sec. 7.4 we summarise these results and point out possible directions for future work. In Appendix 7.5 we detail our tests for numerical accuracy and verify that our two codes give comparable results. Finally, in Appendix 7.6 we discuss the tagging of cells for adaptive mesh refinement used in one of our numerical codes (GRCHOMBO). Throughout this work we use geometrical units ($G = c = 1$).

7.2 Computational Framework and Set of Simulations

7.2.1 Numerical Methods

The simulations reported in this work have been performed with the GRCHOMBO [142, 306] and LEAN [53] codes. We estimate the error budget of our simulations from both codes to be up to 3.5%. Details of our convergence analyses are provided in Appendix 7.5. Though different codes were used for each sequence of configurations, we undertook comparison tests in order to ensure consistent results, and these can also be found in Appendix 7.5.

GRChombo setup

GRCHOMBO [142] is a finite difference numerical relativity code which uses the method of lines with fourth-order Runge-Kutta time stepping. In contrast to previous studies with GRCHOMBO we have implemented sixth-order spatial stencils in order to improve phase accuracy [141]. The Einstein equations are solved by evolving the covariant and conformal Z4 (CCZ4) formulation [140] with the prescription described in Sec. F of [34], namely the replacement $\kappa_1 \rightarrow \kappa_1/\alpha$, in order to stably evolve BHs and maintain spatial covariance. After this replacement and in the notation of Ref. [140], we use the constraint damping parameters $\kappa_1 = 0.1$, $\kappa_2 = 0$ and $\kappa_3 = 1$ in all simulations. However, unlike Refs. [142, 140], we use the conformal factor defined by

$$\chi = \det(\gamma_{ij})^{-1/3}, \quad (7.2.1)$$

where γ_{ij} is the physical spatial metric. GRCHOMBO is built on the CHOMBO [307] library for solving partial differential equations with block-structured adaptive mesh refinement (AMR) which supports nontrivial mesh hierarchies using Berger-Rigoutsos grid generation [308]. The grid comprises a hierarchy of cell-centred Cartesian meshes consisting of $L + 1$ refinement levels labelled from $l = 0, \dots, L$, each with grid spacing $h_l = h_0/2^l$. Given the AMR, the grid configuration changes dynamically during the simulation. The regridding is controlled by the tagging of cells for refinement in the Berger-Rigoutsos algorithm [308], with cells being tagged if the tagging criterion C exceeds a specified threshold value t_R . Details of the tagging criterion used in this work are provided in Appendix 7.6. The Berger-Oliger scheme [308] is used for time stepping on the mesh hierarchy, and we take a Courant-Friedrichs-Lowy (CFL) factor of 1/4 in all simulations. Due to the inherent symmetry of the configurations considered, we employ bitant symmetry in order to reduce the computational expense.

Lean setup

The LEAN code [53] is based on the CACTUS computational toolkit [309] and uses the method of lines with fourth-order Runge-Kutta time stepping and sixth-order spatial stencils for improved phase accuracy [141]. The Einstein equations are implemented in the form of the Baumgarte-Shapiro-Shibata-Nakamura-Oohara-Kojima (BSSNOK) formulation [310, 49, 23] with the moving-puncture gauge [91, 92]. The CARPET driver [311] provides AMR using the technique of “moving boxes.” We use bitant symmetry to exploit the symmetry of the simulations and reduce computational expense. The computational domain comprises a hierarchy of $L + 1$ refinement levels labelled from $l = 0, \dots, l_F, \dots, L$, each with grid spacing $h_l = h_0/2^l$. Before applying the symmetry, for $l \leq l_F$ each level consists of a single fixed cubic grid of half-length¹ $R_l = R_0/2^l$, and for $l_F < l \leq L$, each level consists of two cubic components of half-length $R_l = 2^{L-l} R_L$ centred around each BH. We adopt this notation for consistency with that used to describe GRCHOMBO. This translates into the more conventional LEAN grid setup notation (cf. Ref. [53]) as

$$\left\{ (R_0, \dots, 2^{-l_F} R_0) \times (2^{L-l_F-1} R_L, \dots, R_L), h_L \right\}. \quad (7.2.2)$$

A CFL factor of 1/2 is used in all simulations, and apparent horizons are computed with AHFINDERDIRECT [312, 313].

¹In one departure from this rule, we enhance R_2 by a factor of 4/3 for the simulations of sequence 1q1:2 of Table 7.1.

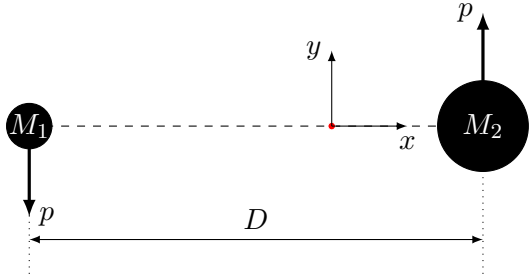


Figure 7.1: Schematic diagram of the initial BH binary setup for an arbitrary configuration in one of the sequences.

Initial Data

For both codes, we use puncture data [314] of Bowen-York [315] type provided by the spectral solver of Ref. [316] in the form of the CACTUS thorn TWO PUNCTURES for LEAN, and a standalone version integrated into GRCHOMBO. In the latter case, we take advantage of the improvements made in Ref. [317] to use spectral interpolation.

7.2.2 Black-Hole Binary Configurations

We follow the construction of sequences of BH binary configurations and the notation of Ref. [235]. In particular, we denote by M_1 and M_2 the initial BH masses. Without loss of generality, since we are only considering unequal masses ($M_1 \neq M_2$), we take $M_2 > M_1$ and denote their sum by $M = M_1 + M_2$. The reduced mass is $\mu = M_1 M_2 / M$ and to quantify the mass ratio, we use either

$$q = \frac{M_1}{M_2} \quad (7.2.3)$$

or the symmetric mass ratio $\eta = \mu/M$. Finally, the total Arnowitt-Deser-Misner (ADM) mass [134] is denoted by M_{ADM} .

In order to construct a sequence for a fixed mass ratio, we first determine an initial quasicircular configuration. We specify the initial coordinate separation D/M along the x axis, and the scale in the codes is fixed by choosing $M_1 = 0.5$. Next, Eq. (65) in Ref. [318] is used to calculate the initial tangential momentum of each BH, $\mathbf{p} = (0, \pm p, 0)$ (as shown in Fig. 7.1). We use a Newton-Raphson method to iteratively solve for the Bowen-York bare mass parameters that give the desired BH masses. The binding energy of this quasicircular configuration is then computed using

$$E_b = M_{\text{ADM}} - M. \quad (7.2.4)$$

The rest of the sequence with increasing orbital eccentricity is constructed by fixing the binding energy and gradually reducing the initial linear momentum parameter p . We decide to reduce the linear momentum rather than, for example, altering its direction, so that the x axis is fixed as the initial apoapsis for all configurations. For a given configuration with fixed p , we iteratively solve for the separation D and bare masses that give the required binding energy and BH masses. The choice to keep the binding energy constant as the momentum parameter (and thus the initial kinetic energy) is reduced means that the initial separation increases along the sequence. This ensures an inspiral phase of comparable duration as the eccentricity increases. The initial orbital angular momentum of the system is given by $L = Dp$ [319]. Even though D increases as p decreases, the initial angular momentum of the system monotonically decreases as p decreases for all but the least one or two eccentric configurations in a sequence.

We have parameterised the configurations within a sequence by their initial tangential momentum p , but we would like to measure the eccentricity of these configurations. Unfortunately, there is no gauge-invariant measure of eccentricity [320] that is valid for the entire inspiral and the ambiguity in any

Sequence	Code	q	E_b/M	r_{ex}/M	v_c (km/s)
sq2:3	GRCHOMBO	2/3	-0.0113386	88	102
sq1:2	LEAN	1/2	-0.0106964	80	149
1q1:2	LEAN	1/2	-0.0090858	80	150
sq1:3	GRCHOMBO	1/3	-0.0093684	65	178

Table 7.1: Sequences of binary BH configurations studied in this work with their mass ratio, binding energy E_b/M , and the GW extraction radius r_{ex} . For reference, we also list for each sequence the kick velocities v_c in the quasicircular limit. These values agree, within the numerical uncertainties, with the results of Ref. [268].

definition is particularly pronounced in the late stages of inspiral from which our simulations start. Following Ref. [235], we use the formalism in Ref. [321] to obtain a PN estimate for the eccentricity. Note that this formalism has three eccentricity parameters— e_t , e_r and e_ϕ —and employs two different types of coordinates: ADM-like and harmonic. The choice of which parameter and coordinate type to use is somewhat arbitrary. We mostly focus on the eccentricity parameter e_t in harmonic coordinates² as in Ref. [288]. This estimate should be taken with a pinch of salt due to the relatively small initial binary separations D in our simulations. Furthermore, e_t has an infinite gradient as a function of the initial orbital angular momentum in the quasicircular limit (see Fig. 1 in Ref. [235]), such that values of $e_t \lesssim 0.1$ are difficult to realise in practice, unless the BHs start from large initial distance. In the head-on limit e_t diverges, and a Keplerian/Newtonian interpretation ceases to be valid. Despite these shortcomings, this estimate provides us with a helpful approximation of the eccentricity and a criterion to quantify deviations away from quasicircularity.

The sequences considered in this work are given in Table 7.1. Note that there are two sequences corresponding to the mass ratio $q = 1/2$. The sequence 1q1:2 has a longer inspiral phase compared to the other sequences. For the nearly quasicircular configurations, the binary completes about six orbits before merger in the 1q1:2 sequence, and about three orbits in all other sequences. The longer sequence of simulations was conducted in order to identify any possible artefacts in the shorter sequences due to the exclusion of the earlier inspiral phase. In addition to the labelling of sequences in Table 7.1, we refer to individual simulations within a sequence by appending “-p” to the sequence label followed by a four digit integer which is given by $10^3 p/M$ truncated appropriately; for example, sq1:2-p0100 denotes the simulation in sequence sq1:2 with initial tangential momentum $p = 0.1 M$.

7.2.3 Diagnostics

For all simulations, we have extracted values of the Weyl scalar Ψ_4 on spheres of finite coordinate radius given in Table 7.1 for each sequence. We also computed the dominant terms in the multipolar decomposition,

$$\Psi_4(t, r, \theta, \phi) = \sum_{\ell=2}^{\infty} \sum_{m=-\ell}^{\ell} \psi_{\ell,m}(t, r) \left[{}_{-2}Y^{\ell,m}(\theta, \phi) \right], \quad (7.2.5)$$

where ${}_{-2}Y^{\ell,m}$ are the usual spin-weight -2 spherical harmonics.

Our main diagnostics are the energy, linear momentum and angular momentum radiated in GWs, which are computed directly from the extracted Ψ_4 values on the spheres using standard methods. For completeness, we reproduce the formulae here.

²The ADM-like estimate of Ref. [321] differs by only a few percent for $e_t \lesssim 0.8$, and would not significantly alter our results.

The radiated energy E^{rad} is given by [322, 323]

$$E^{\text{rad}}(t) = \lim_{r \rightarrow \infty} \frac{r^2}{16\pi} \int_{t_0}^t dt' \oint_{S_r^2} d\Omega \left| \int_{-\infty}^{t'} dt'' \Psi_4 \right|^2. \quad (7.2.6)$$

The radiated linear momentum \mathbf{P}^{rad} is given by

$$\mathbf{P}^{\text{rad}}(t) = \lim_{r \rightarrow \infty} \frac{r^2}{16\pi} \int_{t_0}^t dt' \oint_{S_r^2} d\Omega \hat{\mathbf{e}}_r \left| \int_{-\infty}^{t'} dt'' \Psi_4 \right|^2, \quad (7.2.7)$$

where $\hat{\mathbf{e}}_r$ is the flat-space unit radial vector

$$\hat{\mathbf{e}}_r = (\sin \theta \cos \phi, \sin \theta \sin \phi, \cos \theta). \quad (7.2.8)$$

Finally, the radiated angular momentum \mathbf{J}^{rad} is given by

$$\mathbf{J}^{\text{rad}}(t) = - \lim_{r \rightarrow \infty} \frac{r^2}{16\pi} \text{Re} \int_{t_0}^t dt' \left\{ \oint_{S_r^2} \left(\int_{-\infty}^{t'} dt'' \bar{\Psi}_4 \right) \times \hat{\mathbf{J}} \left(\int_{-\infty}^{t'} dt'' \int_{-\infty}^{t''} dt''' \Psi_4 \right) d\Omega \right\}, \quad (7.2.9)$$

where the angular momentum operator $\hat{\mathbf{J}}$ for spin weight $s = -2$ is given by

$$\hat{\mathbf{J}} = \left(\text{Re} \hat{\mathbf{J}}_+, \text{Im} \hat{\mathbf{J}}_+, \frac{\partial}{\partial \phi} \right), \quad (7.2.10)$$

and

$$\hat{\mathbf{J}}_+ = e^{i\phi} \left(i \frac{\partial}{\partial \theta} - \cot \theta \frac{\partial}{\partial \phi} + 2i \csc \theta \right). \quad (7.2.11)$$

Additionally, we compute the radiated linear momentum from the multipolar amplitudes $\psi_{\ell,m}$ in Eq. (7.2.5) using the formulae of Ref. [324]. From the symmetry of our configurations, the z component vanishes identically: $P_z^{\text{rad}} = 0$. For the components in the orbital plane, we write $P_+^{\text{rad}} = P_x^{\text{rad}} + i P_y^{\text{rad}}$. Then,

$$P_+^{\text{rad}}(t) = \sum_{\tilde{\ell}=2}^{\infty} \sum_{\tilde{m}=-\tilde{\ell}}^{\tilde{\ell}} P_+^{\tilde{\ell},\tilde{m}}, \quad (7.2.12)$$

where

$$P_+^{\tilde{\ell},\tilde{m}}(t) = \lim_{r \rightarrow \infty} \frac{r^2}{8\pi} \int_{t_0}^t dt' \left\{ \left(\int_{-\infty}^{t'} dt'' \psi_{\tilde{\ell},\tilde{m}} \right) \times \left(\int_{-\infty}^{t'} \left[a_{\tilde{\ell},\tilde{m}} \bar{\psi}_{\tilde{\ell},\tilde{m}+1} + b_{\tilde{\ell},-\tilde{m}} \bar{\psi}_{\tilde{\ell}-1,\tilde{m}+1} - b_{\tilde{\ell}+1,\tilde{m}+1} \bar{\psi}_{\tilde{\ell}+1,\tilde{m}+1} \right] dt'' \right) \right\}, \quad (7.2.13)$$

and the coefficients $a_{\ell,m}$ and $b_{\ell,m}$ are given by

$$a_{\ell,m} = \frac{\sqrt{(\ell-m)(\ell+m+1)}}{\ell(\ell+1)}, \quad (7.2.14)$$

$$b_{\ell,m} = \frac{1}{2\ell} \sqrt{\frac{(\ell-2)(\ell+2)(\ell+m)(\ell+m-1)}{(2\ell-1)(\ell+1)}}. \quad (7.2.15)$$

We will find it helpful to define the partial sums,

$$P_+^{\tilde{\ell}} = \sum_{\tilde{m}=-\tilde{\ell}}^{\tilde{\ell}} P_+^{\tilde{\ell},\tilde{m}}, \quad (7.2.16)$$

$$P_+^{<\tilde{\ell}} = \sum_{\ell'=2}^{\tilde{\ell}} P_+^{\ell'}. \quad (7.2.17)$$

In practice, we do not evaluate the limit in Eqs. (7.2.6), (7.2.7), (7.2.9) and (7.2.13), but rather just evaluate them at the finite extraction radius $r = r_{\text{ex}}$, as given in Table 7.1. A discussion of the error this introduces is given in the following section.

In order to exclude the spurious radiation³ inherent in Bowen-York initial data, we start the integration in Eqs. (7.2.6), (7.2.7), (7.2.9), and (7.2.13) at $t_0 = 50M + r_{\text{ex}}$. The recoil velocity is computed from the radiated momentum according to

$$\mathbf{v} = -\frac{\mathbf{P}^{\text{rad}}}{M_{\text{fin}}}, \quad (7.2.18)$$

where M_{fin} is the mass of the BH merger remnant. The quantity M_{fin} can be computed using energy balance:

$$M_{\text{fin}} = M_{\text{ADM}} - \tilde{E}^{\text{rad}}, \quad (7.2.19)$$

where \tilde{E}^{rad} denotes the radiated energy *including* the spurious radiation. We similarly compute the spin of the final BH χ_{fin} (which, by symmetry, must be in the z direction) using the radiated angular momentum:

$$\chi_{\text{fin}} = \frac{L - J_z^{\text{rad}}}{M_{\text{fin}}^2}, \quad (7.2.20)$$

where the initial angular momentum is $L = pD$. For LEAN simulations, we have compared M_{fin} and χ_{fin} with the corresponding values derived from the apparent horizon properties, and find agreement to within $\leq 0.1\%$.

7.3 Results

Using the framework summarised in the previous section, we have simulated four sequences of nonspinning BH binaries, characterised by their mass ratio (7.2.3) and binding energy (7.2.4). The parameters of these sequences are listed in Table 7.1. We have selected our mass ratios such that they cover the regime of maximum recoil, realised for $\eta = 0.195$ or $q = 1/2.77$ (cf. Fig. 7.3). Recall that sequences **sq2:3**, **sq1:2** and **sq1:3** complete about three orbits and sequence **1q1:2** completes about six orbits, respectively, in the quasicircular limit.

Our main results are displayed in Fig. 7.2, where we plot for all sequences the total recoil speed v_{tot} , various truncations of the multipolar contributions to the total recoil according to Eqs. (7.2.12)–(7.2.17), the total radiated GW energy E^{rad} and the dimensionless spin χ_{fin} of the BH resulting from the merger.

Let us first focus on the total recoil v_{tot} , displayed in each of the figure's top panels as the blue solid line. For each mass ratio, the global maximum of the kick velocity is realised for moderate eccentricities $e_t \approx 0.5$. We also illustrate this kick variation in Fig. 7.3, where the solid blue curve shows the quasicircular kick as a function of the symmetric mass ratio η according to Fit 3 in Table V of Ref. [325]. The velocity ranges obtained for our eccentric binaries are overlayed as the vertical bars for each of our sequences. The bar for each constant- η sequence is obtained by starting at the quasicircular limit on the right of each panel in Fig. 7.2 and identifying the minimum and maximum of $v(p)$, excluding the plunge regime to the left of the global maximum.

For our sequences **sq2:3**, **sq1:2** and **1q1:2**, the magnification of the kick through moderate values of the orbital eccentricity is similar to the enhancement by up to 25 % reported in Ref. [288] for the so-called superkick configurations [270, 271]. For **sq1:3** the effect is milder, with a $\sim 12\%$ amplification, but still well above the uncertainty estimates of our simulations. On the other hand, as evidenced by the oscillatory pattern of the function $v(p)$ in Fig. 7.2, appropriate nonzero values of the eccentricity can

³Bowen-York initial data for a black-hole binary is typically thought of as a combination of the “true” black-hole binary solution plus “something else”. While the initial data is constraint satisfying to numerical round off error, it doesn't exactly describe the physics we desire. This “something else” radiates away at early times and contributes to “junk radiation” - this radiation is unphysical and is omitted from our analysis as we are only interested in astrophysical phenomenology here.

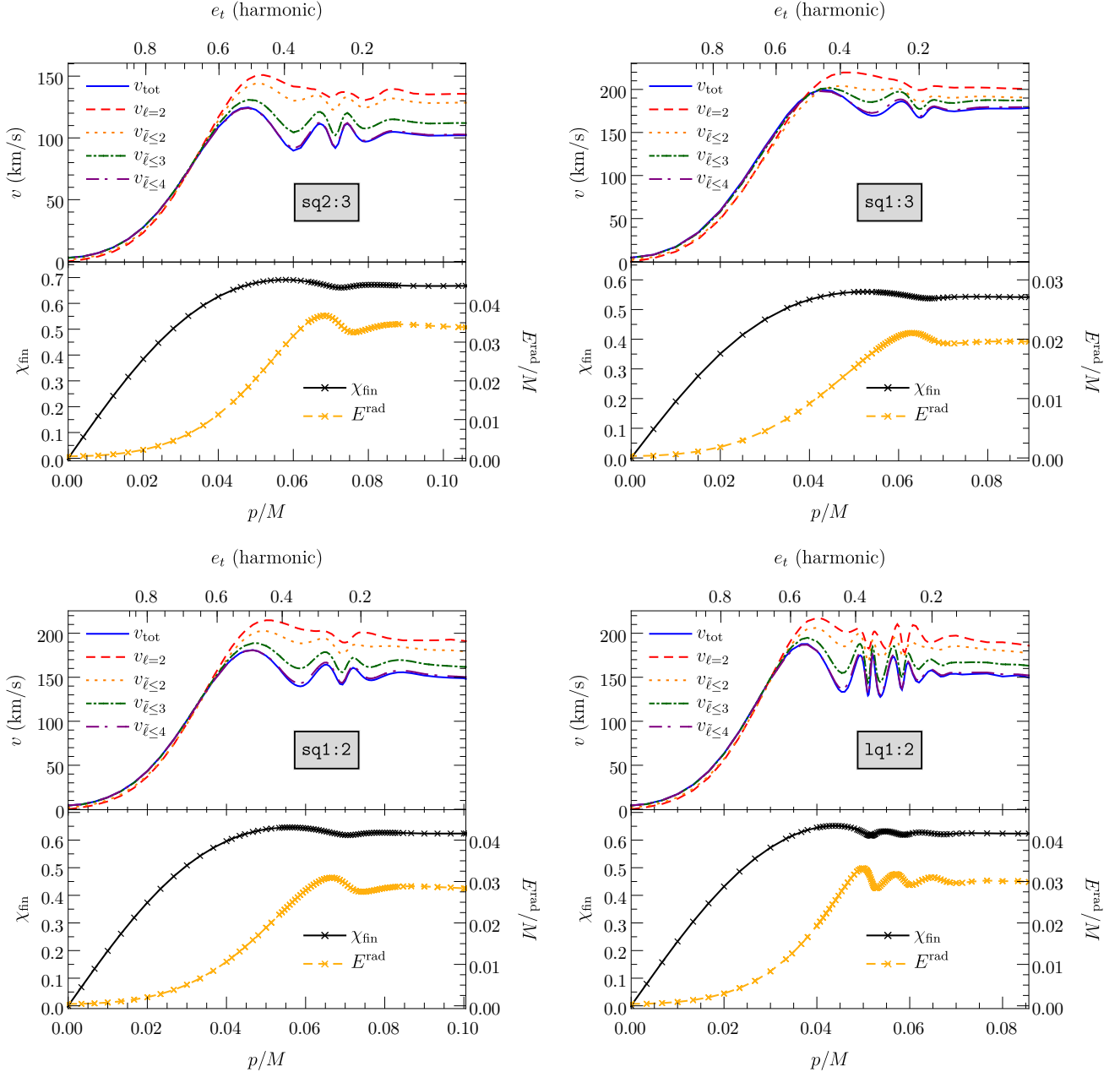


Figure 7.2: For each sequence of simulations in Table 7.1: Top panel: the recoil velocity v is plotted as a function of the initial tangential momentum p/M . The individual curves represent the total kick v_{tot} (blue, solid), the contribution to the kick from $\ell = 2$ modes of Ψ_4 , $\psi_{2,m}$, only in Eqs. (7.2.12)–(7.2.13) $v_{\ell=2}$ (red, dashed), and the contributions to the kick from $P_+^{\leq \tilde{\ell}'}$ defined in Eq. (7.2.17) $v_{\tilde{\ell}\leq \tilde{\ell}'}$ for $\tilde{\ell}' = 2$ (orange, dotted), $\tilde{\ell}' = 3$ (green, dot-dashed) and $\tilde{\ell}' = 4$ (purple, long dot-dashed). Our estimate of the eccentricity (see Sec. 7.2.2) is provided on the upper horizontal axis. Bottom panel: The final BH spin χ_{fin} (black, solid) and the energy radiated in GWs E^{rad} (gold, dashed) are also plotted as functions of p/M . For both curves, the individual simulations performed for this analysis are shown by \times symbols.

also lead to a *reduction* of the maximum kick at a given mass ratio by $\sim 10\%$. This overall modification of the gravitational recoil in the merger of eccentric, nonspinning BH binaries is the first main result of our study.

Besides the global maximum, we also note a number of local minima and maxima in the kick velocity

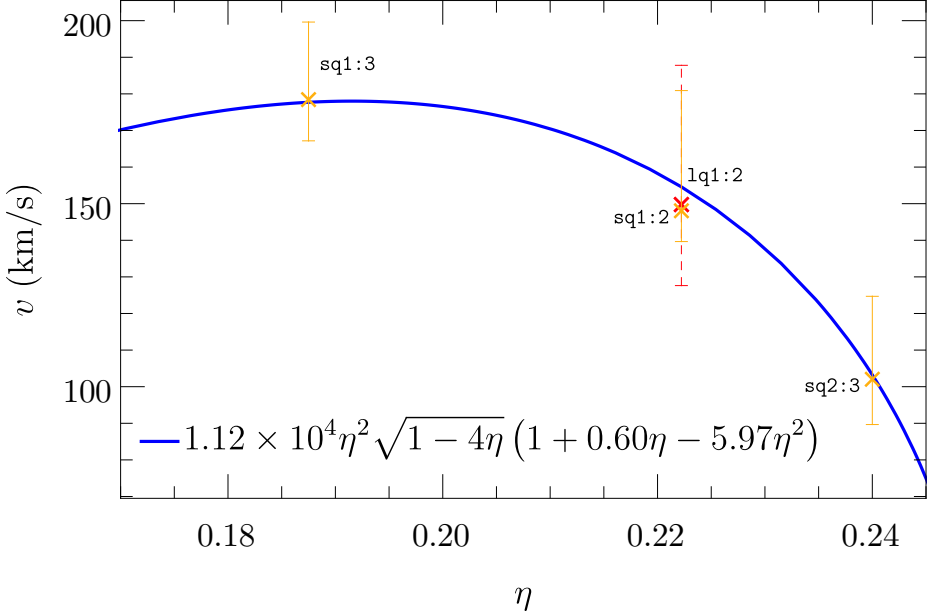


Figure 7.3: The range of recoil velocities obtained for each sequence is plotted against the symmetric mass ratio η . Note that for each sequence we exclude the configurations with $p < p_{\max}$ (i.e. the head-on limit), where $p = p_{\max}$ is the tangential momentum that maximises the kick. The three short sequences are marked in gold and the long sequence is marked in red (dashed). A fitted formula for the quasicircular kick as a function of η from Ref. [325] is also shown in blue for comparison.

as we vary the eccentricity in Fig. 7.2. For all mass ratios ($q = 2/3, 1/2, 1/3$) we see about five local extrema in $v(p)$ in our three short sequences, corresponding to the two upper panels and the bottom-left panel. We notice a similar, albeit less pronounced, oscillatory pattern in the functions $E_{\text{rad}}(p)$ and $\chi_{\text{fin}}(p)$ for the radiated energy and final spin in the lower subpanels in Fig. 7.2. Our results display no systematic correlation, however, between the extrema of the respective quantities; neither global nor local extrema in v , E_{rad} or χ_{fin} coincide in magnitude or their eccentricity values. We believe this diversity is due to the qualitatively different dependence of the radiated quantities on the GW multipoles: overlaps of *different* multipoles for the kick, a sum of terms $\propto \psi_{lm}^2$ for the energy, and the interaction of first and second time integrals for the angular momentum in Eq. (7.2.9).

We added to our study the $q = 1/2$ sequence of longer BH binary inspirals to investigate whether these anomalies in $v = v(p)$ might merely result from ignoring in our simulations the earlier inspiral phase. The remarkable outcome of this test, however, is that the oscillatory behaviour in the kick as a function of eccentricity is *more* pronounced in the long sequence. The solid blue curve in the bottom-right panel of Fig. 7.2 displays significantly more rapid oscillations in the eccentricity regime $0.2 \lesssim e_t \lesssim 0.4$ as compared to the shorter inspiral sequences. This oscillatory behaviour, and the apparent increase in the number of oscillations as we increase the initial separation of the BHs, is the second of our results.

We next attempt to gain insight into the origin of this behaviour. For this purpose, we have computed the multipolar contributions to the total kick according to Eqs. (7.2.13)–(7.2.17). The resulting velocities are displayed in Fig. 7.2 by the additional dashed, dotted and dash-dotted curves. Here, the curves labelled $v_{\ell=2}$ have been computed from the $\ell = 2$ modes of Ψ_4 ($\psi_{2,m}$ only) in Eqs. (7.2.12)–(7.2.13). We computed this additional contribution (red dashed curves in the figure) to determine whether the oscillatory behaviour is also present in the pure quadrupole signal. The answer is yes: the oscillations are clearly perceptible in $v_{\ell=2}$, even though they are a bit milder than in the total kick v_{tot} . Considering all (cumulative) multipolar contributions shown in Fig. 7.2, we notice the following behaviour:

1. The oscillatory dependence of the kick on eccentricity is present at any level of truncating the multipolar contributions in the cumulative sum (7.2.17).

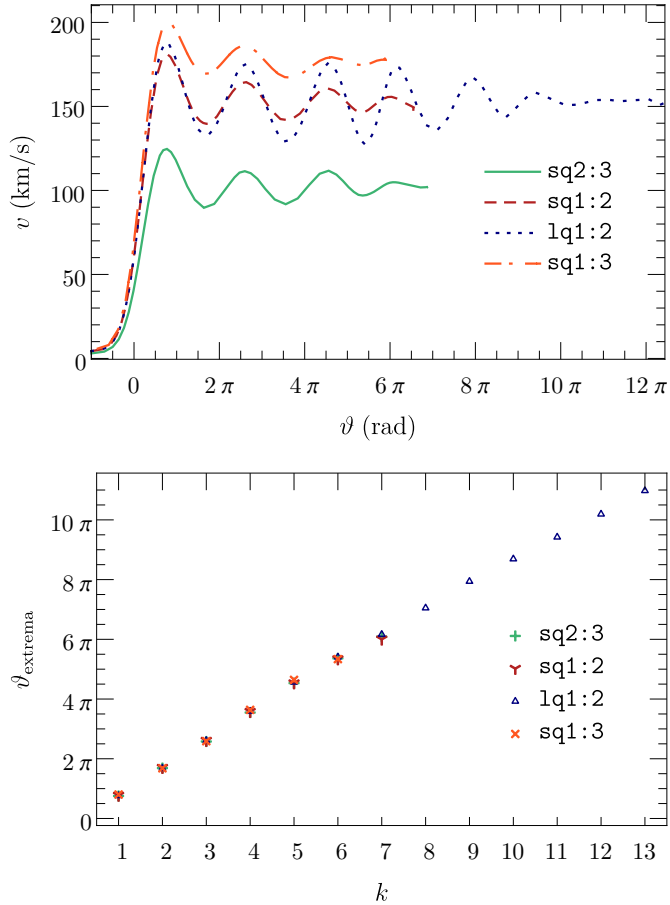


Figure 7.4: Plots involving the angle of the kick ϑ for all sequences. In the left panel we plot the BH recoil velocity v against ϑ . In the right panel we plot the location of the local extrema $\vartheta_{\text{extrema}}$ of the left panel against the index of the extrema k counting rightwards from the global maximum on the left.

2. The partial sum of the kick up to $\tilde{\ell} = 4$ barely differs from the total kick, indicating that higher-order overlap terms do not significantly contribute to the kick.
3. The higher-order contributions $\tilde{\ell} > 2$ to the cumulative kick (7.2.17) systematically decrease the kick, counteracting the pure quadrupole contribution $v_{\ell=2}$.

In short, we have not identified any specific multipoles dominating the variation in the kick function $v = v_{\text{tot}}(p)$.

In our search for an explanation, we turn next to the infall direction of the BH binary just before merger. A well-known feature of the superkicks generated in the inspiral of BHs with opposite spins $\mathbf{S}_1 = -\mathbf{S}_2$ pointing in the orbital plane is the sinusoidal variation with the initial azimuthal angle of the spin vectors; cf. Fig. 4 in Ref. [326]. The initial orientation of the spins can, alternatively, be interpreted as a measure for the angle between the in-plane spin components and the BH binary's infall direction at merger [327]. The superkick is therefore commonly determined by simulating otherwise identical BH binary configurations for different values of this angle and fitting the resulting data with a cosine function; see, e.g., Sec. III A in Ref. [288]. For the eccentric, nonspinning BH binaries considered in this work, it is the initial apsis (either a periapsis or an apoapsis) that defines a reference direction. Unfortunately, neither the apsis nor a “binary infall direction” are rigorously defined quantities in the strong-field regime of general relativity, and we consider instead the orientation of the final kick relative to the x axis, defined by

$$\tilde{\vartheta} = \arg(v_x + iv_y). \quad (7.3.1)$$

For convenience, we define

$$\vartheta = \tilde{\vartheta} + 2n\pi, \quad (7.3.2)$$

where $n \geq 0$ is chosen minimally for each configuration in order to obtain ϑ as a monotonic function of the initial tangential momentum p for each sequence. We will interchangeably refer to ϑ and $\tilde{\vartheta}$ as the angle of the kick. Since all of our simulations start with the BHs located on the x axis with purely tangential initial momentum $\mathbf{p} = (0, \pm p, 0)$ (Fig. 7.1), the x direction can be regarded as the initial direction of the apoapsis. If we furthermore interpret the gravitational recoil to be predominantly generated by the excess beaming of the GWs in the direction of the smaller and faster BH (see Fig. 3 in Ref. [328]) during the short merger phase, the kick direction can serve as an approximate measure for the infall direction of the binary.

We can test this prediction by computing the kick magnitude as a function of the angle ϑ ; if correct, we would expect a periodic variation with a period close to 2π . We do not expect an exact 2π periodicity because the relevant periapsis (or apoapsis) direction should be the last one before merger, and will shift away from the x axis during the inspiral due to apsidal precession—the BH analogue of Mercury’s perihelion precession around the Sun. More specifically, we would expect deviations from a 2π periodicity to be more pronounced for longer inspirals, i.e., lower eccentricity and/or larger initial separations, but only mildly dependent on the mass ratio q . Quite remarkably, all of these features are borne out by the functions $v = v(\vartheta)$ displayed for our four sequences in the left panel of Fig. 7.4 and the location of the extrema in this plot shown in the right panel of Fig. 7.4. For all sequences we observe the same approximate 2π periodicity, with deviations from this value increasing at larger ϑ , i.e. for longer inspirals. Note also that $\vartheta = -\pi$ in the head-on limit, as expected for our initial configurations, that start with the heavier BH located on the positive x axis.

While short of a rigorous proof, this result provides considerable evidence in favour of interpreting the oscillatory dependence of the kick on the eccentricity as a consequence of the corresponding variation in the infall direction as measured relative to the last apoapsis (or periapsis) of the eccentric binary. This interpretation also explains why the longer sequence **1q1:2** exhibits more oscillations than the shorter sequences **sq1:3**, **sq1:2** and **sq2:3**. Let us consider for this purpose two binary configurations that only differ by a tiny amount of eccentricity δe . The longer the inspiral phase, the more time these two binaries have to build up a considerable phase difference and, hence, a different kick and merger GW signal. Note the potentially dramatic consequences of this behaviour for the GW emission from eccentric binaries over astrophysical time scales. For long astrophysical inspirals retaining some eccentricity near merger, the kick and GW merger signal should exhibit critical dependence on the eccentricity. In terms of our Fig. 7.2, the function $v = v(e_t)$ would display a huge number of oscillations rather than the handful observed in our case, and the resulting curve would look like a “band” rather than a single line. Within the band, a very small change δe_t in eccentricity can produce a finite change in the kick and merger waveform.

As indicated by our analysis of the multipolar contributions to the total recoil, the variations in the GW signal are of a complex nature. We defer a more comprehensive analysis of the GW pattern to future work, but merely illustrate with an example the type of variations that are encountered. For this purpose, we show in Fig. 7.5 the $(\ell, m) = (2, 2)$ and $(3, 3)$ multipoles of the GW signal around merger for the configurations **1q1:2-p0537** and **1q1:2-p0567**, corresponding to a local minimum and maximum in the kick, respectively; cf. the bottom-right panel of Fig. 7.2. In Fig. 7.5, the time has been shifted such that $\Delta t = 0$ corresponds to the first occurrence of a common apparent horizon. The main difference perceptible in the figure is the relative phase shift of the $(3, 3)$ mode relative to the dominant quadrupole $(2, 2)$. For the case $p = 0.567M$ with maximal kick, the global peaks of both multipoles are aligned, whereas for $p = 0.537M$ with minimal kick, the global peak of the $(2, 2)$ mode coincides with a minimum in $(\ell, m) = (3, 3)$. We have made similar observations for other pairs of modes such as $(2, 2)$ and $(2, 1)$, and find these pairs to dominate the oscillatory variation in the multipolar series expansion (7.2.17).

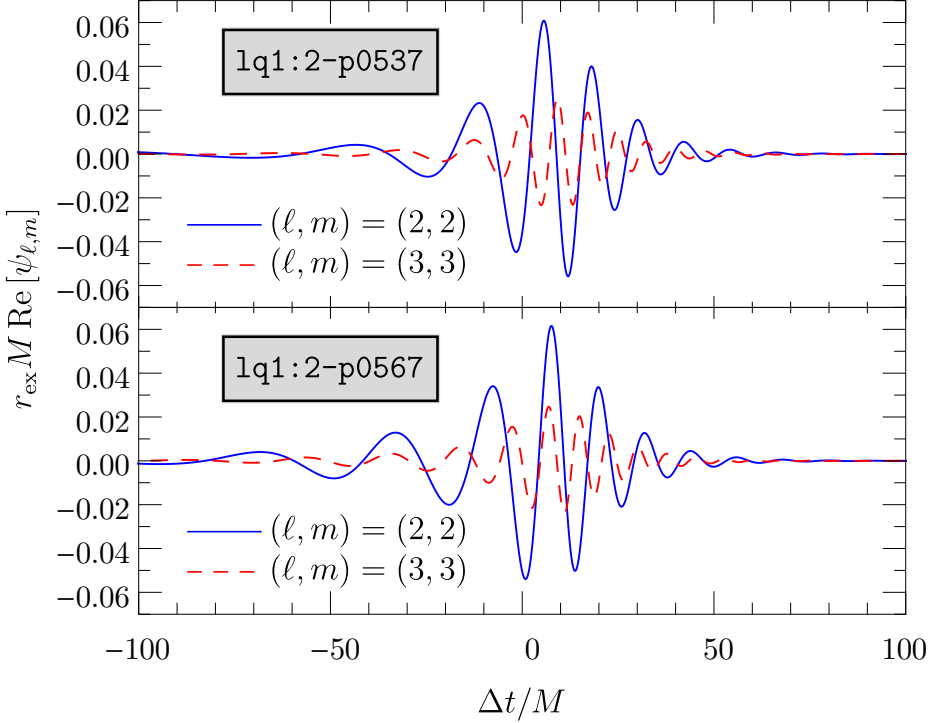


Figure 7.5: The real parts of the $(\ell, m) = (2, 2)$ and $(3, 3)$ modes of Ψ_4 are shown as functions of time for the two binaries of sequence 1q1:2 with $p/M = 0.537$ and $p/M = 0.567$, resulting in kick velocities of $v = 128$ and 173 km/s, respectively.

7.4 Conclusions

In this chapter we have studied the gravitational recoil and GW emission of sequences of nonspinning BH binaries with mass ratios $q = 2/3, 1/2$ and $1/3$, and eccentricity varying from the quasicircular to the head-on limit. For this purpose we have evolved 274 configurations with the GRChombo and LEAN codes. Both codes yield convergent results for the recoil with a total error budget of 3-4 % and exhibit excellent agreement, well within this uncertainty estimate, for a verification configuration simulated with both codes. In order to estimate the impact of variations in the overall length of the inspirals, we have evolved two sequences for the case $q = 1/2$ which complete about three and six orbits, respectively, in the quasicircular limit.

The findings of our study are summarised as follows.

1. For all sequences, the total recoil reaches a global maximum for moderate eccentricities $e \sim 0.5$. As in the case of the enhancement of superkicks studied in Ref. [288], the maximum kick is enhanced by up to about 25 % relative to the value obtained for quasicircular configurations.
2. Besides this global maximum, we observe an oscillatory dependence of the kick v as a function of eccentricity, with several local minima and maxima in the function $v = v(e)$. Appropriate nonzero values of the eccentricity can lead to a *reduction* of the kick by ~ 10 % relative to the quasicircular value instead of an increase. By splitting the kick into separate multipolar contributions, we notice that this oscillatory dependence is already present, albeit in a slightly weaker form, when we consider only quadrupole terms in the series expansion (7.2.12). Further contributions involving $\ell \geq 2$ multipoles tend to decrease the overall kick and mildly enhance the oscillatory variation; see Fig. 7.2.
3. We interpret this oscillatory variation in the kick as a consequence of changes in the angle between the infall direction at merger and the apoapsis (or periapsis) direction. In the absence of rigorous

definitions for either of these directions, we approximate this angular variation by considering the direction of the final kick and the x axis, assuming that the former is related via relativistic GW beaming to the infall direction and by taking into account that our BHs start on the x axis with zero radial momentum. Displayed as a function of this angle, the kick displays the expected periodic behaviour with a period close to but mildly deviating from 2π , presumably due to periapsis precession.

4. We have explored the dependence of this oscillatory behaviour of the recoil by simulating an additional sequence of eccentric binaries with mass ratio $q = 1/2$, but less negative binding energy, corresponding to about six orbits in the quasicircular limit. We find the oscillations in $v = v(e)$ to be more pronounced and numerous than in the shorter sequence. We attribute this feature to the longer available time window during which otherwise identical binaries with tiny differences in the initial eccentricity build up a phase difference prior to merger. This observation raises the intriguing possibility that the total recoil depends highly sensitively on the initial eccentricity.
5. The variations in the kick velocity are accompanied by relative time shifts in the peak amplitudes of subdominant multipoles relative to the peaks of the (2,2) mode; cf. Fig. 7.5. For configurations with a large (small) kick, the peak amplitude of subdominant multipoles tends to be aligned (misaligned) with the quadrupole peak.

Our findings point to a variety of future investigations. While our simulations indicate an increased sensitivity of the GW merger signal to the initial eccentricity for larger initial separations (i.e. longer inspirals), it is not clear how this will be affected by the circularising nature of GW emission. In this context, it will also be important to analyse in more quantitative terms the differences in the GW signals and possible implications for parameter inference in GW observations. A thorough investigation of long eccentric inspirals on astrophysical time scales will likely require PN methods and may benefit greatly from a multi-time-scale analysis in phase space, as applied to spin-precessing BH binaries in Refs. [329, 330] or to the dynamics of binary systems in external gravitational background potentials in Refs. [331, 332]. If there is a single conclusion to draw from the results of this work, it is the surprisingly rich phenomenology of the GW signals of eccentric compact binaries - even in the absence of spins - which merits further investigation.

7.5 Numerical Accuracy

As in Ref. [288], the uncertainty in our numerical results for the recoil velocities has two predominant contributions: the discretisation error and the finite extraction radii for the Weyl scalar Ψ_4 .

To estimate the uncertainty arising from the latter, we have selected a representative sample of the simulations from each sequence and extrapolated the cumulative radiated momentum to infinity from about six extraction radii in the range $r_{\text{ex}}/2 \leq r_{\text{ex}}$ using a Taylor series in $1/r$ as in Ref. [333]. We report the results from the finite extraction radii given in Table 7.1 and estimate the error by comparing with the linear-order extrapolation. For both codes, we estimate that the contribution from this error is about 2% for all sequences.

In order to estimate the error contribution from finite differencing and verify that our codes give consistent results, we have performed simulations of `sq1:2-p0100` (the binary in sequence `sq1:2` with $p/M = 0.1$) with both codes. We discuss the analyses of the convergence of each code separately before comparing.

7.5.1 GRChombo Convergence

For GRCHOMBO, we have performed the simulations of `sq1:2-p0100` with resolutions $h_L = 3M_1/80$, $3M_1/92$ and $3M_1/104$, and we refer to the configurations corresponding to these resolutions as R1, R2 and R3, respectively. The full grid configurations are given in Table 7.2 and the results of this analysis

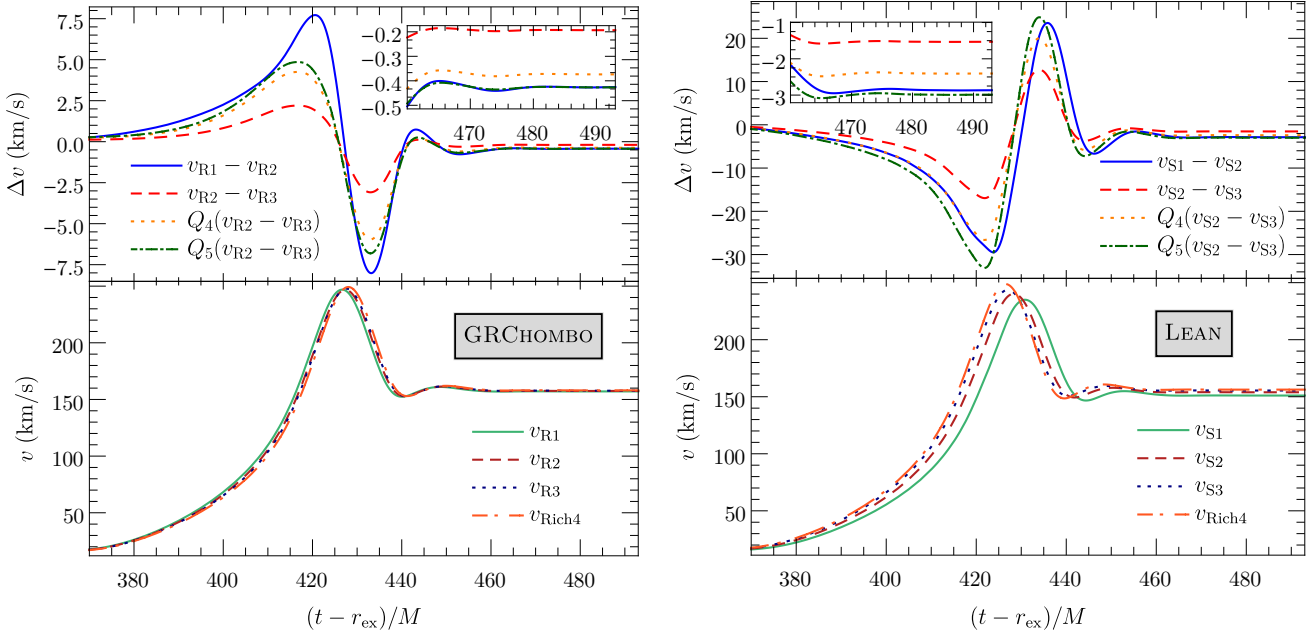


Figure 7.6: For each code, we show convergence plots for the accumulated linear momentum radiated from `sq1:2-p0100` by plotting the BH recoil velocity in the bottom panels. The Richardson extrapolated curve, v_{Rich4} , assuming fourth-order convergence, is also shown in the bottom panel. The grid configurations are given in Table 7.2 for GRChombo and in Table 7.3 for LEAN. The top panel shows the difference between the configurations along with rescalings corresponding to fourth- and fifth-order convergence. The inset shows a magnification of the right side of the plot: the final value of the recoil velocity is what we show in Fig. 7.2.

are shown in the left panel of Fig. 7.6. Around merger, at $(t - r_{\text{ex}})/M \sim 420$, our results exhibit mild overconvergence in the top-left panel of Fig. 7.6. The important results for our analysis in Fig. 7.2, however, are the final kick values after the merged BH has settled down. As can be seen from the inset, the convergence here is close to fifth order. From our convergence analysis, the difference between the result obtained from the R1 simulation and the more conservative fourth-order Richardson-extrapolated result leads to an estimate of the discretisation error of about 1%. A similar error estimate is also obtained for the radiated energy, E^{rad} . From experience, we have found smaller values for the mass ratio $q < 1$ more challenging to accurately simulate than larger values, and we therefore feel justified in using this error estimate (for a $q = 1/2$ configuration) as a conservative estimate for the error in the `sq2:3` sequence simulations ($q = 2/3$). We therefore used the R1 grid configuration for this sequence with $l_1^{\max} = l_2^{\max} = L = 7$ (both BHs are covered by the finest level; see Appendix 7.6 for details).

Label	L	N	t_R	b	h_L/M_i	tagging
R1	7	320	0.012	$0.5M_i$	3/80	Spherical
R2	7	368	0.01043	$0.5M_i$	3/92	Spherical
R3	7	416	0.00923	$0.5M_i$	3/104	Spherical
R4	7	352	0.01091	0.7	3/88	Box

Table 7.2: Grid configurations used for GRChombo simulations. As explained in Sec. 7.2.1 and Appendix 7.6, the total number of refinement levels is $L + 1$, the number of cells along each dimension on the coarsest level is N , t_R is the regridding threshold value, b is the BH tagging buffer parameter that we set proportional to the mass M_i ($i = 1, 2$) of the nearest BH for all configurations except R4, and h_L denotes the grid spacing.

For the `sq1:3` simulations, we used the R4 grid configuration (see Table 7.2) with $l_1^{\max} = L = 7$ and $l_2^{\max} = L - 1 = 6$ (the larger BH is not covered by the finest level: see Appendix 7.6 for details). This corresponds to a resolution of $h_L = 3M_1/88$. We performed a separate convergence analysis of `sq1:3-p0089`, which led to an estimated 1% discretisation error.

Combining both the finite extraction radius and discretisation errors, our estimate for the total error budget of the GRChombo simulations is about 3%.

7.5.2 Lean Convergence

With LEAN, we have simulated `sq1:2-p0100` with resolutions $h_L = M_1/20$, $M_1/24$ and $M_1/32$. We refer to these grid configurations as S1, S2 and S3, respectively (cf. Table 7.3). The right panel of Fig. 7.6 shows convergence between fourth and fifth order. For simulations in `sq1:2`, we used the S2 grid configuration. From the convergence analysis, the difference between the result obtained from the S2 simulation and the fourth-order Richardson extrapolation leads to an estimate of the discretisation error of about 1.5%.

For the `1q1:2` simulations, we have undertaken a separate convergence analysis of `1q1:2-p0086` using the same grid setup as in Table 7.3, but using higher resolutions $h_L/M_1 = 1/24$, $1/28$ and $1/32$. We observe convergence close to fourth order and obtain an error estimate of 1% from the Richardson-extrapolated kick for the medium resolution $h_L/M_1 = 1/28$.

In summary, the LEAN simulations of sequence `sq1:2` are performed with resolution grid S2 of Table 7.3 and an error budget of 3.5%, and those of sequence `1q1:2` with grid S4 of Table 7.3 and an error budget of 3%.

7.5.3 Comparison between GRChombo and Lean

A comparison of the recoil velocity computed from GRChombo and LEAN simulations of `sq1:2-p0100` with the grid configurations R1 and S2 (used for the `sq2:3` and `sq1:2` runs) respectively, is shown in the top panel of Fig. 7.7. The eccentricity estimate for this system is $e_t = 0.10$. We have chosen this configuration for two reasons. First, to determine appropriate resolutions, we had to calibrate our codes' accuracy at the start of our exploration, which we began in the regime of mild eccentricities to acquire an intuitive understanding of their behaviour. Second, configurations with mild eccentricity have a longer inspiral phase than highly eccentric ones, and therefore impose a stronger requirement on phase accuracy. A mildly eccentric binary is therefore ideally suited to obtain a conservative estimate of the numerical accuracy, which is representative across the targeted parameter space.

The final recoil velocities obtained for this configuration with our two codes differ by about 2%, which is well within the error budget of each code. We also show the quadrupole contribution $h_{2,2}^+$ to the ‘+’

Label	L	l_F	R_0	R_L	h_L/M_1
S1	7	4	384	1	1/20
S2	7	4	384	1	1/24
S3	7	4	384	1	1/32
S4	7	4	384	1	1/28

Table 7.3: Grid configurations used for LEAN simulations. As explained in Sec. 7.2.1, the total number of refinement levels is $L + 1$, the number of fixed refinement levels is $l_F + 1$, R_0 is the half-length of the outer grid, R_L is the half-length of one cubic component of the innermost grid, and h_L is the grid spacing on the finest level.

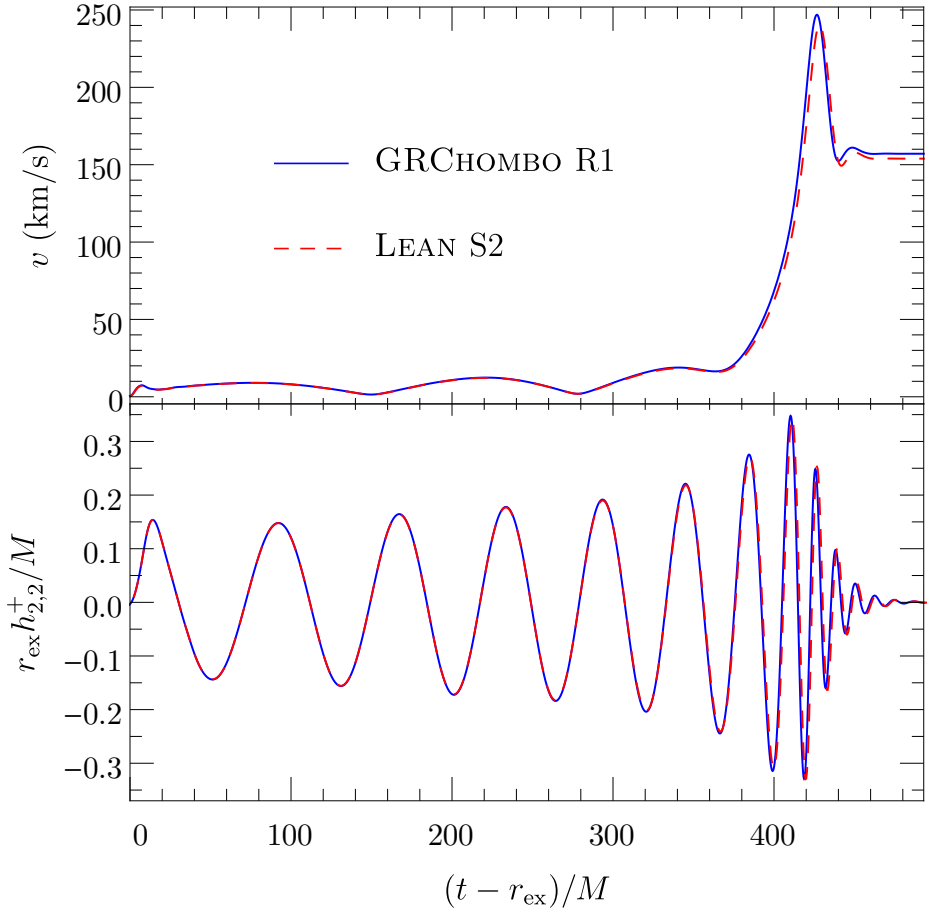


Figure 7.7: Comparison between GRChombo and LEAN for the accumulated linear momentum radiated in GWs in simulations of `sq1:2-p0100` with $e_t = 0.10$. We compare the BH recoil velocity (top panel) and the corresponding plus-polarised $\ell = m = 2$ strain amplitude (bottom panel).

polarisation strain defined by [334]

$$h_{\ell,m}^+(t, r) - i h_{\ell,m}^\times(t, r) = a_{\ell,m} + b_{\ell,m} t + \int_0^t dt' \int_0^{t'} dt'' \psi_{\ell,m}(t'', r), \quad (7.5.1)$$

where the constants $a_{\ell,m}$ and $b_{\ell,m}$ are chosen to minimise linear drift, in the bottom panel of the figure, to better illustrate the agreement between the codes for these grid configurations.

In Fig. 7.6 the differences between the results of different resolutions with LEAN are greater than that of GRChombo. However, we found that LEAN entered the convergent regime at lower resolutions than GRChombo. This is compatible with the observations of Ref. [140] that higher resolutions were required for convergence with CCZ4 compared to BSSNOK.

7.6 GRChombo Tagging Criterion

As explained in Sec. 7.2.1, the regridding is controlled by the tagging of cells for refinement in the Berger-Rigoutsos algorithm [308], with cells being tagged if the tagging criterion C exceeds the specified threshold value t_R as given in Table 7.2. For this work, we use the tagging criterion

$$C = \begin{cases} 0, & \text{if } l \geq l_{\text{BH}}^{\max} \text{ and } r_{\text{BH}} < (M_{\text{BH}} + b), \\ \max(C_\chi, C_{\text{punc}}, C_{\text{ex}}), & \text{otherwise,} \end{cases} \quad (7.6.1)$$

where l_{BH}^{\max} is a specifiable maximum level parameter for each BH (so that it is not unnecessarily over resolved), r_{BH} is the coordinate distance to the puncture, M_{BH} is the mass of the corresponding BH, b is a buffer parameter, and C_χ , C_{punc} , and C_{ex} are given as follows:

1. C_χ tags regions in which the gradients of the conformal factor χ become steep. It is given by

$$C_\chi = h_l \sqrt{\sum_{i,j} (\partial_i \partial_j \chi)^2}, \quad (7.6.2)$$

where h_l is the grid spacing on refinement level l .

2. C_{punc} tags within spheres around each puncture in order to ensure the horizon is suitably well resolved. It is given by

$$C_{\text{punc}} = \begin{cases} 100, & \text{if } r_{\text{BH}} < (M_{\text{BH}} + b)2^{\max(l_{\text{BH}}^{\max}-l-1,2)}, \\ 0, & \text{otherwise.} \end{cases} \quad (7.6.3)$$

3. C_{ex} ensures each sphere on which we extract the Weyl scalar Ψ_4 is suitably well resolved. It is given by

$$C_{\text{ex}} = \begin{cases} 100, & \text{if } r < 1.2r_{\text{ex}} \text{ and } l < l_{\text{ex}}, \\ 0, & \text{otherwise,} \end{cases} \quad (7.6.4)$$

where r is the coordinate distance to the centre of mass, $r = r_{\text{ex}}$ gives the location of the extraction sphere, and l_{ex} is a specifiable extraction level parameter for each sphere.

We also used this tagging criterion with the replacement $r_{\text{BH}} \rightarrow \max(x_{\text{BH}}, y_{\text{BH}}, z_{\text{BH}})$, where, e.g. x_{BH} is the distance to the puncture in the x direction. We refer to this as “box” tagging and the original as “spherical” tagging. Naively, one might hope that C_χ is sufficient to ensure suitable refinement around the BHs, since the gradients of χ become increasingly steep close to the punctures. However we found empirically that, without C_{punc} , the horizons are perturbed significantly by the refinement boundaries, leading to lower accuracy.

Chapter 8

Conclusions and Bibliography

8.1 Concluding Remarks

This thesis starts with a general introduction to differential geometry, tensor calculus and general relativity. Next, a more specialised introduction to the 3+1 spacetime decomposition, numerical relativity and compact objects, with focus on boson stars, was given. After this the details of numerical methods for PDEs and GRCHOMBO, the main numerical code used throughout the thesis, were covered. Along with this, the creation of boson star initial data, including boosts and the naive superposition of solutions, is given in detail along with simple examples of their collisions in three spatial dimensions. The head-on collision result in the prompt collapse to a black hole and the grazing collision (a collision with small impact parameter) results in the formation of a black hole with a quasi-long lived scalar field “wig”. This dynamical formation of a hairy black hole from physical collision initial data certainly warrants further study.

Super-imposing solutions in general relativity generally does not constitute a new solution of Einstein’s equation; the superposed solution will violate the Hamiltonian and momentum constraints in Eqs(2.1.50) and (2.1.52). While constraint satisfying initial data for black-hole binaries is well known at this point, the same cannot be said about boson star binaries. When super-imposing compact objects in general relativity the overall constraint violation reduces with increasing separation and so it is common in the literature to produce boson star binary initial data with plain superposition making the object separation large where possible. The caveat of this approach is that the superposition error decays quite slowly with increasing the separation and a boson-star binary that has an acceptable level of constraint violation would typically require a separation that is too large to be simulated with numerical relativity.

In chapter 4 we have conducted symmetric headon boson star collisions and compare two superposition schemes. The two superposition schemes are the regular naive superposition of section 3.2.5 and the modified superposition scheme of section 4.2.2. Our results showed that the modified superposition scheme is a major improvement over the naive superposition method when measuring the constraint equations. Additionally, naive superposition was observed to induce spurious unphysical behaviour such as excited stars and gravitational collapse. However, the modified superposition scheme is not perfect, there is still some residual constraint violation; on the other hand this scheme could be a useful first guess in a true constraint solver when one becomes available. Given the simplicity of implementation and effectiveness of the modified superposition scheme we recommend its use to the general numerical relativity community. A future study to considering non-symmetric binaries is certainly warranted.

Next the QFS system for a generic continuity equation in curved space is derived in section (5.1.15) and is explicitly given for spherical coordinate surfaces. The QFS system is first used to derive expressions for the Noether charge flux density \mathcal{F} of a complex scalar field and a complex Proca field; both fields have a global $U(1)$ symmetry which gives rise to the conserved Noether charge. Additionally, the QFS system is used to re-derive the well known Noether charge density \mathcal{Q} . Next, expressions for \mathcal{Q} , \mathcal{F} and \mathcal{S} are derived for energy momentum-currents (of matter) where \mathcal{S} represents the creation/destruction of charge; \mathcal{S} is called the source term. These expressions are then given for use with angular momentum explicitly; expressions for the energy density are also given in agreement with the literature [151]. The three variables give an intuitive understanding of the behaviour of angular momentum (or any charge) where \mathcal{Q} is the amount of angular momentum in the matter field, \mathcal{F} is the flux leaving an arbitrary surface and \mathcal{S} is the destruction or creation of angular momentum; the destruction/creation of angular momentum of the matter field can be understood as the transfer of angular momentum between matter and curvature.

In addition to the intuitive understanding of local angular momentum (and charges with continuity equations in general) bought by the QFS system it also has numerical uses. One use is that combining the the \mathcal{Q} and \mathcal{S} variables (as outlined in section 5.1.6) is less prone to oscillations caused by the transfer of energy-momentum between curvature and matter fields. The reduction of oscillation in these variables can assist in obtaining a clean convergence test. Additionally, the QFS equation can be used as an

extra check on the resolution of a numerical relativity evolution. In the continuum limit, the QFS equation 5.1.15 should be obeyed exactly and the error measures defined in section 5.1.6 should vanish. In the case that Einstein’s equation is not assumed to hold in the underlying continuity equation of the QFS system, this error measure will not depend on constraint violation; for example the continuity of energy-momentum currents only assumes that $\nabla_\mu T^{\mu\nu} = 0$.

After the derivation and technical background of the QFS system had been derived, it was applied to an example spacetime. This example consists of the numerical simulation of a boson star collision using the GRCHOMBO code, described in section 3.2.1, ending in the formation of a quasi-stable object. Before the collision of the stars, the angular momentum measure agrees well with the Newtonian limit which is a good check on the normalisation of the QFS system’s angular momentum variable. The relative error (defined in section 5.1.6) of the QFS system is then subjected to a numerical convergence test which shows approximate third order convergence. After 8000 time units the highest resolution simulation shows an approximate error measure of 3%.

Given the ability to measure the flux through an arbitrary surface, the QFS system is well suited to cutting out unwanted volumes or including only desired ones. Including only a given volume is useful if we want to check the resolution (or make more accurate measures) over a finite region of spacetime. An example where we might want a moving volume is to track the flux of a quantity falling into a moving black hole. Cutting out pre-specified volumes could be useful in black-hole spacetimes where we don’t want to perform a measure within a certain radius of the singularity. One caveat of this approach is that the effect of a moving volume (with respect to the coordinates) has not been computed here and would need to be taken into account if it is to be used.

The QFS system is easily included into a numerical code and will hopefully prove useful to the Numerical Relativity community for the better measurement of local energy-momentum of matter and Noether charge aswell as provide a powerful check on simulation resolution.

Combining the aforementioned superposition improvement scheme with the diagnostic power of the QFS system, a boson-star collision with a long-lived remnant was then studied. The boson-star binary performed a grazing collision that promptly collided to form a highly perturbed remnant. This remnant produces a long-lasting gravitational wave (GW) *afterglow* which differs greatly from more traditional GW sources. This gravitational afterglow provides a distinct channel for detection, given its long timescale, and if these kinds of collisions occur in nature with sufficient population their radiation could theoretically result in a stochastic GW background. The reader is reminded that the physical situation has not been fine tuned in any way and is expected to be generic for a finite region of parameter space. Infact, similar behaviour was seen in preliminary testing when varying the impact parameter by an order of magnitude. This simulation highlights the fact that there is more to boson-star collision phenomenology than merger waveforms analogous to black-hole collision waveforms. Further exploration of the parameter space and the resulting afterglow (and different boson star theories) is required to relate theoretical stochastic GW backgrounds to boson star populations.

Our results furthermore demonstrate that boson-star mergers efficiently radiate angular momentum consistent with previous studies. In this collision the angular momentum of the remnant decays with a half-life of $t_{1/2} = 4 \times 10^3 m^{-1}$. Interestingly we also note that the minima and maxima of the (2, 2) and (2, 0) modes of the GW signal are initially anti-aligned but drift to alignment over time (Fig. 6.2). This gradual shift of the GW mode alignment approximately coincides with shedding of angular momentum from the remnant. Therefore we tentatively suggest that the alignment of the GW modes could carry information regarding the angular momentum of the remnant.

Finally, the consequences of non-zero eccentricity on the gravitational wave signal and the kick magnitude and direction of un-equal mass Schwarzschild black-hole binaries has been studied. A kick is a gravitational phenomenon in which a system radiates linear momentum (in gravitational waves) resulting in the centre of mass being “kicked” in the opposite direction. A series of binaries with mass ratios

$q = 2/3$, $1/2$, and $1/3$ are simulated; these binaries perform about 3 orbits in the quasicircular limit. We also examine a comparison set of simulations with $q = 1/2$, and a greater initial separation, which completes approximately six orbits in the quasicircular limit. In all cases the black holes were initially placed on the x-axis with boosts of equal and opposite momentum perpendicular to the x-axis; therefore the x-axis is initially the periapsis.

In the black-hole binaries simulated, a maximum in the kick magnitude is seen for an eccentricity of $e \sim 0.5$ and is approximately 25% larger than the quasi circular case. In addition to this, the kick magnitude is seen to oscillate, with respect to eccentricity, by $\sim 10\%$ of the quasicircular limit. As the eccentricity tends to unity, in the case of a headon collision, the kick magnitude becomes small. These simulations are simulated with two codes, GRCHOMBO and LEAN; both codes show an error budget of 3-4 %.

The oscillatory behaviour of the kick magnitude is attributed to the final infall angle (or direction) with respect to the periapsis of the black holes in merger. The notion of an infall angle in general relativity is not well defined and it is approximated here by considering the angle made by the final kick to the x-axis. When the kick magnitude is plotted as a function of infall angle (in Figure 7.4) it displays the hypothesised oscillatory behaviour with an period close to 2π ; any deviation here is attributed to periapsis precession.

The dependence of the oscillatory behaviour of the kick with respect to the initial eccentricity is explored in the second set of simulations with $q = 1/2$ and a larger initial separation (or a less negative binding energy). The oscillations are more pronounced in this situation which is attributed to the longer infall time which gives more time for phase differences between similar binaries to build up.

While the findings of these black-hole kick simulations answer many questions, they also ask more. From a study of two sets of simulations with different initial separations we are led to believe that the oscillatory dependence of the kick on the initial separation is sensitive; to what extent this is hidden by gravitational circularisation¹ over longer inspirals is unknown. A study of long eccentric inspirals would likely require post Newtonian methods. Other interesting studies could include tracking the precession of the periapsis in this strong gravity regime, kicks in high boost grazing collisions or even the possibility of kicks in compact-object binaries such as boson stars.

¹Gravitational circularisation refers to the natural phenomenon in general relativity where eccentricity is damped over time eventually turning an eccentric binary into a quasi-circular one.

Bibliography

- [1] T. Andrade, L. A. Salo, J. C. Aurrekoetxea, J. Bamber, K. Clough, R. Croft, E. de Jong, A. Drew, A. Duran, P. G. Ferreira, P. Figueras, H. Finkel, T. Fran  a, B.-X. Ge, C. Gu, T. Helfer, J. J  ykk  , C. Joana, M. Kunesch, K. Kornet, E. A. Lim, F. Muia, Z. Nazari, M. Radia, J. Ripley, P. Sheldard, U. Sperhake, D. Traykova, S. Tunyasuvunakool, Z. Wang, J. Y. Widdicombe, and K. Wong, “Grchombo: An adaptable numerical relativity code for fundamental physics,” *Journal of Open Source Software*, vol. 6, no. 68, p. 3703, 2021.
- [2] T. Helfer, U. Sperhake, R. Croft, M. Radia, B.-X. Ge, and E. A. Lim, “Malaise and remedy of binary boson-star initial data,” *Class. Quant. Grav.*, vol. 39, no. 7, p. 074001, 2022.
- [3] R. Croft, “Local continuity of angular momentum and noether charge for matter in general relativity,” *arXiv preprint : https://arxiv.org/abs/2203.13845*, 2022.
- [4] R. Croft, T. Helfer, B.-X. Ge, M. Radia, T. Evstafyeva, E. A. Lim, U. Sperhake, and K. Clough, “The gravitational afterglow of boson stars,” *arXiv preprint : arXiv:2207.05690*, 2022.
- [5] M. Radia, U. Sperhake, E. Berti, and R. Croft, “Anomalies in the gravitational recoil of eccentric black-hole mergers with unequal mass ratios,” *Phys. Rev. D*, vol. 103, no. 10, p. 104006, 2021.
- [6] D. J. Kaup, “Klein-Gordon Geon,” *Phys. Rev.*, vol. 172, pp. 1331–1342, 1968.
- [7] R. Brito, V. Cardoso, C. A. Herdeiro, and E. Radu, “Proca stars: gravitating bose–einstein condensates of massive spin 1 particles,” *Physics Letters B*, vol. 752, pp. 291–295, 2016.
- [8] J.-w. Lee and I.-g. Koh, “Galactic halos as boson stars,” *Physical Review D*, vol. 53, no. 4, p. 2236, 1996.
- [9] F. E. Schunck and E. W. Mielke, “General relativistic boson stars,” *Classical and Quantum Gravity*, vol. 20, no. 20, p. R301, 2003.
- [10] S. M. Carroll, *An introduction to general relativity, Spacetime and geometry*. Cambridge University Press, 2019.
- [11] E. Gourgoulhon, “3+ 1 formalism and bases of numerical relativity,” *arXiv preprint gr-qc/0703035*, 2007.
- [12] C. B  r, *Elementary differential geometry*. Cambridge University Press, 2010.
- [13] A. Einstein *et al.*, “On the electrodynamics of moving bodies,” *Annalen der physik*, vol. 17, no. 10, pp. 891–921, 1905.
- [14]   . Gourgoulhon, *Special relativity in general frames*. Springer, 2016.
- [15] R. M. Wald, *General Relativity*. The University of Chicago Press, Chicago and London, 1984.
- [16] C. W. Misner, K. S. Thorne, and J. A. Wheeler, *Gravitation*. W. H. Freeman, New York, 1973.
- [17] S. M. Carroll, “Lecture notes on general relativity,” 1997. arXiv:gr-qc/9712019.

- [18] G. C. McVittie, “The mass-particle in an expanding universe,” *Monthly Notices of the Royal Astronomical Society*, vol. 93, pp. 325–339, 1933.
- [19] D. Hilbert, “Die grundlagen der physik [foundations of physics],” *Nachrichten von der Gesellschaft der Wissenschaften zu Göttingen–Mathematisch-Physikalische Klasse*, vol. 3, p. 395, 1915.
- [20] T. W. Baumgarte and S. L. Shapiro, *Numerical Relativity: Solving Einstein’s Equations on the Computer*. Cambridge University Press, 2010.
- [21] M. Alcubierre, *Introduction to 3+ 1 numerical relativity*, vol. 140. Oxford University Press, 2008.
- [22] S. Frittelli and R. Gómez, “Ill-posedness in the einstein equations,” *Journal of Mathematical Physics*, vol. 41, no. 8, pp. 5535–5549, 2000.
- [23] T. W. Baumgarte and S. L. Shapiro, “On the Numerical integration of Einstein’s field equations,” *Phys. Rev. D*, vol. 59, p. 024007, 1998. gr-qc/9810065.
- [24] C. Gundlach and J. M. Martín-García, “Well-posedness of formulations of the Einstein equations with dynamical lapse and shift conditions,” *Phys. Rev. D*, vol. 74, p. 024016, 2006. gr-qc/0604035.
- [25] Z. Cao and D. Hilditch, “Numerical stability of the Z4c formulation of general relativity,” *Phys. Rev. D*, vol. 85, p. 124032, 2012. arXiv:1111.2177 [gr-qc].
- [26] C. Gundlach and J. M. Martín-García, “Symmetric hyperbolicity and consistent boundary conditions for second-order Einstein equations,” *Phys. Rev. D*, vol. 70, p. 044032, 2004. gr-qc/0403019.
- [27] D. Garfinkle, “Harmonic coordinate method for simulating generic singularities,” *Phys. Rev. D*, vol. 65, p. 044029, 2002. gr-qc/0110013.
- [28] D. Garfinkle, “Harmonic coordinate method for simulating generic singularities,” *Physical Review D*, vol. 65, no. 4, p. 044029, 2002.
- [29] F. Pretorius, “Numerical relativity using a generalized harmonic decomposition,” *Class. Quantum Grav.*, vol. 22, pp. 425–452, 2005. gr-qc/0407110.
- [30] F. Pretorius, “Evolution of Binary Black-Hole Spacetimes,” *Phys. Rev. Lett.*, vol. 95, p. 121101, 2005. gr-qc/0507014.
- [31] C. Gundlach, G. Calabrese, I. Hinder, and J. M. Martín-García, “Constraint damping in the z4 formulation and harmonic gauge,” *Classical and Quantum Gravity*, vol. 22, no. 17, p. 3767, 2005.
- [32] S. Bernuzzi and D. Hilditch, “Constraint violation in free evolution schemes: Comparing BSSNOK with a conformal decomposition of Z4,” *Phys. Rev. D*, vol. 81, p. 084003, 2010.
- [33] D. Alic, C. Bona-Casas, C. Bona, L. Rezzolla, and C. Palenzuela, “Conformal and covariant formulation of the z4 system with constraint-violation damping,” *Phys. Rev. D*, vol. 85, p. 064040, Mar 2012.
- [34] D. Alic, W. Kastaun, and L. Rezzolla, “Constraint damping of the conformal and covariant formulation of the Z4 system in simulations of binary neutron stars,” *Phys. Rev. D*, vol. 88, no. 6, p. 064049, 2013.
- [35] L. Smarr and J. W. York Jr, “Kinematical conditions in the construction of spacetime,” *Physical Review D*, vol. 17, no. 10, p. 2529, 1978.
- [36] M. Campanelli, C. O. Lousto, P. Marronetti, and Y. Zlochower, “Accurate evolutions of orbiting black-hole binaries without excision,” *Phys. Rev. Lett.*, vol. 96, p. 111101, Mar 2006.
- [37] B. Brügmann, W. Tichy, and N. Jansen, “Numerical simulation of orbiting black holes,” *Phys. Rev. Lett.*, vol. 92, p. 211101, 2004. gr-qc/0312112.

- [38] D. Alic, C. Bona-Casas, C. Bona, L. Rezzolla, and C. Palenzuela, “Conformal and covariant formulation of the z4 system with constraint-violation damping,” *Physical Review D*, vol. 85, no. 6, p. 064040, 2012.
- [39] D. Hilditch, S. Bernuzzi, M. Thierfelder, Z. Cao, W. Tichy, and B. Brügmann, “Compact binary evolutions with the Z4c formulation,” *Phys. Rev. D*, vol. 88, p. 084057, 2013. arXiv:1212.2901 [gr-qc].
- [40] F. E. Schunck and E. W. Mielke, “General relativistic boson stars,” *Class. Quant. Grav.*, vol. 20, pp. R301–R356, 2003.
- [41] S. L. Liebling and C. Palenzuela, “Dynamical Boson Stars,” *Living Rev. Rel.*, vol. 15, p. 6, 2012.
- [42] C. Palenzuela, P. Pani, M. Bezares, V. Cardoso, L. Lehner, and S. Liebling, “Gravitational Wave Signatures of Highly Compact Boson Star Binaries,” *Phys. Rev. D*, vol. 96, no. 10, p. 104058, 2017.
- [43] A. Diez-Tejedor and A. X. Gonzalez-Morales, “No-go theorem for static scalar field dark matter halos with no noether charges,” *Physical Review D*, vol. 88, no. 6, p. 067302, 2013.
- [44] Press, William H. and Teukolsky, Saul A. and Vetterling, William T. and Flannery, Brian P., *Numerical recipes in C (2nd ed.): the art of scientific computing*. New York, NY, USA: Cambridge University Press, 1992.
- [45] M. Alcubierre, B. Brügmann, P. Diener, M. Koppitz, D. Pollney, E. Seidel, and R. Takahashi, “Gauge conditions for long-term numerical black hole evolutions without excision,” *Phys. Rev. D*, vol. 67, p. 084023, 2003. gr-qc/0206072.
- [46] K. Clough, P. Figueras, H. Finkel, M. Kunesch, E. A. Lim, and S. Tunyasuvunakool, “Grchombo: numerical relativity with adaptive mesh refinement,” *Classical and Quantum Gravity*, vol. 32, no. 24, p. 245011, 2015.
- [47] M. J. Berger and J. Oliger, “Adaptive mesh refinement for hyperbolic partial differential equations,” *Journal of computational Physics*, vol. 53, no. 3, pp. 484–512, 1984.
- [48] M. Berger and I. Rigoutsos, “An algorithm for point clustering and grid generation,” *IEEE Transactions on Systems, Man, and Cybernetics*, vol. 21, no. 5, pp. 1278–1286, 1991.
- [49] M. Shibata and T. Nakamura, “Evolution of three-dimensional gravitational waves: Harmonic slicing case,” *Phys. Rev. D*, vol. 52, pp. 5428–5444, 1995.
- [50] T. W. Baumgarte and S. L. Shapiro, “Numerical integration of einstein’s field equations,” *Physical Review D*, vol. 59, no. 2, p. 024007, 1998.
- [51] H.-O. Kreiss and J. Oliger, *Methods for the approximate solution of time dependent problems*. No. 10, International Council of Scientific Unions, World Meteorological Organization, 1973.
- [52] M. Radia, U. Sperhake, E. Berti, and R. Croft, “Anomalies in the gravitational recoil of eccentric black-hole mergers with unequal mass ratios,” *Physical Review D*, vol. 103, no. 10, p. 104006, 2021.
- [53] U. Sperhake, “Binary black-hole evolutions of excision and puncture data,” *Phys. Rev. D*, vol. 76, p. 104015, 2007. gr-qc/0606079.
- [54] F. Löffler, J. Faber, E. Bentivegna, T. Bode, P. Diener, R. Haas, I. Hinder, B. C. Mundim, C. D. Ott, E. Schnetter, *et al.*, “The einstein toolkit: a community computational infrastructure for relativistic astrophysics,” *Classical and Quantum Gravity*, vol. 29, no. 11, p. 115001, 2012.
- [55] M. Zilhão and F. Löffler, “An Introduction to the Einstein Toolkit,” *Int. J. Mod. Phys. A*, vol. 28, p. 1340014, 2013. arXiv:1305.5299 [gr-qc].
- [56] Einstein Toolkit webpage: <http://einstoolkit.org/>.

- [57] T. Helfer, J. C. Aurrekoetxea, and E. A. Lim, “Cosmic string loop collapse in full general relativity,” *Phys. Rev. D*, vol. 99, p. 104028, May 2019.
- [58] J. C. Aurrekoetxea, K. Clough, R. Flauger, and E. A. Lim, “The effects of potential shape on inhomogeneous inflation,” *Journal of Cosmology and Astroparticle Physics*, vol. 2020, pp. 030–030, may 2020.
- [59] T. Andrade, P. Figueras, and U. Sperhake, “Violations of Weak Cosmic Censorship in Black Hole collisions,” 11 2020.
- [60] A. Hadjidimos, “Successive overrelaxation (sor) and related methods,” *Journal of Computational and Applied Mathematics*, vol. 123, no. 1-2, pp. 177–199, 2000.
- [61] R. Arnowitt, S. Deser, and C. W. Misner, “The dynamics of general relativity, gravitation: An introduction to current research,” *Chap*, vol. 7, pp. 227–265, 1962.
- [62] D. J. Kaup, “Klein-gordon geon,” *Phys. Rev.*, vol. 172, pp. 1331–1342, Aug 1968.
- [63] B. P. Abbott *et al.*, “Observation of Gravitational Waves from a Binary Black Hole Merger,” *Phys. Rev. Lett.*, vol. 116, no. 6, p. 061102, 2016.
- [64] B. P. Abbott *et al.*, “GWTC-1: A Gravitational-Wave Transient Catalog of Compact Binary Mergers Observed by LIGO and Virgo during the First and Second Observing Runs,” *Phys. Rev. X*, vol. 9, no. 3, p. 031040, 2019.
- [65] R. Abbott *et al.*, “GWTC-2: Compact Binary Coalescences Observed by LIGO and Virgo During the First Half of the Third Observing Run,” *Phys. Rev. X*, vol. 11, p. 021053, 2021.
- [66] E. Berti *et al.*, “Testing General Relativity with Present and Future Astrophysical Observations,” *Class. Quant. Grav.*, vol. 32, p. 243001, 2015.
- [67] B. P. Abbott *et al.*, “Tests of general relativity with GW150914,” *Phys. Rev. Lett.*, vol. 116, no. 22, p. 221101, 2016.
- [68] B. Abbott *et al.*, “Tests of General Relativity with GW170817,” *Phys. Rev. Lett.*, vol. 123, no. 1, p. 011102, 2019.
- [69] B. Abbott *et al.*, “Tests of General Relativity with the Binary Black Hole Signals from the LIGO-Virgo Catalog GWTC-1,” *Phys. Rev. D*, vol. 100, no. 10, p. 104036, 2019.
- [70] R. Abbott *et al.*, “Tests of general relativity with binary black holes from the second LIGO-Virgo gravitational-wave transient catalog,” *Phys. Rev. D*, vol. 103, no. 12, p. 122002, 2021.
- [71] C. J. Moore, E. Finch, R. Buscicchio, and D. Gerosa, “Testing general relativity with gravitational-wave catalogs: the insidious nature of waveform systematics,” 3 2021.
- [72] D. Trifirò, R. O’Shaughnessy, D. Gerosa, E. Berti, M. Kesden, T. Littenberg, and U. Sperhake, “Distinguishing black-hole spin-orbit resonances by their gravitational wave signatures. II: Full parameter estimation,” *Phys. Rev. D*, vol. 93, no. 4, p. 044071, 2016. arXiv:1507.05587 [gr-qc].
- [73] K. Belczynski *et al.*, “Evolutionary roads leading to low effective spins, high black hole masses, and O1/O2 rates for LIGO/Virgo binary black holes,” *Astron. Astrophys.*, vol. 636, p. A104, 2020.
- [74] R. Abbott *et al.*, “Population Properties of Compact Objects from the Second LIGO-Virgo Gravitational-Wave Transient Catalog,” *Astrophys. J. Lett.*, vol. 913, no. 1, p. L7, 2021.
- [75] V. Baibhav, D. Gerosa, E. Berti, K. W. K. Wong, T. Helfer, and M. Mould, “The mass gap, the spin gap, and the origin of merging binary black holes,” *Phys. Rev. D*, vol. 102, no. 4, p. 043002, 2020.

- [76] D. Gerosa and M. Fishbach, “Hierarchical mergers of stellar-mass black holes and their gravitational-wave signatures,” 5 2021.
- [77] B. P. Abbott *et al.*, “A gravitational-wave standard siren measurement of the Hubble constant,” *Nature*, vol. 551, no. 7678, pp. 85–88, 2017.
- [78] B. P. Abbott *et al.*, “A Gravitational-wave Measurement of the Hubble Constant Following the Second Observing Run of Advanced LIGO and Virgo,” *Astrophys. J.*, vol. 909, no. 2, p. 218, 2021.
- [79] L. Barack *et al.*, “Black holes, gravitational waves and fundamental physics: a roadmap,” *Class. Quant. Grav.*, vol. 36, no. 14, p. 143001, 2019.
- [80] B. P. Abbott *et al.*, “GW170817: Observation of Gravitational Waves from a Binary Neutron S+tar Inspiral,” *Phys. Rev. Lett.*, vol. 119, no. 16, p. 161101, 2017.
- [81] B. P. Abbott *et al.*, “Gravitational Waves and Gamma-rays from a Binary Neutron Star Merger: GW170817 and GRB 170817A,” *Astrophys. J.*, vol. 848, no. 2, p. L13, 2017.
- [82] V. Cardoso, L. Gualtieri, C. Herdeiro, and U. Sperhake, “Exploring New Physics Frontiers Through Numerical Relativity,” *Living Rev. Relativity*, vol. 18, p. 1, 2015. arXiv:1409.0014 [gr-qc].
- [83] R. Brito, V. Cardoso, and P. Pani, “Superradiance,” *Lect. Notes Phys.*, vol. 906, pp. pp.1–237, 2015.
- [84] J. A. Wheeler, “Geons,” *Phys. Rev.*, vol. 97, pp. 511–536, 1955.
- [85] T. W. Baumgarte and S. L. Shapiro, *Numerical Relativity: Starting from Scratch*. Cambridge University Press, 2 2021.
- [86] D. A. Feinblum and W. A. McKinley, “Stable States of a Scalar Particle in Its Own Gravitational Field,” *Phys. Rev.*, vol. 168, no. 5, p. 1445, 1968.
- [87] R. Ruffini and S. Bonazzola, “Systems of selfgravitating particles in general relativity and the concept of an equation of state,” *Phys. Rev.*, vol. 187, pp. 1767–1783, 1969.
- [88] R. Brito, V. Cardoso, C. A. R. Herdeiro, and E. Radu, “Proca stars: Gravitating Bose–Einstein condensates of massive spin 1 particles,” *Phys. Lett.*, vol. B752, pp. 291–295, 2016.
- [89] M. Alcubierre, J. Barranco, A. Bernal, J. C. Degollado, A. Diez-Tejedor, M. Megevand, D. Nunez, and O. Sarbach, “ ℓ -Boson stars,” *Class. Quant. Grav.*, vol. 35, no. 19, p. 19LT01, 2018.
- [90] M. Choptuik, R. Masachs, and B. Way, “Multioscillating Boson Stars,” *Phys. Rev. Lett.*, vol. 123, no. 13, p. 131101, 2019.
- [91] M. Campanelli, C. O. Lousto, P. Marronetti, and Y. Zlochower, “Accurate Evolutions of Orbiting Black-Hole Binaries without Excision,” *Phys. Rev. Lett.*, vol. 96, p. 111101, 2006. gr-qc/0511048.
- [92] J. G. Baker, J. Centrella, D.-I. Choi, M. Koppitz, and J. van Meter, “Gravitational-Wave Extraction from an inspiraling Configuration of Merging Black Holes,” *Phys. Rev. Lett.*, vol. 96, p. 111102, 2006. gr-qc/0511103.
- [93] U. Sperhake, “The numerical relativity breakthrough for binary black holes,” *Class. Quant. Grav.*, vol. 32, no. 12, p. 124011, 2015.
- [94] R. C. Tolman, “Static Solutions of Einstein’s Field Equations for Spheres of Fluid,” *Phys. Rev.*, vol. 55, pp. 364–373, 1939.
- [95] J. R. Oppenheimer and G. M. Volkoff, “On Massive Neutron Cores,” *Phys. Rev.*, vol. 55, pp. 374–381, 1939.
- [96] J. D. Breit, S. Gupta, and A. Zaks, “Cold Bose Stars,” *Phys. Lett. B*, vol. 140, pp. 329–332, 1984.

- [97] M. Gleiser and R. Watkins, “Gravitational Stability of Scalar Matter,” *Nucl. Phys. B*, vol. 319, pp. 733–746, 1989.
- [98] E. Seidel and W.-M. Suen, “Dynamical Evolution of Boson Stars. 1. Perturbing the Ground State,” *Phys. Rev. D*, vol. 42, pp. 384–403, 1990.
- [99] T. D. Lee and Y. Pang, “Nontopological solitons,” *Phys. Rept.*, vol. 221, pp. 251–350, 1992.
- [100] P. Jetzer, “Boson stars,” *Phys. Rept.*, vol. 220, pp. 163–227, 1992.
- [101] A. R. Liddle and M. S. Madsen, “The Structure and formation of boson stars,” *Int. J. Mod. Phys. D*, vol. 1, pp. 101–144, 1992.
- [102] J. Balakrishna, E. Seidel, and W.-M. Suen, “Dynamical evolution of boson stars. 2. Excited states and selfinteracting fields,” *Phys. Rev. D*, vol. 58, p. 104004, 1998.
- [103] M. Colpi, S. L. Shapiro, and I. Wasserman, “Boson Stars: Gravitational Equilibria of Selfinteracting Scalar Fields,” *Phys. Rev. Lett.*, vol. 57, pp. 2485–2488, 1986.
- [104] T. D. Lee, “Soliton Stars and the Critical Masses of Black Holes,” *Phys. Rev. D*, vol. 35, p. 3637, 1987.
- [105] F. E. Schunck and D. F. Torres, “Boson stars with generic selfinteractions,” *Int. J. Mod. Phys. D*, vol. 9, pp. 601–618, 2000.
- [106] B. Hartmann, B. Kleihaus, J. Kunz, and I. Schaffer, “Compact Boson Stars,” *Phys. Lett. B*, vol. 714, pp. 120–126, 2012.
- [107] J. C. Bustillo, N. Sanchis-Gual, A. Torres-Forné, J. A. Font, A. Vajpeyi, R. Smith, C. Herdeiro, E. Radu, and S. H. W. Leong, “GW190521 as a Merger of Proca Stars: A Potential New Vector Boson of $+ 8.7 \times 10^{-13}$ eV,” *Phys. Rev. Lett.*, vol. 126, no. 8, p. 081101, 2021.
- [108] N. Sennett, T. Hinderer, J. Steinhoff, A. Buonanno, and S. Ossokine, “Distinguishing Boson Stars from Black Holes and Neutron Stars from Tidal Interactions in Inspiring Binary Systems,” *Phys. Rev. D*, vol. 96, no. 2, p. 024002, 2017.
- [109] F. Di Giovanni, N. Sanchis-Gual, P. Cerdá-Durán, M. Zilhão, C. Herdeiro, J. A. Font, and E. Radu, “Dynamical bar-mode instability in spinning bosonic stars,” *Phys. Rev. D*, vol. 102, no. 12, p. 124009, 2020.
- [110] A. Toubiana, S. Babak, E. Barausse, and L. Lehner, “Modeling gravitational waves from exotic compact objects,” *Phys. Rev. D*, vol. 103, no. 6, p. 064042, 2021.
- [111] Y. Kobayashi, M. Kasai, and T. Futamase, “Does a boson star rotate?,” *Phys. Rev. D*, vol. 50, pp. 7721–7724, 1994.
- [112] F. E. Schunck and E. W. Mielke, “Rotating boson star as an effective mass torus in general relativity,” *Phys. Lett.*, vol. A249, pp. 389–394, 1998.
- [113] F. D. Ryan, “Spinning boson stars with large selfinteraction,” *Phys. Rev. D*, vol. 55, pp. 6081–6091, 1997.
- [114] S. Yoshida and Y. Eriguchi, “Nonaxisymmetric boson stars in Newtonian gravity,” *Phys. Rev. D*, vol. 56, pp. 6370–6377, 1997.
- [115] S. Yoshida and Y. Eriguchi, “Rotating boson stars in general relativity,” *Phys. Rev. D*, vol. 56, pp. 762–771, 1997.
- [116] S. Yoshida and Y. Eriguchi, “New static axisymmetric and nonvacuum solutions in general relativity: Equilibrium solutions of boson stars,” *Phys. Rev. D*, vol. 55, pp. 1994–2001, 1997.

- [117] F. E. Schunck and E. W. Mielke, “Boson stars: Rotation, formation, and evolution,” *Gen. Rel. Grav.*, vol. 31, p. 787, 1999.
- [118] B. Kleihaus, J. Kunz, and M. List, “Rotating boson stars and Q-balls,” *Phys. Rev. D*, vol. 72, p. 064002, 2005.
- [119] B. Kleihaus, J. Kunz, M. List, and I. Schaffer, “Rotating Boson Stars and Q-Balls. II. Negative Parity and Ergoregions,” *Phys. Rev. D*, vol. 77, p. 064025, 2008.
- [120] B. Kleihaus, J. Kunz, and S. Schneider, “Stable Phases of Boson Stars,” *Phys. Rev. D*, vol. 85, p. 024045, 2012.
- [121] L. G. Collodel, B. Kleihaus, and J. Kunz, “Excited Boson Stars,” *Phys. Rev. D*, vol. 96, no. 8, p. 084066, 2017.
- [122] C. Herdeiro, I. Perapechka, E. Radu, and Ya. Shnir, “Asymptotically flat spinning scalar, Dirac and Proca stars,” *Phys.Lett.B*, vol. 797, p. 134845, 2019.
- [123] N. Sanchis-Gual, F. Di Giovanni, M. Zilhão, C. Herdeiro, P. Cerdá-Durán, J. A. Font, and E. Radu, “Nonlinear Dynamics of Spinning Bosonic Stars: Formation and Stability,” *Phys. Rev. Lett.*, vol. 123, no. 22, p. 221101, 2019.
- [124] A. S. Dmitriev, D. G. Levkov, A. G. Panin, E. K. Pushnaya, and I. I. Tkachev, “Instability of rotating Bose stars,” *Phys. Rev. D*, vol. 104, no. 2, p. 023504, 2021.
- [125] N. Siemonsen and W. E. East, “Stability of rotating scalar boson stars with nonlinear interactions,” *Phys. Rev. D*, vol. 103, no. 4, p. 044022, 2021.
- [126] E. W. Mielke and F. E. Schunck, “Boson stars: Early history and recent prospects,” in *Recent developments in theoretical and experimental general relativity, gravitation, and relativistic field theories. Proceedings, 8th Marcel Grossmann meeting, MG8, Jerusalem, Israel, June 22-27, 1997. Pts. A, B*, pp. 1607–1626, 1997.
- [127] E. W. Mielke and F. E. Schunck, “Boson stars: Alternatives to primordial black holes?,” *Nucl. Phys. B*, vol. 564, pp. 185–203, 2000.
- [128] B. C. Mundim, *A Numerical Study of Boson Star Binaries*. PhD thesis, British Columbia U., 2010.
- [129] C. Palenzuela, I. Olabarrieta, L. Lehner, and S. L. Liebling, “Head-on collisions of boson stars,” *Phys. Rev. D*, vol. 75, p. 064005, 2007.
- [130] M. W. Choptuik and F. Pretorius, “Ultra Relativistic Particle Collisions,” *Phys. Rev. Lett.*, vol. 104, p. 111101, 2010. arXiv:0908.1780 [gr-qc].
- [131] M. Bezares, C. Palenzuela, and C. Bona, “Final fate of compact boson star mergers,” *Phys. Rev. D*, vol. 95, no. 12, p. 124005, 2017.
- [132] C. Palenzuela, L. Lehner, and S. L. Liebling, “Orbital Dynamics of Binary Boson Star Systems,” *Phys. Rev. D*, vol. 77, p. 044036, 2008.
- [133] T. Helfer, E. A. Lim, M. A. G. Garcia, and M. A. Amin, “Gravitational Wave Emission from Collisions of Compact Scalar Solitons,” *Phys. Rev. D*, vol. 99, no. 4, p. 044046, 2019.
- [134] R. Arnowitt, S. Deser, and C. W. Misner, “The dynamics of general relativity,” in *Gravitation an introduction to current research* (L. Witten, ed.), pp. 227–265, John Wiley, New York, 1962.
- [135] M. Shibata, H. Okawa, and T. Yamamoto, “High-velocity collisions of two black holes,” *Phys. Rev. D*, vol. 78, p. 101501(R), 2008. arXiv:0810.4735 [gr-qc].
- [136] H. Okawa, K.-i. Nakao, and M. Shibata, “Is super-Planckian physics visible? Scattering of black holes in 5 dimensions,” *Phys. Rev. D*, vol. 83, p. 121501(R), 2011. arXiv:1105.3331 [gr-qc].

- [137] U. Sperhake, W. Cook, and D. Wang, “The high-energy collision of black holes in higher dimensions,” *Phys. Rev. D*, vol. 100, no. 10, p. 104046, 2020.
- [138] D. R. Brill and R. W. Lindquist, “Interaction Energy in Geometrostatics,” *Phys. Rev.*, vol. 131, pp. 471–476, 1963.
- [139] P. C. Aichelburg and R. U. Sexl, “On the Gravitational field of a massless particle,” *Gen. Rel. Grav.*, vol. 2, pp. 303–312, 1971.
- [140] D. Alic, C. Bona-Casas, C. Bona, L. Rezzolla, and C. Palenzuela, “Conformal and covariant formulation of the Z4 system with constraint-violation damping,” *Phys. Rev. D*, vol. 85, p. 064040, 2012. arXiv:1106.2254 [gr-qc].
- [141] S. Husa, J. A. González, M. D. Hannam, B. Brügmann, and U. Sperhake, “Reducing phase error in long numerical binary black hole evolutions with sixth order finite differencing,” *Class. Quant. Grav.*, vol. 25, p. 105006, 2008. arXiv:0706.0740 [gr-qc].
- [142] K. Clough, P. Figueras, H. Finkel, M. Kunesch, E. A. Lim, and S. Tunyasuvunakool, “GRChombo : Numerical Relativity with Adaptive Mesh Refinement,” *Class. Quant. Grav.*, vol. 32, no. 24, p. 245011, 2015. arXiv:1503.03436 [gr-qc].
- [143] M. Radia, U. Sperhake, K. Clough, A. Drew, E. A. Lim, and J. L. Ripley, “Numerical relativity with adaptive mesh refinement:obtaining accurate+ results with grchombo.” in preparation.
- [144] L. E. Simone, E. Poisson, and C. M. Will, “Head-on collision of compact objects in general relativity: Comparison of post-newtonian and perturbation approaches,” *Physical Review D*, vol. 52, pp. 4481–4496, oct 1995.
- [145] T. Binnington and E. Poisson, “Relativistic theory of tidal Love numbers,” *Phys. Rev. D*, vol. 80, p. 084018, 2009.
- [146] R. Penrose, “Quasi-local mass and angular momentum in general relativity,” *Proceedings of the Royal Society of London. Series A, Mathematical and Physical Sciences*, vol. 381, no. 1780, pp. 53–63, 1982.
- [147] N. Sanchis-Gual, C. Herdeiro, J. A. Font, E. Radu, and F. Di Giovanni, “Head-on collisions and orbital mergers of proca stars,” *Physical Review D*, vol. 99, Jan 2019.
- [148] F. Di Giovanni, N. Sanchis-Gual, P. Cerdá-Durán, M. Zilhão, C. Herdeiro, J. A. Font, and E. Radu, “Dynamical bar-mode instability in spinning bosonic stars,” *Physical Review D*, vol. 102, Dec 2020.
- [149] J. Bamber, K. Clough, P. G. Ferreira, L. Hui, and M. Lagos, “Growth of accretion driven scalar hair around kerr black holes,” *Phys. Rev. D*, vol. 103, p. 044059, Feb 2021.
- [150] W. E. East, “Superradiant instability of massive vector fields around spinning black holes in the relativistic regime,” *Phys. Rev. D*, vol. 96, p. 024004, Jul 2017.
- [151] K. Clough, “Continuity equations for general matter: applications in numerical relativity,” *Classical and Quantum Gravity*, vol. 38, p. 167001, jul 2021.
- [152] R. Arnowitt, S. Deser, and C. W. Misner, “Republication of: The dynamics of general relativity,” *General Relativity and Gravitation*, vol. 40, p. 1997–2027, Aug 2008.
- [153] S. L. Liebling and C. Palenzuela, “Dynamical boson stars,” *Living Reviews in Relativity*, vol. 20, no. 1, p. 5, 2017.
- [154] M. Minamitsuji, “Vector boson star solutions with a quartic order self-interaction,” *Physical Review D*, vol. 97, May 2018.

- [155] M. Zilhão, H. Witek, and V. Cardoso, “Nonlinear interactions between black holes and proca fields,” *Classical and Quantum Gravity*, vol. 32, p. 234003, Nov 2015.
- [156] C. Bona, T. Ledvinka, C. Palenzuela, and M. Žáček, “General-covariant evolution formalism for numerical relativity,” *Phys. Rev. D*, vol. 67, p. 104005, May 2003.
- [157] J. G. Baker, J. Centrella, D.-I. Choi, M. Koppitz, and J. van Meter, “Gravitational-wave extraction from an inspiraling configuration of merging black holes,” *Phys. Rev. Lett.*, vol. 96, p. 111102, Mar 2006.
- [158] T. Helfer, U. Sperhake, R. Croft, M. Radia, B.-X. Ge, and E. A. Lim, “Malaise and remedy of binary boson-star initial data,” 2021.
- [159] K. Clough, P. Figueras, H. Finkel, M. Kunesch, E. A. Lim, and S. Tunyasuvunakool, “GRChombo : Numerical relativity with adaptive mesh refinement,” *Classical and Quantum Gravity*, vol. 32, p. 245011, dec 2015.
- [160] W. H. Press, S. A. Teukolsky, W. T. Vetterling, and B. P. Flannery, *Numerical Recipes in C*. Cambridge, USA: Cambridge University Press, second ed., 1992.
- [161] B. P. Abbott *et al.*, “Observation of Gravitational Waves from a Binary Black Hole Merger,” *Phys. Rev. Lett.*, vol. 116, no. 6, p. 061102, 2016.
- [162] B. P. Abbott *et al.*, “Binary Black Hole Population Properties Inferred from the First and Second Observing Runs of Advanced LIGO and Advanced Virgo,” *Astrophys. J. Lett.*, vol. 882, no. 2, p. L24, 2019.
- [163] “The population of merging compact binaries inferred using gravitational waves through GWTC-3,” 11 2021.
- [164] N. Arkani-Hamed, D. P. Finkbeiner, T. R. Slatyer, and N. Weiner, “A Theory of Dark Matter,” *Phys. Rev. D*, vol. 79, p. 015014, 2009.
- [165] J. L. Feng, “Dark Matter Candidates from Particle Physics and Methods of Detection,” *Ann. Rev. Astron. Astrophys.*, vol. 48, pp. 495–545, 2010.
- [166] D. J. E. Marsh, “Axion Cosmology,” *Phys. Rept.*, vol. 643, pp. 1–79, 2016.
- [167] P. Svrcek and E. Witten, “Axions In String Theory,” *JHEP*, vol. 06, p. 051, 2006.
- [168] J. E. Kim, “Light Pseudoscalars, Particle Physics and Cosmology,” *Phys. Rept.*, vol. 150, pp. 1–177, 1987.
- [169] A. Arvanitaki, S. Dimopoulos, S. Dubovsky, N. Kaloper, and J. March-Russell, “String Axiverse,” *Phys. Rev. D*, vol. 81, p. 123530, 2010. arXiv:0905.4720 [hep-th].
- [170] A. Ringwald, “Searching for axions and ALPs from string theory,” *J. Phys. Conf. Ser.*, vol. 485, p. 012013, 2014.
- [171] F. Wilczek, “Problem of Strong P and T Invariance in the Presence of Instantons,” *Phys. Rev. Lett.*, vol. 40, pp. 279–282, 1978.
- [172] R. D. Peccei and H. R. Quinn, “CP Conservation in the Presence of Instantons,” *Phys. Rev. Lett.*, vol. 38, pp. 1440–1443, 1977.
- [173] S. Weinberg, “A New Light Boson?,” *Phys. Rev. Lett.*, vol. 40, pp. 223–226, 1978.
- [174] J. Y. Widdicombe, T. Helfer, D. J. E. Marsh, and E. A. Lim, “Formation of Relativistic Axion Stars,” *JCAP*, vol. 10, p. 005, 2018.

- [175] M. A. Amin, J. Braden, E. J. Copeland, J. T. Giblin, C. Solorio, Z. J. Weiner, and S.-Y. Zhou, “Gravitational waves from asymmetric oscillon dynamics?,” *Phys. Rev. D*, vol. 98, p. 024040, 2018.
- [176] R. RUFFINI and S. BONAZZOLA, “Systems of self-gravitating particles in general relativity and the concept of an equation of state,” *Phys. Rev.*, vol. 187, pp. 1767–1783, Nov 1969.
- [177] J. A. Wheeler, “Geons,” *Phys. Rev.*, vol. 97, pp. 511–536, Jan 1955.
- [178] L. Visinelli, “Boson Stars and Oscillatons: A Review,” 9 2021.
- [179] D. Guerra, C. F. B. Macedo, and P. Pani, “Axion boson stars,” *JCAP*, vol. 09, no. 09, p. 061, 2019. [Erratum: *JCAP* 06, E01 (2020)].
- [180] M. Vaglio, C. Pacilio, A. Maselli, and P. Pani, “The multipolar structure of rotating boson stars,” 3 2022.
- [181] V. Cardoso, T. Ikeda, Z. Zhong, and M. Zilhão, “The piercing of a boson star by a black hole,” 5 2022.
- [182] M. A. Amin, A. J. Long, Z.-G. Mou, and P. Saffin, “Dipole radiation and beyond from axion stars in electromagnetic fields,” *JHEP*, vol. 06, p. 182, 2021.
- [183] H.-Y. Zhang, M. A. Amin, E. J. Copeland, P. M. Saffin, and K. D. Lozanov, “Classical Decay Rates of Oscillons,” *JCAP*, vol. 07, p. 055, 2020.
- [184] N. Sanchis-Gual, M. Zilhão, C. Herdeiro, F. Di Giovanni, J. A. Font, and E. Radu, “Synchronized gravitational atoms from mergers of bosonic stars,” *Phys. Rev. D*, vol. 102, no. 10, p. 101504, 2020.
- [185] M. Alcubierre, J. Barranco, A. Bernal, J. C. Degollado, A. Diez-Tejedor, V. Jaramillo, M. Megevand, D. Núñez, and O. Sarbach, “Extreme ℓ -boson stars,” 12 2021.
- [186] M. Bošković and E. Barausse, “Soliton boson stars, Q-balls and the causal Buchdahl bound,” 11 2021.
- [187] D. Stefanesei and E. Radu, “Boson stars with negative cosmological constant,” *Nucl. Phys. B*, vol. 665, pp. 594–622, 2003.
- [188] R. Friedberg, T. D. Lee, and Y. Pang, “Scalar Soliton Stars and Black Holes,” *Phys. Rev. D*, vol. 35, p. 3658, 1987.
- [189] P. Jetzer and J. J. van der Bij, “CHARGED BOSON STARS,” *Phys. Lett. B*, vol. 227, pp. 341–346, 1989.
- [190] D. Pugliese, H. Quevedo, J. A. Rueda H., and R. Ruffini, “On charged boson stars,” *Phys. Rev. D*, vol. 88, p. 024053, 2013.
- [191] S. H. Hawley and M. W. Choptuik, “Numerical evidence for ‘multi - scalar stars’,” *Phys. Rev. D*, vol. 67, p. 024010, 2003.
- [192] L. A. Urena-Lopez, S. Valdez-Alvarado, and R. Becerril, “Evolution and stability phi**4 oscillations,” *Class. Quant. Grav.*, vol. 29, p. 065021, 2012.
- [193] F. Muia, M. Cicoli, K. Clough, F. Pedro, F. Quevedo, and G. P. Vacca, “The Fate of Dense Scalar Stars,” *JCAP*, vol. 07, p. 044, 2019.
- [194] T. Helfer, D. J. E. Marsh, K. Clough, M. Fairbairn, E. A. Lim, and R. Becerril, “Black hole formation from axion stars,” *JCAP*, vol. 1703, no. 03, p. 055, 2017.
- [195] S. R. Coleman, “Q-balls,” *Nucl. Phys. B*, vol. 262, no. 2, p. 263, 1985. [Addendum: Nucl.Phys.B 269, 744 (1986)].

- [196] V. Cardoso, L. C. B. Crispino, C. F. B. Macedo, H. Okawa, and P. Pani, “Light rings as observational evidence for event horizons: long-lived modes, ergoregions and nonlinear instabilities of ultracompact objects,” *Phys. Rev. D*, vol. 90, no. 4, p. 044069, 2014.
- [197] M. A. Amin, I. Banik, C. Negreanu, and I.-S. Yang, “Ultrarelativistic oscillon collisions,” *Phys. Rev. D*, vol. 90, no. 8, p. 085024, 2014.
- [198] M. A. Amin, R. Easther, H. Finkel, R. Flauger, and M. P. Hertzberg, “Oscillons After Inflation,” *Phys. Rev. Lett.*, vol. 108, p. 241302, 2012.
- [199] M. A. Amin, R. Easther, and H. Finkel, “Inflaton Fragmentation and Oscillon Formation in Three Dimensions,” *JCAP*, vol. 12, p. 001, 2010.
- [200] M. Minamitsuji, “Vector boson star solutions with a quartic order self-interaction,” *Phys. Rev. D*, vol. 97, no. 10, p. 104023, 2018.
- [201] R. Brito, V. Cardoso, and H. Okawa, “Accretion of dark matter by stars,” *Phys. Rev. Lett.*, vol. 115, no. 11, p. 111301, 2015. arXiv:1508.04773 [gr-qc].
- [202] H.-Y. Zhang, M. Jain, and M. A. Amin, “Polarized Vector Oscillons,” 11 2021.
- [203] J. Calderon Bustillo, N. Sanchis-Gual, S. H. W. Leong, K. Chandra, A. Torres-Forne, J. A. Font, C. Herdeiro, E. Radu, I. C. F. Wong, and T. G. F. Li, “Searching for vector boson-star mergers within LIGO-Virgo intermediate-mass black-hole merger candidates,” 6 2022.
- [204] J. March-Russell and J. a. G. Rosa, “Micro-Bose/Proca dark matter stars from black hole superradiance,” 5 2022.
- [205] M. Gorghetto, E. Hardy, J. March-Russell, N. Song, and S. M. West, “Dark Photon Stars: Formation and Role as Dark Matter Substructure,” 3 2022.
- [206] C. A. R. Herdeiro, A. M. Pombo, E. Radu, P. V. P. Cunha, and N. Sanchis-Gual, “The imitation game: Proca stars that can mimic the Schwarzschild shadow,” *JCAP*, vol. 04, p. 051, 2021.
- [207] M. Minamitsuji, “Proca stars with nonminimal coupling to the Einstein tensor,” *Phys. Rev. D*, vol. 96, no. 4, p. 044017, 2017.
- [208] N. Sanchis-Gual, C. Herdeiro, E. Radu, J. C. Degollado, and J. A. Font, “Numerical evolutions of spherical Proca stars,” *Phys. Rev. D*, vol. 95, no. 10, p. 104028, 2017.
- [209] M. Duarte and R. Brito, “Asymptotically anti-de Sitter Proca Stars,” *Phys. Rev. D*, vol. 94, no. 6, p. 064055, 2016.
- [210] I. Salazar Landea and F. García, “Charged Proca Stars,” *Phys. Rev. D*, vol. 94, no. 10, p. 104006, 2016.
- [211] M. Zilhão, H. Witek, and V. Cardoso, “Nonlinear interactions between black holes and Proca fields,” *Class. Quant. Grav.*, vol. 32, p. 234003, 2015.
- [212] M. Jain and M. A. Amin, “Polarized solitons in higher-spin wave dark matter,” 9 2021.
- [213] C. Herdeiro, G. Panotopoulos, and E. Radu, “Tidal Love numbers of Proca stars,” *JCAP*, vol. 08, p. 029, 2020.
- [214] V. Cardoso, E. Franzin, A. Maselli, P. Pani, and G. Raposo, “Testing strong-field gravity with tidal Love numbers,” *Phys. Rev. D*, vol. 95, no. 8, p. 084014, 2017. [Addendum: Phys.Rev.D 95, 089901 (2017)].
- [215] M. D. Diamond, D. E. Kaplan, and S. Rajendran, “Binary Collisions of Dark Matter Blobs,” 12 2021.

- [216] C. Pacilio, M. Vaglio, A. Maselli, and P. Pani, “Gravitational-wave detectors as particle-physics laboratories: Constraining scalar interactions with a coherent inspiral model of boson-star binaries,” *Phys. Rev. D*, vol. 102, no. 8, p. 083002, 2020.
- [217] M. A. Amin and Z.-G. Mou, “Electromagnetic Bursts from Mergers of Oscillons in Axion-like Fields,” *JCAP*, vol. 02, p. 024, 2021.
- [218] N. Sanchis-Gual, C. Herdeiro, J. A. Font, E. Radu, and F. Di Giovanni, “Head-on collisions and orbital mergers of Proca stars,” *Phys. Rev. D*, vol. 99, no. 2, p. 024017, 2019.
- [219] J. Y. Widdicombe, T. Helfer, and E. A. Lim, “Black hole formation in relativistic Oscillaton collisions,” *JCAP*, vol. 2001, no. 01, p. 027, 2020.
- [220] M. Bezares and C. Palenzuela, “Gravitational Waves from Dark Boson Star binary mergers,” *Class. Quant. Grav.*, vol. 35, no. 23, p. 234002, 2018.
- [221] T. Dietrich, F. Day, K. Clough, M. Coughlin, and J. Niemeyer, “Neutron star–axion star collisions in the light of multimessenger astronomy,” *Mon. Not. Roy. Astron. Soc.*, vol. 483, no. 1, pp. 908–914, 2019.
- [222] T. Dietrich, S. Ossokine, and K. Clough, “Full 3D numerical relativity simulations of neutron star–boson star collisions with BAM,” *Class. Quant. Grav.*, vol. 36, no. 2, p. 025002, 2019.
- [223] V. Jaramillo, N. Sanchis-Gual, J. Barranco, A. Bernal, J. C. Degollado, C. Herdeiro, M. Megevand, and D. Núñez, “Head-on collisions of ℓ -boson stars,” 2 2022.
- [224] M. Bezares, M. Bošković, S. Liebling, C. Palenzuela, P. Pani, and E. Barausse, “Gravitational waves and kicks from the merger of unequal mass, highly compact boson stars,” *Phys. Rev. D*, vol. 105, no. 6, p. 064067, 2022.
- [225] C. F. B. Macedo, P. Pani, V. Cardoso, and L. C. B. Crispino, “Astrophysical signatures of boson stars: quasinormal modes and inspiral resonances,” *Phys. Rev. D*, vol. 88, no. 6, p. 064046, 2013.
- [226] M. Gleiser, “Stability of Boson Stars,” *Phys. Rev. D*, vol. 38, p. 2376, 1988. [Erratum: Phys.Rev.D 39, 1257 (1989)].
- [227] P. Jetzer, “Dynamical Instability of Bosonic Stellar Configurations,” *Nucl. Phys. B*, vol. 316, pp. 411–428, 1989.
- [228] M. Radia, U. Sperhake, A. Drew, K. Clough, E. A. Lim, J. L. Ripley, J. C. Aurrekoetxea, T. França, and T. Helfer, “Lessons for adaptive mesh refinement in numerical relativity,” 12 2021.
- [229] T. Andrade *et al.*, “GRChombo: An adaptable numerical relativity code for fundamental physics,” *J. Open Source Softw.*, vol. 6, p. 3703, 2021.
- [230] P. Grandclément, C. Somé, and E. Gourgoulhon, “Models of rotating boson stars and geodesics around them: New type of orbits,” *Phys. Rev. D*, vol. 90, p. 024068, Jul 2014.
- [231] F. E. Schunck and E. W. Mielke, “Rotating boson stars.,” in *Relativity and Scientific Computing. Computer Algebra, Numerics, Visualization*, pp. 138–151, Jan. 1996.
- [232] C. F. B. Macedo, V. Cardoso, L. C. B. Crispino, and P. Pani, “Quasinormal modes of relativistic stars and interacting fields,” *Phys. Rev. D*, vol. 93, no. 6, p. 064053, 2016.
- [233] S. Yoshida, Y. Eriguchi, and T. Futamase, “Quasinormal modes of boson stars,” *Phys. Rev. D*, vol. 50, pp. 6235–6246, 1994.
- [234] C. Vásquez Flores, A. Parisi, C.-S. Chen, and G. Lugones, “Fundamental oscillation modes of self-interacting bosonic dark stars,” *JCAP*, vol. 06, p. 051, 2019.

- [235] U. Sperhake, E. Berti, V. Cardoso, J. A. González, B. Brügmann, and M. Ansorg, “Eccentric binary black-hole mergers: The transition from inspiral to plunge in general relativity,” *Phys. Rev. D*, vol. 78, p. 064069, 2008. arXiv:0710.3823 [gr-qc].
- [236] N. Aggarwal *et al.*, “Challenges and opportunities of gravitational-wave searches at MHz to GHz frequencies,” *Living Rev. Rel.*, vol. 24, no. 1, p. 4, 2021.
- [237] L. Badurina *et al.*, “AION: An Atom Interferometer Observatory and Network,” *JCAP*, vol. 05, p. 011, 2020.
- [238] B. P. Abbott *et al.*, “All-sky search for continuous gravitational waves from isolated neutron stars using Advanced LIGO O2 data,” *Phys. Rev. D*, vol. 100, no. 2, p. 024004, 2019.
- [239] R. Abbott *et al.*, “All-sky search for continuous gravitational waves from isolated neutron stars in the early O3 LIGO data,” *Phys. Rev. D*, vol. 104, no. 8, p. 082004, 2021.
- [240] R. Abbott *et al.*, “All-sky search for gravitational wave emission from scalar boson clouds around spinning black holes in LIGO O3 data,” 11 2021.
- [241] R. Abbott *et al.*, “All-sky, all-frequency directional search for persistent gravitational-waves from Advanced LIGO’s and Advanced Virgo’s first three observing runs,” 10 2021.
- [242] R. Abbott *et al.*, “Search for continuous gravitational wave emission from the Milky Way center in O3 LIGO–Virgo data,” 4 2022.
- [243] R. Abbott *et al.*, “All-sky search for continuous gravitational waves from isolated neutron stars using Advanced LIGO and Advanced Virgo O3 data,” 1 2022.
- [244] R. Abbott *et al.*, “Searches for Gravitational Waves from Known Pulsars at Two Harmonics in the Second and Third LIGO-Virgo Observing Runs,” 11 2021.
- [245] R. Abbott *et al.*, “Search for continuous gravitational waves from 20 accreting millisecond X-ray pulsars in O3 LIGO data,” 9 2021.
- [246] D. Croon, M. Gleiser, S. Mohapatra, and C. Sun, “Gravitational Radiation Background from Boson Star Binaries,” *Phys. Lett. B*, vol. 783, pp. 158–162, 2018.
- [247] K. Clough, “Continuity equations for general matter: applications in numerical relativity,” 4 2021.
- [248] E. Jones, T. Oliphant, P. Peterson, and Others, “SciPy: Open source scientific tools for python,” 2001.
- [249] P. R. Saulson, “Josh Goldberg and the physical reality of gravitational waves,” *Gen. Rel. Grav.*, vol. 43, pp. 3289–3299, 2011.
- [250] M. Campanelli, C. O. Lousto, and Y. Zlochower, “Spinning-black-hole binaries: The orbital hang up,” *Phys. Rev. D*, vol. 74, p. 041501, 2006. gr-qc/0604012.
- [251] U. Sperhake, V. Cardoso, F. Pretorius, E. Berti, T. Hinderer, and N. Yunes, “Cross section, final spin and zoom-whirl behavior in high-energy black hole collisions,” *Phys. Rev. Lett.*, vol. 103, p. 131102, 2009. arXiv:0907.1252 [gr-qc].
- [252] W. B. Bonnor and M. A. Rotenberg, “Transport of momentum by gravitational waves: the linear approximation,” *Proc. R. Soc. A*, vol. 265, pp. 109–116, Dec. 1961.
- [253] A. Peres, “Classical Radiation Recoil,” *Phys. Rev.*, vol. 128, pp. 2471–2475, 1962.
- [254] J. D. Bekenstein, “Gravitational-Radiation Recoil and Runaway Black Holes,” *Astrophys. J.*, vol. 183, pp. 657–664, 1973.

- [255] D. Gerosa and C. J. Moore, “Black hole kicks as new gravitational wave observables,” *Phys. Rev. Lett.*, vol. 117, no. 1, p. 011101, 2016. arXiv:1606.04226 [gr-qc].
- [256] J. Calderón Bustillo, J. A. Clark, P. Laguna, and D. Shoemaker, “Tracking black hole kicks from gravitational wave observations,” *Phys. Rev. Lett.*, vol. 121, no. 19, p. 191102, 2018.
- [257] C. O. Lousto and J. Healy, “Kicking gravitational wave detectors with recoiling black holes,” *Phys. Rev. D*, vol. 100, no. 10, p. 104039, 2019.
- [258] V. Varma, M. Isi, and S. Biscoveanu, “Extracting the Gravitational Recoil from Black Hole Merger Signals,” *Phys. Rev. Lett.*, vol. 124, no. 10, p. 101104, 2020.
- [259] V. Cardoso and C. F. B. Macedo, “Drifting through the medium: Kicks and self-propulsion of binaries within accretion discs and other environments,” *Mon. Not. R. Astron. Soc.*, vol. 498, no. 2, pp. 1963–1972, 2020.
- [260] M. J. Fitchett, “The influence of gravitational wave momentum losses on the centre of mass motion of a Newtonian binary system,” *Mon. Not. R. Astron. Soc.*, vol. 203, pp. 1049–1062, Aug. 1983.
- [261] L. Blanchet, M. S. S. Qusailah, and C. M. Will, “Gravitational recoil of inspiralling black hole binaries to second post-Newtonian order,” *Astrophys. J.*, vol. 635, pp. 508–515, 2005. astro-ph/0507692.
- [262] S. A. Hughes, M. Favata, and D. E. Holz, “How black holes get their kicks: Radiation recoil in binary black hole mergers,” in *Conference on Growing Black Holes: Accretion in a Cosmological Context Garching, Germany, June 21-25, 2004*, 2004. astro-ph/0408492.
- [263] T. Damour and A. Gopakumar, “Gravitational recoil during binary black hole coalescence using the effective one body approach,” *Phys. Rev. D*, vol. 73, p. 124006, 2006. gr-qc/0602117.
- [264] C. F. Sopuerta, N. Yunes, and P. Laguna, “Gravitational Recoil from Binary Black Hole Mergers: The Close-Limit Approximation,” *Phys. Rev. D*, vol. 74, p. 124010, 2006. [Erratum: Phys. Rev.D78,049901(2008)].
- [265] C. F. Sopuerta, N. Yunes, and P. Laguna, “Gravitational recoil velocities from eccentric binary black hole mergers,” *Astrophys. J.*, vol. 656, pp. L9–L12, 2007. astro-ph/0611110.
- [266] A. Le Tiec, L. Blanchet, and C. M. Will, “Gravitational-Wave Recoil from the Ringdown Phase of Coalescing Black Hole Binaries,” *Classical Quantum Gravity.*, vol. 27, p. 012001, 2010.
- [267] J. G. Baker, J. Centrella, D.-I. Choi, M. Koppitz, J. van Meter, and M. C. Miller, “Getting a kick out of numerical relativity,” *Astrophys. J.*, vol. 653, pp. L93–L96, 2006. gr-qc/0603204.
- [268] J. A. González, U. Sperhake, B. Brügmann, M. D. Hannam, and S. Husa, “The maximum kick from nonspinning black-hole binary inspiral,” *Phys. Rev. Lett.*, vol. 98, p. 091101, 2007. gr-qc/0610154.
- [269] F. Herrmann, I. Hinder, D. Shoemaker, and P. Laguna, “Unequal mass binary black hole plunges and gravitational recoil,” *Classical Quantum Gravity.*, vol. 24, no. 12, pp. S33–S42, 2007.
- [270] J. A. González, M. D. Hannam, U. Sperhake, B. Brügmann, and S. Husa, “Supermassive kicks for spinning black holes,” *Phys. Rev. Lett.*, vol. 98, p. 231101, 2007. gr-qc/0702052.
- [271] M. Campanelli, C. O. Lousto, Y. Zlochower, and D. Merritt, “Maximum gravitational recoil,” *Phys. Rev. Lett.*, vol. 98, p. 231102, 2007. gr-qc/0702133.
- [272] M. Campanelli, C. O. Lousto, Y. Zlochower, and D. Merritt, “Large Merger Recoils and Spin Flips From Generic Black-Hole Binaries,” *Astrophys. J.*, vol. 659, pp. L5–L8, 2007. gr-qc/0701164.
- [273] C. O. Lousto and Y. Zlochower, “Hangup Kicks: Still Larger Recoils by Partial Spin/Orbit Alignment of Black-Hole Binaries,” *Phys. Rev. Lett.*, vol. 107, p. 231102, 2011. arXiv:1108.2009 [gr-qc].

- [274] J. D. Schnittman and A. Buonanno, “The distribution of recoil velocities from merging black holes,” *Astrophys. J.*, vol. 662, pp. L63–L66, 2007. astro-ph/0702641.
- [275] M. Dotti, M. Volonteri, A. Perego, M. Colpi, M. Ruszkowski, and F. Haardt, “Dual black holes in merger remnants. II: spin evolution and gravitational recoil,” *MNRAS*, vol. 402, pp. 682–690, 2009. arXiv:0910.5729 [astro-ph].
- [276] M. Kesden, U. Sperhake, and E. Berti, “Relativistic Suppression of Black Hole Recoils,” *Astrophys. J.*, vol. 715, pp. 1006–1011, 2010. arXiv:1003.4993 [astro-ph].
- [277] C. O. Lousto, Y. Zlochower, M. Dotti, and M. Volonteri, “Gravitational Recoil From Accretion-Aligned Black-Hole Binaries,” *Phys. Rev. D*, vol. 85, p. 084015, 2012. arXiv:1201.1923 [gr-qc].
- [278] E. Berti, M. Kesden, and U. Sperhake, “Effects of post-Newtonian Spin Alignment on the Distribution of Black-Hole Recoils,” *Phys. Rev. D*, vol. 85, p. 124049, 2012. arXiv:1203.2920 [astro-ph].
- [279] S. Komossa, “Recoiling black holes: electromagnetic signatures, candidates, and astrophysical implications,” *Adv. Astron.*, vol. 2012, p. 364973, 2012. arXiv:1202.1977 [astro-ph].
- [280] M. Colpi, “Massive binary black holes in galactic nuclei and their path to coalescence,” *Space Sci. Rev.*, vol. 183, no. 1-4, pp. 189–221, 2014.
- [281] L. Blecha, D. Sijacki, L. Z. Kelley, P. Torrey, M. Vogelsberger, D. Nelson, V. Springel, G. Snyder, and L. Hernquist, “Recoiling black holes: prospects for detection and implications of spin alignment,” 2015. arXiv:1508.01524 [astro-ph].
- [282] D. Merritt, M. Milosavljević, M. Favata, S. Hughes, and D. Holz, “Consequences of gravitational radiation recoil,” *Astrophys. J.*, vol. 607, pp. L9–L12, 2004. astro-ph/0402057.
- [283] M. J. Benacquista and J. M. B. Downing, “Relativistic Binaries in Globular Clusters,” *Living Rev. Rel.*, vol. 16, p. 4, 2013.
- [284] J. Morawski, M. Giersz, A. Askar, and K. Belczynski, “MOCCA-SURVEY Database I: Assessing GW kick retention fractions for BH-BH mergers in globular clusters,” *Mon. Not. Roy. Astron. Soc.*, vol. 481, no. 2, pp. 2168–2179, 2018.
- [285] Z. Haiman, “Constraints from gravitational recoil on the growth of supermassive black holes at high redshift,” *Astrophys. J.*, vol. 613, pp. 36–40, 2004. astro-ph/0404196.
- [286] M. J. Graham, K. E. S. Ford, B. McKernan, N. P. Ross, D. Stern, K. Burdge, M. Coughlin, *et al.*, “Candidate Electromagnetic Counterpart to the Binary Black Hole Merger Gravitational Wave Event S190521g,” *Phys. Rev. Lett.*, vol. 124, no. 25, p. 251102, 2020.
- [287] H.-Y. Chen, C.-J. Haster, S. Vitale, W. M. Farr, and M. Isi, “A Standard Siren Cosmological Measurement from the Potential GW190521 Electromagnetic Counterpart ZTF19abanrhr.” 9 2020.
- [288] U. Sperhake, R. Rosca-Mead, D. Gerosa, and E. Berti, “Amplification of superkicks in black-hole binaries through orbital eccentricity,” *Phys. Rev. D*, vol. 101, no. 2, p. 024044, 2020.
- [289] J. Samsing and E. Ramirez-Ruiz, “On the Assembly Rate of Highly Eccentric Binary Black Hole Mergers,” *Astrophys. J. Lett.*, vol. 840, no. 2, p. L14, 2017.
- [290] J. Samsing, “Eccentric Black Hole Mergers Forming in Globular Clusters,” *Phys. Rev. D*, vol. 97, no. 10, p. 103014, 2018.
- [291] J. Samsing, A. Askar, and M. Giersz, “MOCCA-SURVEY Database. I. Eccentric Black Hole Mergers during Binary–Single Interactions in Globular Clusters,” *Astrophys. J.*, vol. 855, no. 2, p. 124, 2018.

- [292] C. L. Rodriguez, P. Amaro-Seoane, S. Chatterjee, K. Kremer, F. A. Rasio, J. Samsing, C. S. Ye, and M. Zevin, “Post-Newtonian Dynamics in Dense Star Clusters: Formation, Masses, and Merger Rates of Highly-Eccentric Black Hole Binaries,” *Phys. Rev. D*, vol. 98, no. 12, p. 123005, 2018.
- [293] J. Samsing, I. Bartos, D. D’Orazio, Z. Haiman, B. Kocsis, N. Leigh, B. Liu, M. Pessah, and H. Tagawa, “Active Galactic Nuclei as Factories for Eccentric Black Hole Mergers.” 10 2020.
- [294] H. Tagawa, B. Kocsis, Z. Haiman, I. Bartos, K. Omukai, and J. Samsing, “Eccentric Black Hole Mergers in Active Galactic Nuclei,” *Astrophys.J.Lett.*, vol. 907, no. arXiv:2010.10526, p. L20, 2021.
- [295] V. Cardoso, C. F. B. Macedo, and R. Vicente, “Eccentricity evolution of compact binaries and applications to gravitational-wave physics,” *Phys. Rev. D*, vol. 103, no. 2, 2021.
- [296] B. Abbott *et al.*, “Search for Eccentric Binary Black Hole Mergers with Advanced LIGO and Advanced Virgo during their First and Second Observing Runs,” *Astrophys. J.*, vol. 883, no. 2, p. 149, 2019.
- [297] R. Abbott *et al.*, “GW190521: A Binary Black Hole Merger with a Total Mass of 150 M_\odot ,” *Phys. Rev. Lett.*, vol. 125, no. 10, p. 101102, 2020.
- [298] I. M. Romero-Shaw, P. D. Lasky, E. Thrane, and J. C. Bustillo, “GW190521: Orbital eccentricity and signatures of dynamical formation in a binary black hole merger signal,” *Astrophys.J.Lett.*, vol. 903, no. 1, p. L5, 2020.
- [299] V. Gayathri, J. Healy, J. Lange, B. O’Brien, M. Szczepanczyk, I. Bartos, M. Campanelli, S. Klimenko, C. Lousto, and R. O’Shaughnessy, “GW190521 as a Highly Eccentric Black Hole Merger.” 9 2020.
- [300] A. Nishizawa, E. Berti, A. Klein, and A. Sesana, “eLISA eccentricity measurements as tracers of binary black hole formation,” *Phys. Rev. D*, vol. 94, no. 6, p. 064020, 2016.
- [301] K. Breivik, C. L. Rodriguez, S. L. Larson, V. Kalogera, and F. A. Rasio, “Distinguishing Between Formation Channels for Binary Black Holes with LISA,” *Astrophys. J. Lett.*, vol. 830, no. 1, p. L18, 2016.
- [302] A. Nishizawa, A. Sesana, E. Berti, and A. Klein, “Constraining stellar binary black hole formation scenarios with eLISA eccentricity measurements,” *Mon. Not. R. Astron. Soc.*, vol. 465, no. 4, pp. 4375–4380, 2017.
- [303] C. Roedig and A. Sesana, “Origin and Implications of high eccentricities in massive black hole binaries at sub-pc scales,” *J. Phys. Conf. Ser.*, vol. 363, p. 012035, 2012.
- [304] M. Bonetti, A. Sesana, F. Haardt, E. Barausse, and M. Colpi, “Post-Newtonian Evolution of Massive Black Hole Triplets in Galactic Nuclei: IV. Implications for LISA,” 2018.
- [305] E. Huerta *et al.*, “Physics of eccentric binary black hole mergers: A numerical relativity perspective,” *Phys. Rev. D*, vol. 100, no. 6, p. 064003, 2019.
- [306] <http://www.grchombo.org/>.
- [307] M. Adams *et al.*, “Chombo Software Package for AMR Applications - Design Document,” Tech. Rep. LBNL-6616E, Lawrence Berkeley National Laboratory, 2019.
- [308] M. Berger and I. Rigoutsos, “An algorithm for point clustering and grid generation,” *IEEE Trans. Sys. Man & Cybernet.*, vol. 21, no. 5, pp. 1278–1286, 1991.
- [309] T. Goodale, G. Allen, G. Lanfermann, J. Massó, T. Radke, E. Seidel, and J. Shalf, “The Cactus framework and toolkit: Design and applications,” in *Vector and Parallel Processing – VEP-PAR’2002, 5th International Conference, Lecture Notes in Computer Science*, (Berlin), Springer, 2003.

- [310] T. Nakamura, K. Oohara, and Y. Kojima, “General Relativistic Collapse To Black Holes And Gravitational Waves From Black Holes,” *Prog. Theor. Phys. Suppl.*, vol. 90, pp. 1–218, 1987.
- [311] E. Schnetter, S. H. Hawley, and I. Hawke, “Evolutions in 3-D numerical relativity using fixed mesh refinement,” *Class. Quant. Grav.*, vol. 21, pp. 1465–1488, 2004. gr-qc/0310042.
- [312] J. Thornburg, “Finding apparent horizons in numerical relativity,” *Phys. Rev. D*, vol. 54, pp. 4899–4918, 1996. gr-qc/9508014.
- [313] J. Thornburg, “A Fast apparent horizon finder for three-dimensional Cartesian grids in numerical relativity,” *Class. Quant. Grav.*, vol. 21, pp. 743–766, 2004. gr-qc/0306056.
- [314] S. Brandt and B. Brügmann, “A Simple construction of initial data for multiple black holes,” *Phys. Rev. Lett.*, vol. 78, pp. 3606–3609, 1997. gr-qc/9703066.
- [315] J. M. Bowen and J. W. York, Jr., “Time-asymmetric initial data for black holes and black-hole collisions,” *Phys. Rev. D*, vol. 21, pp. 2047–2056, 1980.
- [316] M. Ansorg, B. Brügmann, and W. Tichy, “A single-domain spectral method for black hole puncture data,” *Phys. Rev. D*, vol. 70, p. 064011, 2004. gr-qc/0404056.
- [317] V. Paschalidis, Z. B. Etienne, R. Gold, and S. L. Shapiro, “An efficient spectral interpolation routine for the TwoPunctures code.” 4 2013.
- [318] B. Brügmann, J. A. González, M. D. Hannam, S. Husa, U. Sperhake, and W. Tichy, “Calibration of Moving Puncture Simulations,” *Phys. Rev. D*, vol. 77, p. 024027, 2008. gr-qc/0610128.
- [319] J. W. York, Jr., *Initial data for collisions of black holes and other gravitational miscellany*, p. 89. Cambridge, England: Cambridge University Press, Jan. 1989.
- [320] N. Loutrel, S. Liebersbach, N. Yunes, and N. Cornish, “The eccentric behavior of inspiralling compact binaries,” *Classical Quantum Gravity.*, vol. 36, no. 2, p. 025004, 2019.
- [321] R.-M. Memmesheimer, A. Gopakumar, and G. Schaefer, “Third post-Newtonian accurate generalized quasi-Keplerian parametrization for compact binaries in eccentric orbits,” *Phys. Rev. D*, vol. 70, p. 104011, 2004.
- [322] M. Campanelli and C. O. Lousto, “Second order gauge invariant gravitational perturbations of a Kerr black hole,” *Phys. Rev. D*, vol. 59, p. 124022, 1999. gr-qc/9811019.
- [323] C. O. Lousto and Y. Zlochower, “A practical formula for the radiated angular momentum,” *Phys. Rev. D*, vol. 76, p. 041502, 2007. gr-qc/0703061.
- [324] M. Ruiz, R. Takahashi, M. Alcubierre, and D. Nuñez, “Multipole expansions for energy and momenta carried by gravitational waves,” *Gen. Rel. Grav.*, vol. 40, pp. 1705–1729, 2008. arXiv:0707.4654 [gr-qc].
- [325] J. Healy, C. O. Lousto, and Y. Zlochower, “Nonspinning binary black hole merger scenario revisited,” *Phys. Rev. D*, vol. 96, no. 2, p. 024031, 2017.
- [326] B. Brügmann, J. A. González, M. D. Hannam, S. Husa, and U. Sperhake, “Exploring black hole superkicks,” *Phys. Rev. D*, vol. 77, p. 124047, 2008.
- [327] C. O. Lousto, H. Nakano, Y. Zlochower, and M. Campanelli, “Statistical studies of Spinning Black-Hole Binaries,” *Phys. Rev. D*, vol. 81, p. 084023, 2010. [Erratum: Phys.Rev.D 82, 129902 (2010)].
- [328] A. G. Wiseman, “Coalescing binary systems of compact objects to (post)5/2 Newtonian order. 2. Higher order wave forms and radiation recoil,” *Phys. Rev. D*, vol. 46, pp. 1517–1539, 1992.

- [329] M. Kesden, D. Gerosa, R. O’Shaughnessy, E. Berti, and U. Sperhake, “Effective potentials and morphological transitions for binary black-hole spin precession,” *Phys. Rev. Lett.*, vol. 114, no. 8, p. 081103, 2015. arXiv:1411.0674 [gr-qc].
- [330] D. Gerosa, M. Kesden, U. Sperhake, E. Berti, and R. O’Shaughnessy, “Multi-timescale analysis of phase transitions in precessing black-hole binaries,” *Phys. Rev. D*, vol. 92, no. 6, p. 064016, 2015. arXiv:1506.03492 [gr-qc].
- [331] C. Hamilton and R. R. Rafikov, “Secular dynamics of binaries in stellar clusters - I. General formulation and dependence on cluster potential,” *Mon. Not. Roy. Astron. Soc.*, vol. 488, no. 4, pp. 5489–5511, 2019.
- [332] C. Hamilton and R. R. Rafikov, “Secular dynamics of binaries in stellar clusters - II. Dynamical evolution,” *Mon. Not. Roy. Astron. Soc.*, vol. 488, no. 4, pp. 5512–5535, 2019.
- [333] U. Sperhake, B. Brügmann, D. Müller, and C. F. Sopuerta, “11-orbit inspiral of a mass ratio 4:1 black-hole binary,” *Class. Quant. Grav.*, vol. 28, p. 134004, 2011. arXiv:1012.3173 [gr-qc].
- [334] N. T. Bishop and L. Rezzolla, “Extraction of gravitational waves in numerical relativity,” *Living Reviews in Relativity*, vol. 20, no. 1, p. 1, 2016. arXiv:1606.02532 [gr-qc].